Process Intensification through Electric Field Enhanced Crystallisation and Particle Separation

Carlos Moreno Leon

Supervisor: Professor Joop ter Horst

Second Supervisor: Professor Sudipta Roy

October 2020

Thesis submitted in satisfaction with the requirements of the Strathclyde Institute of Pharmacy and Biomedical Sciences at the University of Strathclyde for the Degree of Doctor of Philosophy.

I declare that this thesis is the result of the author's original research. It has been composed by the author and has not been previously submitted for examination which has led to the award of a degree. The work contained herein is my own except where explicitly stated otherwise in the text. Due references have been provided on all supporting literatures and resources.

Signed:

Date:

For Marcela

Acknowledgements

I would like to say thanks to all the people that have supported me and contributed to the completion of this PhD dissertation during these four years of work.

First and foremost, I would like to express my deepest gratitude to my supervisor Prof. Joop Ter Horst as his guidance, encouragement, and endless support have been invaluable during my PhD, and for that I am most grateful. It has been a privilege working in your group and I sincerely wish that our paths will cross in the future. Many thanks also to Prof. Sudipta Roy for your words of wisdom, providing me with interesting perspectives, and your supervision these last four years.

I wish to show my gratitude to my hosts and colleagues at Delf University of Technology where I spent 3 months on an academic placement. I really appreciated you offering me your space, academic guidance, as well as making me feel very welcome in your team. I am specially indebted to Dr. Weiwei Li, who not only took the time to explain me the separation method I have been using during the last four years but also showed me the Delft and introduced me to people who I always remember (Dr. Herman Kramer, Dr. Antoine van der Heijden, and Dr. Marloes Reus). Thank you for your friendship, I enjoyed visiting you for your viva and the party celebration.

I would like to extend a thank you to Dr. Todd Green for providing me with a working space in the electrochemistry lab for the first years of work and for helping me to setup the equipment I used during most of my PhD. To Dr. Cameron Brown for offering his programming skills to help me analysing the produced data, and Dr. Ali Anwar who help design and build the electrophoresis cell.

I would like to acknowledge the financial support of the EPRSC, and the training and support that the CMAC has provided me with. I would also like to say thank you to my former and present colleagues at the CMAC, I have especially enjoyed the project discussions, football

games, and conference trips. I would like to also thank the National Facility team, and within the NF team, I would like to pay my special regards to Dr Alan Martin, whose advice in the area of crystallography has been undoubtedly useful for the completion of this dissertation. Also to the administration team for all the assistant during the last four years. Thanks to Rebekah Russell and Dr. Ian Houson who make possible my industrial placement at Pfizer, Ireland. Further, I wish to express my deepest gratitude to my industrial supervisors Imelda O'Connor and Dr. Lorna Moynihan for the opportunity and fantastic experience of working in your group.

To my family, huge thanks, as having your support and motivation, even from far away has been fundamental in keeping my motivation throughout these years, particularly during difficult times. I am really looking forward to spending a nice and long vacation either in the sunny Malaga or the Scottish chilly summer. A special thanks to Marcela for your patience and encouragement, as well as putting up with my exceptionally optimistic perspective of time and deadlines.

Abstract

Crystallisation is a fundamental unit operation in purification and separation process. It has been amply adopted in the pharmaceutical and fine chemical industry as a product of high purity can be obtained in a particulate solid form. This unit operation allows for tailoring product characteristics, providing extensive benefits to industries that operate in highly regulated environments. In particular, the pharmaceutical industry must abide with a complex set of regulations and laws imposed on drug products intended to protect the health of the public. Thus, in order to gain a competitive edge, pharmaceutical industries invest significant time and resources to optimize the manufacturing process. In this context, increasing research is focused on the optimization of crystallisation. One of the major issues that may occur during the purification process is the concomitant crystallisation of other substances together with the Active Pharmaceutical Ingredient (API), which may reduce the purity of the product below the compliance level.

This thesis explores the effects of an externally applied electric field on suspended crystals and on crystallisation, aiming at the understanding of the fundamental principles of the interaction of the electric field with suspensions of particles and solutions of small organic molecules such as pharmaceutical compounds. Then, electric fields can be exploited as a process intensification tool to aid purification processes. For instance, rather than alleviating a concomitant crystallisation problem, the use of an externally applied field could make use of a concomitantly crystallising system to purify and separate two crystalline products in a single process step.

The manipulation of suspended particles driven by electric field requires elevated electric fields which might result in the generation of electric current into the fluid system, inducing undesired chemical reactions that may affect the final product. To minimize electric current, non-polar solvents constitute of small molecules such as dioxane can be used. In Chapter 3, the solution behaviour of a number of APIs in non-polar solvents are studied in order to define

suitable systems that resist electrolysis under strong electric fields, and therefore allow for the design of crystallisation processes under such conditions. From a number of thermodynamic models, the van ’t Hoff equations presented good correlation values to the experimental data, and therefore it can be used to extrapolate and interpolate solubility data at any given temperature. In addition, solution behaviour was studied from determined activity coefficients, which showed that all the studied systems positively or negatively deviated from ideality. The Wilson activity coefficient model was used to predict these deviations.

From well-defined systems, particle and solution properties can then be related to the electric field phenomena, leading to the identification of the scientific principles behind the interactions between the particles and the electric field. Suspensions of APIs of small organic molecules in different apolar solvent were studied under the presence of non-uniform and uniform electric fields in Chapter 4, which enabled to assess the electrokinetic phenomena associated to the motion of the suspended crystalline particles. Under an electric field, suspended particles travelled to and accumulated on a particular electrode. The greater dielectric properties of the organic compounds compared to that of the apolar solvents induces a motion of particles towards an electrode by positive dielectrophoresis. The collection of particles on an electrode of a particular charge is due to electrophoretic forces acting on the surface charge of the particle. The collection on a specific electrode was anticipated by the sign of the zeta-potential of the solid phase. Other phenomena such as electro-osmosis and electrorheological fluids were observed in the studied systems in the presence of a strong electric field.

The investigation of equilibrated suspensions in an electric field raises the question of the effects of the energy input in metastable systems. Chapter 5 explores the effect of strong electric fields in crystallisation processes of solutions of a small organic compound (isonicotinamide) in a non-polar solvent (dioxane). An electric field directly applied to a supersaturated solution of isonicotinamide in 1,4-dioxane enhances the nucleation kinetics of the small organic molecules. Thus, in the presence of an electric field, nucleation occurs at higher temperatures and shorter induction times for a given solution composition compared to crystallisation processes in the absence of an externally applied field. A plausible explanation is the accumulation of monomers of the crystalline compound in the vicinity of the electrodes due to electrokinetic forces. This phenomenon could increase the local supersaturation, resulting in an effective increase of the frequency of successful attachment of building units.

Then, the combined action of the electric field effects on suspended particles and crystallisation from solution can be applied to developing means to exploit the electric field phenomena for the separation of heterogeneous suspensions. In Chapter 6, a number of multi-component mixtures have been successfully separated in-situ by the use of inhomogeneous electric fields. The separation of two crystallising compounds that collect on opposite electrodes under the electric field was achieved with high purity values by cooling crystallisation in the presence of the field. In addition, the separation of compounds that collect on counter electrodes was carried out by a two-step seeding/cooling crystallisation method driven by electric fields. Thus, the separation method can potential be implemented as a tool to aid separation and purification processes.

This thesis investigated the scientific principles behind the interaction of the electric field with both particle suspensions and crystallising solutions. By relating particle and solution properties to the observed phenomena, we were able to anticipate the behaviour of particles and solutions in an electric field, and then exploit the phenomena to separate complex mixtures of two crystallising compounds in situ. The gained knowledge can be applied as an intensification tool to aid purification and separation processes.

List of Figures

List of Tables

Contents

Chapter 1. Introduction

Highly regulated industries such as pharmaceuticals abide with strict regulations and laws imposed by regulatory bodies and governments on their manufactured products intended to protect the health of the general public. Since the conditions of the manufacturing process significantly affect the properties of the drug product, any change in production must obtain the approval of regulators before commercialization. Therefore, production has been traditionally carried out by following a series of defined steps validated at the end of the drug development, while the optimization of the process has been frequently neglected. This business model allowed the industry to fast release the medicine into the market in order to maximize profits during the patent protection period.[1] However, the success of this business model has declined over the last decade, primarily due to increasing research costs on the development of new drug substances, strict regulation requirements, and growing competition from generic manufactures.[2] Consequently, the industry research attention has been shifted towards the manufacturing process, which offers a window of opportunity to gain competitive advantages through process optimization.

Current trends on research concerning manufacturing processes of active pharmaceutical ingredients (APIs) have contributed to a significant progression in science and engineering that has permitted the industry to become more competitive through cutting production costs and reducing product time delivery. Particularly, many research efforts have been done on the development of innovative separation-control technologies. Drug formulation usually consist of several reaction steps, in which separation processes are essential to isolate the valuable product from any impurities that may remain at the end of the process.[3,4] The removal of impurities is especially relevant in the pharmaceutical industry, as the biological activity of the commercial medicine can be significantly influenced by the presence of undesired substances. For instance, manufacturers are demanded to remove any toxic precursors that are employed to trigger complex reactions for the synthesis of pharmaceuticals.[5,6]

One example of the research focus on the improvement of separation processes is the use of alternative energy sources as a process intensification tool in crystallisation, aiming at maximizing the phase separation efficiency while attaining or exceeding production demands.[7] Crystallisation is amply adopted in the pharmaceutical industry as a high purity product can be produced in a particulate form in a single step.[8] Additionally, the properties of the API can be tailored during crystallisation, and therefore by optimizing the process further purification and/or separation operations may be unnecessary. On this basis, external fields offer an excellent control over mass and heat transfer that proved beneficial for crystallisation processes. The most common energy sources applied to crystallisation include ultrasound, microwave, laser, electric fields, and magnetic fields.[1] Table 1.1 compiles a series of publications on crystallisation assisted by the listed energy domains.

Table 1.1. Examples of separation intensification methods used for the separation and purification of pharmaceutical and biopharmaceutical products based on the use of external fields

Energy Source	**Examples of crystallisation assisted by external field**	**Reference**
Ultrasound	Accelerated co-crystallisation of caffeine and maleic acid by ultrasound.	[9]
	Improved purity of paracetamol though sonocrystallisation.	[10]
	Protein crystallisation promotion by ultrasound irradiation.	[11]
	Polymorphism and particle size control of paracetamol by ultrasound assisted crystallisation.	[12]
	Agglomeration control during crystallisation processes assisted by ultrasound.	[13]
Microwave	Evaporative crystallisation of glutathione tripeptide assisted by microwave heating.	[14]
	Crystallisation enhancement and particle size control using microwave heating.	[15]
	Co-crystallisation of sulfamethazine/nicotinamide by microwave irradiation.	[16]
Laser	Laser promotes crystallisation of glycine in aqueous solutions.	[17]
	Acceleration of protein crystallisation by laser irradiation.	[18]
	Non-photochemical laser irradiation promotes crystallisation of sulfathiazole.	[19]
	Polymorphism control of paracetamol during crystallisation by double-pulse laser irradiation.	[20]
	Crystal shape control of protein and amino acids during crystal growth by laser ablation.	[21]
Electric Field	Continuous flow crystallisation of proteins assisted by electric fields.	[22]
	Polymorphic crystallisation control by electric fields.	[23]
	Spatial and temporal control over nucleation of proteins by localized weak DC electric fields.	[24]
	Nucleation control and decreased induction time on crystallisation of lysozymes.	[25]
	Microfluidic device for particle manipulation and crystallisation control by electric fields..	[26]
Magnetic Field	Crystallisation rate control of paracetamol by static magnetic fields.	[27]
	Development of a superconducting magnet for crystallisation of proteins of enhanced quality.	[28]
	Crystal quality improved by strong magnetic fields.	[29]
	Enhancement of protein crystal quality in the presence of strong magnetic fields.	[30]

Despite the advantages offered by these technique, the direct application of the purification process to heterogeneous solution may cause concomitant crystallisation, which affects the quality of the API.[31] Therefore, a separation method that combines crystallisation and in-situ particle isolation is desired to optimize the separation and purification process. In this context, electric fields not only present a positive effect on crystallisation from solution, but the use of this energy input has also been implemented as a process tool for the manipulation of suspended particles. Numerous electric field separation methods have been emerged over the last decades, exploiting electrokinetic phenomena such as electrophoresis and dielectrophoresis for the separation, trapping, and focussing of solid particles in suspensions.[32–34] However, the use of these techniques have been merely applied to colloidal suspension in fluid media with no dissolved species. Only recently, Li et al.[35] developed a hybrid separation method based on the combined effects of crystallisation and electric fields. In this work, the isolation of the different compounds in a heterogeneous suspension was completed with product purities higher than 90%. The authors also observed that the isolated crystals continue growing over the experimental period, which was ascribed to the slow reduction of the temperature in the presence of the electric field. Thus, this novel technique emerges as a powerful intensification tool for simultaneous separation and purification operations. However, the focus attention of Li’s work was the separation of complex mixtures, and the mechanistic phenomena behind the purification technique has not yet been clarified. Therefore, a concise investigation into the mechanistic principles of the interaction of the electric field with both solution and suspensions is needed to further develop the introduced purification and separation technique and to address its scope and applicability.

1.1. Crystallisation

Crystallisation is a fundamental unit operation in the pharmaceutical industry, widely used for the purification of APIs and intermediate products. This unit operation offers a relative low energy consumption method to obtain a product of high quality in a particulate form, which is considered as an industrial advantage in terms of downstream processes, formulation, storage, and transport.[8]

This unit operation can be described as a phase transition, in which a metastable system attempts thermodynamic equilibrium through the formation and growth of a daughter phase.

In the pharmaceutical industry, the formation of the solid phase is commonly induced from solution, [36] being the chemical potential (μ) difference between the liquid and solid states the driving force for crystallisation. For binary systems, the chemical potential difference is given by:

$$\Delta\mu = \mu_l - \mu_s \tag{1.1}$$

where μ_l and μ_s are the chemical potential of the solute in solution and in a solid state, respectively. Crystallisation occurs spontaneously when the chemical potential difference is positive ($\Delta\mu > 0$), and the solution is said to be supersaturated. A binary system is in equilibrium (saturated) when $\Delta\mu = 0$ and is undersaturated if $\Delta\mu < 0$. The chemical potential difference is often expressed in terms of the superaturation (S) as:

$$\Delta\mu = k_B T \ln S \tag{1.2}$$

here, μ_0 is the standard potential, k_B refers to the Boltzmann's constant, and T is the absolute temperature. For non-dissociated systems, supersaturation can be approximated to a function of the concentration of the solute in solution (c) and the concentration at equilibrium (c^*) at a defined pressure and temperature:

$$S = \frac{c}{c^*} \tag{1.3}$$

This expression permits to simply identify supersaturated solutions ($S > 1$) provided the solubility of the solute in the liquid medium is available. The solubility is a paramount factor to crystallisation processes. It defines the equilibrium between the solid and liquid phases for a specific temperature, and it is commonly represented by a graphical representation of the saturated concentration versus the absolute temperature. Figure 1.1 shows a typical temperature-dependent solubility diagram for a binary system in which the equilibrium concentration increases with increasing temperature. Three distinctive regions can be identified in the diagram: 1) the stable (undersaturated) zone, 2) the metastable (supersaturated) zone, and 3) the labile (unstable) zone. In the undersaturated zone, the system is thermodynamically stable, and concentration of the solute is insufficient to promote crystallisation ($S < 1$). In the metastable region, crystallisation can be triggered by fluctuation in the thermodynamic variables. Spontaneous nucleation occurs in the labile zone.

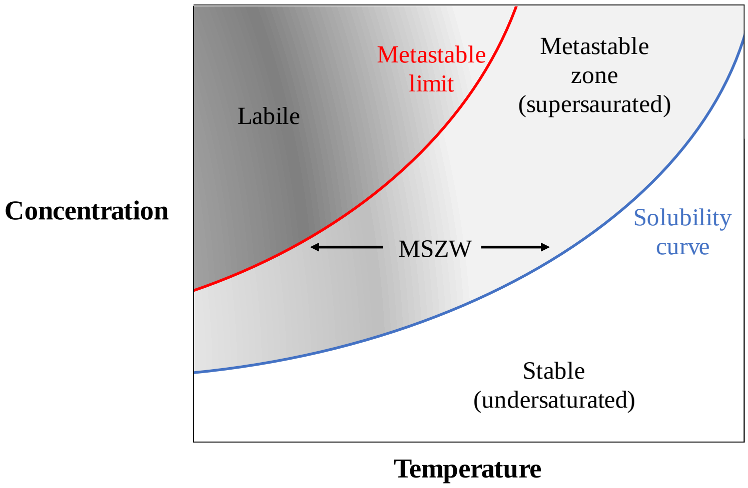

Figure 1.1. Schematic of a temperature-dependent solubility diagram. Three separated regions can be differentiated: 1) the undersaturated zone, where crystallisation is not attainable, 2) the metastable zone, in which crystallisation can be induced by thermodynamic changes in the systems, and 3) the labile zone, where nucleation occurs spontaneously. The metastable zone is limited by the solubility curve (blue) and the metastable limit (red). The area between these boundaries is the metastable zone width (MSZW).

To induce crystallisation, the system composition must exceed the solubility curve in order to reach a supersaturated state. This has been traditionally carried out by variations in temperature, solvent removal, or addition of a drowning-out or reaction agents. For instance, a binary system placed in the undersaturated region can be moved within the metastable zone by increasing the solute concentration through solvent evaporation or by decreasing the solubility via temperature reduction. These crystallisation methods and others are explained in more detail elsewhere.[8]

1.1.1. Crystal nucleation and growth

Nucleation is the initial sub-process in the formation of a crystalline solid phase. Once a thermodynamic fluctuation is induced in a metastable system, a daughter phase commences to form in order for the system to return to a thermodynamic equilibrium state. Nucleation can be classified into primary if the process take place in the absence of parent crystals, or secondary when parent crystals are present in solution. Primary nucleation occurs either in a clear solution (homogeneous) or in the presence of foreign particles or substrates (heterogeneous). Figure 1.2 shows a schematic of the different nucleation phenomena. An in-depth study of the nucleation process was conducted by Kashchiev.[37]

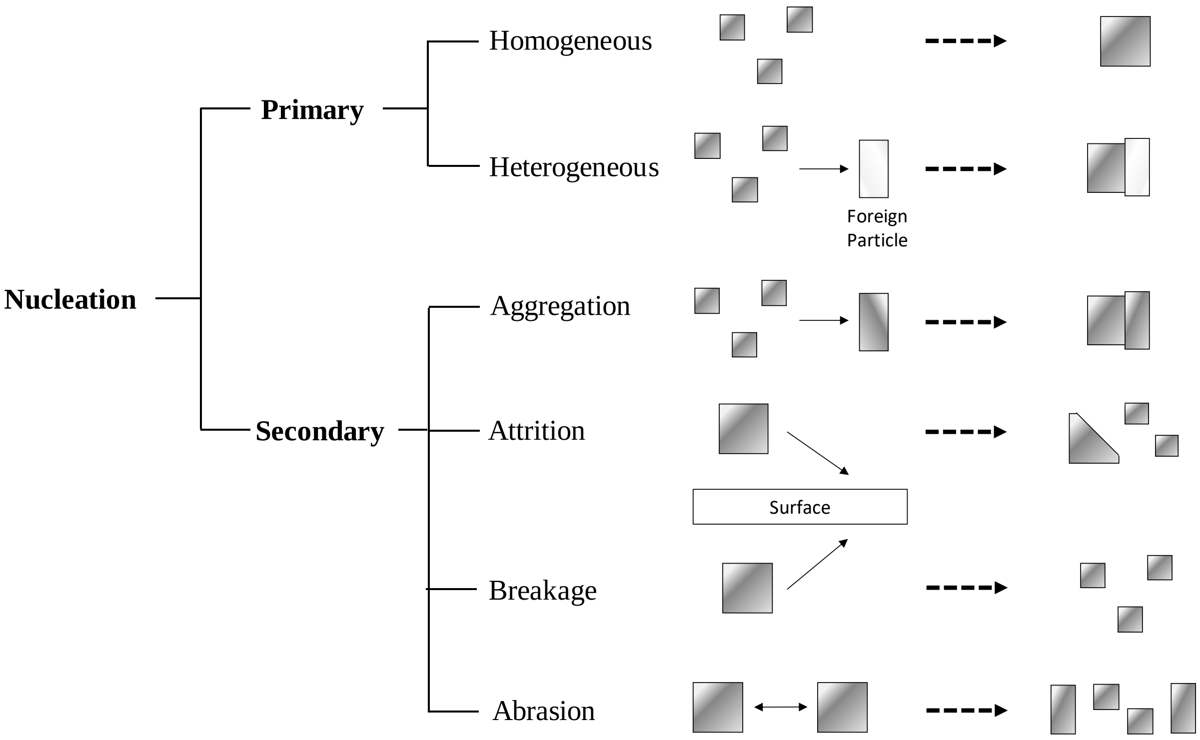

Figure 1.2. Nucleation can be classified into primary and secondary. Primary nucleation occurs in the absence of parent crystals and can be further divided into homogeneous nucleation if the process takes place in the bulk solution, or heterogeneous nucleation when foreign particles are presence. Secondary nucleation occurs in the presence of parent crystals, added to a clear solution or originated from an existing parent phase.

1.1.1.1. Primary Nucleation: The Classical Nucleation Theory

In low and large scale crystallisation processes, heterogeneous primary nucleation is the main mechanism due to the inevitable presence of foreign particles in the crystallisation vessels during operations. Only under extreme conditions homogeneous nucleation has been observed.[8] However, the former mechanism is not fully understood as the nature and number of the heterogeneous particles are usually unknown. Therefore, primary nucleation processes are commonly described through homogeneous nucleation. According to the classical nucleation theory (CNT), nucleation is the result of bimolecular collisions which repeated occurrence may result in the formation of a stable cluster with distinct properties from the surrounding medium. Figure 1.3 presents a schematic of attachment and detachment process to form a cluster of n building units. This theory was formulated for the nucleation of liquid droplets in a vapour phase, however its principles are applicable to explain the nucleation process of crystalline material from solution.[36]

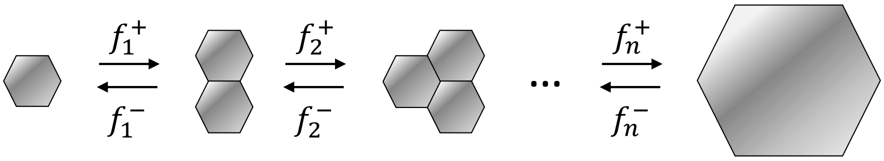

Figure 1.3. Schematic of the cluster formation described by the Classical Nucleation Theory (CNT). The process of the formation of the solid phase consists on a series of individual collisions in which a single monomer may or may not incorporate to the cluster and form a thermodynamic stable structure. In the figure, the terms f_i^+ and f_i^-respectively represent the rate of the attachment and detachment reactions.

Nucleation can be described thermodynamically as a trade-off between the energy loss to form the daughter phase (ΔG_S) and the energy gain from the transition to a more stable phase (ΔG_V). In a homogeneous an isotropic system, the work to form a spherical cluster of size r is given by:

$$\Delta G = \Delta G_S - \Delta G_V = 4\pi r^2 \gamma - \frac{4}{3v} \pi r^3 k_B T \ln S \tag{1.4}$$

where v is the molecular volume, and γ is the interfacial tension between the bulk medium and the new phase. Equation (1.4), shows that small clusters dissolve in order to reduce their radius and decrease the positive contribution of the surface term to the total energy. On the other hand, the volume term dominates on cluster of larger sizes, with the consequent decrease of the free energy through nucleation. Thus, the total energy reaches a maximum value over the progression from a surface to a volume dominant state. This energy barrier determines the minimum size of a cluster (r^*) for spontaneous nucleation to occur. A cluster size r^* is called nucleus. The critical size can be obtained by the minimization of equation (1.4) with respect to the radius:

$$r^* = \frac{32\pi\gamma^3 v^2}{3(k_B T \ln S)^3} \tag{1.5}$$

and the critical nucleation work can be determined by the substitution of equation (1.5) into equation (1.4):

$$\Delta G^* = \frac{16\pi\gamma^3 v^2}{3(k_B T \ln S)^2} \tag{1.6}$$

The equation shows the thermodynamic dependency of nucleation on supersaturation. A large supersaturation value reduces the nucleation work, while a low value is associated to an elevated energy barrier for nucleation. The thermodynamic factors regarding nucleation are depicted in Figure 1.4.

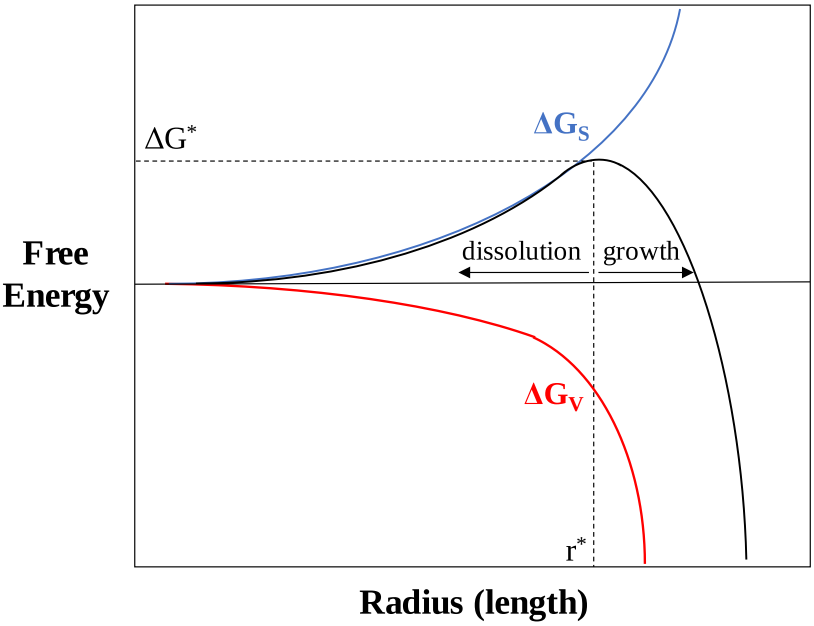

Figure 1.4. The Gibbs free energy of cluster formation is given by the balance of the energy required to form a surface with distinct properties from the surrounded medium (ΔG_S) and the volume energy(ΔG_V) as a result of the formation of a more stable phase. The energy barrier for nucleation (ΔG^*) represents the state at which the cluster is thermodynamic stable. At ΔG^*, the cluster neither dissolves nor grows. This energy barrier is reached when the addition/attachment of building units form a cluster of a size r* known as nucleus.

The CNT defines the stationary nucleation rate J as the number of nuclei formed per unit time and volume:

$$J = A \exp\left(\frac{-B}{\ln^2 S}\right) = f^* z C_0 \exp\left(\frac{-\Delta G^*}{k_B T}\right) \tag{1.7}$$

in this equation, A is the pre-exponential factor and B is a thermodynamic factor. The pre-exponential factor can be expressed as a product of the frequency of attachment of building units (f^*), the concentration of nucleus sites in equilibrium (C_0), and the Zeldovich factor (z), which accounts for the deviation of the actual nuclei concentration from the concentration at equilibrium. Based on the theoretical work conducted by Kashchiev, the equations for the attachment frequency and the Zeldovich factor become:

$$f^* = \frac{\delta a D C}{d} \tag{1.8}$$

$$z = \frac{\ln^2 S}{\sqrt{12\pi k_B T B}} \tag{1.9}$$

where, a is the area of the area of the nucleus surface, D is the diffusion coefficient of the monomer in the medium, C is the actual concentration of nuclei, d refers to the monomer diameter, δ is a coefficient that accounts for the building units that do not attach to the cluster, and B refers to the thermodynamic factor in the stationary nucleation rate equation.

1.1.1.2. Secondary nucleation

Secondary nucleation occurs in the presence of crystals of the same molecular species. Following the formation of the crystal, the depletion of supersaturation leads to a secondary nucleation dominant state, in which nuclei are generated from the existing parent crystals by forces originated in the crystalliser. The main nucleation mechanisms include attrition, shear, initial breeding, dendritic, and collisions between crystals.[8]

1.1.1.3. Crystal Growth

Once the clusters have reached the critical size, the formed nuclei start to grow. Crystal growth can be explained by the diffusion of solute molecules towards the nucleus surface and their subsequent incorporation in the crystal lattice. Apart from hydrodynamic factors, crystal growth is greatly influence by supersaturation and the solubility of the solute in the liquid medium. These properties determine the number of available molecules and their deposition velocity onto the crystal.[38]

1.1.2. Crystal Quality

The quality of crystalline products is given by their size, shape, purity, and crystalline form, and relates to the physicochemical properties of the final product. The importance to reduce the presence of impurities to very low levels have been previously discussed. Apart from purity, control over other quality factors is essential in crystallisation. For instance, the polymorphic form of the crystal influences the dissolution rate and bioavailability of the API.[39] Polymorphism refers to the molecular arrangement in the crystal lattice, and the ability of a crystal to exist in more than one crystalline structure.[36] Polymorphism dictates the shape of the crystal, which together with the particle size distribution affect downstream processes. Needle-like crystals and very fine powder fractions have a negative impact on filtration, drying, and storage operations.[8]

Crystal properties are defined during nucleation and growth. Therefore, crystallisation control is paramount to obtain a crystallised API with the desired quality attributes. In crystallisation from solution, process control has been traditionally conducted via supersaturation. A solubility diagram, derived from a comprehensive knowledge of the thermodynamics and kinetics of the system, allows to predict the effects of supersaturation on crystallisation, which can be used to design operation conditions.[40] Other routes to control crystallisation processes include the use of auxiliaries phases such as seeds or residues. Allahyarov et al.[41] claimed that seeding promotes heterogeneous nucleation on the surface of the seeds and stimulates the formation of a crystal with pre-defined characteristics. On the other hand, residues interact with the drug substance to form multicomponent crystals of enhanced physicochemical properties, while preserving the chemical properties of the API.[41] Multicomponent crystals can be classified according to the residue that coexists with the pharmaceutical molecule in the crystal lattice into: 1) solvate if the residue is the solvent, 2) salt when ions coexist with the API, and 3) co-crystals, which are multicomponent crystals of two or more neutral species that are solid at room temperature. Alternative methods to control crystal quality include the use of external energy fields. These methods offer an excellent crystallisation control by acting on the local conditions.[42] Among the different forms of energy input, laser radiation, microwaves, acoustic, magnetic, and electric fields have been extensively investigated in crystallisation control.[1]

Quality control through crystallisation becomes more challenging when the purification process is applied to heterogeneous solutions of substances that may concomitant crystallise alongside the API, affecting the quality of the drug product. For instance, in the fermentation production of L-isoleucine, two isomorphic amino acids are formed (L-leucine and L-valine) that may incorporate in the crystal lattice upon the crystallisation, influencing quality factors of L-isoleucine such as crystal size, morphology, and purity.[43] Extensive research effort has been conducted to improve the purification process in order to circumvent additional purification and isolation steps required to meet the regulatory compliance and standards imposed in drug products. Recently, Li et al.[43] developed a technique to separate the different crystalline substances in complex mixtures by the use of electric field. Although this novel technique proved to effectively separate the compounds in suspension during crystallisation from solution with high purity levels, the mechanistic models behind the purification method is not fully understand. Thus, in order to further developed the purification technique driven by electric fields, the interaction between the field and suspended crystalline particles and between the field and solutions must be investigated.

1.2. Interaction Between Electric Fields and Heterogeneous Solutions

The majority of solids in contact with a fluid medium develop an electrical layer as a result of molecular interaction with the ionic species present in the liquid. This interaction originates localized region of electric charges, which in the presence of an electric field induces a phenomenological motion of the solid particle known as electrokinetics. The fundamental aspects of electric fields, and the most common migration phenomena affecting dispersed particles in heterogeneous solutions is discussed in this chapter section, with focused attention on the interaction between strong direct-current (DC) electric fields and neutral particles in the millimetre-scale.

1.2.1. Fundamentals Aspects Governing Electrostatics

Prior to describe the motion phenomena of particles in suspension driven by the application of an electric field, the basic principles regarding the interaction of the electric field with solid particles is discussed.

1.2.1.1. The (quasi-)Electrostatic Approximation

The static or quasi-electrostatic approximation is commonly applied to electrohydrodynamic systems.[44,45] According to A. Castellanos,[46] the electromagnetic equations that describe the transport phenomena can be reduced to the electrostatic approximation when the energy stored in the magnetic field (W_H) is minor compared to that of the electric field (W_E):

$$\frac{W_H}{W_E} = \frac{\mu_H \boldsymbol{H}^2}{\varepsilon \boldsymbol{E}^2} \ll 1 \quad \textbf{(1.10)}$$

here, μ_H is the magnetic permittivity, ε refers to the permittivity (also known as relative permittivity or dielectric constant), $\boldsymbol{E}$ is the electric field, and $\boldsymbol{H}$ is the magnetic field. Under a direct-current (DC) electric field, conduction currents dominate and the magnetic field can be approximated to $H \approx \sigma El$, with l the length of the system. The inequality expresses that the quasi-static approximation on the millimetre scale is valid in a fluid medium having a conductivity (σ) under 0.1 Sm^{-1}, which is easily satisfied in weakly-polar media with conductivities $\leq 10^{-5}$ Sm^{-1}. On the other hand, in the presence of an alternating-current (AC) electric field, displacement currents dominate and the magnetic field is given by: $H \approx \varepsilon\omega$, which can be considered small compared to the electric field when the frequency ω is lower than 10 MHz. Under these conditions, the Maxwell equations for the (quasi-)electrostatic limit are a valid simplification of the electromagnetic phenomena:[46,47]

$$\nabla \times \boldsymbol{E} = 0 \tag{1.11}$$

$$\nabla \cdot \boldsymbol{E} = \frac{\rho_e}{\varepsilon_0} \tag{1.12}$$

$$\nabla \cdot \boldsymbol{j} + \frac{\partial \rho_e}{\partial t} = 0 \tag{1.13}$$

where ρ_e is the electric charge density, and $\boldsymbol{j}$ refers to the electrical current given by the Ohm's law: $\boldsymbol{j} = \sigma\boldsymbol{E}$. Equation (1.11) describes that the curl of the electric field is zero, and therefore by the definition of the curl $\boldsymbol{E}$ can be expressed as a gradient of a scalar such as $\nabla \times E = \nabla(-\nabla U) = 0$. Thus, equation (1.12) takes the form of a Poisson's equation:

$$\nabla^2 U = -\frac{\rho_e}{\varepsilon_0} \tag{1.14}$$

here, ε_0 refers to the permittivity of the free space. In a region where the charge responsible of the field lies outside the region domain, i.e. in a charge-free region or where there are no unpaired charges, the Poisson's equation follows the Laplace's approximation:[45]

$$\nabla^2 U = 0 \tag{1.15}$$

1.2.1.2. Polarization

On the basis of the ability of a material to conduct electric current, materials can be classified into conductors and dielectrics. Conductors comprise electrons that are not bound to specific atoms, and therefore they can freely move through the material volume facilitating the flow of electric charge. Unlike conductors, a dielectric material is an electric insulator which charges are bounded to specific atoms or molecules. Since these charges can only move short distances from their equilibrium positions, dielectrics restrain the conduction of electricity. In an external electric field, the nuclei and electrons of a dielectric move in opposite directions to align with the electric field leading to the formation of dipole moments in the atoms and/or molecules of the material (Figure 1.5).

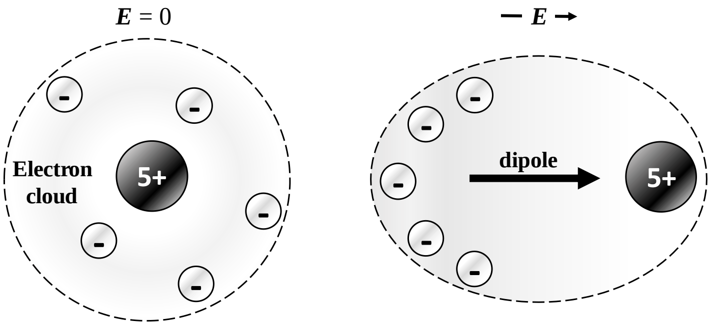

Figure 1.5. Schematic of the polarization phenomenon. The application of an electric field to dielectric materials induces the formation of a dipole as a result of the alignment of charges with opposite polarity along the applied field. The positive and negative charges attract one another by Coulomb forces, keeping the atom together. Extreme electric field may lead to the complete separation of the charges, ionizing the atom.

The charge displacement phenomenon in an electric field is referred to as polarization $\boldsymbol{P_e}$. The polarization process can be categorized into four main mechanisms, with the total polarizability being the sum of all the polarization phenomena. Electronic polarization occurs when neutral atoms or molecules experience a distribution of their charges under an external electric field and form a dipole. Ionic polarization describes the displacement of ions from their centre of symmetry inside an ionic crystal. Molecules with a permanent dipole moment, polar molecules such as water, rotates to align the dipole to the electric field; this mechanism is called orientational polarization. The accumulation of charges in the boundaries of different materials or in specific locations of the molecules is known as interfacial or Maxwell-Wagner polarization. Polarization can be quantitative described by the product of a proportional factor and the electric field strength $\boldsymbol{E}$:

$$\boldsymbol{P_e} = \varepsilon_0 \chi_e \boldsymbol{E} \qquad \textbf{(1.16)}$$

where χ_e is a proportional factor called electric susceptibility, which is an intrinsic property of the dielectric material. A close-related property of a dielectric to the electric susceptibility is permittivity ε that defines the extend of the polarization of a material under an external electric field:

$$\varepsilon = \varepsilon_0 (1 + \chi_e) \qquad \textbf{(1.17)}$$

For convenience, the dielectric property is expressed in terms of its relative value to that of the value of the free space

$$\varepsilon_c = {}^{\varepsilon}/_{\varepsilon_0} \quad \textbf{(1.18)}$$

where ε_c is the relative permittivity or dielectric constant of the material.

1.2.1.3. The Electrical Double Layer (EDL)

When a solid material is placed in an electrolyte, the surface charges of the solid interact with dissolved ions present in the fluid medium. This electrical interaction can be described by the Coulomb's law as repulsion forces F_C between charges of the same sign (co-ions) and attraction forces between unlike ions (counter-ions). The electrostatic force between two stationary point of charges q_1 and q_2 separated by a distance d is given by:

$$F_C = k_C \frac{q_1 q_2}{d^2} \quad \textbf{(1.19)}$$

where k_C is the Coulomb constant. Thus, a solid particle will attract counter-ions that accumulate in the vicinity of the solid phase, generating a local ionic concentration gradient. The region of greater ionic strength surrounding the particle is referred as to the Electrical Double Layer (EDL), which can be divided into two distinct sub-layers: 1) the Stern layer, and 2) the diffuse layer. The Stern layer is localized at the immediate interface between the solid and the medium, where ions electrochemically bound to the surface forming a compact layer of an approximately thickness of two solvated ions.[45] The diffuse layer is delimited by the Stern layer and the bulk medium. In this region Columbic forces are significant, but not sufficiently strong to cause the absorption of ions onto the solid surface. Therefore, the interface between the two layers (slipping plane) defines the separation of the mobile fluid medium and the stationary fluid bounded to the solid phase. As the magnitude of the interaction force decreases as a function of the distance between charges according to the Coulomb's law, there is a limit beyond which no interaction occurs between the surface charges and the ions in solution. The electroneutrality condition is reached in the bulk medium, where co-ions and counter-ions are in equilibrium.

Hughes[44] explained the behaviour of the double layer and its characteristic size from the Gouy-Chapman model. Based on this model, the electrical potential across the EDL of a solid particle at any distance in the x-axis can be estimated by:

$$U(x) = U_0 \exp\left(\frac{-d_x}{\lambda_D}\right) \tag{1.20}$$

where U_0 is the electrical potential at the solid surface, and λ_D is the Debye length, which is given by the following expression:

$$\lambda_D = \sqrt{\frac{\varepsilon_m \varepsilon_0 k_B T}{\sum_i (z_i e)^2 c_i}} \tag{1.21}$$

in equation (1.21), ε_m refers to the dielectric constant of the medium, e is the elementary charge unit, and c_i and z_i respectively refer to the concentration and valence of the specie i. The Debye length represents the distance at which the potential falls a value equal to e^{-1}, and is proportional to the dielectric properties of the medium and the temperature, and inversely proportional to the strength of the electrolyte.[45]

The potential at the slipping plane is referred to as the zeta-potential ζ. This parameter represents the charge developed at the interface between the solid phase and the surrounded medium, and it is used to predict the behaviour of the dispersed particles. Figure 1.6 shows a schematic of the EDL and the electric potential distribution across the different layers.

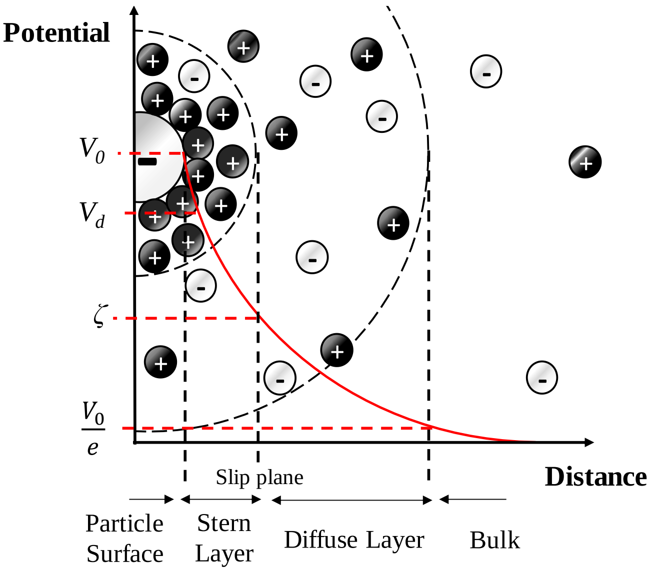

Figure 1.6. Schematic diagram of the electrical double layer (EDL) based on the Gouy-Chapman-Stern model. The negative particle attracts positively charged ions to the surface, and forms a compact layer known as the Stern layer. A second layer, the diffused layer, consists on ions loosely bounded to the negative particle. Ions in the diffuse layer are freely diffused and do not move with the particle. Beyond the diffuse layer, electrical neutrality characterizes the bulk solution. The energy potential across the different layers is depicted with a red curve. At the slip plane (boundary between the stern and diffused layers), the electrical potential is the zeta-potential (ζ). V_0 and V_d are respectively the potential of the negative particle and the potential at the stern layer, and e refers to the elementary unit of charge.

1.2.1.4. Charging Mechanism in non-Aqueous Systems

An elevated voltage is usually required in separation techniques driven by electric fields in order to balance sedimentation and viscous forces. Consequently, electric currents likely evolve in an electrolyte solution, which may induce undesired effects such as electrolysis and the consequent product degration.[48] In a heterogeneous system, free and bound charges accumulate on the interface between the material and its surrounding medium, being the former responsible for the electric current.[49] Since the number of free charges in a fluid media is related to its ionic strength, liquids/solvents are classified into polar and non-polar based on their electrical conduction. Polar solvents present large ionic strength and generally have large dielectric constants. Conversely, non-polar solvents are poorly dissociated and are characterized by low permittivity values and strong electric resistance. Thus, to minimize undesired reactions, non-polar solvents are commonly used in electrohydrodynamic systems.

In aqueous systems, the ionization of surface groups on the particle surface and/or the absorption of ions present in solution promote the generation of charges on the surface of the solid phase. In contrast, the presence of ionic species in non-aqueous solutions is scarce, and the charging mechanism in the absence of charging agents is not well understood. The research community assumes a mechanism based on the preferential absorption of ions from the non-polar medium, in which traces of water, impurities in solution, and the dissociation of surface groups are the most plausible sources of charged species.[50,51] Lyklema,[52] proposed a proton acceptor-donor mechanism, similar to the Bronsted-Lowry acid-base theory to explain the charge transfer between the non-polar medium (HM) and the solid phases (SH):

$$\mathbf{SH_2^+ + M^- \leftrightarrow SH + HM \leftrightarrow S^- + H_2M^+}$$

The charge mechanism is then dependent on the relative acid strength of the solid and liquid phases. The presence of ionic species in dielectric systems implies that an EDL exists around the particle, with non-zero net potential associated to the solid phase. Thus, dispersed particles in a non-polar medium will respond to an external electrical stimulus, which can be controlled to enable the manipulation of the particles through electric fields.

1.2.2. Electrokinetic Forces

Electrokinetics refers to the physicochemical phenomena derived from an applied electric field to a heterogeneous solution that result in an electrically driven motion of the solid and/or liquid phases in the solution. Amongst the different forms of electrokinetics, electro-osmosis (EO), electrophoresis (EP) and dielectrophoresis (DEP) have been widely studied and effectively used for the manipulation of fluids and micron and sub-micron particles in fluid media. Due to the strong electric field requirements to manipulated solid particles in a fluid medium, electrokinetic phenomena are implemented in micro-scale devices. In return, micro-devices offer a simple adaptation to different operations and lower requirements of sample volumes. Additionally, the reduction of voltage requirements and sample size supresses the generation of electrochemical reactions as well as convective and diffusion phenomena.[53]

1.2.2.1. Electro-osmosis (EO)

Hydrodynamically, the EDL can be viewed as two different layers: 1) an immediate layer consisted of charges bounded to the surface, and 2) a layer of mobile counter-ions that are loosely attracted by Columbic forces to the surface. Since the EDL bears an excess of counter ions, electroneutrality is not maintained. In the presence of an electric field, a redistribution of charges in the EDL of a solid object occurs due to Coulomb forces. The charges or ionic species in the first and second layers of the EDL move in opposite direction and align to the field. A fluid flow is originated as a result of the combined effect of viscous and electrostatic forces caused by the motion of ions.[44] The circulation of fluid in the vicinity of a solid surface is known as electro-osmotic flow (EOF).

The flow velocity can be obtained from the Navier-Stokes equation for an incompressible Newtonian fluid:

$$\rho \frac{\partial \boldsymbol{v}}{\partial t} = -\nabla P + \eta \nabla^2 \boldsymbol{v} + \boldsymbol{F_C} \tag{1.22}$$

where ρ and η are the density and viscosity of the medium, $\boldsymbol{v}$ is the flow velocity, P is the pressure, and $\boldsymbol{F_C}$ refers to the Columbic forces. For an incompressible and isotropic medium, the velocity of the fluid due to an electric field magnitude $\boldsymbol{E}$ can be determined from the Helmholtz–Smoluchowski slip approximation:

$$\boldsymbol{v_{EO}} = -\frac{\varepsilon_0 \varepsilon_m \zeta}{\eta} \boldsymbol{E} \tag{1.23}$$

This expression assumes the absence of pressure gradient and uniform surface zeta potential (ζ). The motion of the liquid caused by electro-osmosis presents a flat flow profile, due to the uniformly attraction of ions, with a velocity drop near the walls of the conduction channel as result of friction forces. A schematic of the EOF profile is depicted in Figure 1.7. Electro-osmosis has been implemented in the field of microfluidics for the mixing and pumping of liquids without the need of moving parts.[54,55]

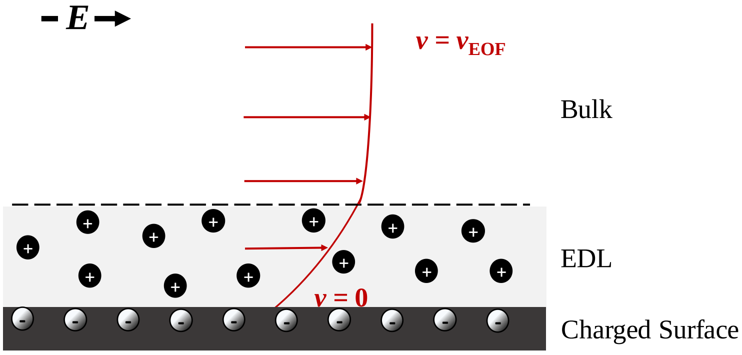

Figure 1.7. Schematic of the electro-osmotic flow (EOF) in the vicinity of a charged surface. The application of an electric field to a fluidic medium with imbalanced charges induces a flow, which velocity is proportional to the applied potential. It is assumed that the fluid follows with a flat flow profile outside the Electrical Double Layer (EDL), with an effective slip velocity given by v_{EOF}.

1.2.2.2. Electrophoresis (EP)

Electrophoresis describes the migration phenomenon of charged particles with respect to a static medium under an electric field. Upon the application of the field, electrophoretic forces exerted on the charged particles induce their motion towards the electrode of opposite charge. The exerted force $\boldsymbol{F_{EP}}$ on a suspended particle having a charge q under an applied field $\boldsymbol{E}$ can be expressed as:

$$\boldsymbol{F_{EP}} = q\boldsymbol{E} \tag{1.24}$$

The orientation of the applied electric field and the sign of the charge determines the direction of the electrophoretic force. This electrokinetic phenomenon only occurs under DC electric fields, since an AC electric field periodically reverses the field direction and therefore, the particle vibrates with no net movement over a time period.

In heterogeneous solutions, an EDL screens the surface of the particle from the bulk medium. The application of the electric field triggers the interaction of ionic species between the inner and outer side of the EDL, which causes the EOF. At the same time, the charges on the particle surface initiate a motion which opposes the fluid flow. This electrophoretic mobility (μ_{EP}) depends on the thickness of the EDL compare to the particle diameter, and can be described by the Henry's equation:

$$\mu_{EP} = \frac{2\varepsilon_0\varepsilon_m\zeta}{3\eta} f(\kappa a) \quad \textbf{(1.25)}$$

here η is the dynamic viscosity of the medium, and the $f(\kappa a)$ is the Henry's function. According to this function, the electrophoretic mobility is dependent of the radius of the particle a, and the Debye–Hückel constant κ, i.e. the reciprocal of the Debye length $\left(\kappa = {}^{1}/_{\lambda_D}\right)$.

In electrolyte solutions, the EDL is approximated to a flat surface and therefore, the ratio of the particle radius to the EDL thickness is > 1. Under this condition, the mobility of dispersed particles with respect to the fluid is commonly given by the Helmholtz–Smoluchowski approximation ($f(\kappa a)$ = 1.5):[50]

$$\mu_{EP} = \frac{\varepsilon_0\varepsilon_m\zeta}{\eta} \quad \textbf{(1.26)}$$

The velocity of a particle in a fluidic medium as a result of the electrophoretic forces can be easily determined by multiplying μ_{EP} by the imposed electric field ($\boldsymbol{v}_{EP} = \mu_{EP}\boldsymbol{E}$). A schematic diagram of the electrophoresis phenomenon is depicted in Figure 1.8.

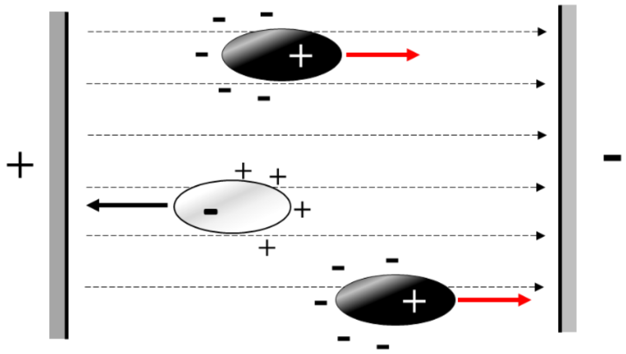

Figure 1.8. Schematic diagram showing the principle of the electrophoresis (EP) phenomenon. Upon imposing an electric field in a solution, charged particles travel to the electrode of opposite polarity due to Coulomb forces. The broken arrows represent the electric field lines, and the red and black arrows are respectively the direction of the positive and negative particles.

Small particles or particles in low concentrated electrolytes present a thick EDL, equal or greater to the radius of the particle. In this case, the electrophoretic mobility is given by the Hückel–Onsager limit ($f(\kappa a)$ = 1):[45,50]

$$\mu_{EP} = \frac{2\varepsilon_0 \varepsilon_m \zeta}{3\eta} \tag{1.27}$$

Electrostatic mobility differences in an electric field experienced by particles of dissimilar physicochemical nature can be exploited in electrophoresis separation and purification techniques. Currently, two main electrophoresis driven techniques, gel and capillary electrophoresis, are commonly used for the separation and purification of biopharmaceutical products. Gel electrophoresis (GE) utilizes electrophoretic forces to generate the motion of particles in a porous matrix gel. Particles of different sizes migrate at dissimilar velocities in the gel which acts as a sieve for the larger analytes. Agarose and polyacrilamide, with large and small pore sizes, are the conventional support matrices used in GE. The principle of the technique is presented in Figure 1.9. Separation and characterization of biological particles, amino acids, and proteins has been documented using GE.[56–58]

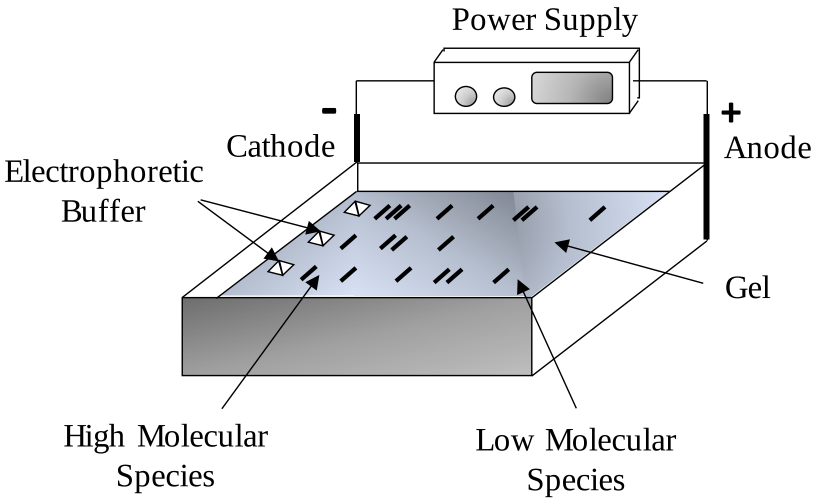

Figure 1.9. Schematic of the Gel Electrophoresis technique. The analyte in the buffer start to migrate in the gel matrix when a potential is applied in the system. The gel matrix minimizes convective phenomena and acts as a sieve of the analytes, inducing concentration gradients of the species with equivalent physicochemical characteristics in different bands.

Capillary electrophoresis (CE) is based on the mobility difference of particles that travel through a thin capillary filled with a background supporting medium. The application of an electric field to the electrolyte reservoirs situated at both ends of the capillary induces the separation of the dispersed particles discriminating by size, charge, and other physicochemical characteristics of the particles. A detector, usually situated at one end of the capillary, detects and quantifies the analytes. A schematic of the CE setup is displayed in Figure 1.10. CE provides a larger throughput, and a faster and superior resolution than gel electrophoresis. The electrophoresis technique enables the analysis of biological and non-biological material.[59] Additionally, the separation and isolation of heterogeneous solutions can be attained by CE. For instance, Huge et al.[60] reported the isolation of oligonucleotides against thrombin enzymes by adapting the capillary to an automated collector. Other than the application for the separation of biomolecules,[59,61] CE has been extensively adopted in the pharmaceutical industry for the analysis of APIs, drug impurities, and for chiral separation.[62–65]

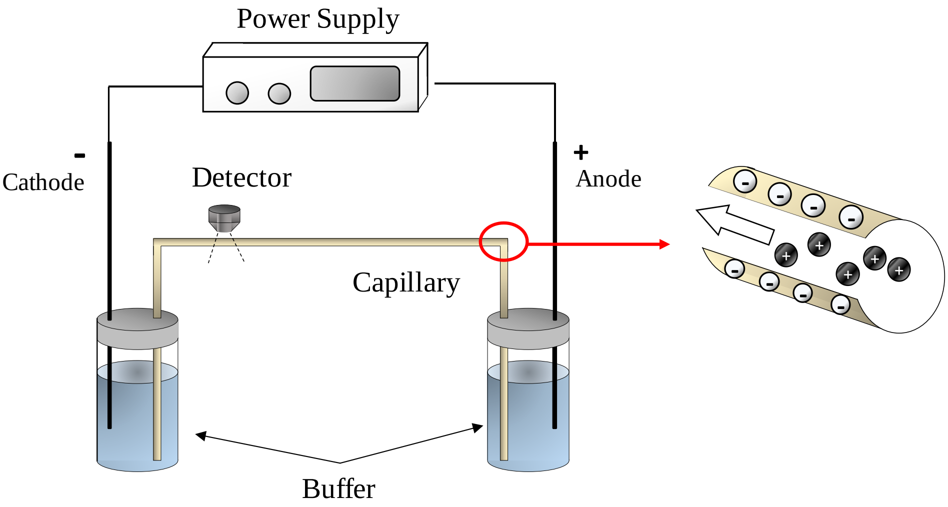

Figure 1.10. Schematic diagram of the capillary electrophoresis technique. A motion of the analytes in a buffer solution through a capillary is triggered when an electric field is applied between electrodes placed in separate solutions. Charged particles are attracted to the electrode of opposite polarity, experiencing dissimilar dragging forces depending on their electric properties. The separation of the different molecular species in a heterogeneous solution occurs while they migrate along the capillary.

Despite the robust separation technique for charged particles provided by EP, the manipulation of neutral or weakly charged particles by the use of electrophoretic forces is inefficient and other methods such as dielectrophoresis are required.

1.2.2.3. Dielectrophoresis (DEP)

Dielectrophoresis (DEP) is an electrokinetic phenomenon that occurs in the presence of non-uniform electric fields. The interaction of the non-uniform electric field with polarizable particles induces unbalanced forces on both sides of the formed dipole, exerting a force on the particle which triggers the mechanical motion of the particle with respect the fluid medium. Based on the direction of the translational dielectrophoretic force experienced by the particle, the phenomenon is classified into positive and negative DEP. Positive DEP occurs when the solid phase is more polarizable than the surrounding medium. In such a case, a larger accumulation of charges is induced in the particle side of the solid/liquid interface upon the application of the electric field and consequent formation of the dipole. The pole facing the strong electric field region is subjected to a greater force, and the particle is pulled towards the electric field maxima. Contrary, in a more polarizable medium, a greater number of charges accumulates in the liquid side of the interface. Thus, the particle is repelled from the stronger field density. No migration occurs when the solid and liquid phases are equally polarizable or in a uniform electric field, since equal forces are exerted on each side of the dipole.[66] Figure 1.11 shows a schematic diagram of the DEP phenomenon.

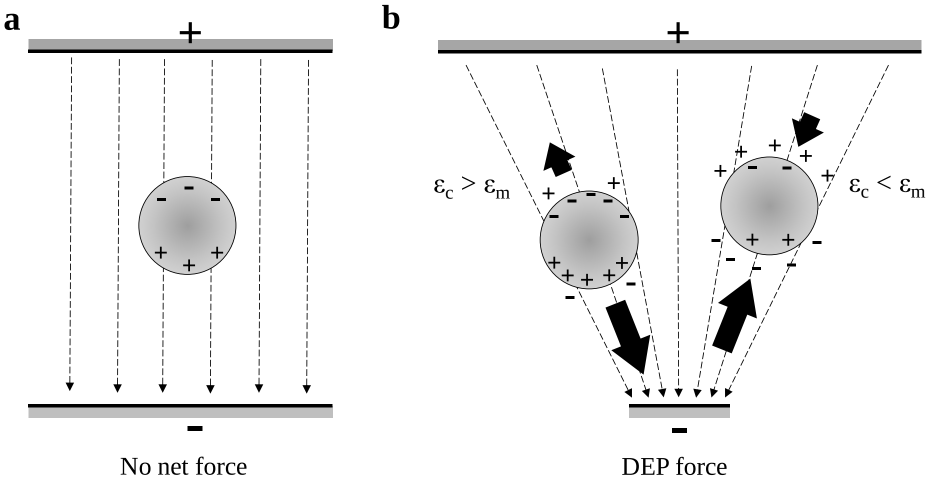

Figure 1.11. Schematic of the dielectrophoresis (DEP) effect on an ideal dielectric particle. Under a uniform electric field (a), the solid particle does not move since negative and positive particle are equally attracted to the positive and negative electrodes. In a non-uniform field (b), difference forces act on both sides of the formed dipole, with a strength that depends on the polarity of the solid particle and the surrounding medium. If the particle is more polarizable than the surrounding medium, a dielectric net force towards the strong electric field density region (situated in the negatively charged electrode) is exerted on the particle (positive DEP). Conversely, if the particle is less polarizable than the medium, the particle is repelled from the strong electric field region (negative DEP). The dashed lines are a guide to the eye representing the electric field.

In an asymmetrical electric field, the translational force experienced by a spherical particle of radius r is given by:[66]

$$\boldsymbol{F_{DEP}} = 2\pi r^3 \varepsilon_m \varepsilon_0 \left(\frac{\varepsilon_c - \varepsilon_m}{\varepsilon_c + 2\varepsilon_m}\right) \nabla \boldsymbol{E}^2 \qquad \textbf{(1.28)}$$

where ∇ is the field gradient and the term between brackets is commonly refer to as Clasius-Mossotti factor. Using this term, the velocity experienced by the particle due to action of the dielectric force towards to or away from the electric field maxima can be expressed as:

$$\boldsymbol{v_{DEP}} = \frac{r^2 \varepsilon_m}{3\eta} f_{CM} \nabla \boldsymbol{E}^2 \tag{1.29}$$

Note that equation (1.28) is the classical dielectrophoresis equation given by Pohl for a spherical particle embedded in a homogeneous medium. However, more recent studies include a complex permittivity term instead of the relative permittivity in order to account for the effect of frequency in dielectrophoresis phenomena. According to this studies, the Classius-Mossotti factor has two limiting values.[67–69] At low frequencies and/or under DC electric fields the Classius-Mossotti factor can be approximate to:

$$f_{CM} = \frac{\sigma_c - \sigma_m}{\sigma_c + \sigma_m} \tag{1.30}$$

where σ represents the conductivity, and the subscripts c and m refers to the particle and medium. According to equation (1.28) and equation (1.30), if the particle is more polarizable than the medium $f_{CM} > 0$, there is a greater charge accumulation on the particle side of the interface, inducing a motion of the solid phase towards the field maxima. This phenomenon is called positive dielectrophoresis. Conversely, a more polarizable medium compared to the solids induces $f_{CM} < 0$ a motion away from the strong electric field medium known as negative dielectrophoresis, a large number of charges are located in the medium side of the EDL.

Since the dispersed particles in a heterogeneous solution experience dissimilar dielectrophoretic forces based on their dielectric properties and size, DEP methods can effectively be used for a variety of applications, including separation, purification, sorting, and characterization of micro and nano-scale particles.[44,70] The development and application of these methods have been drastically increased during the last decades due to advances in microfabrication technologies. The strong electric fields required for the manipulation of nano and micro-scale particles can be easily generated in microfluidic devices, which geometry and electrode configuration strongly influence the electric field gradient. Classical configurations of microfluidic-DEP systems are depicted in Figure 1.12.

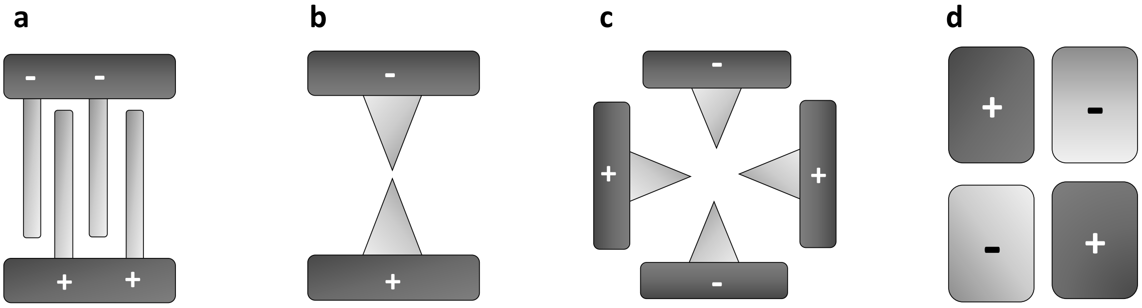

Figure 1.12. Schematic diagram of classical electrode designs on DEP technologies, including: parallel interdigitated electrodes (a), pair micro-tip electrodes (b), multiple micro-tip electrodes (c), and polynomial electrodes (d).

To date, DEP systems can be classified on the basis of the electrode integration into either electrode-based DEP (eDEP) or insulator-based DEP (iDEP).[70] The former systems enable stronger electric field gradients by integrating the electrodes within the microchannel. However, the direct contact between the electrode and solution may induce undesired phenomena such as Joule heating effect or electrolysis.[48] The second approach comprises electrodes situated outside the micro-channel and insulator constrictions that create the inhomogeneity of the field. Particle discrimination can be realized for both systems by the difference interactions of the particle with the electrodes while moving along the microchannel and/or the use of bifurcated outlets. Comprehensive reviews on the DEP phenomenon and applications can be found elsewhere.[70–73]

1.2.2.4. Other Forces and Phenomena Acting on Particles in Suspension

Solid particles in suspensions experience different phenomena that oppose the electrokinetic forces, reducing the velocity of the suspended particles in the presence of an externally applied electric field. For instance, thermal diffusion caused by Joule effect or Brownian motion may induce the generation of forces or random motion direction exerted on the particles. However, under strong electric fields, deterministic particle movement can be induced and other forces rather than electrokinetics are not usually considered for the mechanical motion of the particles.

Viscous drag. Viscous drag forces (F_η), arise when an object is in a moving fluid. Friction forces act opposite to the motion of the particle and flow due to the viscosity of the medium, which result in a reduction of the velocity of the solid material. For a spherical solid of radius r with a velocity v, the drag force can be written as:

$$F_{\eta} = -6\pi r\eta v \tag{1.31}$$

Gravity. Any suspended particles in a fluid are under the influence of gravity ($\boldsymbol{g}$), which force vector follows the direction of the gravitational acceleration. For a solid particle of volume V and density ρ_c in a fluid medium of density ρ_m, the magnitude of this force ($\boldsymbol{F_g}$) is given by:

$$\boldsymbol{F_g} = V(\rho_c - \rho_m)\boldsymbol{g} \tag{1.32}$$

The magnitude of the gravitational force is proportional to the size of the particle, and it is counteracted by the viscous drag. Thus, particles under 250 nm diameter in a fluid medium are not strongly influenced by the action of gravity.[44] The behaviour of the suspended particles under the action of this force is dictated by the difference between the density of the particle and the medium. Consequently, when the density of the object is greater than that of the medium density, the gravitational force acts downwards and particles will sink over time; while in a denser medium an upward force arises and particles will float.

Brownian motion. The Brownian motion refers to the random displacement of a particle caused by collisions with adjacent particles in the medium with a zero force and velocity average since collisions of different particles neutralize each other. The net displacement over set time period t on a single spherical particle of radius r in one is given by:

$$\Delta d = \sqrt{\frac{k_B T t}{3\pi\eta r}} \tag{1.33}$$

From equation (1.33), it can be perceived that the effect of the Brownian motion diminishes for larger particles, since bigger particles receive impacts in all directions resulting in a null-net displacement.

Joule heating. A potential difference applied between two electrodes may supply a current flow and trigger a motion of the species in solution, which in term can cause a localised heating of the medium. This phenomenon is referred to as Joule heating effect. This phenomenon is negligible in low conductivity media and uncommonly observed in the micro and millimetre-scale.[44] Gradients of temperature and temperature-dependant properties such as conductivity and permittivity arise when the liquid temperature increases, pulling downwards the cooling liquid and producing convective flows. The gradient of temperature is usually expressed as a function of the applied voltage (U), the thermal conductivity (K_m), and electrical conductivity (σ_m) of the medium:

$$\Delta T = \frac{\sigma_m U^2}{K_m} \tag{1.34}$$

1.3. Crystallisation Intensification through Electric Fields

As previously discussed, the technique developed by Li et al.[35] enables the in-situ separation of compounds in complex mixtures during crystallisation. In order to optimize this technique, the effects of the electric field on crystallising solution must be understood. The use of electric fields to enhance the crystallisation process and to control crystal qualities has been actively investigated in the pharmaceutical industry, and specifically in the production of biopharmaceuticals.[1] A review on crystallisation assisted by electric fields with focus attention on protein crystallisation have been published by Alexander and Radacsi.[74]

One of the first documented research on macromolecule crystallisation assisted by electric fields was conducted by Aubry's group.[75] A direct current (DC) electric field externally applied to sitting protein-rich drops produced a lower number of crystals of larger size compared to unelectrified crystallisation experiments. The observed phenomenon indicates a promotion of crystal growth in detriment of nucleation in the presence of the field. Penkova[76] described a similar effect of the field on the crystallisation of ferritin, apoferritin, and lysozyme crystals under a DC voltage ranging between 2 and 6 kVcm^{-1}. They related the crystallisation enhancement to an electrically driven flow of protein molecules positively charged migrating towards the cathode side of the droplet. This electromigration phenomenon may cause concentration gradients within the solution, and consequently an increase of the local supersaturation. In addition, improved quality of the formed crystals assessed by x-ray diffraction analysis has been documented and related to the orientation of the molecules with the field direction.[77–79]

The potential requirements to influence crystallisation parameters can be reduced by the use of electric fields in direct contact with the solution. Under internally applied weak electric fields, identical results to those observed using externally applied fields, including increase of nucleation rates, lower number of crystals, and crystals with larger size and better quality characteristics have been reported.[25,80,81] Hammadi et al.[24] demonstrated that nucleation processes can be spatially and temporally controlled by the use of internally applied electric fields. They used a custom-made cell with at least one sharp electrode, generating large field gradients within the cell and high current density near the tip. By using an agarose medium to reduce convection and adjusting the applied voltage, nucleation of lysozymes occurred on the sharp electrode.

Although most of the APIs produced by crystallisation processes are small molecules,[8] research on the application of electric fields to solutions of small organic molecules is to the best of our knowledge, scarce. Documented effects published in this field includes polymorphism control of glycine,[23,82] and nucleation enhancement of sucrose.[83]

1.4. Aim and objectives

A separation technique that combines the intensification of crystallisation driven by electric fields with the in-situ isolation of the API product could bring forth an enhanced purification method in terms of process time and operation costs. In this context, the Electric Field Enhanced Crystallisation (EFEC) technique developed by Li et al.,[35] showed to effectively separate a mixed of suspended particles on opposite electrode while continue crystallising on the electrode surface in the presence of strong inhomogeneous electric fields.

An inhomogeneous direct-current (DC) electric field exerts a translational force on the dispersed material in a dielectric fluid medium, with a selective collection of the crystals on one of two electrodes. Li[35] reported the separation of a mixed suspension of phenazine (PHZ) and caffeine (CAF), that collect at opposite electrodes in 1,4-dioxane at 30 °C when a potential difference of 7.5 kV is imposed between two rod shaped electrodes immersed into the suspension. The immobilization of the crystals on the surface of the electrodes, which allows for the recovery of the solid material, is induced by crystal growth through decreasing the temperature. The recovered solids showed 97 wt% of PHZ and 91 wt% of CAF on the cathode and anode, respectively.

This thesis builds on the current knowledge of the EFEC technique, with the aim of exploiting electric field phenomena to enhance crystallisation processes. To achieve this, it seems essential to conduct a more exhaustive research on the effects of electric field on crystallisation of APIs of organic molecules, to investigate whether their crystallisation behaviour is influenced by the field. This together with the identification of the scientific principles behind the interaction of the electric field and suspended particles, will allow us to develop new means to exploit the electric field phenomena. The aims and objectives of this thesis are summarized in Figure 1.13.

First, we need well-defined systems in order to enable an accurate study of the effects of electric fields. The temperature dependent solubility of an organic compound is important information for the design of crystallisation processes, also in the presence of an electric field. However, solubility data in isolator solvents such as cyclopentyl methyl ether (CPME) is not accessible from literature. In Chapter 3, the objective therefore is to accurately describe solubilities and to understand underlying principles that determine solubilities of organic compounds in apolar solvents. To achieve this, the temperature dependent solubility of a large number of organic compounds is determined in the three non-polar solvents dioxane, CPME, and toluene.

Subsequently, our objective in Chapter 4 is to identify the scientific principles behind the effect of electric fields on well-defined equilibrated suspensions. Chapter 4 describes the behaviour of a comprehensive number of solvents and crystalline particles in suspension under an inhomogeneous electric field, which allows for: 1) the identification of electrochemically stable solvent, and 2) monitoring the particle motion of particles in suspension. The particular collection of the suspended particles on one of the two electrodes in contact with a defined suspension allows to relate particle and solution properties to the electric field phenomena. Additionally, to corroborate the initial assumptions for the EFEC technique, the electrophoretic phenomenon that may occur in organic particle suspensions is studied in a custom-made micro-device.

Then, we pursue to understand the effect of electric fields on crystallising solutions. The influence of electric fields on protein crystallisation has been described in literature, however thermodynamic and kinetic crystallisation behaviour of small organic molecules in the presence of an electric field have not been given much attention. Thus, in Chapter 5 the objective is to understand the electric field effect on solubility and nucleation rate of small organic compounds. We therefore examine and compare the crystallisation of isonicotinamide in 1,4-dioxane in the presence and absence of an inhomogeneous DC electric field. From probability models, crucial parameters of crystallisation processes such as cloud point and induction times can be made available. The determination of such parameters allows for the interpretation of plausible mechanisms of crystallisation driven by electric fields.

Finally, in Chapter 6 the objective is to apply the gained knowledge to achieve electric field enhanced separations. In Chapter 6, EFEC is applied to the separation of mixtures of particles that could be the result of crystallisation processes. In addition to the separation of crystals that collect on counter electrodes, the purification technique is modified for the separation of compounds that collect on the same electrode under a non-uniform electric field.

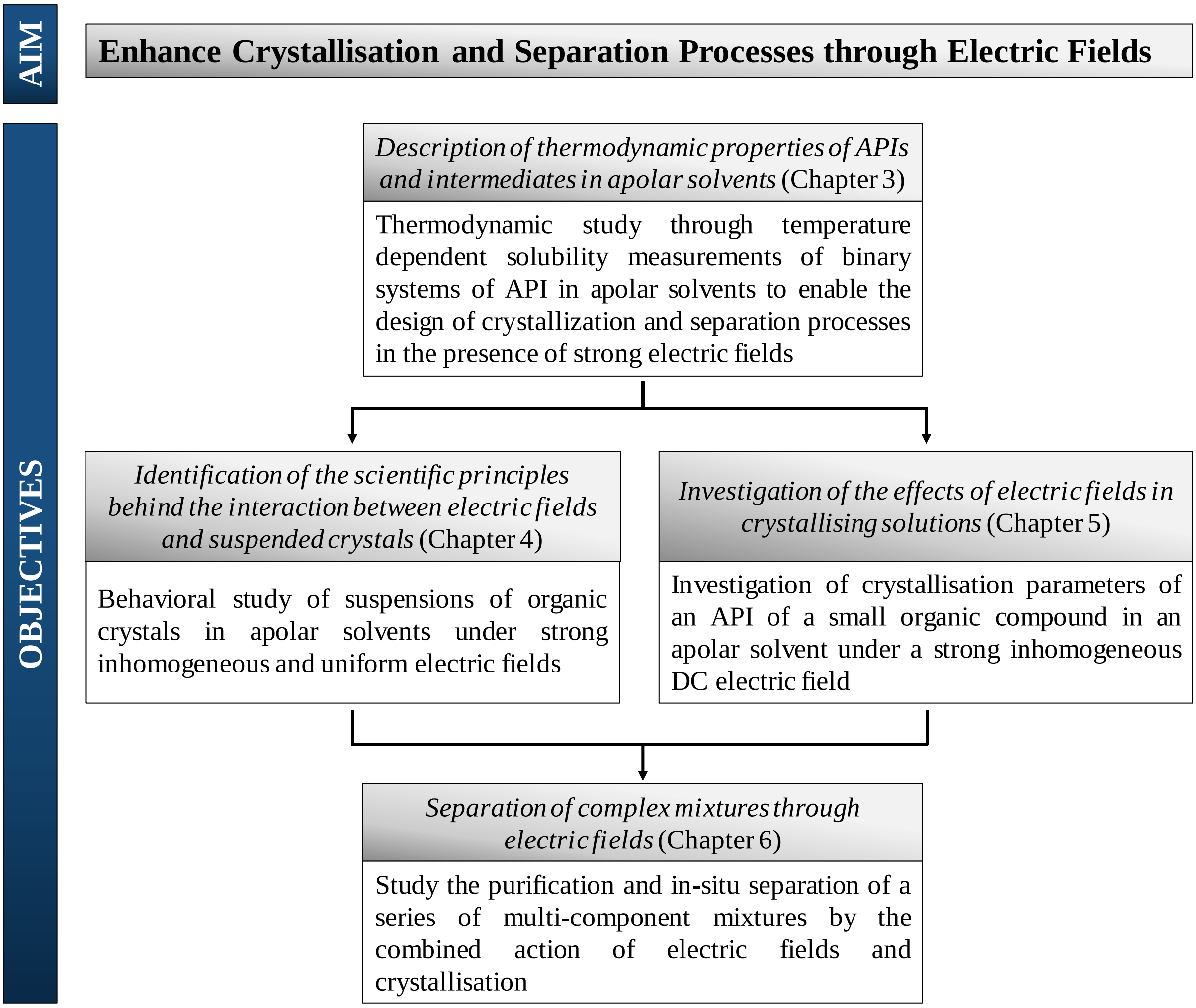

Figure 1.13. Summary outline of the thesis work showing the thesis structure and interconnection of chapters, as well as the aim and individual objectives addressed in each experimental chapter.

1.5. References

1. Wang, J., Li, F. & Lakerveld, R. Process intensification for pharmaceutical crystallization. *Chem. Eng. Process. - Process Intensif.* **127**, 111–126 (2018).
2. Strube, J. *et al.* Process intensification in biologics manufacturing. *Chem. Eng. Process. - Process Intensif.* **133**, 278–293 (2018).
3. Jiménez-González, C. *et al.* Key green engineering research areas for sustainable manufacturing: A perspective from pharmaceutical and fine chemicals manufacturers. *Org. Process Res. Dev.* **15**, 900–911 (2011).
4. Wang, H. *et al.* A review of process intensification applied to solids handling. *Chem. Eng. Process. Process Intensif.* **118**, 78–107 (2017).
5. Gutmann, B., Cantillo, D. & Kappe, C. O. Continuous-flow technology - A tool for the safe manufacturing of active pharmaceutical ingredients. *Angew. Chemie - Int. Ed.* **54**, 6688–6728 (2015).
6. Pohl, P., Bielawska-Pohl, A., Dzimitrowicz, A., Jamroz, P. & Welna, M. Impact and practicability of recently introduced requirements on elemental impurities. *TrAC - Trends Anal. Chem.* **101**, 43–55 (2018).
7. Stankiewicz, A. I. & Moulijn, J. A. Process Intensification: Transforming Chemical Engineering. *Chem. Eng. Process* 22–34 (2000).
8. ter Horst, J. H., Schmidt, C. & Ulrich, J. *Fundamentals of Industrial Crystallization. Handbook of Crystal Growth: Bulk Crystal Growth: Second Edition* **2**, (Elsevier B.V., 2015).
9. Apshingekar, P. P., Aher, S., Kelly, A. L., Brown, E. C. & Paradkar, A. Synthesis of Caffeine/Maleic Acid Co-crystal by Ultrasound-assisted Slurry Co-crystallization. *J. Pharm. Sci.* **106**, 66–70 (2017).
10. Forbes, C., Nguyen, T. T. H., O'Leary, R. L. & Price, C. J. Elucidating the mechanism of paracetamol sonocrystallization for product purity enhancement. **045017**, 045017 (2018).
11. Kakinouchi, K. *et al.* Effect of ultrasonic irradiation on protein crystallization. *J. Cryst. Growth* **292**, 437–440 (2006).
12. Kaur Bhangu, S., Ashokkumar, M. & Lee, J. Ultrasound Assisted Crystallization of Paracetamol: Crystal Size Distribution and Polymorph Control. *Cryst. Growth Des.* **16**, 1934–1941 (2016).
13. Gielen, B., Jordens, J., Thomassen, L. C. J., Braeken, L. & Van Gerven, T. Agglomeration control during ultrasonic crystallization of an active pharmaceutical ingredient. *Crystals* **7**, 1–20 (2017).
14. Constance, E. N. *et al.* Effect of Microwave Heating on the Crystallization of Glutathione Tripeptide on Silver Nanoparticle Films. *J. Phys. Chem. C* **121**, 5585–5593 (2017).
15. Kacker, R. *et al.* Microwave Assisted Direct Nucleation Control for Batch Crystallization: Crystal Size Control with Reduced Batch Time. *Cryst. Growth Des.* **16**, 440–446 (2016).
16. Ahuja, D. *et al.* Microwave assisted slurry conversion crystallization for manufacturing of new co-crystals of sulfamethazine and sulfamerazine. *CrystEngComm* **22**, 1381–1394 (2020).
17. Javid, N., Kendall, T., Burns, I. S. & Sefcik, J. Filtration suppresses laser-induced nucleation of glycine in aqueous solutions. *Cryst. Growth Des.* **16**, 4196–4202 (2016).
18. Iefuji, N. *et al.* Laser-induced nucleation in protein crystallization: Local increase in protein concentration induced by femtosecond laser irradiation. *J. Cryst. Growth* **318**, 741–744 (2011).
19. Li, W. *et al.* Non-Photochemical Laser-Induced Nucleation of Sulfathiazole in a Water/Ethanol Mixture. *Cryst. Growth Des.* **16**, 2514–2526 (2016).
20. Wang, S. *et al.* Polymorph-Controlled Crystallization of Acetaminophen through Femtosecond Laser Irradiation. *Cryst. Growth Des.* **19**, 3265–3271 (2019).
21. Wu, C. S., Ikeyama, J., Nakabayashi, S., Sugiyama, T. & Yoshikawa, H. Y. Growth Promotion of Targeted Crystal Face by Nanoprocessing via Laser Ablation. *J. Phys. Chem. C* **123**, 24919–24926 (2019).
22. Li, F. & Lakerveld, R. Electric-Field-Assisted Protein Crystallization in Continuous Flow. *Cryst. Growth Des.* **18**, 2964–2971 (2018).

23. Adrjanowicz, K., Paluch, M. & Richert, R. Formation of new polymorphs and control of crystallization in molecular glass-formers by electric field. *Phys. Chem. Chem. Phys.* **20**, 925–931 (2018).

24. Hammadi, Z., Astier, J. P., Morin, R. & Veesler, S. Spatial and temporal control of nucleation by localized DC electric field. *Cryst. Growth Des.* **9**, 3346–3347 (2009).

25. Moreno, A. & Sazaki, G. The use of a new ad hoc growth cell with parallel electrodes for the nucleation control of lysozyme. *J. Cryst. Growth* **264**, 438–444 (2004).

26. Li, F. & Lakerveld, R. Influence of Alternating Electric Fields on Protein Crystallization in Microfluidic Devices with Patterned Electrodes in a Parallel-Plate Configuration. *Cryst. Growth Des.* **17**, 3062–3070 (2017).

27. Sudha, C., Parimaladevi, P. & Srinivasan, K. A novel method for the separation of mono and ortho polymorphs of paracetamol in gel matrix. *Mater. Sci. Eng. C* **47**, 150–155 (2015).

28. Okada, R. *et al.* Test Results of a Nb 3 Al / Nb 3 Sn Subscale Magnet for Accelerator Application. **25**, (2015).

29. Ramachandran, N. & Leslie, F. W. Using magnetic fields to control convection during protein crystallization - Analysis and validation studies. *J. Cryst. Growth* **274**, 297–306 (2005).

30. Surade, S., Ochi, T., Nietlispach, D., Chirgadze, D. & Moreno, A. Investigations into protein crystallization in the presence of a strong magnetic field. *Cryst. Growth Des.* **10**, 691–699 (2010).

31. Urwin, S. J. *et al.* A Structured Approach To Cope with Impurities during Industrial Crystallization Development. *Org. Process Res. Dev.* **24**, 1443–1456 (2020).

32. Pethig, R. Review—Where Is Dielectrophoresis (DEP) Going? *J. Electrochem. Soc.* **164**, B3049–B3055 (2017).

33. Nuchtavorn, N., Suntornsuk, W., Lunte, S. M. & Suntornsuk, L. Recent applications of microchip electrophoresis to biomedical analysis. *J. Pharm. Biomed. Anal.* **113**, 72–96 (2015).

34. Romero-Creel, M. F., Goodrich, E., Polniak, D. V. & Lapizco-Encinas, B. H. Assessment of sub-micron particles by exploiting charge differences with dielectrophoresis. *Micromachines* **8**, (2017).

35. Li, W. W., Radacsi, N., Kramer, H. J. M., van der Heijden, A. E. D. M. & ter Horst, J. H. Solid Separation from a Mixed Suspension through Electric-Field-Enhanced Crystallization. *Angew. Chemie Int. Ed.* 1–5 (2016).

36. Mullin, J. W. *Crystallization (Fourth Edition)*. (Butterworth-Heinemann, 2001).

37. Kashchiev, D. *Nucleation : basic theory with applications*. (Butterworth Heinemann, 2000).

38. Veesler, S. & Puel, F. *Crystallization of Pharmaceutical Crystals. Handbook of Crystal Growth: Second Edition* **1**, (Elsevier B.V., 2014).

39. Singhal, D. & Curatolo, W. Drug polymorphism and dosage form design: A practical perspective. *Adv. Drug Deliv. Rev.* **56**, 335–347 (2004).

40. Ulrich, J. & Jones, M. Industrial crystallization: Developments in research and technology. *Chem. Eng. Res. Des.* **82**, 1567–1570 (2004).

41. Grothe, E., Meekes, H., Vlieg, E., Ter Horst, J. H. & De Gelder, R. Solvates, Salts, and Cocrystals: A Proposal for a Feasible Classification System. *Cryst. Growth Des.* **16**, 3237–3243 (2016).

42. Revalor, E. *et al.* Usual and unusual crystallization from solution. *J. Cryst. Growth* **312**, 939–946 (2010).

43. Koolman, H. C. & Rousseau, R. W. Effects of Isomorphic Compounds on the Purity and Morphology of L-Isoleucine Crystals. *AIChE J.* **42**, 147–153 (1996).

44. Hughes, M. P. *Nanoelectromechanics in engineering and biology*. (CRC Press, 2003).

45. Morgan, H., Gerrn, N. G. & Sun, T. Electrokinetics Of Particles And Fluids. in *Micro/Nano Technology Systems for Biomedical Applications: Microfluidics, Optics, and Surface Chemistry* 1–43 (2010).

46. Castellanos, A., Ramos, A., González, A., Green, N. G. & Morgan, H. Electrohydrodynamics and dielectrophoresis in microsystems: Scaling laws. *J. Phys. D. Appl. Phys.* **36**, 2584–2597 (2003).

47. Ramos, A. Electrohydrodynamic Pumping in Microsystems. *Electrokinet. Electrohydrodynamics Microsystems* 127–175 (2011). doi:10.1007/978-3-7091-0900-7_5

48. Hammadi, Z. & Veesler, S. S. New approaches on crystallization under electric fields. *Prog. Biophys. Mol. Biol.* **101**, 38–44 (2009).

49. Green, N. G. Electrostatics and Quasielectrostatics. in *Electrokinetics and Electrohydrodynamics in Microsystems* (ed. Ramos, A.) 29–60 (Springer Wien New York, 2011).

50. Hao, T. *Electrorheological Fluids: The Non-aqueous Suspensions.* (Elsevier B.V., 2005).

51. Ohshima, H. & Furusawa, K. *Electrical Phenomena at Interfaces: Fundamentals: Measurements, and Applications.* (Marcel Dekker, Inc., 1998).

52. Lyklema, J. Principles of the stability of lyophobic colloidal dispersions in non-aqueous media. *Adv. Colloid Interface Sci.* **2**, 67–114 (1968).

53. Bayraktar, T. & Pidugu, S. B. Characterization of liquid flows in microfluidic systems. *Int. J. Heat Mass Transf.* **49**, 815–824 (2006).

54. Ramos, A. Electrohydrodynamic Pumping in Microsystems. in *Electrokinetics and Electrohydrodynamics in Microsystems* (ed. Ramos, A.) 127–176 (Springer Wien New York, 2011).

55. Ward, K. & Fan, Z. H. Mixing in microfluidic devices and enhancement methods. *J. Micromechanics Microengineering* **25**, (2015).

56. Xuan, J. & Lee, M. L. Analytical Methods Size separation of biomolecules and bioparticles using micro/nanofabricated structures. *Anal. Methods* **6**, 27–37 (2014).

57. Sheen, H. Quantitation of yeast total proteins in sodium dodecyl sulfate-polyacrylamide gel electrophoresis sample buffer for uniform loading. *Anal. Biochem.* **498**, 95–97 (2016).

58. Hellman, L. & Fried, M. Electrophoretic mobility shift assay (EMSA) for detecting protein–nucleic acid interactions. *Nat. Protoc.* **2**, 1849–1861 (2007).

59. Sekhon, B. An overview of capillary electrophoresis: pharmaceutical, biopharmaceutical and biotechnology applications. *J. Pharm. Educ. Res.* **2**, (2011).

60. Huge, B. J., Flaherty, R. J., Dada, O. O. & Dovichi, N. J. Capillary electrophoresis coupled with automated fraction collection. *Talanta* **130**, 288–293 (2014).

61. Zhu, Z., Lu, J. J. & Liu, S. Analytica Chimica Acta Protein separation by capillary gel electrophoresis : A review. *Anal. Chim. Acta* **709**, 21–31 (2012).

62. Kyu, H., Truong, C. Q. & Yusung, X. M. Determination of S-(-) -lansoprazole in dexlansoprazole preparation by capillary zone electrophoresis. *Arch. Pharm. Res.* **40**, 962–971 (2017).

63. Sánchez-lópez, E., Montealegre, C., Marina, M. L. & Crego, A. L. Development of chiral methodologies by capillary electrophoresis with ultraviolet and mass spectrometry detection for duloxetine analysis in pharmaceutical formulations. *J. Chromatogr. A* **1363**, 356–362 (2014).

64. Cunha, R. R., Chaves, S. C., Ribeiro, M. M. A. C., Santos, W. T. P. Dos & Richter, E. M. Simultaneous determination of caffeine , paracetamol , and ibuprofen in pharmaceutical formulations by high-performance liquid chromatography with UV detection and by capillary electrophoresis with conductivity detection. *J. Sep. Sci.* **38**, 1657–1662 (2015).

65. Ran, K. *et al.* Determination of the R-enantiomer of valsartan in pharmaceutical formulation by capillary electrophoresis. *Arch. Pharm. Res.* **38**, 826–833 (2015).

66. Pohl, H. A. Some effects of nonuniform fields on dielectrics. *J. Appl. Phys.* **29**, 1182–1188 (1958).

67. Pethig, R. Dielectrophoresis: Status of the theory, technology, and applications. *Biomicrofluidics* **4**, (2010).

68. Huang, J. P., Karttunen, M., Yu, K. W. & Dong, L. Dielectrophoresis of charged colloidal suspensions. *Phys. Rev. E - Stat. Nonlinear Soft Matter Phys.* **67**, 021403 (2002).

69. Zhang, C., Khoshmanesh, K., Mitchell, A. & Kalantar-Zadeh, K. Dielectrophoresis for manipulation of micro/nano particles in microfluidic systems. *Anal. Bioanal. Chem.* **396**, 401–420 (2010).

70. Lapizco-Encinas, B. H. On the recent developments of insulator-based dielectrophoresis : A review. *Electrophoresis* **40**, 358–375 (2019).

71. Dash, S. & Mohanty, S. Dielectrophoretic separation of micron and submicron particles: A review. *Electrophoresis* **35**, 2656–2672 (2014).

72. Pethig, R. Review—Where Is Dielectrophoresis (DEP) Going? *J. Electrochem. Soc.* **164**, B3049–B3055 (2017).

73. Kim, D., Sonker, M. & Ros, A. Dielectrophoresis: From Molecular to Micrometer-Scale Analytes. *Anal. Chem.* **91**, 277–295 (2019).

74. Alexander, L. F. & Radacsi, N. Application of electric fields for controlling crystallization. *CrystEngComm* **21**, 5014–5031 (2019).

75. Taleb, M. *et al.* Crystallization of proteins under an external electric field. *J. Cryst. Growth* **200**, 575–582 (1999).

76. Penkova, A. *et al.* Enhancement and suppression of protein crystal nucleation due to electrically driven convection. *J. Cryst. Growth* **275**, 1527–1532 (2005).

77. Rubin, E., Owen, C. & Stojanoff, V. Crystallization under an External Electric Field: A Case Study of Glucose Isomerase. *Crystals* **7**, 206 (2017).

78. Pareja-Rivera, C. *et al.* Recent advances in the understanding of the influence of electric and magnetic fields on protein crystal growth. *Cryst. Growth Des.* **17**, 135–145 (2017).

79. Taleb, M., Didierjean, C., Jelsch, C., Mangeot, J. P. & Aubry, A. Equilibrium kinetics of lysozyme crystallization under an external electric field. *J. Cryst. Growth* **232**, 250–255 (2001).

80. Mirkin, N., Frontana-Uribe, B. A., Rodríguez-Romero, A., Hernández-Santoyo, A. & Moreno, A. The influence of an internal electric field upon protein crystallization using the gel-acupuncture method. *Acta Crystallogr. - Sect. D Biol. Crystallogr.* **59**, 1533–1538 (2003).

81. Wakamatsu, T. Low Applied Voltage Effects on Thaumatin Protein Crystallization. *Trans. Mater. Res. Soc. Japan* **41**, 13–15 (2016).

82. Aber, J. E., Arnold, S., Garetz, B. A. & Myerson, A. S. Strong dc Electric Field Applied to Supersaturated Aqueous Glycine Solution Induces Nucleation of the Polymorph. *Phys. Rev. Lett.* **145503**, 1–4 (2005).

83. Hu, B., Huang, K., Zhang, P. & Zhong, X. Z. Pulsed Electric Field Effects on Sucrose Nucleation at Low Supersaturation. *Sugar Tech* **17**, 77–84 (2015).

Chapter 2. Methods

A variety of analytical techniques for the in-situ monitoring of the separation processes driven by an electric field, and for the off-line characterisation of the obtained products from crystallization and separation operations, have been used to interpret and support the outcome of the research that conform the present thesis. The current chapter addresses the fundamental principles of the main techniques and equipment used for the completion of the experimental work.

2.1. Differential Scanning Calorimetry (DSC)

DSC is a thermo-analytical technique used to identify physicochemical changes of a substance as a function of the temperature. In a DSC analysis, exothermic and endothermic events associated to material transitions are captured, and these events are represented by peaks in a heat flux (dQ/dt) *vs.* absolute temperature (T) diagram called thermogram.[1] Figure 2.1 shows the thermo-physical transitions commonly displayed in DSC thermograms. This technique is widely implemented in the chemical industry for quality control applications, since the thermal properties of a substance are related to its specific physical properties. For instance, the melting point of a material provides qualitative information of its purity by a simple comparison to that of the pure solid.[2]

Commercial DSCs operate on the basis of two distinctive mechanisms: heat-flow and power-compensation.[3] In heat-flow equipment, a reference material and the sample in a solid or liquid state are placed in separated thermoelectric blocks within the same furnace. Over a programme temperature range, the DSC instrument measures temperature differences between the sample and the reference to determine the heat emitted or absorbed by the former.

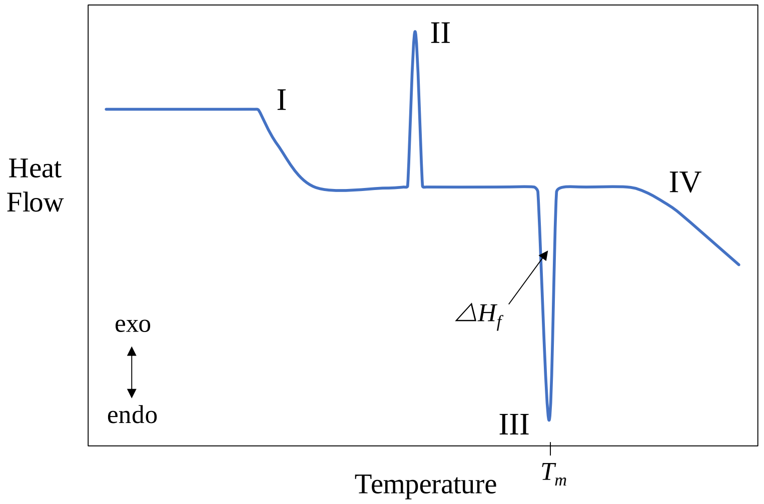

Figure 2.1. DSC curve presenting common thermal events, including: I. glass transition, II. crystallisation, III. melting, and IV. decomposition. The melting temperature is represented by T_m. The area under the curve of the endothermic event given by the melting temperature is the enthalpy of fusion of the material (ΔH_f).

In power-compensation DSC equipment, the samples are placed in different furnaces set at the same temperature. In the event of a thermal transition experienced by the sample, the resulting energy excess is compensated for the reference to maintain the same temperature than that of the analysed sample. The energy difference between the sample and the reference is measured and plotted as a function of the temperature.

2.2. High-Performance Liquid Chromatographic (HPLC)

HPLC is a physical separation method that enables the qualitative and quantitative identification of the different constituents of a sample mixture in a liquid phase. This analytical technique is widely used in the pharmaceutical industry as it provides very accurate result for the identification of multiple components and requires minimal sample size. In HPLC, the sample is dispensed and dissolved in an eluent called mobile phase, which is pumped through a column that contains a packing material made of small-size particles referred to as stationary phase.[4] Depending on the physicochemical properties of the analytes, the species in a sample mixture experience different molecular interaction with the stationary phase, inducing their separation as they leave the column at different times. The time at which a substance abandon the column and it is detected is called retention time. Commonly an ultraviolet (UV) detection unit is adapted at the end of the column, so that each analyte is detected as they elude the colulmn. A schematic diagram of an HPLC equipment is shown in Figure 2.2.

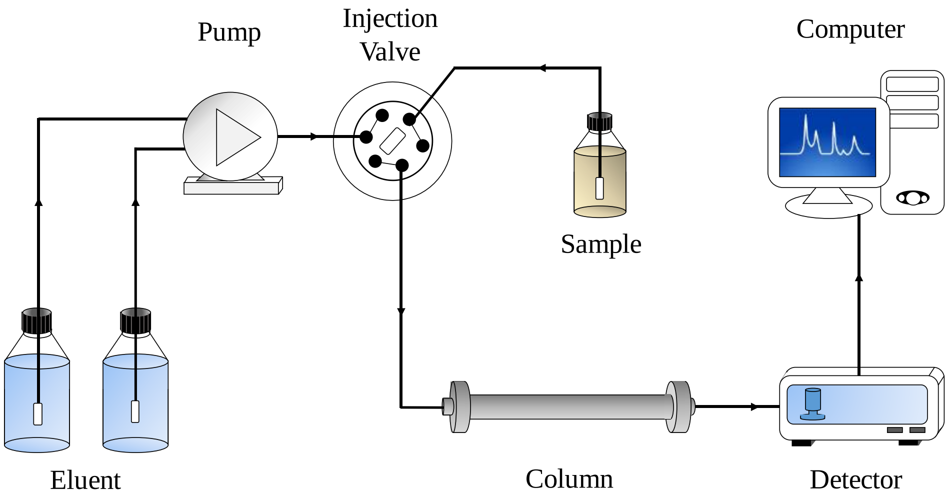

Figure 2.2. Schematic layout of a HPLC system. The main components of a HPLC system are: an eluent reservoir, a high-pressure pump, an injection system, a column, and a detection unit. The high-pressure pump is used to deliver the eluent (mobile phase) through the system. The sample is injected in the flow stream by an injection system. The mobile phase is directed towards the column where the different species in the sample are separated due to dissimilar molecular interactions of the analytes with the packed particles such as surface adsorption, ion exchange, and steric effects. As the analytes are eluted from the column, they are detected in the detection unit, which generates a signal that is translated by a processing system to generate a chromatogram.

The particular retention time of each analyte in the sample and their measured UV absorbance are plotted in a chromatogram. Figure 2.3 presents the chrogratogram of a sample mixture of aspirin and salsalate. Under equal conditions, the retention time of an analyte remain unchanged, and the chromatografic peak area is typically a function of the concentration of the analyte. Thus, the identification and quantification of a compound can be realised by using simple linear calibration models.

HPCL can be classified on the basis of the chemical properties of the mobile and stationary phases as normal phase and reverse phase. The normal phase method uses a column packed with polar particles and a non-polar eluent. Thus, polar analytes experience stronger molecular interactions with the particles of the stationary phase and show longer retention times compared to non-polar analytes. Conversely, the reverse phase HPLC consists on a polar mobile phase that flows through a non-polar column.

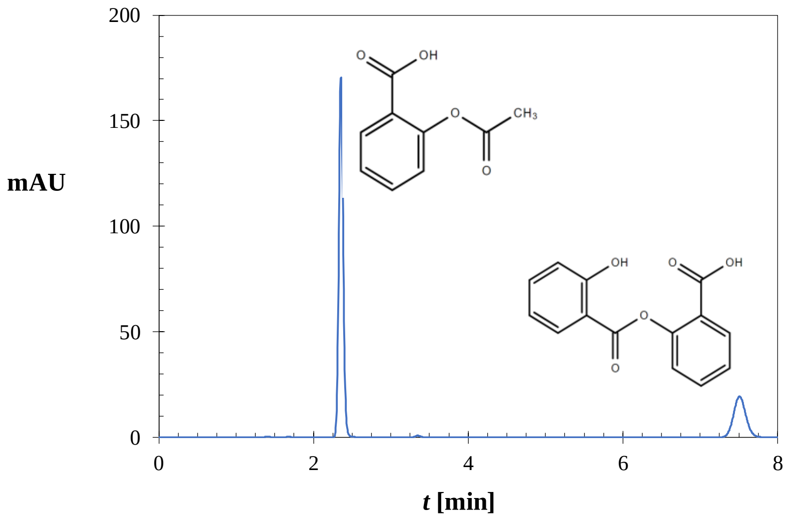

Figure 2.3. Reverse-phase HPLC chrogratogram of aspiring (at *ca*. 2.3 min) and salsalate (at *ca*. 7.6 min). Salsalate presents a strong affinity to the stationary phase than aspirin, so that the retention time of the former analyte indicates a stronger apolar nature compared to that of aspirin. In addition, the greater area under the aspirin peak indicates a greater amount of this compound in the analysed sample.

2.3. Karl Fischer Titration

The titration method makes use of the principles of the Bunsen reaction to quantitatively determine trace amounts of water contained in liquids or solids.

$$\mathbf{I_2 + SO_2 + H_2O \rightarrow 2HI + SO_3}$$

During the titration with iodine, water and the titration agent are consumed in a 1:1 ratio. Once the water is consumed, the excess of iodine in solution is detected, and the water content can be calculated from the concentration of iodine.[5]

Two distinct Karl Fischer titration methods are commonly employed for water determination: volumetric and coulometric titrations. In volumetric Karl Fischer titration, a solution of known iodine concentration is added to the sample, and the water content is calculated from the volume of the reagent employed. In contrast, during the coulometric titration, iodine is electrolytically generated from the iodine-containing reagent during the titration, and the electrical current used to generate iodine is measured as a function of time. Since one mole of water is consumed for each mole of iodine, the water content can be estimated from the amount of current used to generate iodine (Q): [6]

$$m = \frac{M_m \cdot Q}{z \cdot F} \tag{2.1}$$

where m is the mass of converted substance (I_2), M_m refers to the molecular mass, z is the equivalence number, and F is the Faraday constant (96485 C/mol).

2.4. Electrophoretic Light Scattering (ELS)

Electrophoretic Light Scattering (ELS) is an analytical technique that measures the mobility of charged particles in suspension driven by an electric field.

Upon the application of an electric field to a suspension, electrophoretic forces exert a translational motion of suspended charged particles towards the electrode of opposite charge. In a ELS equipment, an electrophoresis cell is illuminated by a light beam, which is scattered by the moving particles generating a frequency change from the incident light beam. This phenomenon known as Doppler shift is dependent upon the mobility of the particles in the suspension, and thus upon the charges carried by the dispersed particles.[7] The scattered light is collected at an optic system at well-defined angles θ that determine the scattering vector $\boldsymbol{q_e}$. A second light beam with a frequency equivalent to a steady motion in the electrophoresis cell is collected in the same optic system, where both the scattered and the reference beams are combined. The mixed signal is passed to a detector and processed by Fourier analysis to transform the time-based signal into a frequency spectrum. The Doppler shift of the scattered light is then translated to the electrophoretic mobility of the particles from which the potential at the hydrodynamic slipping plane of the particle, referred to as zeta-potential, is calculated from the Smoluchowski or the Huckel equations.[8] Figure 2.4 presents a schematic diagram of an ELS instrument.

An alternative approach to measure the electrophoretic mobility of suspended particle is to analyse the phase difference between the scattered light and the reference beam. The Phase Analysis Light Scattering method (PALS) measures the phase shift of the scattered light by the charged particles under motion. Consecutive samples of the phase shift yield a time dependent phase change $\varphi(t)$, from which the electrophoretic mobility is estimated provided the electric field and the scatter vector are known:[9]

$$\varphi(t) = |\boldsymbol{q_e}|\mu_{EP}E(t) \tag{2.2}$$

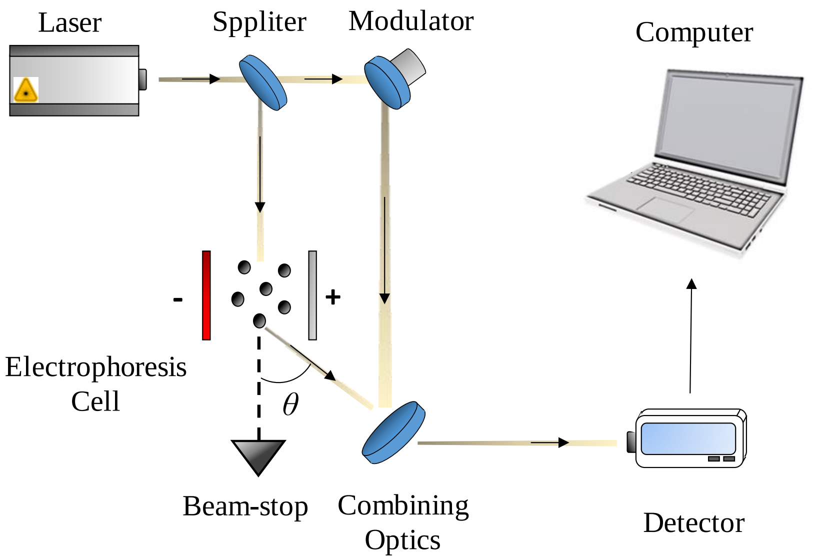

Figure 2.4. Schematic diagram of an Electrophoretic Light Scattering (ELS) instrument. In an ELS equipment, a light radiation (laser) emitted from a light source is split into two portions: an incident beam to the electrophoresis cell and a beam directed to a modulator. The incident beam illuminates the electrophoretic cell and is scattered by the moving particles with a Doppler frequency shift that is proportional to the mobility of the dispersed particles. The scattered beam is collected at well-defined angles *θ*, and it is combined with the reference beam reflected by a modulator that provides a beam with a constant unshifted frequency. The mixed signal is passed to a detector, and the Doppler shift of the scattered light is measured. The mobility and zeta-potential of the particles in suspension are calculated from the measured frequency shift.

PALS measures the frequency change over the entire signal instead of the frequency shift of individual particles, and provides an average value of the electrophoretic mobility. The measurement of the phase change between the scattered beam and the reference beam requires only a fraction of the frequency oscillation. Therefore, this method offers a more efficient measurement of the change in position of particles that experience low mobility in an electric field, since small displacements requires a longer measuring times in ELS for unambiguous detection of the Doppler shift.

2.5. Proton - Nuclear Magnetic Resonance (^{1}H-NMR)

This analytical technique is based on the interaction that takes place under a strong magnetic field between a radiofrequency electromagnetic radiation and the nuclei that conform the characterised material. This interaction induces the oscillation of the nuclei between energy levels when they absorb electromagnetic radiation at a precise frequency. The energy absorption is then detected and the signal is translated to a NMR spectrum, which enables the identification of the molecular structure of the material as well as to determine their molecular composition and molecular interactions.[10]

Nuclei with odd atomic number possess an overall spin angular momentum, and behave as small magnets with an associated magnetic field. In the absence of an external stimulus, a nucleus spins on its axis with a random orientation. When the nuclei are placed in a strong magnetic field H_0, they may adopt two different orientations with distinct energy states that is represented by a magnetic quantum number m. The higher energy level (m = 1/2) corresponds to the spin oriented against the direction of the external magnetic, while the spin orientation aligned to the external field presents the lowest energy state (m = -1/2). Figure 2.5 presents a schematic diagram of the different energy states of the spinning nucleus. The energy difference between the two states $\Delta E'$ is proportional to the applied magnetic field H_0 at the nucleus, and is given by the following equation:[9]

$$\Delta E' = \tilde{\gamma}\hbar H_0 \tag{2.3}$$

where $\tilde{\gamma}$ is a proportional constant called gyromagnetic ratio, and $\hbar = h/2\pi$ (h is the Plack's constant).

In a magnetic field, the nucleus experiences a change in the orientation on the rotational axis. When the frequency of an introduced oscillatory radiofrequency radiation matches that of the rotational motion of the spinning nucleus, the system is in resonance, and the nucleus can absorb the radiated energy. This energy absorption induces a switch on the spin orientation from the lowest to the highest energy state when the absorbed energy is equal to that of the different between the two orientation states $\Delta E'$. The nucleus can return to the lowest energy orientation by transferring energy to the surrounding nuclei.[11] NMR measures the absorbed/released energy to make a state transition, and the measurements are processed to generate peak signals in a NMR spectrum.

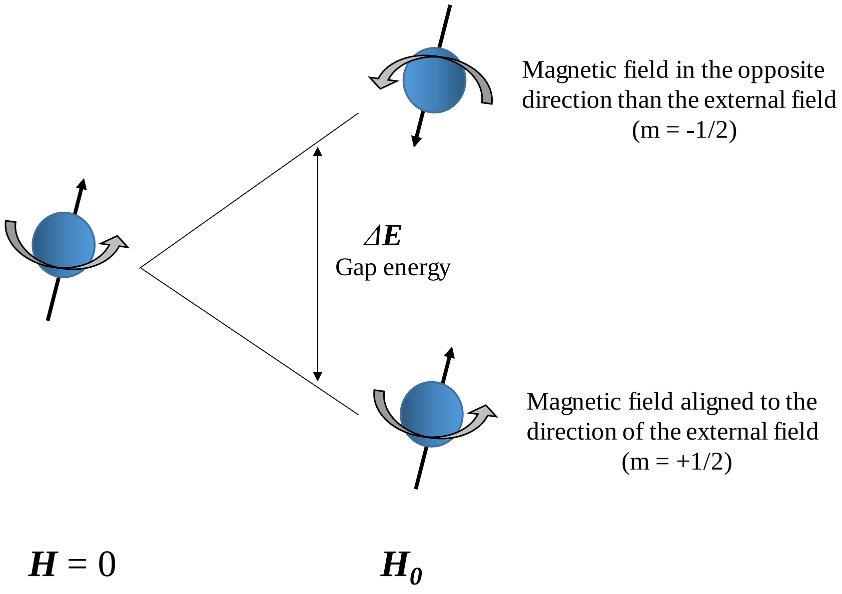

Figure 2.5. In the absence of the field (*H* = 0) the nuclei that conform the material are randomly oriented. In the presence of an external magnetic field H_0, the hydrogen nucleus present spins with distinct energy levels, being the difference of these levels given by *ΔE'*. The spin of the highest energy is oriented in the opposite direction than the external field, while the spin of the lowest energy level is aligned to the external field. The grey arrow represents the direction of the spin.

The hydrogens that conform a molecule experience dissimilar magnetic fields due to differences of the local electronic environment induced by structural features of the molecule, such as different binding partners or bonding lengths. Nuclei will require higher or lower frequencies to resonance based on the electron density surrounding them, which is translated into peaks at different positions in the NMR spectrum. The position in the spectrum at which a hydrogen atom exhibits resonance with respect to a given standard is called chemical shift $\tilde{\delta}$, which is conventionally given in ppm units. The area of the NMR peaks is proportional to the number of hydrogen nuclei with the same chemical environment. These peaks can be split into sub-peaks that provide information regarding the number of existing neighbouring nuclei. Provided that a hydrogen nucleus has neighbouring nuclei, its peak in the spectrum is symmetrically split into N+1 peaks, being N the number of hydrogens on nearby atoms. As an example, the molecule of ethanol presents hydrogen nuclei with three different chemical environments, that are represented in a ^{1}H-NMR spectrum by three peaks groups (Figure 2.6). The nucleus bonded to the oxygen (-OH) has not neighbouring hydrogens, and therefore shows a single peak in the spectrum. The hydrogens bonded to carbon atoms feels two or three nuclei if they respectively belong to a –CH3 or –CH2 group, and give rise to a split of the signal into three and four sub-peaks.

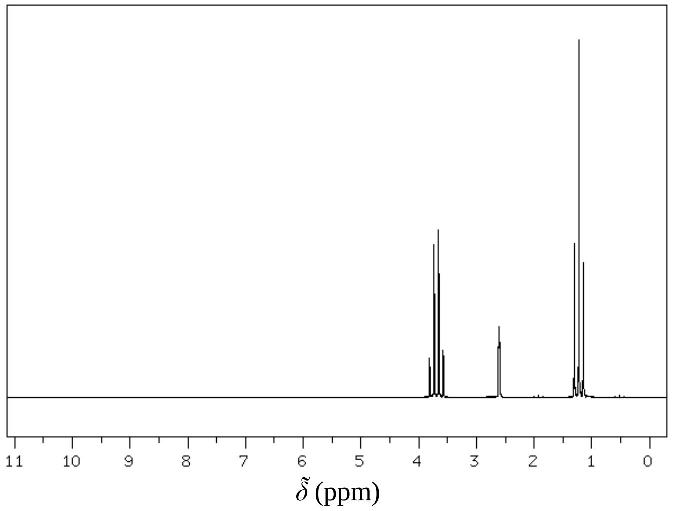

Figure 2.6. ^{1}H-NMR spectrum of ethanol. Each group of peaks correspond to hydrogen nuclei with different chemical environments.

2.6. X-ray powder diffraction

X-ray powder diffraction is a non-destructive analytical method routinely used in the pharmaceutical industry to identify the crystalline structure, composition, and physical properties of drug products.[12]

In X-ray powder diffraction, a finely ground and homogenised bulk sample is illuminated by high-frequency short-wavelength electromagnetic radiation. X-rays are produced in a sealed tube upon the collision of electron emitted at elevated velocity from a heated filament with a metal surface (anode). The metal target determines the wavelength of the X-ray radiation. In crystallography, a copper target (λ_w = 1.5405 Å) is commonly used. The X-ray source collimates and filtrate the radiation to produce a concentrated and monochromatic X-ray beam. An X-ray with a wavelength of the same order of magnitude as the d-spacing (distance between crystal planes) may produce constructive or destructive interference. When the beam is irradiated to the sample, it is partially diffracted by the atoms in a crystalline layer and part of the incident beam passes through into a consecutive crystalline layer, where is again partially scattered. At specific angles θ, the scattered X-rays interfere constructively. This phenomenon results in the diffracted X-rays reaching the detector at the same point along the wavelength.[13] In contrast, when the X- rays are not in phase, destructive interference occurs and the X-rays are detected at different points along the wavelength.

As shown in Figure 2.7, in order to produce a constructive interference, the bottom path needs to travel an additional distance that must be a multiple of the wavelength.

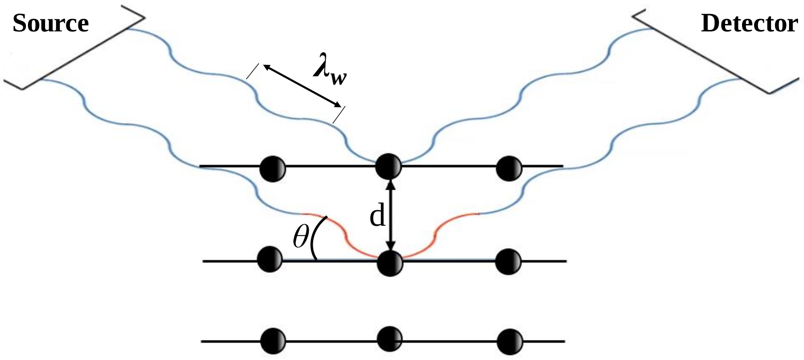

Figure 2.7. Schematic diagram of the constructive interference of the waves with the atoms in a crystalline sample. The angle at which the X-ray hits the atom is denoted by θ, and wavelength and the distance between atom layers are respectively λ and d. The red line fraction represents the additional travel that the bottom path must travel to hit the detector at the same point along the wavelength as the top path.

The condition for constructive interference is given by the Bragg's law, that relates the angle of the incident beam to the distance between atom layers:

$$n\lambda_w = 2dsin\theta \tag{2.4}$$

where n is an integer, d is the distance between atom layers, and λ_w refers to the wavelength. According to the Bragg's law, constructive interference occurs when the path-length difference is equal to an integer number of the wavelength. In conventional X-ray equipment, the X-ray source and the detector rotate (Figure 2.8) in order to scan the sample through a range of diffraction angles, which brings the different atom layers into Bragg's condition. Thus, all possible diffraction directions of the randomly oriented crystalline planes are captured by the equipment.

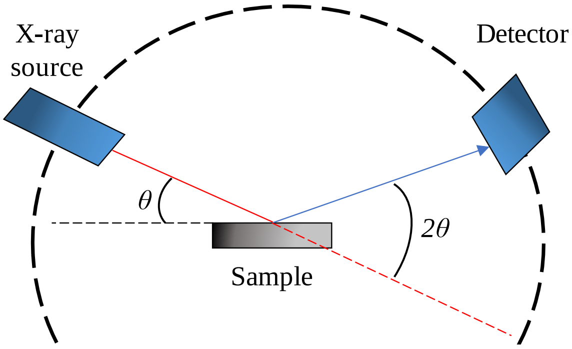

Figure 2.8. The X-ray and detector rotate in order to collect all possible diffractions, i.e. bring the atom planes into the Bragg's condition. The red line represents the emitted X-ray beam and the blue line is the diffracted electromagnetic radiation.

The signals collected from constructive interferences and picked up at the detector are translated into intensity peaks, which area is determined by the number of diffracted X-rays for a given angle. These peaks are then recorded at their corresponding 2θ values to generate a diffraction pattern. The outcome of scanning angles that results in destructive interference is the background in a diffraction pattern. The diffraction pattern is unique for each crystalline material and it can be used for identification purposes.[14] As an example, the diffraction pattern of the polymorphic form I of isonicotinamide is shown in Figure 2.9.

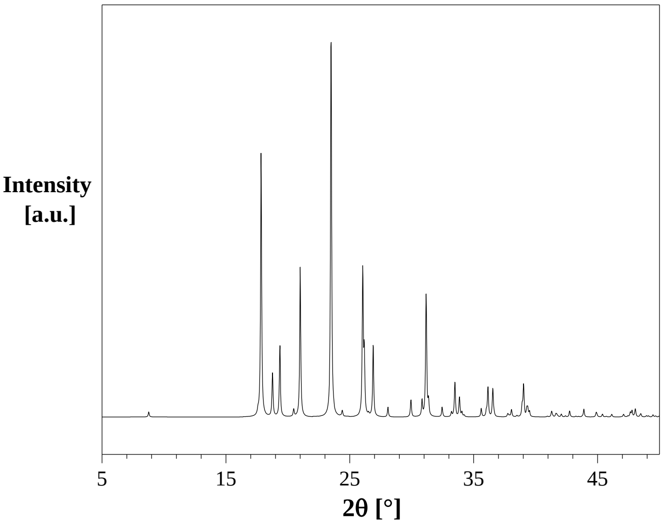

Figure 2.9. Diffraction pattern of isonicotinamide Form I obtained from the Cambridge Crystallographic Data Centre (CCDC - EHOWIH01).[15] The peaks in the diffraction pattern are obtained when the incident X-rays with a specific angle is diffracted by the atoms in the sample. The background data occurs when destructive interferences take place at certain angles.

2.7. References

1. Wu, C. S., Ikeyama, J., Nakabayashi, S., Sugiyama, T. & Yoshikawa, H. Y. Growth Promotion of Targeted Crystal Face by Nanoprocessing via Laser Ablation. *J. Phys. Chem. C* **123**, 24919–24926 (2019).
2. Rafiquzzaman, S. M., Rahman, M. A. & Kong, I. S. Ultrasonic-Assisted Extraction of Carrageenan. in *Seaweed Polysaccharides: Isolation, Biological and Biomedical Applications* 75–81 (Elsevier Inc., 2017).
3. Gill, P., Tohidi Moghadam, T. & Ranjbar, B. Differential Scanning Calorimetry Techniques: Applications in Biology and Nanoscience. *J. Biomol. Tech.* **21**, 167–193 (2010).
4. Dong, M. . *Modern HPLC for practicing scientists*. (John Wiley & Sons, Inc., 2006).
5. Koch, M., Tenbohlen, S., Blennow, J. & Hoehlein, I. Reliability and Improvements of Water Titration by the Karl Fischer Technique. in *15th International Symposium on High Voltage Engineering* **15**, 27–31 (2007).
6. Bruttel, P. & Schlink, R. Water Determination by Karl Fischer Titration. *Metrohm Monograph* 1–80 (2003).
7. Corbett, J. C. & McNeil-Watson, F. *Electrophoretic Light Scattering. Encyclopedia of Biophysics* (Springer Berlin Heidelberg, 2018).
8. Huang, G. *et al.* Symmetric electrophoretic light scattering for determination of the zeta potential of colloidal systems. *Colloids Surfaces A Physicochem. Eng. Asp.* **587**, 124339 (2020).
9. Corbett, J. C. W., McNeil-Watson, F., Jack, R. O. & Howarth, M. Measuring surface zeta potential using phase analysis light scattering in a simple dip cell arrangement. *Colloids Surfaces A Physicochem. Eng. Asp.* **396**, 169–176 (2012).
10. Bovey, F. A., Mirau, P. A. & Gutowsky, H. . *Nuclear Magnetic Resonance Spectroscopy*. (Elsevier, 1988).
11. Rahman, A. U. & Choudhary, M. I. *Solving Problems with NMR Spectroscopy*. (Academic Press, 2015).
12. Thakral, N. K., Zanon, R. L., Kelly, R. C. & Thakral, S. Applications of Powder X-Ray Diffraction in Small Molecule Pharmaceuticals: Achievements and Aspirations. *J. Pharm. Sci.* **107**, 2969–2982 (2018).
13. Pecharsky, V. & Zavalij, P. *Fundamentals of Powder Diffraction and Structural Characterization of Materials*. (Springer Science & Business Media, 2008).
14. Kohli, R. & Mittal, K. . *Developments in Surface Contamination and Cleaning: Fundamentals and Applied Aspects*. (William Andrew, 2015).
15. Aakeröy, C. B., Beatty, A. M., Helfrich, B. A. & Nieuwenhuyzen, M. Do polymorphic compounds make good cocrystallizing agents? A structural case study that demonstrates the importance of synthon flexibility. *Cryst. Growth Des.* **3**, 159–165 (2003).

Chapter 3. Solubility of 18 APIs and Intermediates in non-Polar Solvents

Abstract

The temperature dependent solubility of 18 organic compounds, of which some are active pharmaceutical ingredients, was measured in pure 1,4-dioxane, toluene and cyclopentyl methyl ether over a temperature range between 0 and 70 °C using a turbidity method. The solubility of the studied compounds in the three solvents increases with temperature in all binary solute/solvent systems, and all compounds exhibit a higher solubility in 1,4-dioxane than in toluene and cyclopentyl methyl ether. A number of thermodynamic models including van 't Hoff, Apelblat, λh, Margules, van Laar, Wilson, and the Non-Randomness Two Liquids (NRTL) were used for the correlation of the experimental data using the relative standard deviation describing the goodness of the correlation. The NRTL and the van 't Hoff equations present closer overall correlations, with the Apelblat model providing lower deviations to the experimental data in dioxane and cyclopentyl methyl ether. The Margules and the λh models show relatively poor correlations, with a deviation larger than 5% for several compounds in the three solvent systems. The activity coefficient of the binary systems was calculated to investigate solution behaviour. All the compounds in toluene presented a positive deviation from ideal solution, while positive and negative deviations were observed for the model compounds in the other two apolar solvents. The energy interaction was further analysed by using the regressed Wilson parameters from the calculated activity coefficient and the solubility data, which permitted to easily differentiate the deviations of the studied systems from ideality.

3.1. Introduction

In the manufacturing of highly regulated products such as pharmaceuticals and fine chemicals, crystallisation from solution is commonly employed, since this separation technology enables the formation of a crystalline particulate product with a purity close to 100% in a single step.[1] The design and optimization of the purification process require the knowledge of the phase equilibrium thermodynamics, which demands, on one hand, accurate solubility measurements as a function of the temperature and, on the other hand, accurate thermodynamic models to describe these solubilities.

The temperature dependent solubility of crystal compounds in a specific solvent strongly relates to design process parameters such as productivity, yield, and purity of the crystallisation process.[2,3] Thermodynamic solubility information of a binary system is difficult to predict as it depends on both solid state properties such as heat of fusion and melting temperature and non-ideal solution behaviour which are both difficult to estimate accurately. Over the last decades, efficient experimental methods have been developed to access reliable solubility data.[3] Amongst them, a temperature variation approach has been implemented in automated and commercially available equipment, which allows for faster measurements at the same time that minimizes physical labour.[3] As solubility generally increases with temperature, by increasing the temperature of a suspension, the solids gradually dissolve and the system turns into a clear solution. This change of the system from suspension to clear solution can be captured by turbidity measurements, resulting in a clear point temperature for a given sample composition, which can be assumed equal to the saturation temperature of the system if the temperature increase is sufficiently slow and the equilibrium between solid and solution is rapidly reached.[4] Solubility data can then be correlated, interpolated and extrapolated for any given temperature by using thermodynamic models such as van ’t Hoff or the activity coefficient model of Wilson.[5]

In this contribution we analyse the temperature dependent solubility of 18 organic compounds of which some are API in the non-polar solvents 1,4-dioxane, toluene, and cyclopentyl methyl ether (CPME) at a temperature range between 0 and 70 °C. Following solubility analysis, the activity coefficients of the experimental solute-solvent systems are calculated from experimental data and the ideal solubility. Then, six thermodynamic models were used to correlate the measured and calculated activity coefficient. The gained information alongside the Hansen parameters of the solvents, and the thermodynamic properties of the equilibrium are used to rationalise the measured solubility and the solution behaviour.

3.2. Materials and methods

3.2.1. Materials

Details of the 18 model compounds and 3 solvents used in this study are listed in Table 3.1, and their chemical structure are presented in Figure 3.1. All the materials were used as received without further purification.

Table 3.1. Details of the crystalline materials used in the present study. Alongside the CAS number of the product, the number between brackets refers to the supplier: [A] Sigma-Aldrich (Merck KGaA, Germany), [B] VWR Chemicals (Avantor, UK), and [C] Tokio Chemicals Industry Co., Ltd. (Japan).

Material	Acronym	Chemical Formula	Purity [%] ≥	Molecular Weight [g/mol]	CAS Number
2-Aminobenzoic acid	2ABA	$C_7H_7NO_2$	98	137.1	118-92-3 [A]
4-Aminobenzoic acid	4ABA	$C_7H_7NO_3$	99	137.1	150-13-0 [B]
4-Aminophenol	4AMP	$C_7H_7NO_4$	98	109.1	123-30-8 [A]
Aspirin	ASP	$C_9H_8O_4$	99	180.2	50-78-2 [B]
Caffeine	CAF	$C_8H_{10}N_4O_2$		194.2	58-08-2 [A]
Carbamazepine	CBZ	$C_{15}H_{12}N_2O$		236.3	298-46-4 [A]
2-Hydroxybenzoic acid	2HBA	$C_7H_6O_3$		138.1	69-72-7 [A]
3-Hydroxybenzoic acid	3HBA	$C_7H_6O_4$	99	138.1	99-06-9 [A]
4-Hydroxybenzoic acid	4HBA	$C_7H_6O_5$	99	138.1	99-96-7 [A]
Isonicotinamide	INA	$C_6H_6N_2O$	99	122.1	1453-82-3 [A]
RS-Naproxen	RS-NPX	$C_{14}H_{13}NaO_3$	98	230.3	23981-80-8 [C]
S-Naproxen	S-NPX	$C_{14}H_{13}NaO_3$	99	230.3	22204-53-1 [C]
Nicotinamide	NA	$C_6H_6N_2O$	9.5	122.1	98-92-0 [A]
4-Nitrobenzoic acid	4NBA	$C_7H_5NO_4$	98	167.1	62-23-7 [A]
Paracetamol	PCT	$C_8H_9NO_2$		151.2	103-90-2 [A]
Phenazine	PHZ	$C_{12}H_8N_2$	99	180.2	92-82-0 [B]
Picolinamide	PIC	$C_6H_6N_2O$	98	122.1	1452-77-3 [A]
Salycylsalicylic acid	SSA	$C_{14}H_{10}O_5$		258.2	552-94-3 [B]
Cyclopentyl methyl ether	CPME	$C_6H_{12}O$	99.9	100.2	5614-37-9 [B]
1,4-Dioxane	dioxane	$C_4H_8O_2$	99.8	88.1	123-91-1 [A]
Toluene	toluene	C_7H_8	98	92.1	108-88-3 [B]

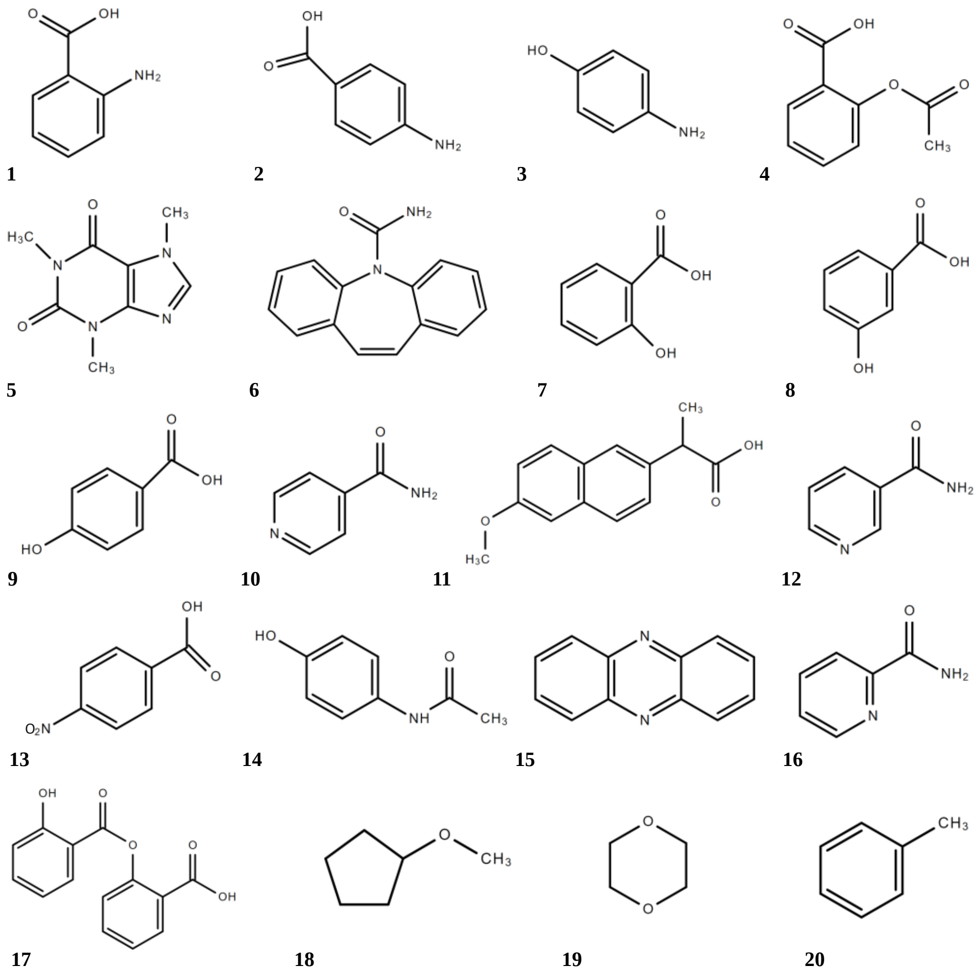

Figure 3.1. Molecular structure of the experimental compounds and solvents used in this study: 1) 2ABA, 2) 4ABA, 3) 4AMP, 4) ASP, 5) CAF, 6) CBZ, 7)2HBA, 8) 3HBA, 9) 4HBA, 10) INA, 11) NPX, 12) NA, 13) 4NBA, 14) PCT, 15) PHZ, 16) PIC, 17) SSA, 18) CPME, 19) dioxane, and 20) toluene.

3.2.2. Differential Scanning Calorimetry (DSC)

The melting point (T_m) and enthalpy of fusion (ΔH_f) of each model compound was measured in a DSC214 Polyma calorimeter (Netzsch Geratebau GmbH, UK), calibrated using indium as a standard substance. Approximately 5 mg of pure compounds, exactly weighted using an analytical balance (Sartorius Quintix-124-1S), were placed into 25 µL aluminium pans with pierced lids. The samples were subjected to a heating cycle from 20 °C to a maximum of 250 °C at a rate of 10 Kmin^{-1} while being continuously purged with helium. The analysis proceeded using an empty aluminium pan as a reference, and the retrieved data was processed by the Netzsch Proteus software (v.6.1) to obtain the melting temperature and the enthalpy of fusion of a given crystalline compound based on the onset temperature and the area under the main thermodynamic event in the generated DSC curve.

3.2.3. Solubility

The temperature dependent solubility of 10 APIs and intermediates commonly used in the pharmaceutical industry, 2ABA, 2HBA, ASP, CAF, CBZ, RS-NPX, S-NPX, PHZ, PIC, and SSA, have been studied at a temperature range between 12 °C and 70 °C in pure 1,4-dioxane, and between 0 °C and 70 °C in toluene and CPME was measured in a Crystal16 setup (Technobis Crystallisation Systems, The Netherlands). The lower melting temperatures of toluene and CPME compared to that of 1,4-dioxane allowed for a lower bottom temperature. In addition, solubility measurements in 1,4-dioxane at the same temperature range were carried out on 8 additional organic compounds: 4ABA, 4AMP, 3HBA, 4HBA, 4NBA, INA, NA, and PCT. These latter 8 compounds presented fouling, floating, or solubility levels below the equipment limit of around 1 mg/ml in toluene and CPME that prevented accurate clear point temperature determinations in these solvents. The solvents dioxane, CPME, and toluene were chosen because of their small dielectric properties.

Solubility measurements were carried out on suspensions of accurately known composition of the model compound in the pure solvent system individually prepared in 1.8 mL high-performance liquid chromatography (HPLC) glass vial. Both the amount of model compound and the amount of added solvent were weighted in an analytical balance (Mettler Toledo AG204) with a precision of ±0.1 mg. A coated polytetrafluoroethylene (PTFE) magnetic stirrer was added to the vials before sealing, and the vials were loaded into the Crystal16 equipment (Technobis, the Netherlands). The Crystal16 allows for solubility determination of 16 samples in parallel and automatically by coupling temperature control and light transmission measurements. The solute excess samples were magnetically stirred at 700 rpm while being subjected to a minimum of 3 consecutive cycles of heating and cooling alternated by an isothermal step at the lowest and highest temperature for 1 h. The heating rate was set at 0.3 °C /min, with that rate being previously reported to be sufficiently slow to accurately determine the temperature at which the suspension becomes a clear solution.[4] Cooling was carried out at a maximum rate of 1 °C /min. The clear point temperature for a given sample composition is obtained from the light transmission through the sample during the heating part of the temperature cycle and is the temperature at which the light transmission reaches 100%. Figure 3.2 presents a typical measurement outcome of the temperature and transmission as a function of time for a single experiment.

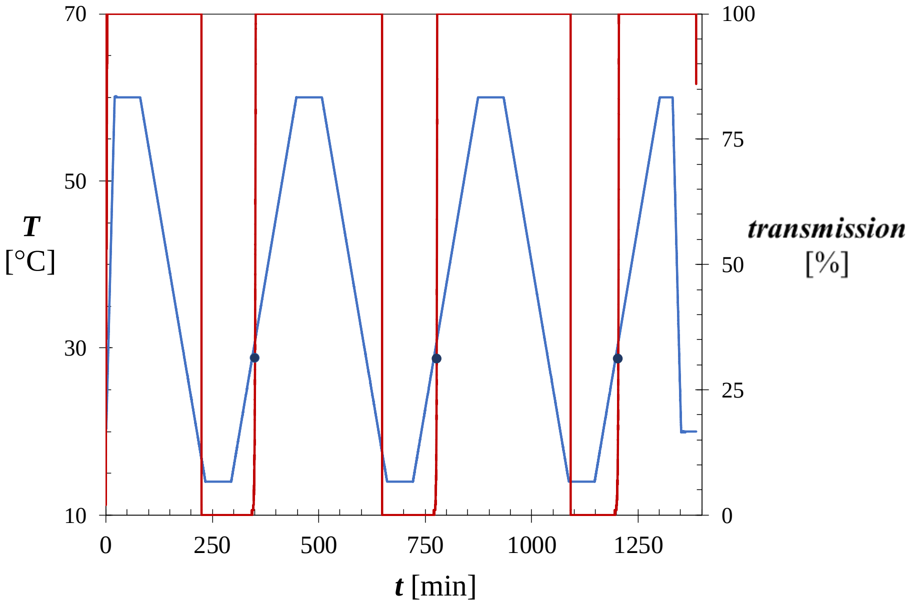

Figure 3.2. Temperature cycle for picolinamide in dioxane as a function of the temperature. The blue line represents the temperature and the red line is the measured light transmission over the experimental period. During heating, the clear point is taken at the point where the transmission line reaches 100%. The blue circles indicate the temperature point where the transmission reaches 100%. This temperature, assuming that equilibrium has been achieved, is referred to as the saturation temperature T_S. For the composition of picolinamide in dioxane represented in the graph, T_S = 31.1 ± 0.2 °C.

We assume that the heating rate of 0.3 °C per minute is sufficiently slow so that the determined clear point temperature is equal to the saturation temperature of the sample composition.[4] If the differences of the clear point temperatures measured in consecutive temperature cycles for a suspension were lower than 3 °C, then the average value was taken as the saturation temperature of that sample composition. Otherwise, the measurement was discarded. A minimum of 4 solubility data points over the temperature range was measured over the temperature range for each binary system. According to Black et al.,[6] this number of data points exceed the minimum number to evaluate solubility models and design cooling crystallisation process.

3.2.4. X-ray Powder Diffraction (XRPD)

To investigate the crystal structure of the different organic compounds in the selected isolating solvents, suspensions of approximately 5 mL of these compounds in the pure solvent were prepared and kept at room temperature under gentle stirring for a minimum of 5 days. Following equilibration for 5 days, the samples were filtered under reduced pressured over a

Buchner funnel. The recovered solids and the purchased material were separately loaded on a multi-well plate supported on a polyamide film and the crystalline phase was identified using a Bruker D8 Discover diffractometer (GX002103 - Priscilla) equipped with a Cu anode (Cu Kα1 λ = 1.54056 Å), monochromator, and a Vantec PSD detector. The XRPD spectra were recorded over a 2θ range of 4 to 35° at a scan rate of 0.015° per second.

3.3. Thermodynamic models

For modelling purposes, the measured solubility in mg/mL units was transformed into mole fraction solubility (x_2) using the following expression:

$$x_2 = \frac{{m_2}/{M_2}}{{m_1}/{M_1} + {m_2}/{M_2}} \tag{3.1}$$

where m_i represent the mass, M_i stands for the molecular mass, and the subscripts 1 and 2 refers to solvent and solute, respectively.

Solubility behaviour can be accurately described by thermodynamic equations, allowing for the interpolation and extrapolation of miscibility data at any given temperature. For this, the algebraic expression proposed by Prausnitz[7] enables solubility prediction for ideal binary systems based on parameters accessible from thermal analysis:

$$\ln\left(x_2^{id}\right) = \frac{-\Delta H_f}{R}\left(\frac{1}{T} - \frac{1}{T_m}\right) - \frac{1}{RT}\int_{T_m}^{T} \Delta C_p \, dT + \frac{1}{R}\int_{T_m}^{T} \frac{\Delta C_p}{T} dT \tag{3.2}$$

here, x_2^{id} stands for the ideal mole fraction solubility of the solute, ΔH_f refers to the enthalpy of fusion, R is the gas constant, and T_m is the melting temperature. The significance of the molar heat capacity ΔC_p is negligible compared to that of the enthalpy of fusion,[8,9] and thus equation (3.2) can be reduced to the following expression with minor loss of accuracy on solubility prediction for ideal systems:

$$\ln\left(x_2^{id}\right) = \frac{-\Delta H_f}{R}\left(\frac{1}{T} - \frac{1}{T_m}\right) \tag{3.3}$$

Ideal behaviour is associated to equal solute-solute, solvent-solvent, and solvent-solute interaction energies, and therefore a dissolution process of an ideal system proceeds without net energy change.[10] However, most systems deviate from this behaviour and present significant differences of their molecular interaction energies, which leads to solubility behaviour deviating from an ideal one.[2] To account for these deviations from ideality and provide a closer description of the solid-liquid equilibrium, the van't Hoff equation replaces the heat of fusion ΔH_f by the enthalpy of dissolution ΔH_{dis} and the melting temperature T_m by a transition temperature T_0.

$$\ln(x_2) = \frac{-\Delta H_{dis}}{R}\left(\frac{1}{T} - \frac{1}{T_0}\right) \tag{3.4}$$

By plotting the natural logarithm $\ln(x_2)$ of the mole fraction solubility as a function of the inverse temperature, the two parameters of the van't Hoff equation can be determined from the slope and intercept of the fitted linear line to the experimental data.

Solubility data of non-ideal systems have also been extensively correlated by the use of the Apelblat equation.[11] Apelblat proposed a three parameter semi-empirical equation for the correlation of solubility data, which reported excellent fitting results for binary systems:[9,12,13]

$$\ln(x_2) = a_A + \frac{b_A}{T} + c_A \ln(T) \tag{3.5}$$

The parameter c_A accounts for the differences in heat capacity of the solid phase and the liquefied solute at the solution temperature. Compared to equation (3.4), Apelblat's equation contains an additional temperature dependent term associated to an additional fitting parameter.

In addition to the van 't Hoff equation and the Apelblat model, Buchowski et al.[14] proposed another two parameter model, known as λh model, to extrapolate and/or interpolate mole fraction solubilities at any given temperature:

$$\ln\left(1 + \frac{\lambda(1 - x_2)}{x_2}\right) = \lambda h\left(\frac{1}{T} - \frac{1}{T_m}\right) \tag{3.6}$$

Instead of describing solubility from the Prauznit's expression, Buchowski studied the activities of the solvent and solute as a function of temperature in order to account in the solubility estimation for the deviations from ideal solution due to associated systems. The two constants of the λh model are regressed parameters from the experimental data. The first parameter (λ) refers to the mean association number. Buchowski stated that deviations from $\lambda = 1$ reflects non-ideal behaviours due to self-association. The second factor (h) relates to the enthalpy of dissolution, and therefore the λh model accounts for the different molecular interaction energies associated to the mixing of solvent and solute.

Solubility models based on the energy excess of the mixture offer a more rigorous thermodynamic approach for data correlation. A general expression to represent the Gibbs free energy excess of mixing in binary mixtures is given by:[5]

$$G^E = RT(n_1 \ln(\gamma_1) + n_2 \ln(\gamma_2)) \tag{3.7}$$

where G^E is the total excess Gibbs energy, n_i stands for the number of moles, γ_i is the activity coefficient, and the subscripts 1 and 2 refer to solvent and solute, respectively. The activity coefficient describes the extent to which a system deviates from ideal thermodynamic behaviour. It can be estimated from experimentally determined solubility data x_i and the ideal solubility x_i^id:

$$x_i^{id} = x_i \gamma_i \tag{3.8}$$

Ideal behaviour occurs when $\gamma = 1$ ($x_i^{id} = x_i$) and is well-described by equation (3.3). An activity coefficient lower than 1 ($\gamma < 1$) indicates a negative deviation from ideal behaviour, and positive deviations occur when $\gamma > 1$.

The derivative of equation (3.7) at constant pressure and temperature relates the excess Gibbs energy G^E to the activity coefficient of the solute (i=2) and solvent (i=1):[5]

$$\left(\frac{dG^E}{n_i}\right)_{P,T,n_j} = RT\ln(\gamma_i) \tag{3.9}$$

This expression allowed for the development of different activity coefficient models accounting for the effect of the solute concentration on the activity coefficient. A simple and comprehensive relation of the mole fraction solubility and the activity coefficient was given by Margules: [5]

$$\ln \gamma_i = \frac{a_M}{RT}(1 - x_i)^2 \tag{3.10}$$

where a_M is a constant which can be regressed from the experimental data, and the suffix refers to the solvent (i = 1) or solute (i = 2). The one-parameter equation implies a symmetrical behaviour of the activity coefficients γ_1 and γ_2 for solvent and solute.

Van Laar's model introduces a second parameter to compensate these limitations and describe asymmetric systems. According to van Laar's model, the activity coefficients of solvent and solute are given by:

$$\ln\gamma_1 = \frac{a_L}{RT\left(1+\frac{a_L x_1}{b_L x_2}\right)^2} \tag{3.11}$$

$$\ln\gamma_2 = \frac{b_L}{RT\left(1+\frac{b_L x_2}{a_L x_1}\right)^2} \tag{3.12}$$

Despite being widely used due to their simplicity, solubility data correlation of strong non-ideal systems by the Margules and Van Laar's models are imprecise, and other Gibbs energy-based models are used to obtain more accurate representations of the solute-solvent systems. In this context, Wilson[15] proposed a two-parameter equation from a molecular interpretation of the non-ideal effect through the local composition. The local composition concept for a binary system of species *i* and *j* is illustrated in Figure 3.3. According to this model, the activity coefficients of the solvent and solute are respectively given by:[5]

$$\ln(\gamma_1) = x_2\left(\frac{\Lambda_{12}}{x_1+\Lambda_{12}x_2} - \frac{\Lambda_{21}}{x_2+\Lambda_{21}x_1}\right) - \ln(x_1+\Lambda_{12}x_2) \tag{3.13}$$

$$\ln(\gamma_2) = -x_1\left(\frac{\Lambda_{12}}{x_1+\Lambda_{12}x_2} - \frac{\Lambda_{21}}{x_2+\Lambda_{21}x_1}\right) - \ln(x_2+\Lambda_{21}x_1) \tag{3.14}$$

where:

$$\Lambda_{ij} = \frac{v_j}{v_i}\exp\left(-\frac{\lambda_{ij}-\lambda_{ii}}{RT}\right) \tag{3.15}$$

here, λ_{ij} refers to the interaction energy between a molecule *i* and a molecule *j*, and v_i is the molar volume of a molecule *i*. As it can be deduced from equation (3.15), this model considers the dissimilar interaction energies λ_{11} between solvent molecules, λ_{22} between solute molecules and $\lambda_{12} = \lambda_{21}$ between solute and solvent molecules, and differentiates between the size of each species in the binary solution by introducing the molecular volume of the solvent (v_1) and the solute (v_2). The cross-interaction energies (λ_{12}-λ_{11}) and (λ_{21}-λ_{22}) are the two adjustable parameters of the Wilson equation that can be regressed from experimental data.

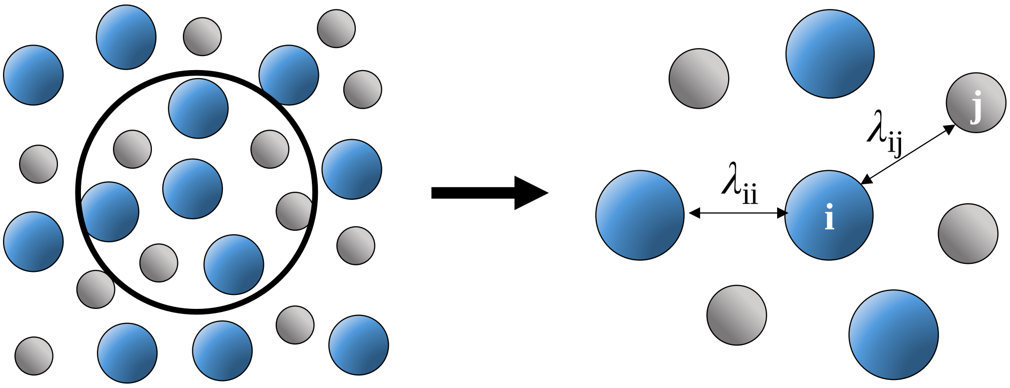

Figure 3.3. Schematic diagram of the molecular composition concept described by the Wilson model. The diagram shows molecules *i* and *j* of different sizes, and describes their interactions from the molecule *i* at centre.

On the basis of the local composition concept proposed by Wilson, Renon and Prausnitz[16] derived the non-random two liquids (NRTL) equation. This model describes the excess of Gibbs energy as the sum of the different and distinct energy changes associated to the incorporation of the molecular species *i* and *j* from a pure liquid state to a mixed solution of both species. The semi-empirical equation describes the activity coefficient using two adjustable parameters (g_{12} and g_{21}) and a pre-defined constant (α) which value depend on the chemical composition of the mixture. According to the NRTL model, the activity coefficient as a function of the solubility mole fraction can be expressed as:

$$\ln(\gamma_i) = x_j^2 \left[\tau_{ji} \left(\frac{G_{ji}}{x_i + G_{ji} x_j} \right)^2 + \tau_{ij} \frac{G_{ij}}{\left(x_j + G_{ij} x_i\right)^2} \right] \qquad \textbf{(3.16)}$$

where:

$$\tau_{ij} = \frac{g_{ij}}{RT} \qquad \textbf{(3.17)}$$

$$G_{ij} = \exp\left(-\alpha \tau_{ij}\right) \qquad \textbf{(3.18)}$$

here, g_{ij} is the cross-interaction energy between the molecule *j* and molecule *i*, and α stands for the non-randomness of the distribution of the molecular species in the mixture. The non-randomness parameter is usually set between 0.2 and 0.47, however some authors assert that this parameter offers a better solubility correlation if it is adjusted from experimental data.[17]

3.4. Results

3.4.1. Solid Phase Characterisation

Thermal Analysis. The determined enthalpy of fusion (ΔH_f) and melting temperature (T_m) of the model compounds are compared to the literature data in Table 3.2. The experimental T_m of all compounds are similar to the reported melting temperature, with a maximum absolute temperature difference of 1% for SSA. The difference of the ΔH_f with the literature data was larger than 5% for 2ABA, 4ABA, 2HBA, 4AMP, ASP, CAF, INA, PCT, and SSA. A series of compounds, including 2ABA, 4ABA, 4HBA, INA, and PCT were reanalysed by DSC to confirm the repeatability of the thermal analysis method. The analysis provided similar ΔH_f and T_m values as can be seen in Table 3.2. Presence of impurities or imperfections in purchased material, sample-to-sample variation and measurement errors may significance contribute to the data deviations compared to the reported thermodynamic properties.

Table 3.2. Enthalpy of fusion (ΔH_f) and melting temperature (T_m) obtained by DSC analysis for 18 APIs and intermediates compounds used in this work. The thermodynamic values of the organic compounds reported in the literature are tabulated alongside the measured data. The crystalline structure information was obtained by XRPD analysis carried out on the purchased material (provided in appendix A.1). The compounds with an * presented two thermal events during DSC heating.

Compound	***Polymorphic Form***	**ΔH_f [kJ/mol]**	**T_m [°C]**	**Literature**		
				ΔH_f [kJ/mol]	**T_m [°C]**	**Ref.**
2ABA*	I	23.5; 23.5	145.4; 145.5	20.7	145	[18]
4ABA	I	26.3; 26.5	187.8; 187.8	23.2; 25.5	187.2; 187.6	[19]
4AMP		32.6	189.4	26	189.4	[20]
ASP	I	31.8	139.1	29.8	140.9	[21]
CAF*	β	20.8	235.8	21.9; 19.9	237.1; 236.4	[22,23]
CBZ*	III	26.7	189.9	25.6	192.1	[24]
2HBA		25.4	158.7	27.1; 24.6	161.0; 158.9	[20,24]
3HBA	I	36.9	201.2	36.5	203.3	[25]
4HBA		33.7; 33.9	214.9; 215.1	31.0; 30.9	214.9; 215.0	[25,26]
INA*	I	24.7; 25.0	156.2; 156.1	26.8	157.9	[27]
NA	I	24.7	128.3	23.8; 25.5	130.6; 128.5	[24,28]
4NBA	II	35.2	239.6	36.9	239.6	[20]
RS-NPX		35.8	156	33.2	155.8	[29]
S-NPX		34.0	155.9	31.7	156.2	[29]
PCT	I	29.3; 29.3	168.9; 168.9	27.6	170.1	[30]
PHZ		24.8	174.6	24.9	174.8	[31]
PIC*	II	19.4	106.3	19.4	106.4	[32]
SSA		32.6	143.9	29	157.1	[33]

The DSC plots, including the ΔH_f, the peak temperature, and the onset temperature for the model compounds investigated in this study are given in appendix A.1. A small exothermal event preceding the major one was detected during the DSC measurement for 2ABA, CAF, CBZ, INA, and PIC, which may indicate the presence of impurities or a different polymorphic form in a residual amount alongside the main form of the compound, for which the melting temperature and heat of fusion are determined. The crystalline phase was studied by XRPD, and the identified crystalline structure of the initial material is listed in Table 3.2.

Crystalline Phase Analysis. In general, the model compounds suspended in the apolar solvents did not show phase transitions compared to the raw material after stirring the suspensions for 5 days at ambient temperature. The XRPD spectra of all the crystalline samples from the equilibrated systems can be consulted in the appendix A.2. In dioxane, however, 2ABA, 4NBA, 4HBA, and CBZ did show indications of a phase transition. Figure 3.4 shows the diffraction patterns of the purchased material of these four compounds compared to those after suspension equilibration in the non-polar solvent. The sample from the 2ABA suspension in dioxane retained the initial form I,[34] with extra peaks at *ca.*11, 15, and 27° that may indicate a partial transformation to the polymorphic form II. [35] The recovered crystals from 4NBA suspension exhibited a similar pattern to the polymorphic form I reported in the literature,[36] while the XRPD data from the purchased material was identified as form II[37] according to the reference pattern NBZOAC14 from the Cambridge Crystallographic Data Centre (CCDC). The diffractogram of 4HBA suspended in dioxane was equivalent to a reported solvate,[38] with extra peaks at approximately 18° and 25° that suggest the presence of the pure crystalline phase of 4HBA.[39] The diffraction spectra from the equilibrated CBZ crystals in the non-polar solvent differed from the polymorphic forms listed in the CCDC database. A solvate between CBZ and 1,4-dioxane has been previously reported and could explain the observed difference.[40,41].

3.4.2. Solubility

Figure 3.5 shows the temperature dependent solubility in mg/ml of the compounds in 1,4-dioxane. The solubility magnitude of the solutes at 45 °C decreases in the following order: SSA > 2HBA > 2ABA > PIC > ASP > S-NPX > 3HBA > RS-NPX > 4HBA > 4ABA > 4NBA > PHZ > CBZ > NA > 4AMP > INA > CAF, with data for PCT only obtained above 60 °C.

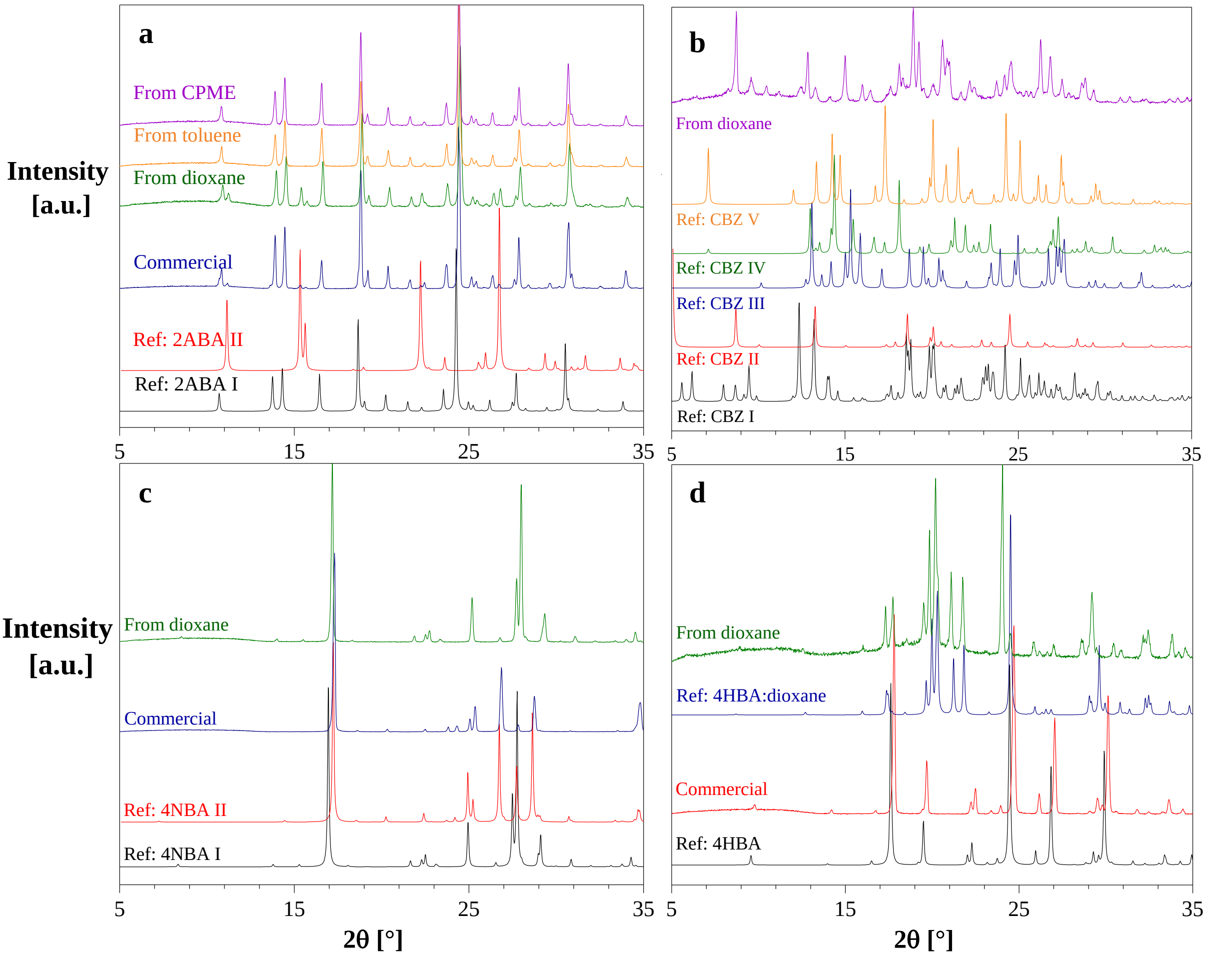

Figure 3.4. **a:** The diffraction patterns retrieved from 2ABA after equilibration showed that the compound retained the polymorphic form I (CCDC – AMBACO01) in toluene and CPME. Additional peaks at *ca.* 7 and 15° indicates partial transformation to form II (CCDC – AMBACO03) when the compound is suspended in dioxane. **b:** The pattern of the CBZ crystals in 1,4-dioxane differs from all known CBZ forms; CBZ I (CCDC – CBMZPN11), CBZ II (CCDC – CBMZPN03), CBZ IV (CCDC – CBMZPN12), and CBZ V (CCDC - CBMZPN16). **c:** NBA in 1,4-dioxane shows a transition from the polymorphic structure II (CCDC - NBZOAC14) to form I (CCDC - NBZOAC15). **d:** 4HBA in 1,4-dioxane shows a transition from 4HBA (CCDC – JOZZIH01) to the solvate 4HBA:dioxane (CCDC - PATGEZ).

The ortho isomers of hydoxybenzoic acid (2HBA), aminobenzoic acid (2ABA), and pyridinecarboxamide (PIC) present greater solubility values in dioxane than the analogous meta and para isomer molecules. The ortho isomer of pyridinecarboxilamide (PIC) presents the greatest temperature dependence, depicted by the larger slope of the estimated trendline to the solubility data. The temperature dependence solubility of the rest of the studied compounds is similar over the experimental temperature range. In the solvent CPME, the solubility order of the studied solutes follows a similar trend to that in dioxane although, as can be seen in Figure 3.5 and 3.6, the solubility of the compounds is lower in CPME.

In toluene, the studied compounds, with the exception of CAF and PHZ, present a considerably lower solubility (Figure 3.7). For instance, at approximately 45 °C the solubility of SSA in dioxane and CPME are respectively 37 and 14 times higher than that in toluene. CAF and PHZ are only slightly less soluble in CPME.

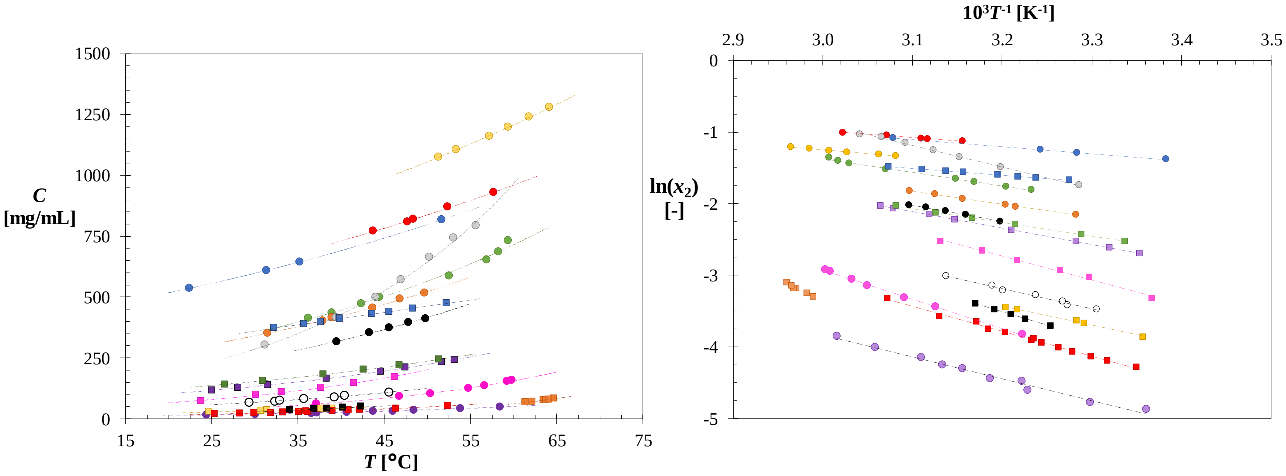

Figure 3.5. Temperature dependent solubility in mg/mL (left) and the van 't Hoff plot (right) of 2ABA (●), 2HBA (●), ASP (●), CAF (●), CBZ (●), RS-NPX (●), S-NPX (●), PHZ (○), PIC (●), SSA (●), 3HBA (■), 4ABA (■),4AMP (■), 4HBA (■), INA (■), NA (■), 4NBA (■), and PCT (■) in 1,4-dioxane over a temperature range between 15 to 65 °C. The lines are added as a guide to the eye.

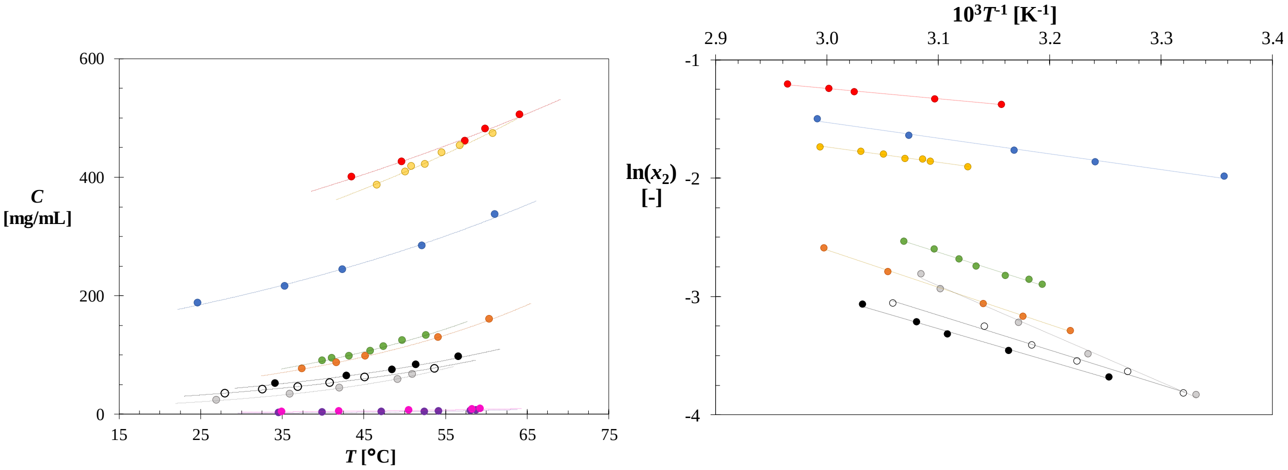

Figure 3.6. Temperature dependent solubility in mg/mL (left) and the van 't Hoff plot (right) of 2ABA (●), 2HBA (●), ASP (●), CAF (●), CBZ (●), RS-NPX (●), S-NPX (●), PHZ (○), PIC (●), and SSA (●) in pure CPME between 5 and 65 °C. The lines are added as a guide to the eye.

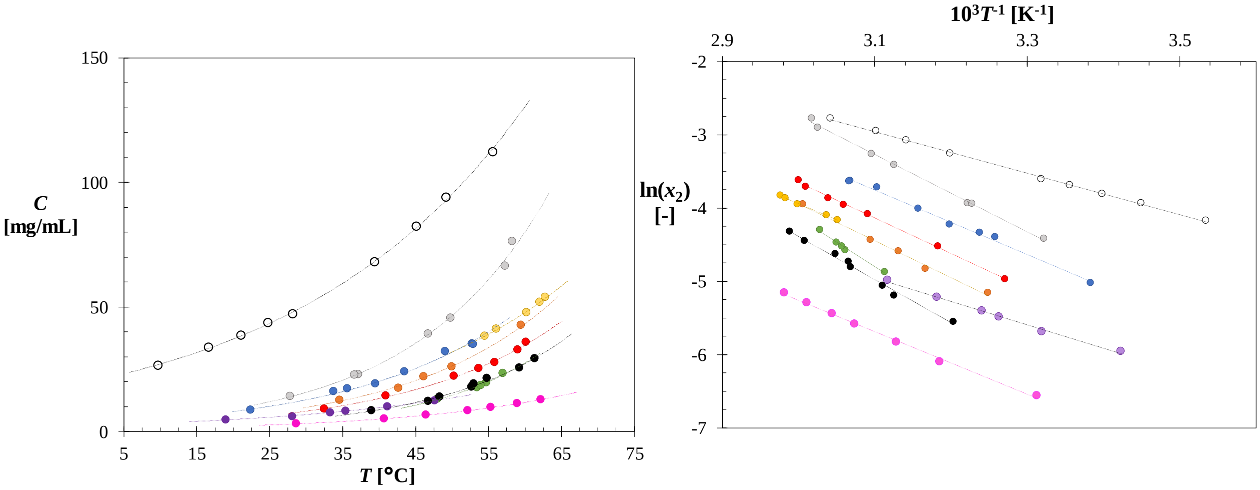

Figure 3.7. Temperature dependent solubility in mg/mL (left) and the van ‘t Hoff plot (right) of 2ABA (●), 2HBA (●), ASP (●), CAF (●), CBZ (●), RS-NPX (●), S-NPX (●), PHZ (○), PIC (●), and SSA (●) in toluene over a temperature range between 5 and 65 °C. The lines are added as a guide to the eye.

3.4.3. Thermodynamic model regression

3.4.3.1. Semi-empirical solubility models

The parameters of the van ’t Hoff equation were estimated from the van ’t Hoff plots of the studied compounds in the three solvents systems (appendix A.3). The parameters of the Apelblat and the λh semi-empirical models were regressed from the experimental data using a non-linear least-squared algorithm implemented in Matlab 2018a. Table 3.3 presents the estimated factors for the three empirical models from the experimental mole fraction solubility of the studied solutes across the three apolar solvents.

The goodness of the fit to the experimental data is discussed later using the relative standard deviation and the values are listed in Table 3.5. A small difference between the enthalpy of dissolution $\triangle H_{dis}$ regressed from the van ’t Hoff equation and the enthalpy of fusion $\triangle H_f$ measured from the thermal analysis indicates a solution behaviour close to ideality. For instance, the binary systems of PHZ in the three non-polar solvents present similar values of $\triangle H_{dis}$ and $\triangle H_f$, that may suggest a closer ideal behaviour than that of the other compounds in the same solvent systems.

Table 3.3. Regressed parameters of the van 't Hoff (ΔH_{dis} and T_0), Apelblat (a_A, b_A, and c_A), and the λh model (λ and h) obtained from the correlation to the experimental solubility data.

Solvent	**Solute**	**van't Hoff**		**Apelblat**			**λh**	
		ΔH_{dis} [kJ/mol]	**T_0 [°C]**	**$10^{-1}a_A$ [-]**	**$10^{-3}b_A$ [K^{-1}]**	**c_A [-]**	**λ [-]**	**$10^{-3}h$ [K^{-1}]**
dioxane	2ABA	8.14	235	-2.30	0.17	3.71	0.13	2.53
	2HBA	7.80	240	-0.05	-0.82	0.35	0.11	2.24
	ASP	16.0	164	-30.7	12.8	45.9	0.54	3.04
	CAF	24.0	327	-16.6	4.89	25.4	0.31	8.50
	CBZ	34.1	164	-32.9	12.0	50.0	3.53	1.39
	RS-NPX	18.9	179	-0.02	-2.01	0.77	0.78	3.01
	S-NPX	15.1	205	-1.50	-0.94	2.78	0.44	3.53
	PHZ	23.5	209	-9.76	1.93	15.4	0.58	4.78
	PIC	25.0	96.6	-4.77	-0.36	8.25	1.64	2.03
	SSA	8.82	276	-6.55	2.22	9.92	0.01	4.10
	4ABA	19.0	187	-0.70	-1.73	1.77	1.02	2.25
	4AMP	22.2	249	-0.51	-2.18	1.50	0.73	4.11
	3HBA	7.86	390	4.31	-2.89	-6.17	0.17	2.79
	4HBA	15.8	224	-1.34	-1.11	2.56	0.90	2.09
	INA	28.9	200	-20.8	6.49	31.9	0.55	6.68
	NA	30.7	172	-21.2	6.50	32.7	0.65	6.73
	4NBA	27.8	147	36.2	-19.5	-52.6	3.64	0.87
	PCT	53.8	130	0.05	-5.60	2.23	2.91	2.05
CPME	2ABA	11.0	269	-13.8	5.24	20.8	0.13	4.81
	2HBA	7.27	361	-13.2	5.54	19.7	0.002	3.57
	ASP	24.8	177	-39.7	16.1	59.7	0.43	6.47
	CAF	38.8	279	-0.01	-4.04	1.15	0.76	6.65
	CBZ	26.4	516	-0.05	-3.23	0.81	0.13	31.1
	RS-NPX	23.0	248	-48.0	20.0	71.8	0.41	7.66
	S-NPX	26.2	187	-25.1	9.07	38.0	0.54	5.65
	PHZ	24.4	222	6.92	-5.87	-9.37	0.45	6.19
	PIC	33.9	146	-51.3	20.2	77.5	0.27	13.7
	SSA	10.8	330	35.2	-18.1	-51.5	0.01	7.58
toluene	2ABA	36.5	172	15.3	-10.9	-21.3	0.68	6.99
	2HBA	40.3	172	-32.9	11.3	50.2	0.77	6.42
	ASP	55.5	147	-0.17	-5.96	2.66	0.89	7.79
	CAF	26.5	373	-75.6	31.7	113	0.40	8.66
	CBZ	35.6	291	0.06	-4.45	1.29	0.37	13.5
	RS-NPX	49.1	170	28.3	-18.7	-39.7	0.79	7.81
	S-NPX	42.0	177	-40.7	14.9	61.7	0.66	7.95
	PHZ	23.6	213	-4.07	-0.75	6.94	0.58	4.83
	PIC	43.9	130	-31.9	10.29	49.1	0.39	13.2
	SSA	36.2	204	-186	86.8	275	0.76	7.97

3.4.3.2. *Activity coefficient-based models*

To evaluate the activity coefficient γ_2 of the studied organic compounds, first the ideal solubility of the solute x_2^{id} was calculated from equation (3.3) using the data obtained from the thermal analysis. Then, equation (3.8) was solved for γ_2 from the calculated x_2^{id} and the experimental data x_2.

Figure 3.8 to 3.10 shows the temperature dependent activity coefficients γ_2 for each compound in the different organic solvents as a function of the temperature. Within the experimental temperature range, the binary systems in general deviate from ideality ($\gamma_2 = 1$), with a clear tendency towards ideal solutions at increasing temperature. By defining an arbitrary boundary value, such as $-0.25 < \ln \gamma_2 < 0.25$, we can identify the close-to-ideal systems. For instance, the activity coefficients of CAF, PHZ, and PIC in 1,4-dioxane, 2ABA, ASP and NPX in CPME, and PHZ in toluene are close or within the defined boundaries. The activity coefficients of all the studied compounds are positive in toluene, which corresponds to a positive deviation from ideality. In the two other apolar solvents, the pyridinecarboxilamide compounds, CBZ, CAF, PHZ, and PCT show a positive deviation, while the activity coefficient of the other compounds is lower than one, showing a negative deviation.

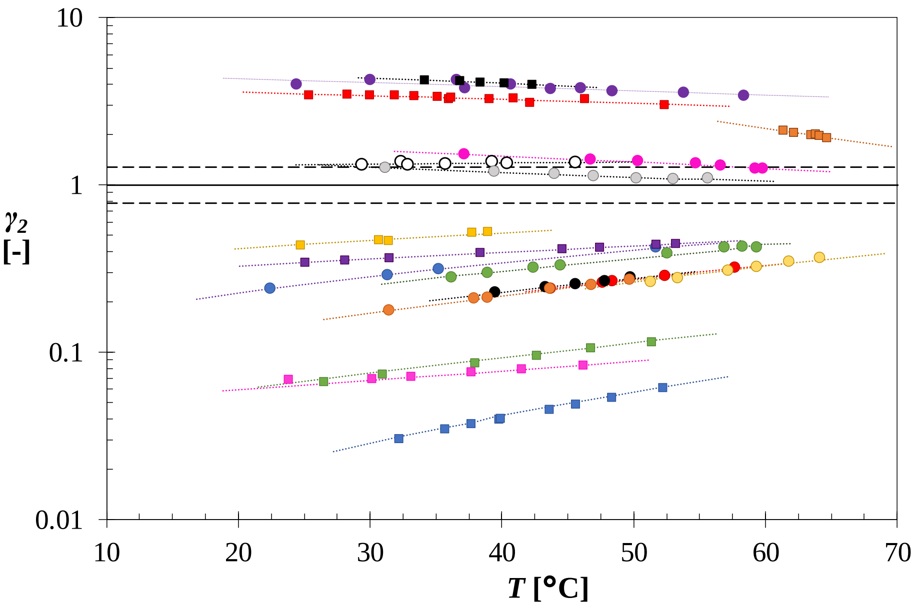

Figure 3.8. Activity coefficient as a function of the absolute temperature of 2ABA (●), 2HBA (●), ASP (●), CAF (●), CBZ (●), RS-NPX (●), S-NPX (●), PHZ (○), PIC (●), SSA (●), 3HBA (■), 4ABA (■),4AMP (■), 4HBA (■), INA (■), NA (■), 4NBA (■), and PCT (■) in 1,4-dioxane over a temperature range of 14 to 65 °C. The lines for each solute were drawn using the parameters from the regression with the Wilson model. The broken lines represent an arbitrary boundary values used to visually identify the close-to-ideal binary systems.

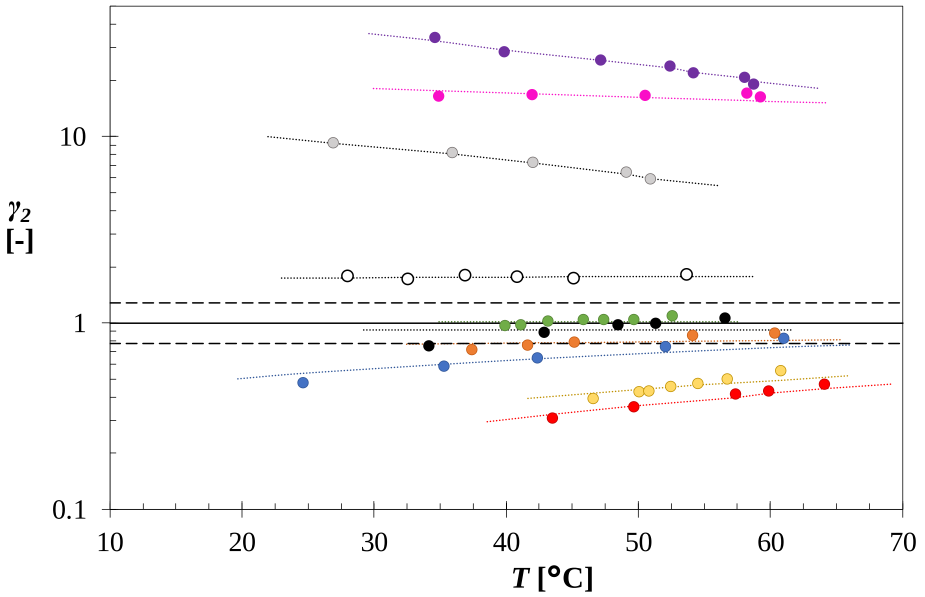

Figure 3.9. Activity coefficient as a function of the absolute temperature of the studied organic solutes in CPME, including: 2ABA (●), 2HBA (●), ASP (●), CAF (●), CBZ (●), RS-NPX (●), S-NPX (●), PHZ (**O**), PIC (●), and SSA (●) over a temperature range of 10 to 70 °C. The lines for each solute were drawn using the parameters from the regression with the Wilson model. The dashed lines depict the area within the systems are close to an ideal solution behaviour.

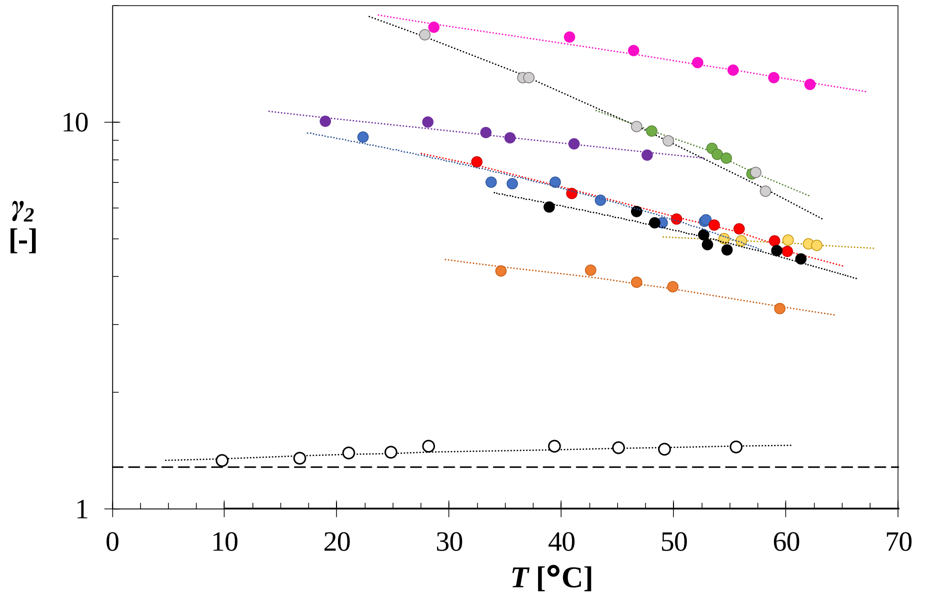

Figure 3.10. Activity coefficient as a function of the absolute temperature of 2ABA (●), 2HBA (●), ASP (●), CAF (●), CBZ (●), RS-NPX (●), S-NPX (●), PHZ (**O**), PIC (●), and SSA (●) in toluene between 10 to 70 °C. The discontinued lines are the trendlines to the determined activity coefficient. The lines for each solute were drawn using the parameters from the regression with the Wilson model. The dashed line represents an arbitrary boundary $\ln\gamma_2 < 0.25$, below which the binary systems present a close-to-ideal behaviour.

Interestingly, the enantiopure and racemic compounds of the chiral compound (NPX) present dissimilar behaviour in the three solvent systems. The activity coefficients of the racemic compound (RS-NPX) and the S-enantiomer are similar in 1,4-dioxane over the experimental temperature range, however, they differ in CPME, as the racemic RS-NPX shows behaviour closer to an ideal solution. The compound NPX, which negatively deviate from ideality in dioxane and CPME, have positive activity coefficients in toluene. In the latter apolar solvent, the enantiopure chiral compound S-NPX is closer to an ideal solution than the racemic compound RS-NPX. This seems to indicate that the interactions between the two different enantiomers (R and S) differs from that between equal enantiomers (e.g., S and S) in CPME and toluene while it is close to equal in dioxane. Perhaps the self-association of NPX in CPME and toluene is promoted due to the solvent apolarity, while in dioxane NPX is less prone to self-association as it can hydrogen bond with the solvent. In such a case, solution of RS-NPX should be consider as three-component solutions.

Similar activity coefficients were calculated for PHZ across the three solvent systems over the experimental temperature range. The magnitude of γ_2 for the binary systems including PHZ, are positive and showed a trend towards slightly larger values at increasing temperature. These may relate to measurement errors either in the solubility or in the thermal analysis. Since PHZ systems show close-to-ideal behaviours with activity coefficients (γ_2) close to 1, less accuracy on the regression of the activity coefficient is expected due to errors in solubility and thermal analysis.

Following determination of γ_2, a series of thermodynamic models based on the excess Gibbs energy of solution (Margules, Van Laar, Wilson, and NRTL) were used to correlate the activity coefficient. Table 3.4 displays the parameters for these models regressed using non-linear least squared methods using the activity coefficients determined from the experimental data. The regression of the NRTL parameters was conducted using two different approaches. On the basis of Renon's work,[16] who assigned an α value ranging from 0.20 to 0.47 according to the chemical nature of the components binary systems. The non-randomness constant was set as 0.3, which is the value suggested by Renon and Prausnitzs for mixtures of non-polar liquids and mixtures of apolar and polar species. Additionally, the activity coefficient was correlated from the NRTL model using α as an adjustable parameter. Thus, we can compare the best fitting results between the two-parameters and the three-parameters NRTL models.

Table 3.4. Regressed parameters of the Margules (a_M), van Laar (a_L and b_L), and Wilson (λ_{12}- λ_{22} and λ_{21}- λ_{11}) models alongside the 2 parameters (g_{12}-g_{22}, and g_{21}-g_{11}) and the three parameters (α, g_{12}-g_{22}, and g_{21}-g_{11}) NRTL models for the studied solute-solvent systems.

		Margules	**van Laar**		**Wilson**		**NRTL (α = 0.3)**		**NRTL (unrestricted α)**		
Solvent	**Solute**	a_M [kJ/mol]	a_L [kJ/mol]	b_L [kJ/mol]	λ_{12}- λ_{22} [kJ/mol]	λ_{21}- λ_{11} [kJ/mol]	g_{12}-g_{22} [kJ/mol]	g_{21}-g_{11} [kJ/mol]	α [-]	g_{12}-g_{22} [kJ/mol]	g_{21}-g_{11} [kJ/mol]
dioxane	2ABA	-5.86	-4.80	-10.8	-4.48	-0.67	-0.42	-4.61	0.43	-0.02	-4.79
	2HBA	-8.03	-7.27	-11.7	-5.17	-2.35	-1.60	-5.68	0.48	-2.11	-4.93
	ASP	-4.37	-3.40	-5.69	-1.81	-1.72	0.35	-3.80	4.04	-1.65	-1.73
	CAF	3.61	2.18	3.67	1.80	1.94	12.0	-4.56	0.17	24.1	-9.81
	CBZ	0.89	0.15	1.70	-0.62	3.88	11.0	-5.02	0.34	10.0	-4.48
	RS-NPX	-4.71	-2.88	-6.02	-1.34	-1.62	1.56	-4.38	0.18	3.83	-6.15
	S-NPX	-5.26	-3.10	-7.66	-1.82	-1.35	0.43	-0.04	0.88	-0.71	-2.66
	PHZ	0.83	17.5	0.77	5.66	-2.50	-2.15	5.56	0.43	-1.44	5.39
	PIC	0.69	0.51	1.81	-1.61	4.83	0.54	0.17	0.75	2.87	-0.86
	SSA	-6.18	-5.26	-8.12	-4.96	-0.36	0.42	-5.49	0.60	4.06	-7.44
	4ABA	-2.97	-2.33	-3.19	-1.30	-1.16	-0.33	-2.17	0.88	-1.07	-1.31
	4AMP	-1.96	-0.35	-2.77	-3.61	6.10	8.73	-5.46	0.13	19.2	-11.5
	3HBA	-12.8	-9.63	-17.3	-5.59	-4.23	-3.92	-6.08	0.12	1.14	-11.1
	4HBA	-7.74	-6.25	-8.34	-2.42	-3.75	-2.83	-3.57	0.87	-3.42	-2.27
	INA	3.21	4.40	3.17	2.42	1.62	1.41	2.36	0.85	2.67	7.21
	NA	3.88	4.28	3.86	2.61	2.25	2.22	2.15	0.29	2.21	2.14
	4NBA	-7.43	-30.3	-6.78	0.22	-7.24	-8.39	1.66	0.94	-6.55	-0.21
	PCT	2.11	0.40	3.89	-1.74	7.82	12.0	-4.83	0.24	14.2	-6.09
CPME	2ABA	-1.70	-1.21	-15.7	-4.14	19.8	5.93	-4.51	2.80	0.97	-1.31
	2HBA	-4.89	5.09	-92.9	-6.46	2.92	1.18	-5.02	0.82	3.11	-6.67
	ASP	0.04	0.06	0.04	-1.43	2.22	0.02	0.02	0.30	-2.78	16.1
	CAF	8.66	0.54	9.31	-1.36	11.6	10.8	-1.68	0.84	9.56	-0.13
	CBZ	7.50	4263	7.46	36.7	3.79	5.05	17.2	0.03	-16.1	33.1
	RS-NPX	-0.24	-0.07	-9.75	-1.00	1.96	-0.005	-0.23	0.02	58.0	-40.5
	S-NPX	-0.70	1.28	-0.59	-1.03	1.57	-0.14	-0.53	0.03	43.8	-31.4
	PHZ	1.56	45.3	1.47	7.77	-1.32	-1.56	6.28	0.17	1.03	76.7
	PIC	5.65	3.24	6.00	1.46	5.36	5.93	0.11	0.56	5.44	11.6
	SSA	-3.04	-1.85	-4.75	-3.27	7.10	1.32	-3.40	2.17	1.35	-2.07
toluene	2ABA	5.12	1.31	5.66	-1.18	7.24	11.5	-3.63	0.99	5.20	4.80
	2HBA	4.89	1.05	5.58	-1.73	8.07	12.8	-4.24	1.13	5.08	3.60
	ASP	5.88	0.86	6.76	-1.03	8.56	15.3	-4.83	0.13	30.7	-12.4
	CAF	5.72	17.4	5.68	3.08	3.58	3.64	2.95	0.70	4.46	3.53
	CBZ	7.23	2.36	7.32	2.22	5.27	19.6	-5.88	0.31	18.9	-5.63
	RS-NPX	4.49	0.62	5.00	-0.59	6.63	16.1	-5.63	0.28	17.1	-6.11
	S-NPX	3.64	1.00	3.85	0.37	3.72	11.8	-4.57	0.18	20.3	-8.72
	PHZ	0.91	21.3	0.85	6.68	-2.03	-2.11	6.09	0.03	-11.8	15.4
	PIC	6.77	2.29	7.57	0.48	7.56	9.77	-1.72	0.68	6.54	4.58
	SSA	4.54	489	4.38	7.60	0.62	1.24	6.84	0.40	3.36	18.9

3.4.4. Accuracy

The goodness of fit of the analysed models was determined by the relative standard deviation of the fitted data (x_i^{cal}) to the experimental mole fraction solubility (x_i) at a given temperature. The relative standard deviation (s) was calculated using the following expression:

$$s\,[\%] = \sqrt{\frac{1}{(N-1)}\sum_{i=1}^{N}\left(\frac{x_{i-}x_i^{cal}}{x_i}\right)^2} \cdot 100 \qquad \textbf{(3.19)}$$

where N is the number of experimental data points. The relative standard deviation gives the average percentile deviation between a measurement point and the model estimation. Understanding that, and considering the general low solubility values of the studied compounds in CPME and toluene, a standard deviation lower than 5% would be a reasonable upper error to describe the binary systems. If a model gives an error larger 5%, we considered that the model does not describe the experimental data with sufficient accuracy. The relative standard deviations for each system are shown in Table 3.5. In general, there is a good agreement between the correlated and experimental solubilities obtained from each thermodynamic model across the three solvent systems, with poorer correlations in CPME. The calculated standard deviation was lower than 5% for all the studied binary systems using the van 't Hoff equation, which alongside the Apelblat and the three parameters NRTL models presented the best overall correlations.

The Apelblat model showed the lowest s average in dioxane and CPME, with values of 0.88% and 1.62%, respectively. However, the calculated overall s value in toluene for the semi-empirical model was larger than the s magnitudes obtained from the binary systems in toluene using van 't Hoff or the three parameters NRTL models. The lowest calculated average s for the toluene systems (1.75%) was given by the three parameters NRTL model. The use of an additional adjustable constant (α) considerably reduced the overall s for all the studied systems compared to that of the two parameters NRTL model. The Margules model showed poorer fitted solubility data across the three non-polar solvent systems, with an average deviation from the experimental data over 5% for the binary systems in CPME and toluene. A maximum error of *ca.* 16.5% was obtained from the Margules model for PIC in toluene.

3.5. Discussion

The analysis of the temperature dependent solubility of a number of APIs and intermediates in three non-polar solvents showed that the compounds are significantly more soluble in 1,4-dioxane and present a lower solubility in toluene.

Table 3.5. Relative standard deviation in percentage units of the calculated mole fraction solubilities by the thermodynamic models (x^{cal}) with respect to the experimental data (x).

Solvent	**Solute**	***s* (%)**							
		van't Hoff	**Apelblat**	**λh**	**Margules**	**van Laar**	**Wilson**	**NRTL (α = 0.3)**	**NRTL (unrestricted α)**
dioxane	2ABA	0.22	0.03	0.17	7.51	0.36	0.75	2.68	0.52
	2HBA	0.20	0.20	0.21	0.42	0.04	0.65	1.14	0.60
	ASP	1.43	1.16	1.36	5.40	2.65	2.58	2.54	2.09
	CAF	4.88	3.34	5.73	2.34	2.44	3.52	2.81	1.82
	CBZ	1.31	0.66	5.45	5.66	1.05	0.90	0.37	0.39
	RS-NPX	0.54	0.55	0.80	3.06	0.97	0.98	0.93	0.92
	S-NPX	0.51	0.51	0.50	6.25	1.08	1.11	2.35	1.02
	PHZ	1.60	1.59	1.60	2.35	2.10	1.52	1.54	1.54
	PIC	1.17	1.29	1.15	3.07	0.98	0.95	3.00	0.91
	SSA	0.11	0.08	0.46	6.72	5.51	2.61	4.33	0.70
	4ABA	0.38	0.38	0.38	1.80	0.62	0.60	0.56	0.54
	4AMP	1.19	1.23	2.49	5.86	2.42	2.21	2.71	1.47
	3HBA	0.32	0.31	0.37	10.4	9.17	3.93	4.84	1.27
	4HBA	0.35	0.36	0.36	5.25	2.37	3.58	0.73	0.62
	INA	1.85	1.86	2.75	1.82	1.79	1.74	1.75	1.65
	NA	0.27	0.23	2.40	0.29	0.26	0.26	0.25	0.25
	4NBA	2.24	1.16	3.51	8.54	3.90	4.35	5.73	2.27
	PCT	0.89	0.91	1.16	2.64	0.56	0.51	0.44	0.42
Average		*1.08*	*0.88*	*1.71*	*4.41*	*2.13*	*1.82*	*2.15*	*1.06*
CPME	2ABA	1.59	0.39	0.90	15.5	4.90	8.64	11.8	8.62
	2HBA	0.52	0.35	0.90	9.31	7.90	4.26	6.41	2.30
	ASP	0.92	0.73	1.01	4.08	4.06	4.02	4.08	1.53
	CAF	3.30	4.64	5.09	10.3	2.88	3.72	9.20	3.43
	CBZ	2.07	4.29	10.0	10.6	10.0	6.37	4.81	2.05
	RS-NPX	1.73	1.15	4.92	12.3	8.74	12.5	12.3	0.63
	S-NPX	0.98	0.28	0.96	7.10	8.21	6.80	7.04	0.12
	PHZ	2.01	1.91	2.16	3.84	3.02	2.02	2.04	1.94
	PIC	2.83	1.97	2.60	5.34	1.09	1.17	1.10	0.91
	SSA	0.62	0.49	0.74	8.83	7.04	6.27	7.69	4.69
Average		*1.66*	*1.62*	*2.93*	*8.72*	*5.79*	*5.58*	*6.64*	*2.62*
toluene	2ABA	3.55	3.72	6.30	8.91	3.77	3.38	3.73	3.37
	2HBA	2.15	3.15	2.52	10.3	2.02	1.73	2.18	1.73
	ASP	2.25	2.30	2.48	6.15	1.10	1.13	0.74	0.27
	CAF	2.41	5.83	5.38	2.37	2.38	2.21	2.28	2.17
	CBZ	2.80	7.08	9.57	3.12	2.29	2.22	0.93	0.88
	RS-NPX	3.73	4.32	4.15	7.31	3.03	2.95	2.75	2.75
	S-NPX	3.53	3.00	4.03	4.66	2.57	2.69	1.83	1.35
	PHZ	1.70	1.35	1.81	5.61	4.64	1.57	1.58	1.43
	PIC	2.86	2.57	2.81	16.5	3.51	2.26	3.32	2.83
	SSA	0.84	0.85	5.89	1.46	0.91	0.77	0.79	0.76
Average		*2.58*	*3.42*	*4.49*	*6.64*	*2.62*	*2.09*	*2.01*	*1.75*
Overall Average		**1.63**	**1.74**	**2.76**	**6.13**	**3.22**	**2.88**	**3.30**	**1.65**

To make a comparative analysis of the solubilities in the three experimental solvents, a number of properties including the dipole moment (μ), dielectric constant (ε), hydrogen bond acceptor counts (h_a), hydrogen bond donor counts (h_d), and the Hansen parameters: dispersion solubility (δ_d), polar solubility (δ_P), and hydrogen bonding solubility (δ_H) were gathered from the literature.[42–46] The Hansen solubility model is based on the cohesive energy density of a fluid media, which can be divided into three components: atomic dispersion, polar interaction, and hydrogen bonding.[43] According to the Hansen model, the affinity between two molecular species is inversely proportional to their parameters distance (R_a), which is given by the following expression:

$$R_a = \sqrt{4(\delta_{d1} - \delta_{d2})^2 + \left(\delta_{p1} - \delta_{p2}\right)^2 + (\delta_{H1} - \delta_{H2})^2} \quad \textbf{(3.20)}$$

As shown in Table 3.6, the dielectric constant and the dipole moment of the solvents, that are related to van der Waals interactions, do not explain the considerably greater solubility of the studied compounds in dioxane, since this solvent presents a lower value compared to toluene and CPME. The calculated Hansen parameter distance R_a between the non-polar solvents and 2HBA, ASP, CAF, and CBZ showed that these compounds presents a higher compatibility with dioxane. However, in opposition to our findings, NPX gave a lower R_a value in CPME. Additionally, the CAF and CBZ values in CPME and toluene do not agree with the measured solubilities. On the contrary, the hydrogen bond interactions and Hansen hydrogen parameter better describe the obtained experimental results. The two oxygen atoms of the ether groups in the heterocyclic diethyl ether molecule offers hydrogen acceptor sites that promotes these type of interactions. Zou *et al.*[47] state that molecular interactions between a solute and a non-polar solvent takes places through van der Waals forces. However, the ability of 1,4-dioxane to form hydrogen bonding has been confirmed by dielectric spectroscopy methods.[48,49] The low hydrogen bonding propensity of toluene results from the lack of hydrogen donor or acceptor sites may explain the low solubility values measured in this solvent. On the other hand, the hindrance effect of the methyl group of CPME, as shown in Figure 3.1, may contribute to a lower solubility compared to that in 1,4-dioxane.[50]

Although the potential formation of hydrogen bonds may explain the significantly higher solubility of organic molecules that contain hydrogen donor groups such as carboxylic acid or amines, it may be difficult to interpret the larger solubility of PHZ compared to INA, NA, or CBZ in 1,4-dioxane based on such property.

Table 3.6. Electric and Hassen properties of selected solutes and solvents. The solute and solvent properties were collected from the literature.[42–45] The hydrogen bond donor and acceptor counts were obtained from the computed properties of the different molecular species provided by PubChem.[46]

Solvent/ Solute	**μ (D)**	**ε [-]**	**h_a [-]**	**h_d [-]**	**δ_d [MPa$^{1/2}$]**	**δ_p [MPa$^{1/2}$]**	**δ_H [MPa$^{1/2}$]**	**R_a [MPa$^{1/2}$]**		
								dioxane	**toluene**	**CPME**
dioxane	0	2.2	0	2	19	1.8	7.4	-	-	-
toluene	0.4	2.4	0	0	18	1.4	2.0	-	-	-
CPME	1.3	4.8	0	1	16	4.3	4.3	-	-	-
CAF	-	-	0	3	20	10	13	10	14	12
CBZ	-	-	1	1	21	8.1	4.47	7.9	9.2	10
2HBA	-	-	2	3	19	9.0	13.7	9.6	14	12
ASP	-	-	1	4	19	6.9	9.7	5.6	10	8.1
NPX	-	-	1	3	17	12	9.9	11	13	10

The calculated *Ra* values neither provides reliable information of the systems on the non-polar solvents as they differ from the experimental observations. This equation perhaps captures only solution properties, and then results only in a number that states how different the solvent and solute are. Since the solubility of a compound is determined by solid state as well as solution properties, a large *Ra* magnitude may mean a large positive or negative deviation from ideality, which would be either mean a higher or lower solubility. Thus, other properties of the system such as the activity coefficient, which is determined by the enthalpy of fusion and the melting temperature of the solid provides a more accurate information of the solution behaviour.

The measured temperature dependent solubility was correlated by a series of thermodynamic models. Overall, the van 't Hoff and the three parameters NRTL models provide the best fitting to the experimental data. The former model permits to compare the enthalpy and set point temperature estimated from the van 't Hoff plots against the enthalpy of fusion and melting temperature, which may give some information regarding the factors that affect the deviation from ideal solutions. A linear dependency of ln x_2 with T^{-1}, as observed for most of the studied binary systems, does not necessary imply an ideal thermodynamic behaviour since the slope and intercept of the fitted line may differ from $-\Delta H_f/R$ and $-\Delta H_f/RT_m$.[2] By plotting the ratio of the van't Hoff parameters to the enthalpy of fusion and melting temperature, we can identify the weight of these thermodynamic parameters on the deviations from ideal solution, i.e the calculated distance of the pair ($\Delta H_{dis}/\Delta H_f$, T_0/T_m) for a given solution from the origin (1, 1) in Figure 3.11 can be seen as a measure of the non-ideality of a binary system. In addition, Figure 3.11 permits to identify positive and negative deviations from ideal solutions. If $T_0 > T_m$ and $\Delta H_{dis} > \Delta H_f$ we have positive deviations as γ_2 is greater than 1, that is in the upper quadrants of Figure 3.11 Systems negatively deviating from ideality are in the bottom quadrant of Figure 3.11. However, behaviours close to ideality present some mixed behaviour where the change in heat of dissolution and T_0 seem to counteract.

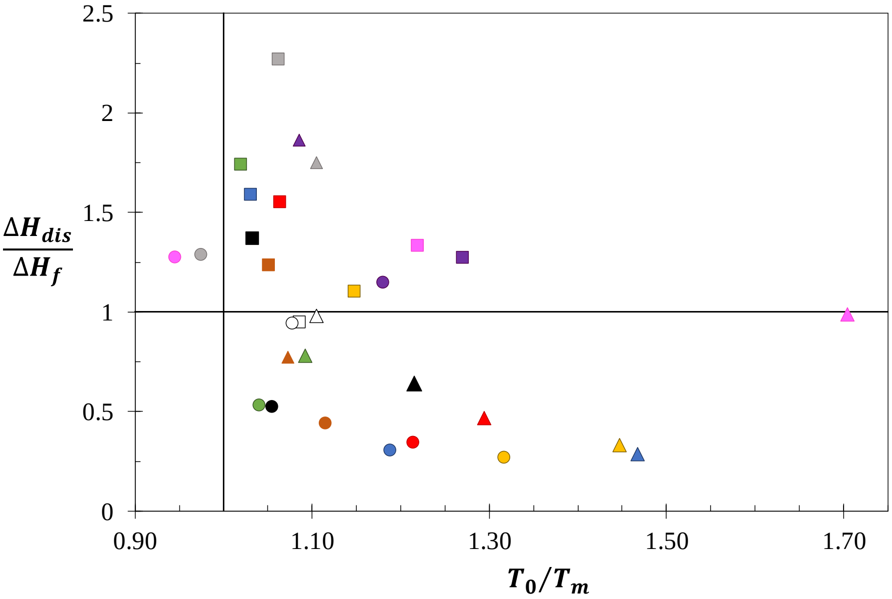

Figure 3.11. Deviation of the solute-solvent systems with respect to the ideal solubility based on the ratio $\Delta H_{dis}/\Delta H_f$ of the regressed enthalpy of dissolution ΔH_{dis} and the compound's enthalpy of fusion ΔH_f and the ratio T_0/T_m of the regressed temperature T_0 and the compound's melting temperature T_m. These deviations were estimated for 2ABA (blue), 2HBA (red), ASP (green), CAF (purple), CBZ (pink), RS-NPX (black), S-NPX (orange), PHZ (white), PIC (grey), and SSA (yellow) in the three experimental apolar solvents: 1,4-dioxane (○), CPME (Δ), and toluene (☐).

A more detailed information of the solute-solvent interactions can be obtained from the activity coefficient of the solute γ_2, determined from the solubility and solid state properties. The activity coefficient was correlated by thermodynamic models based on the Gibbs free energy excess of mixing for which the determined parameters describe the interaction of a molecule with its surroundings. As an example, the Wilson model parameters (λ_{ij}) refers to the interaction energies between a species j surrounding by molecules i. Orye and Prausnitz[51] expressed that, although they do not have a rigorous definition, these parameters provide qualitative information of the molecular interactions in the solution. Figure 3.12 shows that the compounds with activity coefficient values $\gamma_2 < 1$ have negative λ_{12}-λ_{22}, with the exception of 4NBA in dioxane that presented a slightly positive value combined with a strongly negative value of λ_{21}-λ_{11}, which gave an interaction energy pair (-7.2, 0.2) in Figure 3.12. Compounds of positive activity coefficient are bounded to at least one positive Wilson parameter, indicating that the energy interactions between the different molecular species in a binary system define the solution behaviour.

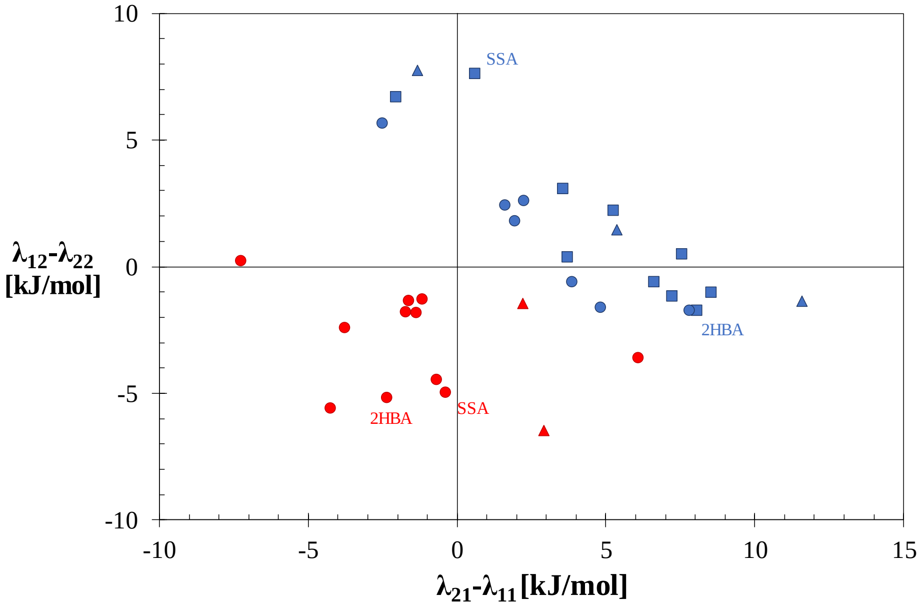

Figure 3.12. Wilson interaction energy parameters λ_{12}-λ_{22} against λ_{21}-λ_{11} estimated on compounds with positive (blue) and negative (red) deviations from ideality in dioxane (○), CPME (△), and toluene (□). Only the compounds that shows s values lower than 5% for the regression with the Wilson equation (table 3.5) are included, as the parameters were deemed to represent the binary systems with sufficient accuracy. In the figure, the different solution behaviour of 2HBA and SSA in dioxane (red) and in tolune (blue) are represented. In dioxane, 2HBA and SSA present a negative deviation from ideality, while the deviation is positive for these compounds in toluene.

3.6. Conclusions

The solubility data and the activity coefficient of 18 APIs and intermediates in three non-polar solvents over a temperature range of 0 to 70 °C were determined from experimental clear point temperature measurements and solid state properties. Under working conditions, the studied organic compounds all showed greater solubility in 1,4-dioxane, that may be explained by the greater hydrogen bonding propensity of the solvent. In addition, subtler physical and thermodynamic properties and the intermolecular interactions between the solute and solvent molecules may influence the activity coefficient that determines solubility. The experimental data was modelled by three semi-empirical equations: van ’t Hoff, Apelblat, and the λh model, and by four activity coefficient models: Margules, van Laar, Wilson, and NRTL. The parameters of each model were regressed by fitting the experimental activity coefficient data to the corresponding thermodynamic equation. The correlation goodness of the back calculated mole fraction solubilities was assessed by the relative standard deviation. According to the relative standard deviation, the van 't Hoff equation and the three parameters NRTL provides the best overall fitting results for the studied systems, and can be used to accurately predict the saturation of the studied organic compounds in the non-polar solvent and hence for the design of purification processes. The activity coefficient of the model compounds was calculated and correlated using excess of energy models across the three apolar solvents. The regressed parameters from the Wilson equation provides some qualitative information of the interaction energy in the binary systems, and according to these parameters we can deduce the solution behaviour. Additionally, the van 't Hoff enthalpy of dissolution and the transition temperature permit to identify close-to-ideal systems.

3.7. References

1. ter Horst, J. H., Schmidt, C. & Ulrich, J. *Fundamentals of Industrial Crystallization. Handbook of Crystal Growth: Bulk Crystal Growth: Second Edition* 2, (Elsevier B.V., 2015).
2. Mullin, J. W. *Crystallization (Fourth Edition).* (Butterworth-Heinemann, 2001).
3. Reus, M. A., Heijden, A. E. D. M. Van Der & Horst, J. H. Solubility Determination from Clear Points upon Solvent Addition. *Org. Process Res. Dev.* 19, 1004–1011 (2015).
4. Ter Horst, J. H., Deij, M. A. & Cains, P. W. Discovering New Co-Crystals. *Cryst. Growth Des.* 9, 1531–1537 (2009).
5. Poling, B. E., Prausnitz, J. M. & O'Connell, J. P. *The Properties of Gases and Liquids (Fifth Edition).* (McGraw-Hill, 2001).
6. Black, S., Dang, L., Liu, C. & Wei, H. On the measurement of solubility. *Org. Process Res. Dev.* 17, 486–492 (2013).
7. Prausnitz, J. M., Lichtenthaler, R. N. & Azevedo, E. G. *Molecular Thermodynamics of Fluid Phase Equilibria.* (Prentice-Hall Englewood Cliffs, 1999).
8. Wang, J., Xu, A. & Xu, R. Solubility and solution thermodynamics of 4-hydroxybenzaldehyde in twelve organic solvents from T = (278.15 to 318.15) K. *J. Mol. Liq.* 237, 226–235 (2017).
9. Wan, Y. *et al.* Solid-liquid equilibrium solubility and thermodynamic properties of cis-5-norbornene-endo-2,3-dicarboxylic anhydride in fourteen pure solvents and three binary solvents at various temperatures. *J. Mol. Liq.* 297, 111396 (2020).
10. Augustijns, P. & Brewster, M. *Solvent Systems and Their Selection in Pharmaceutics and Biopharmaceutics.* (Springer-Verlag New York, 2007).
11. Apelblat, A. & Manzurola, E. Solubilities of o-acetylsalicylic, 4-aminosalicylic, 3,5-dinitrosalicylic, and p-toluic acid, and magnesium-DL-aspartate in water from T = (278 to 348) K. *J. Chem. Thermodyn.* 31, 85–91 (1999).

12. Anwer, K., Muqtader, M., Ali, R., Alalaiwe, A. & Shakeel, F. Estimating the Solubility, Solution Thermodynamics, and Molecular Interaction of Aliskiren Hemifumarate in Alkylimidazolium Based Ionic Liquids. *Molecules* 24, 1–13 (2019)

13. Li, W. *et al.* Solubility measurement, correlation and mixing thermodynamics properties of dapsone in twelve mono solvents. *J. Mol. Liq.* 280, 175–181 (2019).

14. Buchowski, H., Ksiazczak, A. & Pietrzyk, S. Solvent activity along a saturation line and solubility of hydrogen-bonding solids. *J. Phys. Chem.* 84, 975–979 (1980).

15. Wilson, G. M. Vapor-Liquid Equilibrium. XI. A New Expression for the Excess Free Energy of Mixing. *J. Am. Chem. Soc.* 86, 127–130 (1964).

16. Renon, H. & Prausnitz, J. M. Local Compositions in Thermodynamic Excess Functions for Liquid Mixtures. *AIChE J.* 14, 135–144 (1968).

17. Long, B., Li, J., Zhang, R. & Wan, L. Solubility of benzoic acid in acetone, 2-propanol, acetic acid and cyclohexane: Experimental measurement and thermodynamic modeling. *Fluid Phase Equilib.* 297, 113–120 (2010).

18. Acree, W. E. Thermodynamic Properties of Organic Compounds: Enthalpy of Fusion and Melting Point Temperature Compilation. *Thermochim. Acta* 189, 37–56 (1991).

19. Gracin, S. & Rasmuson, Å. C. Polymorphism and crystallization of p-aminobenzoic acid. *Cryst. Growth Des.* 4, 1013–1023 (2004).

20. Domalski, E. S. & Hearing, E. D. Heat Capacities and Entropies of Organic Compounds in the Condensed Phase Volume II. *J. Phys. Chem. Ref. Data* 19, 881–1047 (1990).

21. Kirklin, D. R. Enthalpy of combustion of acetylsalicylic acid. *J. Chem. Thermodyn.* 32, 701–709 (2000).

22. Pinto, S. S. & Diogo, H. P. Thermochemical study of two anhydrous polymorphs of caffeine. *J. Chem. Thermodyn.* 38, 1515–1522 (2006).

23. Dong, J. X., Li, Q., Tan, Z. C., Zhang, Z. H. & Liu, Y. The standard molar enthalpy of formation, molar heat capacities, and thermal stability of anhydrous caffeine. *J. Chem. Thermodyn.* 39, 108–114 (2007).

24. Good, D. J. & Naír, R. H. Solubility advantage of pharmaceutical cocrystals. *Cryst. Growth Des.* 9, 2252–2264 (2009).

25. Pinto, S. S. *et al.* Energetics of hydroxybenzoic acids and of the corresponding carboxyphenoxyl radicals. Intramolecular hydrogen bonding in 2-hydroxybenzoic acid. *J. Phys. Chem. A* 109, 9700–9708 (2005).

26. Armstrong, N. A., James, K. C. & Wong, C. K. Inter -relationships between solubilities, distribution coefficients and melting points of some substituted benzoic and phenylacetic acids. *J. pharm. Pharmacol.* 31, 627–631 (1979).

27. Negoro, H., Miki, T., Ueda, S., Sanada, T. & Okada, R. Solubility phenomena of pyridine-and pyrazinemonocarboxamides. II. Heats of fusion of picolinamide, nicotinamide, isonicotinamide, and pyrazinecarboxamide. *Yakugaku Zasshi* 80, 670–673 (1960).

28. Nicoli, S. *et al.* Ethyl-paraben and nicotinamide mixtures: Apparent solubility, thermal behavior and x-ray structure of the 1:1 co-crystal. *J. Pharm. Sci.* 97, 4830–4839 (2008).

29. Braun, D. E. *et al.* Racemic naproxen: A multidisciplinary structural and thermodynamic comparison with the enantiopure form. *Cryst. Growth Des.* 11, 5659–5669 (2011).

30. Mota, F. L., Carneiro, A. P., Queimada, A. J., Pinho, S. P. & Macedo, E. A. Temperature and solvent effects in the solubility of some pharmaceutical compounds: Measurements and modeling. *Eur. J. Pharm. Sci.* 37, 499–507 (2009).

31. Chirico, R. D., Kazakov, A. F. & Steele, W. V. Thermodynamic properties of three-ring aza-aromatics. 1. Experimental results for phenazine and acridine, and mutual validation of experiments and computational methods. *J. Chem. Thermodyn.* 42, 571–580 (2010).

32. Évora, A. O. L. *et al.* Resolved structures of two picolinamide polymorphs. Investigation of the dimorphic system behaviour under conditions relevant to co-crystal synthesis. *CrystEngComm* 14, 8649–8657 (2012).

33. Ramos, J. J. M., Diogo, H. P., Godinho, M. H., Cruz, C. & Merkel, K. Anomalous thermal behavior of salicylsalicylic acid and evidence for a monotropic transition to a nematic phase. *J. Phys. Chem. B* 108, 7955–7962 (2004).

34. Brown, C. J. The Crystal Structure of Anthranilic Acid. *Proc. R. Soc. A* 185–199 (1968).

35. Boone, C. D. G., Derissen, J. L. & Schoone, J. C. Anthranilic Acid II (o-Aminobenzoic Acid). *Acta Crystallogr. Sect. B* B33, 3205–3206 (1977).

36. Wang, Q. CCDC 1499185: Experimental Crystal Structure Determination. *CSD Commun.* (2016).

37. Light, M. E. CCDC 1476879: Experimental Crystal Structure Determination. *CSD Commun.* (2016).

38. Kingsbury, C., Commons, C. J., Sanchez-Arlt, R. W., Abrahams, B. F. & Robson, R. CCDC 1557139: Experimental Crystal Structure Determination. *CSD Commun.* (2017).

39. Du, J. J. *et al.* Using Electron Density to Predict Synthon Formation in a 4-Hydroxybenzoic Acid: 4,4′-Bipyridine Cocrystal. *Cryst. Growth Des.* 18, 1786–1798 (2018).

40. Hilfiker, R. *et al.* Polymorphism - Integrated approach from high-throughput screening to crystallization optimization. *J. Therm. Anal. Calorim.* 73, 429–440 (2003).

41. Florence, A. J. *et al.* An automated parallel crystallisation search for predicted crystal structures and packing motifs of carbamazepine. *J. Pharm. Sci.* 95, 1918–1930 (2006).

42. Smallwood, I. M. Handbook of Organic Solvent Properties. *Butterworth-Heinemann* 332 (1996).

43. Salem, A., Nagy, S., Pál, S. & Széchenyi, A. Reliability of the Hansen solubility parameters as co-crystal formation prediction tool. *Int. J. Pharm.* 558, 319–327 (2019).

44. Hansen, C. M. *Hansen solubility parameters: A user's handbook: Second edition*. *Hansen Solubility Parameters: A Users Handbook, Second Edition* (2007).

45. Bustamante, P., Peña, M. A. & Barra, J. Partial-solubility parameters of naproxen and sodium diclofenac. *J. Pharm. Pharmacol.* 50, 975–982 (1998).

46. PubChem. Available at: https://pubchem.ncbi.nlm.nih.gov/. (Accessed: 9th August 2020)

47. Zou, F. *et al.* Experimental measurement and modelling of solubility of inosine-5′-monophosphate disodium in pure and mixed solvents. *J. Chem. Thermodyn.* 77, 14–22 (2014).

48. Sengwa, R. J., Sankhla, S. & Khatri, V. Dielectric characterization and molecular interaction behaviour in binary mixtures of amides with dimethylsulphoxide and 1,4-dioxane. *J. Mol. Liq.* 151, 17–22 (2010).

49. Schrödle, S., Hefter, G. & Buchner, R. Dielectric spectroscopy of hydrogen bond dynamics and microheterogenity of water + dioxane mixtures. *J. Phys. Chem. B* 111, 5946–5955 (2007).

50. Zou, Z., Sun, X., Yu, Y., Fang, X. & Xu, L. Determination and correlation of solubility and solution thermodynamics of musk ketone in twelve pure solvents. *J. Mol. Liq.* 293, (2019).

51. Orye, R. V. & Prausimitz, J. M. Multicomponent equilibria: With the wilson equation. *Ind. Eng. Chem.* 57, 18–26 (1965).

Chapter 4. Electric Field Effects on Crystals of Organic Compounds in Apolar Solvents

Abstract

Under a strong electric field, suspended particles in a fluid medium experience dissimilar dragging forces based on their electrical properties. This allows for the selective manipulation of the different phases in a mixture, and therefore electric fields have been used for the development of process intensification techniques.[1] Here we report the behaviour of crystalline particles of a series of organic compounds under strong uniform and non-uniform electric fields of maximum magnitude of 1.4 kV/mm, generated in custom-made electric cells developed for this study. No detectable electric currents were observed in the studied solutions with apolar solvents such as 1,4-dioxane. Under a non-uniform electric field, a swirl motion was observed in pure solvents with a dielectric constant $\varepsilon > 4.3$, which increased with increasing electric field magnitude and electrical conductivity of the solvent. The flow-motion, related to the electro-osmosis phenomenon, presented augmented velocity in solutions of organic compounds in cyclopentyl methyl ether and anisole compared to the pure solvents. The application of strong electric fields to suspensions of crystalline particles of organic compounds reveal the presence of the electrokinetic phenomena electrophoresis and dielectrophoresis. The initially resting particles on the bottom of the device commence to move around the electrode as they are attracted to the strong electric field regions by positive dielectrophoresis. The selective motion towards one of the electrodes indicate the presence of electrophoretic forces acting on the particle. The electrophoresis phenomenon was corroborated by zeta-potential measurements, with maximum magnitude value of 127 mV for nicotinamide in 1,4-dioxane and a minimum value of 0.01 mV for 4-hydroxybenzoic acid in cyclopentyl methyl ether. The sign of the measured zeta-potential of the suspended particles coincided with the observed behaviour. The electrophoretic forces on non-polar organic crystals was further investigated in a customised

electrophoresis cell. Caffeine and phenylanaline particles collected at the same electrode in the presence of a uniform electric field to that of the observed behaviour in a non-uniform field. However, nicotinamide particles in cyclopentyl methyl ether seem to form an electrorheological fluid. The gained understanding of the electrical driven interactions in non-aqueous crystalline dispersions obtained through this study can be used to develop efficient separation method.

4.1. Introduction

Separation processes are essential in the manufacturing of chemicals for the isolation of a valuable product from complex mixtures.[1] These processes are especially relevant in the pharmaceutical industry, as the presence of impurities may reduce the quality of the drug substance and affect the activity, efficiency, and bioavailability of the medicine.[2] Additionally, highly complex synthetic routes of drug products can include bioactive and/or potentially harmful intermediates products that trigger or accelerate certain reactions that must be retained from entering the product stream.[3–5] Therefore, the pharmaceutical industry is legally required to adhere to very low impurities levels.[6,7] However, the isolation of a high-purity product by standard methods, such as crystallisation or filtration, becomes a challenging task if various species with similar properties are in the same stream.[8–10] External fields such as magnetic, acoustic, and electric fields have been actively studied for the development of new separation processes or to improve the separation performance of existing processes.[11–13] In particular, the use of electrical fields allows for the selective manipulation of the species in heterogeneous solutions onto which new separation technologies can be based.[14,15]

The term electrokinetics describes a collection of motion phenomena experienced by liquids and/or solid particles in heterogeneous solutions in the presence of an electric field due to the presence of the double layer at the interface.[16] The separation of heterogeneous phases in a mixed solution through electric field driven techniques exploits three main electrokinetic phenomena: electro-osmosis, electrophoresis, and dielectrophoresis. The application of an electric field to a fluid media triggers a motion of ions, which drags the surrounding liquid by electrostatic interactions.[16]

Electrophoresis induces a dragging motion on charged particles towards an electrode of opposite polarity in the presence of an electric field.[17] Thus, a mixture of two particle species can be separated on the basis of their migration velocities and/or directions in the applied field.[18] Electrophoresis based techniques offer an efficient separation of particles with similar properties and therefore, they have been amply applied to the isolation and identification of proteins, chiral compounds, and bioparticles.[19,20] On the other hand, dielectrophoresis enables the manipulation of non-polar particles by using non-uniform electric field.[18,21] Upon the application of the electric field to a heterogeneous solution, dielectrophoretic forces act on suspended uncharged but polarizable particles, inducing a migration phenomenon on the solid phase towards the regions of strongest electric field gradient if the polarizability of the particle is greater than that of the solution (positive electrophoresis). In the opposite case, negative dielectrophoresis occurs and the particles migrate towards the weak electric field gradient. Numerous reviews reported on dielectrophoresis reveal the potential of its use on separation processes, such as the separation of polar and apolar particles, continuous separation, and size discrimination.[18,22] In addition, the combined use of electrophoresis and dielectrophoresis can be exploited, obtaining a greater manipulation control and enhanced separation of the particles in a fluid media. For instance, Pysher and Hayes[23] developed a device to selectively separate the bioparticles that travel through a micro-channel based on the dissimilar interfacial interaction of each of the species with an applied DC electric field.

More recently, Li et al.[9] successfully purified and physically separated phenazine and caffeine crystals on opposite electrodes from their mixture in a 1,4-dioxane suspension. A selected motion towards one of the electrodes occurs when a strong potential difference of 7.5 kV is applied to pure suspensions of crystals of organic compounds. They exploited this phenomenon for the separation of the complex mixture. By applying a strong non-uniform electric field, they observed a collection of crystalline particles of dissimilar morphology and colour on different electrodes. A cooling crystallisation step induces the immobilization of phenazine and caffeine on opposite electrode, from where they were collected with purity values higher than 94 %wt. This novel technique offers a simple and efficient alternative to current separation methods for pharmaceutical products. However, despite the potential applications of the technique developed by Li et al.[9] for the purification and isolation of crystallisation products, little is known about the mechanisms underlying the interfacial effects of the electric field between the particle and fluid medium, which permits the manipulation of the suspended crystals

The main aim of this work is to build on the current knowledge of electroseparation techniques in order to gain a deeper understanding of interfacial interactions that occurs in crystalline suspensions under an electric field. For this, the behaviour of active pharmaceutical compounds and intermediates, including chiral compounds, co-crystals, and different polymorphic forms of the same crystalline compound have been studied under strong non-uniform DC electric fields, aiming to relate particle and solution properties to the various electrokinetic phenomena. Additionally, a custom-made device was produced to monitor the effects of a uniform electric field on crystalline particles under an optical microscope. The knowledge gained from the behavioural studies under uniform and non-uniform electric fields may allow for the identification of means to exploit the electric field phenomena to increase the performance of the separation technique.

4.2. Materials and Methods

4.2.1. Materials

The compounds used in this work are listed in Table 4.1. All the solutes and reagents were used without further purification.

4.2.2. Solvent-mediated Crystal Transformation

Cooling crystallisation and solvent-mediated transformation of 2ABA, 3ABA, 4ABA, and INA were carried out to produce different polymorphic forms of each compound. The crystalline structures of the supplied material were identified by diffraction analysis to be form I for 2ABA, 4ABA, and INA, and form III for 3ABA. Form II of 2ABA appeared upon cooling a clear solution of approximately 120 mg/mL of the purchased compound in water/ethanol mixtures (50:50 %v/v) at a cooling rate of 3.3 °C/min from 65 to 45 °C.[24] The third polymorphic form of 2ABA was produced by heating a slurry of the 2ABA form I in water/ethanol mixtures (50:50 %v/v) to 55 °C and left it under gentle stirring for approximately 15 h.[24] Pure suspensions of 3ABA, 4ABA, and INA in different solvents were heated until complete dissolution of the crystalline material. By cooling at slow rate under stirring, recrystallisation occurred with phase transformation for 3ABA in acetonitrile (polymorphic form II),[25] 4ABA (form IV) in water,[26] and INA in 2-propanol (form II)[27] and 1,4-dioxane (form III).

Table 4.1. Details of the compounds, solutes and reagents used in this study.

Material	Acronym	CAS Number	Purity [%] ≥	Molecular Mass [g/mol]	Supplier
Organic Compound					
2-Aminobenzoic acid	2ABA	118-92-3	98	137.14	Sigma-Aldrich (Merck KGaA, Germany)
3-Aminobenzoic acid	3ABA	99-05-8	98	137.14	Alfa Aesar (Thermo Fisher Scientific, UK)
4-Aminobenzoic acid	4ABA	150-13-0	99	137.14	VWR Chemicals (Avantor, UK)
4-Aminophenol	4AMP	123-30-8	98	109.13	Sigma-Aldrich (Merck KGaA, Germany)
Aspirin	ASP	50-78-2	99	180.16	VWR Chemicals (Avantor, UK)
Caffeine	CAF	58-08-2		194.19	Sigma-Aldrich (Merck KGaA, Germany)
Carbamazepine	CBZ	298-46-4		236.27	Sigma-Aldrich (Merck KGaA, Germany)
2,4-Dihydrobenzoic acid	2,4DHBA	89-86-1	97	154.12	Sigma-Aldrich (Merck KGaA, Germany)
3,5-Dihydrobenzoic acid	3,5DHBA	99-10-5	97	154.12	Sigma-Aldrich (Merck KGaA, Germany)
2-Hydroxybenzoic acid	2HBA	69-72-7		138.12	Sigma-Aldrich (Merck KGaA, Germany)
3-Hydroxybenzoic acid	3HBA	99-06-9	99	138.12	Sigma-Aldrich (Merck KGaA, Germany)
4-Hydroxybenzoic acid	4HBA	99-96-7	99	138.12	Sigma-Aldrich (Merck KGaA, Germany)
Isonicotinamide	INA	1453-82-3	99	122.12	Sigma-Aldrich (Merck KGaA, Germany)
Nicotinamide	NA	98-92-0	99.5	122.12	Sigma-Aldrich (Merck KGaA, Germany)
3-Nitrobenzoic acid	3NBA	121-92-6	99	166.12	Sigma-Aldrich (Merck KGaA, Germany)
4-Nitrobenzoic acid	4NBA	62-23-7	98	167.12	Sigma-Aldrich (Merck KGaA, Germany)
Paracetamol	PCT	103-90-2		151.16	Sigma-Aldrich (Merck KGaA, Germany)
Phenazine	PHZ	92-82-0	99	180.21	VWR Chemicals (Avantor, UK)
Picolinamide	PIC	1452-77-3	98	122.12	Sigma-Aldrich (Merck KGaA, Germany)
Salicylsalicylic acid	SSA	552-94-3		258.23	VWR Chemicals (Avantor, UK)
Theobromine	THB	83-67-0	98	180.16	Sigma-Aldrich (Merck KGaA, Germany)
Theophyline	THP	58-55-9	99	180.16	Sigma-Aldrich (Merck KGaA, Germany)
RS-Naproxen	RS-Npx	23981-80-8	98	230.26	Tokio Chemical Industry Co., Ltd. (Japan)
S-Naproxen	S-Npx	22204-53-1	99	230.26	Tokio Chemical Industry Co., Ltd. (Japan)
DL-Valine	DL-Val	516-06-3	99	117.15	Sigma-Aldrich (Merck KGaA, Germany)
L-Valine	L-Val	72-18-4	98	117.15	Sigma-Aldrich (Merck KGaA, Germany)
D-Valine	D-Val	640-68-6	98	117.15	Sigma-Aldrich (Merck KGaA, Germany)
DL-Phenylalanine	DL-Phe	150-30-1	98	165.19	Sigma-Aldrich (Merck KGaA, Germany)
L-Phenylalanine	L-Phe	63-91-2	98	165.19	Sigma-Aldrich (Merck KGaA, Germany)
D-Phenylalanine	D-Phe	673-06-3	98	165.19	Sigma-Aldrich (Merck KGaA, Germany)
Solvent					
Anisole		100-66-3	99.7	108.14	Sigma-Aldrich (Merck KGaA, Germany)
Cyclopentyl methyl ether	CPME	5614-37-9	99.9	100.16	VWR Chemicals (Avantor, UK)
Diethyl ether		60-29-7	99.7	74.12	Sigma-Aldrich (Merck KGaA, Germany)
1,4-Dioxane	dioxane	123-91-1	99.8	88.11	Sigma-Aldrich (Merck KGaA, Germany)
Hexane		110-54-3	95	86.18	Sigma-Aldrich (Merck KGaA, Germany)
Methyl isobutyl ketone		108-10-1	97	100.16	VWR Chemicals (Avantor, UK)
Tert butyl methyl ether		1634-04-4	99	88.15	Alfa Aesar (Thermo Fisher Scientific, UK)
Pyridine		110-86-1	99.8	79.1	Alfa Aesar (Thermo Fisher Scientific, UK)
Tetrahydrofuran		109-99-9	99.9	72.11	Alfa Aesar (Thermo Fisher Scientific, UK)
Toluene		108-88-3	98	92.14	VWR Chemicals (Avantor, UK)
Xylene		1330-20-7	98	106.17	VWR Chemicals (Avantor, UK)

4.2.3. Co-Crystal Screening

A co-crystallisation screening following a method described in the literature[28] was carried out based on solubility measurements obtained in Chapter 3. Mixed solutions of INA and a co-former A (4HBA, CBZ, and NA) in 1,4-dioxane were prepared using the saturation composition x_{INA}* and x_A* at a chosen temperature $30 < T^* < 50$ °C of both compounds. Following dissolution at elevated temperature (approximately 65 °C), the solutions underwent cooling crystallisation under a constant stirring of 700 rpm, which resulted in a recrystallised product. The produced suspension was then heated at a rate of 0.3 °C/min in order to determine the saturation temperature T_S of the solid phase. A more stable phase may form if the saturation temperature T_S is greater than the chosen saturation temperature T^* of the pure components INA and A.[28] Further characterization of the recovered crystalline samples after recrystallisation was performed by x-ray diffraction to verify the formation of a new phase.

4.2.4. Non-Uniform Electric Field Studies

Figure 4.1 represents the set-up used to conduct non-uniform electric field experiments. This set-up comprises an electrostatic cell with a high DC power supply and a water bath. The electrostatic cell consists of an 8 mL glass cylinder and two rod shaped cupper electrodes of 1 mm diameter (99.999% purity) supplied by Alfa Aesar (Thermo Fisher Scientific, United Kingdom). The rod electrodes are inserted through the orifices of a solvent addition cap procured from Technobis Crystallisation Systems (The Netherlands), so that the electrodes are kept parallel to each other separated by 6 mm measured from their centre. Once the cap is attached to the vial, the electrodes rest from the top of the cell to approximately 3-4 mm from the bottom of the cylinder. Provided that approximately 75% of the cell would be occupied by a fluid media, the upper part of the electrodes is fitted with polytetrafluoroethylene (PTFE) sleeves to prevent electric discharge during testing.

The outer end of the electrodes is soldered to Hirschman test leads of 4 mm diameter (32 A and 1 kV) that are connected to a FuG HCP 140-12500 power supply (FuG Elektronik GmbH, Germany). A 300 mL jacketed reactor connected to a bath/circulator Lauda Eco RE 420 (Lauda-Brinkmann, United States) permits temperature control with ±0.1 °C accuracy.

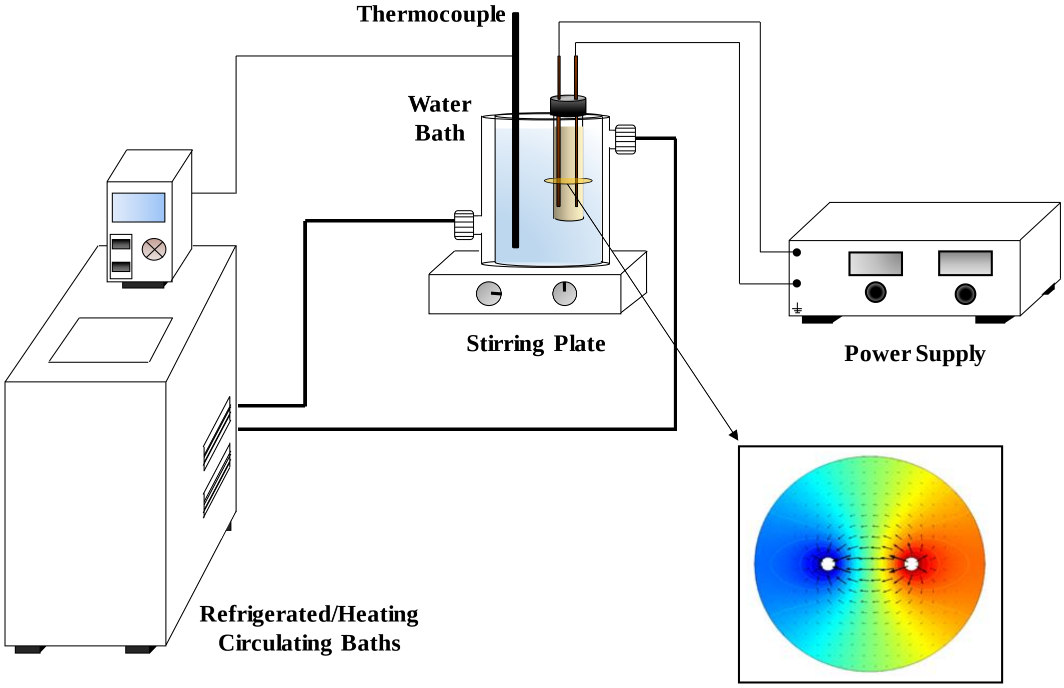

Figure 4.1. Schematic diagram of the non-uniform electric field set-up, which comprises a custom-made electrostatic cell connected to a high DC power supply. The cell consists on an 8 mL glass vial within two rod shape copper electrodes rest parallel to each other. The figure shows a cross section of the cell with the electrodes represented by white circles. The colours of the section depict a potential distribution for a simulated applied potential with an aleatory magnitude, and the black arrows refer to the direction and intensity of the generated electric field. A 300 mL jacket reactor connected to a bath circulator allows for temperature control in real-time via an adapted thermocouple and the command console.

4.2.4.1. Electric Field *Modelling*

The electric field distribution and field magnitude were estimated using the AC/DC module of COMSOL Multiphysics v 5.4. A 2D model of a horizontal cross section of the electrostatic cell was captured by the software, which creates a mesh of over 10^5 elements from which the potential distribution is solved by the Laplace's equation:

$$\nabla^2 U = 0 \tag{4.1}$$

where U is the electric potential in voltage units, and ∇ represents the vector gradient. To solve equation (4.1), the following boundary conditions were applied: 1) one of the electrodes was set at the applied potential, 2) the second electrode and the walls of the cylinder were grounded (U = 0), and 3) no electrical current occurs in the system. The electric field magnitude E can then be calculated from the norm of the potential distribution:

$$\boldsymbol{E} = -\nabla U \tag{4.2}$$

4.2.4.2. Solvent Screening

A solvent screening based on the generation of current upon applying a strong electric field was conducted on the pure solvents in Table 4.1, all of which have a dielectric constant ε_m lower than 13.1, to determine their suitability for electric field experiments without inducing the degradation of the solvent. Approximately 7 mL of a pure solvent was added to the non-uniform electrostatic cell before gradually applying a DC potential difference of 9 kV, that was sustained for a maximum of 30 min at room temperature provided no measurable current was observed. The experiments were interrupted if an electrical current above 0.002 mA was detected, and the solvent was deemed unsuitable for electric field experiments. The electric current limit was defined as twice the detection limit of the used equipment (0.001 mA).

4.2.4.3. Suspension behaviour under electric fields

The selected compounds in this study were equilibrated under stirring at T^* = 20 °C in the non-polar solvents, including 1,4-dioxane, toluene, and CPME. Following equilibration after a minimum of 10 h, the pure suspensions were filtered through a 0.45 μm PTFE membrane syringe filter (VWR, USA) into an 8 mL glass vial containing a PTFE coated magnetic stirrer. A pre-weighted amount ranging between 50 to 100 mg of the crystalline organic compound was added to the filtered solution before the vial was placed in a paraffin oil bath (Nujol light oil; Alfa Aesar, United Kingdom) set at T^* for 1 h. Therefore, as not all the solubilities were determined in the experimental solvents, a consistent suspension density ranging between 7 to 14 mg/mL was obtained for all the studied systems. Subsequently, the magnetic stirrer was removed and the cap was replaced by the anti-solvent lid with the rod electrodes. The non-uniform electrostatic cell was placed in a water bath set at the initial temperature (T^*), and a potential difference was gradually imposed between the electrodes. The motion of the crystals induced by the electric field was monitored and recorded.

4.2.5. Phase Analysis Light Scattering

The zeta-potential and electrophoretic mobility were measured by phase analysis light scattering in a NanoBrook ZetaPALS equipment (Brookheaven Instruments, USA). The ZetaPALS equipment estimates the mobility of the dispersed particles from the measured phase shift of the scattered laser light signal that occurs upon the laser beam irradiates a solid particle.

In a uniform electric field, the particle velocity $\boldsymbol{v_{EP}}$ is directly proportional to the electrophoretic mobility μ_{EP} and the applied field $\boldsymbol{E}$:

$$\boldsymbol{v_{EP}} = \mu_{EP}\boldsymbol{E} \tag{4.3}$$

where the magnitude of the uniform electric field is given by the following expression:

$$E = \frac{U}{d} \tag{4.4}$$

here, d refers to the nominal distance between the electrodes. Thus, the electrophoretic mobility can be calculated, and enables the estimation of the zeta-potential ζ. This parameter is used to characterize the effective electric charge of a solid phase in a given fluidic medium. In non-aqueous systems, the zeta-potential takes the form of the Hückel equation:[29]

$$\zeta = \frac{3\mu_{EP}\eta}{2\varepsilon_0\varepsilon_m} \tag{4.5}$$

where η refers to the viscosity of the fluid medium, and ε_0 and ε_m are the permittivity of the free space and the dielectric constant of the medium, respectively.

Before analysis, the crystalline material was subjected to ball milling using a Ball Mills (Retsch GmbH, Germany) for approximately60 min with a low vibrational frequency (5-10 Hz) to minimize the mechanical polymorphic transformation of the studied organic compounds.[30] Following milling, the obtained material was sieved through a 45 µm mesh using a vibratory Sieve Shaker Fritsch Analysette 3 Pro (Fritsch GmbH, Germany). The crystals that passed through the mesh were milled for a second time under the same conditions. In parallel, an equilibrated suspension of the studied compound in a non-polar solvent is filtered through a 0.45 µm PTFE membrane syringe filter (VWR, USA) into a glass vial. A suspension with a density of approximately 10 mg/mL of the pre-treated crystals in the filtered saturated solution was placed in an ultrasonic bath for 10 min. Subsequently, the suspension was filtered through a 10 µm PTFE membrane syringe filter (VWR, USA) into a 12 mm square glass vial for zeta-potential analysis, making sure that the suspension to be analysed contains a limited amount of crystals smaller than 10 µm.

The analysis in the ZetaPALS equipment was conducted at 25 °C, under an applied potential of 100 V to increase particle displacement, and the frequency was kept in auto mode. The average of a minimum of 5 consecutive measurements were taken as the zeta-potential magnitude, being each run the mean value of the phase shift of the laser measured for the detected particles after 30 cycles of 2π. Due to the rapid sedimentation rate of the particles, the measurements were conducted over the course of 60 min. In the event of this experimental period was surpassed, the analysis was re-run using a fresh suspension prepared as previously described.

4.2.6. Uniform Electric Field Studies

Electric field experiments in a uniform electric field were conducted using a custom-made electrophoresis device and an optical microscope (shown in Figure 4.2). The electrophoresis device was manufactured using 4 components: PTFE sheet of 10 mm thickness, standard glass microscope slide, M3 screw plugs, and glue epoxy Loctite HY 4090. The PTFE sheet was machined using an Axminster CNC mill to 85 mm length x 29 mm width with an internal opening of 50 mm x 7 mm. This gave the overall profile of the PTFE housing with holes drilled for the electrical cables and for the PTFE screw plug. The clearance between the electrical cable diameter and hole was tight to ensure no leakage of the fluid, however as a safety precaution epoxy was applied on the PTFE face and electrical cable. The cables are soldered to copper foil sheets of 99.999% purity and 1 mm thick, and placed on the two parallel long internal walls of the device. The outer dimensions are machined to the glass slide dimension which is epoxied onto the PTFE housing. A P240 grit wet/dry sandpaper is used to score the surfaces to aid adhesion. The parallel electrode plates allow the generation of a near-uniform electric field in the device. Due to the rapid degradation of the epoxy by the experimental solvents1,4-dioxane and toluene, these solvents were not suitable for the device. On the other hand, CPME could be used for 3 to 5 consecutive electrophoretic experiments before bubbles emerged from the suspension enclosed in the device; once air was observed within the system, the cell was cleaned and re-sealed with the glue epoxy.

A pure suspension of approximately 25 mg/mL of particles of the selected compound in one of the non-polar solvents was left under stirring overnight. The suspension was transferred to the electrophoresis cell by the means of a syringe, verifying the absence of air bubbles in the suspension. The device was placed on the microscope stage adaptor for microfluidic devices of a Nikon stereoscopic microscope SMZ 745T (Nikon Instruments Inc., USA). The microscope is equipped with a QICam Fast 1394 Digital Camera (Teledyne Photometrics, USA) supported in QCapture Pro 7.

Individual electrostatic experiments for a single solute-solvent system were carried out using potential difference ranging between 0.5 to 5 kV, that were generated within a few seconds after setting the target potential supplied by a FuG HCP 140-12500 power supply (FuG Elektronik GmbH, Germany). The particle motion was recorded at a set exposure time of 31.25 ms, reaching approximately 31 frames per second. To evaluate the velocity and displacement of the dispersed crystals, pre-treated images were analysed using a particle image velocimetry tool for Matlab R2018a (PIVlab).[31] Particle trajectories in the x-axis between the two electrodes are calculated based on the Fourier transformation, using a single step cross correlation analysis with an interrogation windows of 128 x 128 px. Post processing was limited to smooth the velocity vector in the x direction and using the standard deviation to validate the estimated data.

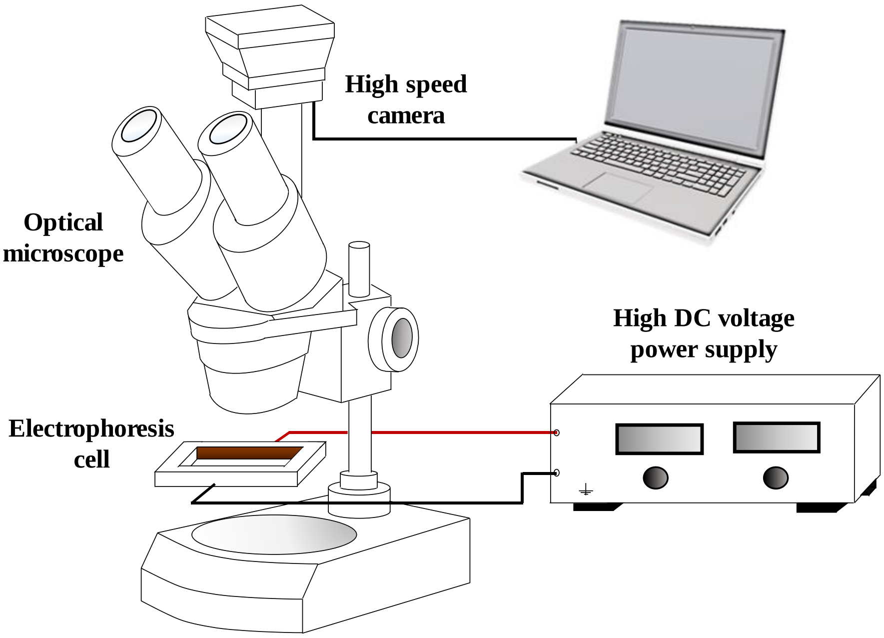

Figure 4.2. Schematic of the electrophoresis setup. The setup consists of an optical microscope (Nikon stereoscopic microscope SMZ 745) with an attached high speed camera (QIcam Fast 1394 Digital Camera) used to monitor and record the mobility of particles in a custom-made electrophoresis cell, induced by a uniform electric field generated by the means of a high DC power supply (FuG HCP 140-12500).

4.2.7. X-Ray Power Diffraction (XRPD)

The crystalline structure of the solid samples was identified in a Bruker D8 Discover diffractometer (GX002103 - Priscilla) equipped with a Cu anode (Cu Kα1 $\lambda = 1.54056$ Å) and a Vantec PSD detector using monochromic radiation. The samples were mounted on a multi-well plate supported on polyimide film, and data acquisition was carried out with a 0.015° step size per second from a 2θ range of from 4 to 35°.

4.2.8. Karl Fisher Titration

The residual water content of the nonpolar solvents was assessed in triplicate by Karl Fischer titration using methanol and Hydranal in a Hybrid Karl Fischer Moisture Titrator MKH-700 (Kyoto Electronics Ltd., Japan). A pre-weighted amount of the solvent, estimated from the mass difference of an empty syringe compared to the syringe filled with the solvent, was injected into the sample cell for analysis. The measurement resulted in a water content in units of %wt.

4.3. Results

4.3.1. Solvent Screening

Faradaic reactions are likely to occur in processes driven by strong electric fields due to the generation of electric currents. To avoid such chemical reactions that may lead to the degradation of the organic compounds in the experimental systems, weak polar solvents with small electrical conductivities are used here. Lykema[32] classified weak polar solvent into three categories based upon their dielectric constant ε_m as: 1) Semi-polar ($\varepsilon_m \geq 11$), 2) low-polar ($5 \leq \varepsilon_m \leq 11$), and 3) apolar or non-polar ($\varepsilon_m < 5$) solvents. In this work, a number of weak polar organic solvents including hydrocarbons, ethers, and ketones were subjected to a DC potential difference of 9 kV in the set-up shown in Figure 4.1. Table 4.2 shows the screening result for the experimental solvents. The current was always below the set limit value when a potential difference was applied to non-polar solvents. Slight disturbances of the air-liquid interface were observed above a potential difference of 3 kV in solvents with a dielectric constant $4 \leq \varepsilon < 5$: anisole, CPME, diethyl ether, and ter-butyl methyl ether. Our results are in accordance with the findings reported by Chang et al.[33] who identified a positive relation between the electro-osmotic flow and the dielectric constant of weak polar solvents. The fluid motion proportionally increased with the applied electric field, creating a perceivable whirl flow patterns within the glass cylinder at elevated voltage values.

Electric current and vigorous electroosmotic disturbances were detected upon the application of a potential difference to semi-polar (methyl isobutyl ketone and pyridine) and low-polar (tetrahydrofuran) solvents. Therefore, semi-polar and low-polar solvents were discarded for further test, and the non-polar solvents dioxane, CPME, and toluene were selected due to the absence of a measured electric current. The application of an electric field to pure solutions of the majority of the studied compounds in non-polar solvents slightly increases the swirl motion. However, the electric field applied to solutions of SSA, aminobenzoic acid, hydroxybenzoic acid, and nitrobenzoic acid compounds in 1,4-dioxane or CPME significantly increases the electro-osmotic flow and induces electric current above 0.002 mA. A common characteristic of these compounds is a considerable large solubility (> 200 mg/mL) in the mentioned non-polar solvents. The high solubility may be related to a strong solute-solvent interactions and the dissociation of the solute.[34] The presence of a larger number of ionic species in solution may increase the conductivity of the system and promotes the generation of electric current provided the existence of a strong electric field.

Table 4.2. Electric field screening results of experimental weak-polar solvents. The incompatibility of a solvent for electric field experiments was based on the detection of an electric current $I > 0.002$ mA by a FuG HCP power supply. Suitable solvents and solvents incompatible to electric field experiments are represented by (+) and (-) symbols, respectively. The electric properties of the solvents: dielectric constant ε and electrical conductivity κ were gathered from the literature.[35–37] The electrical conductivity of the solvents marked with an asterisk (*) were estimated according to $\kappa = \frac{l \cdot I}{U \cdot A}$, where l is the distance between electrodes and A is the electrode area.

Solvent	ε [-]	κ [Scm^{-1}]	I [mA]	**Suitability**
Anisole	4.4	$< 1.2 \cdot 10^{-8}$*	≤ 0.002	+
CPME	4.8	$< 1.2 \cdot 10^{-8}$*	≤ 0.002	+
Diethyl ether	4.3	$3.0 \cdot 10^{-16}$	≤ 0.002	+
Dioxane	2.2	$5.0 \cdot 10^{-15}$	≤ 0.002	+
Hexane	1.9	$1.0 \cdot 10^{-16}$	≤ 0.002	+
Methyl isobutyl ketone	13.1	$5.0 \cdot 10^{-8}$	0.018 (at 230 V)	-
Tert butyl methyl ether	4.5	$< 1.2 \cdot 10^{-8}$*	≤ 0.002	+
Pyridine	12.9	$4.0 \cdot 10^{-8}$	0.033 (at 180 V)	-
Tetrahydrofuran	7.5	$4.5 \cdot 10^{-5}$	0.036 (at 154 V)	-
Toluene	2.4	$8.0 \cdot 10^{-16}$	≤ 0.002	+
Xylene	2.3	$8.0 \cdot 10^{-16}$	≤ 0.002	+

4.3.2. Electric Field Modelling

Upon the application of a DC voltage, a non-uniform field arises as a result of the electrostatic cell geometry in which cross-sectionally two decentralized electrodes are positioned at a distance of 6 mm from each other (see figure cross section in Figure 4.1). As shown in Figure 4.3, the electric field modelling indicates that an applied voltage of 3 kV generates two different field gradients in the cylindrical cell: 1) from the cell walls (set as a boundary condition as $E = 0$ V/mm) to a local maximum at the electrode surface ($E \approx 0.8$ kV/mm), and 2) a second field gradient from a field maxima located at the electrode surface facing the counter electrode ($E \approx 1.4$ kV/mm) to the midpoint between the electrodes ($E \approx 0.4$ kV/mm).

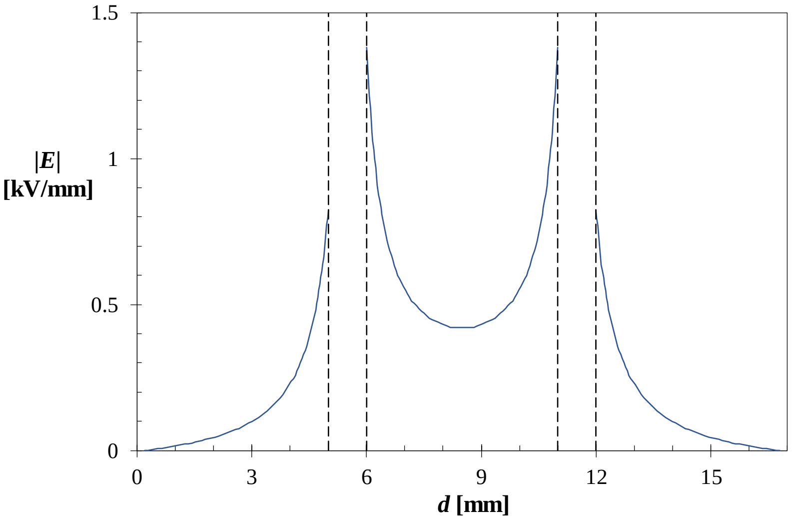

Figure 4.3. Distribution of the absolute electric field magnitude across the cylindrical electric cell. The gradient of the non-uniform electric field is represented by regions of electric field minima located at the cylinder walls and at the mid-point between the electrodes. The field maxima are on the electrode surface, represented by black discontinued lines.

4.3.3. Behaviour of Suspended Crystals in non-Uniform Electric Fields

Crystalline particles initially resting at the bottom of the cylindrical electric cell, are dragged and commence moving around the electrodes upon applying a strong potential difference. The moving crystals in the vicinity of the electrodes are attracted by one of the copper wires while being repelled by the opposite one. It was observed that a given compound is always attracted by an electrode of a certain polarity. By switching the field polarity once the crystals were resting on one of the electrode's surface, a migration of particles towards the opposite electrode corroborated the particular motion. This motion varies depending on the crystalline solute, which hints that electrophoretic forces act on surface charges present on the crystals, which alongside dielectrophoresis forces emerging in the non-uniform field, seems to cause the migration phenomenon. Additionally, the observed solution behaviour in the presence of the field suggest that electro-osmotic flow may contribute to the circular motion of the particles around the electrodes. The observed behaviour confirms Li's work, who recorded the motion of isonicotinamide crystals in 1,4-dioxane under an inhomogeneous electric field.[9]

The electric field driven motion of the particles seems to be solvent dependent and occurs when the applied potential surpasses a threshold value of approximately 2.5 kV for most of the 1,4-dioxane and CPME suspensions, and between 4 to 5 kV for the majority of the dispersions in toluene. The higher solubilities of most of the compounds in former solvents compared to that in toluene may increase the conductivity of the suspension, triggering electro-osmosis at lower potential values which assists the migration phenomena. In this work, the behaviour of a number of APIs and intermediates grouped as: 1) single compounds (including different polymorphic forms of the same compound), 2) co-crystal systems, and 3) chiral compounds were studied under strong inhomogeneous electric fields.

The specific motion of the particles towards one of the electrodes (anode or cathode) was recorded for 22 single compounds in the neat non-polar solvents, as shown in Table 4.3. The crystalline structure of the untreated suspensions was identified (see appendices A.2 and B.1). Most of the studied compounds collect at the same electrode independently of the solvent used. However, 3ABA, 4AMP and 4HBA crystals dispersed in toluene exhibited a different behaviour than that observed for the same pure compounds in 1,4-dioxane and in CPME. In toluene, these compounds migrate towards the anode in the presence of a non-uniform electric field, while they collected on the cathode in suspension of dioxane or CPME. To investigate whether the observed behaviour of these compounds was related to a different solid phase in toluene, pure suspensions of 3ABA in toluene and CPME, and suspensions of 4HBA in the three apolar solvents were prepared at room temperature. The slurries were stirred for 5 days at room temperature before recovering the crystals for XRPD analysis. The diffractogram patterns (see appendix B.2) of 3ABA and 4HBA were identical in toluene and CPME. In dioxane, 4HBA showed the pattern of a known solvate.[38] Apparently crystal structure does not explain the different behaviour in toluene compared to that in dioxane or CPME. A number of compounds were analysed after the application of the electric field and were compared to the diffractograms of the input material (see appendix B.3). No difference was observed between the XRPD data before and after the application of the electric field.

Interesting results were obtained from a comparative analysis of aminobenzoic acid isomers (2ABA, 3ABA, and 4ABA) and amongst the isomers of pyridinecarboxamide (INA, NA, and PIC). The aminobenzoic isomers collected on both electrodes in the presence of the field, however a dominant fraction always accumulated on the same electrode when suspended in the same solvent system. For instance, 3ABA preferentially collects on the working electrode when an electric field is applied to toluene suspension, while a small amount of crystals collects on the counter electrode. The accumulation of crystals on both electrodes suggests that dissimilar electrophoretic and/or dielectrophoretic forces exerted on the individual dispersed crystals, so each particle might experience a different force, either depending on their location in the electric field or on their surface charge or polarization.

Additionally, pyridine derivatives (such as INA), as well as aminobenzoic acids, move towards different electrodes in the presence of a non-uniform electric field. INA accumulates on the positive electrode while the meta and ortho-isomers of the pyridine compounds collect on the negative electrode. Assuming that the crystals are charged in the non-polar solvent, an electrical double layer (EDL) surrounds the solid phase and the zeta-potential can be measured.[29] The zeta-potential is the potential difference between a stationary phase formed by the solid surface and bounded ions and a mobile bulk medium phase. Therefore, this factor can be seen as the effective charge of the solid phase. Under DC voltage and under uniform electric fields, the zeta-potential is directly proportional to the surface charge density ρ_e of the solid phase:

$$\rho_e = \frac{\zeta \varepsilon_m \varepsilon_0}{r} \tag{4.6}$$

where r is the radius of the particle. Therefore, the sign of the zeta-potential indicates the sign of the surface charge and thus the preferred electrode the particles would collect onto based on electrophoretic forces.

As seen in Table 4.3, the mean zeta-potential value for INA was ζ = -8.82 ± 5.98 mV and presents a mobility μ_{EP} = -(0.05 ± 0.03) $\mu\text{m}\cdot\text{s}^{-1}\text{cmV}^{-1}$ in CPME at 25 °C under an electric field magnitude of 27.8 V/mm. Under the same conditions, ζ = 53.5 ± 4.39 mV and μ_{EP} = (0.27 ± 0.02) $\mu\text{m}\cdot\text{s}^{-1}\text{cmV}^{-1}$ for NA and ζ = 18.9 ± 6.35 mV and μ_{EP} = (0.1 ± 0.03) $\mu\text{m}\cdot\text{s}^{-1}\text{cmV}^{-1}$ for PIC. The sign of the zeta-potential agrees with the experimental observations. The measured mobilities show large differences amongst the various crystalline compounds that may be exploited to separate them from a mixture by electrophoresis.

Table 4.3. The application of a non-uniform electric field triggers a specific motion of the suspended crystals in an apolar solvent towards the anode A or cathode C. Single organic compound behaviour in three nonpolar solvents (1,4-dioxane, toluene, and CPME) in the presence of a strong potential difference alongside the measured zeta-potential ζ and mobility μ_{EP} for some systems were recorded. The symbol * indicates that the collection of the crystals was mainly on the indicated electrode, with a population of crystals lower than 5% of the total amount of suspended material collected on the opposite electrode as well. In the even an electric current higher than 0.002 mA was detected, the experiment was interrupted and the no measurements were carried out.

Compound	**Polymorphic form**	**Solvent**			**ζ [mV]**			**μ_{EP} [(µm/s)/(V/cm)]**		
		1,4-dioxane	**Toluene**	**CPME**	**1,4-dioxane**	**Toluene**	**CPME**	**1,4-dioxane**	**Toluene**	**CPME**
2ABA	I		A^*							
3ABA	III		A^*	C^*						
4ABA	I	C	C^*	C						
4AMP		C	A	C						
ASP	I	A	A	A						
CAF	β	A	A	A			-17.0 ± 5.8			-0.09 ± 0.03
CBZ	III	C	C	C						
2,4DHBA	II		A							
3,5DHBA	II		A							
2HBA			A							
3HBA	I		A							
4HBA		C	A	C		-21.9 ± 20.2	2.6 ± 1.6		-0.06 ± 0.05	0.01 ± 0.01
INA	I	A	A	A	-85.2 ± 77.9		-8.8 ± 6.0	-0.08 ± 0.07		-0.05 ± 0.03
NA	I	C	C	C	127 ± 8.1		53.5 ± 4.4	0.12 ± 0.01		0.27 ± 0.02
3NBA	I		A							
4NBA	II		A	A						
PIC	II	C	C	C			18.9 ± 6.3			0.10 ± 0.03
PCT	I	A	A	A			-3.7 ± 3.9			-0.02 ± 0.02
PHZ		C	C	C						
SSA			C	C						
THB			A							
THP	II	A	A	A						

4.3.3.1. Polymorphs

To investigate the effect of the surface characteristics of a particle on the electric field driven motion, a number of polymorphic forms of INA and the aminobenzoic acid isomers 2ABA, 3ABA and 4ABA were suspended in apolar solvents and subjected to strong inhomogeneous electric fields.

Figure 4.4 shows the XRPD patterns of the different crystalline structures used compared to the referenced diffractograms gathered from the Cambridge Crystallographic Data Centre (CCDC). Particles in the suspensions of INA form I, II and III move towards the anode, while 4ABA form I and IV move towards the cathode in all 3 solvents in the inhomogeneous electric field experiments. A small amount of crystals was also observed on the anode for the suspensions of 4ABA in toluene. The three different forms of 2ABA suspended in toluene and 3ABA forms II, and III suspended in toluene and CPME show the same behaviour. For these compounds, the different polymorphs in the same solvent present a main fraction of crystals that accumulated on one electrode and a small portion of crystals on the opposite electrode. From the obtained findings, the observed behaviour suggests that the studied polymorphic forms do not influence the particle motion in the experimental solvents. The observed behaviour of the different polymorphic forms of the studied organic compounds is given in Table 4.4.

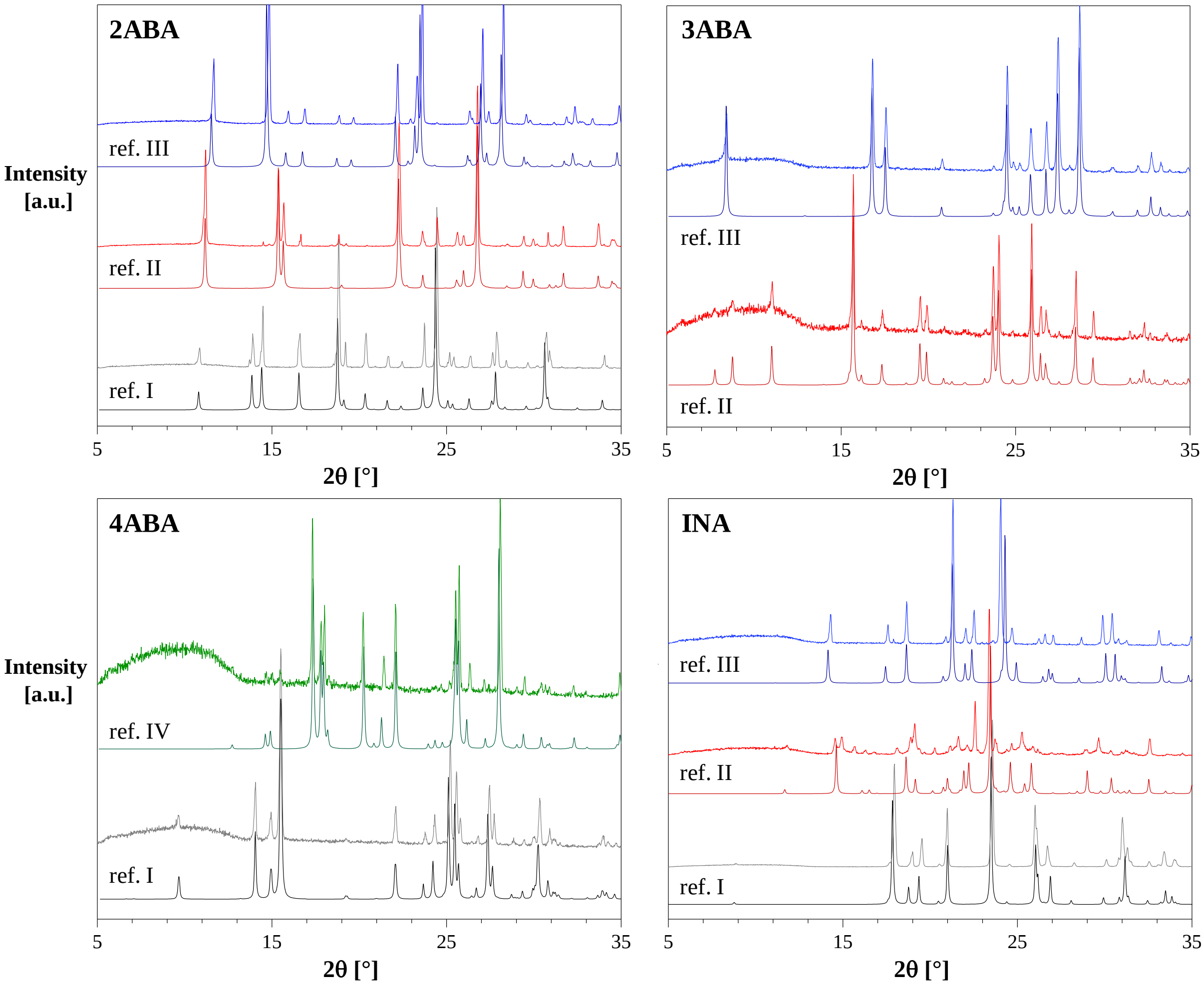

Figure 4.4. XRPD patterns of different polymorphic forms of 2ABA, 3ABA, 4ABA, and INA produced in this work. The diffraction patterns of the produced crystals are compared with the appropriate reference diffractogram from the Cambridge Crystallographic Data Centre (CCDC): 2ABA form I (CCDC - AMBACO01),[39] 2ABA form II (CCDC - AMBACO03),[40] 2ABA form III (CCDC - AMBACO06),[41] 3ABA form II (CCDC - AMBNZA),[42] 3ABA form III (CCDC – AMBNZA01),[43] 4ABA form I (CCDC - AMBNAC01),[44] 4ABA form IV (CCDC - AMBNAC),[45] INA form I (CCDC - EHOWIH01),[46] INA form II (CCDC - EHOWIH02),[46] and INA form III (CCDC - EHOWIH03).[47] The black patterns refer to the form I of each produced polymorph-reference pair, the red patterns are the form II, and form III and IV are represented by blue and green patterns, respectively.

Table 4.4. Individual behaviour of the different produced polymorphic forms of 2ABA, 3ABA, 4ABA, and INA upon imposing a strong non-uniform field to pure suspensions of the crystalline particles in 1,4-dioxane, toluene, or CPME. Suspended crystal collect on the anode A or cathode B in the presence of an inhomogeneous electric field. Some compounds accumulate on both electrodes, with a main fraction (greater than 95% of the total amount of suspended material) found on one of the electrodes *.

Compound	**Polymorphic form**	**Solvent**		
		1,4-dioxane	**Toluene**	**CPME**
2ABA	I		A*	
	II		A*	
	III		A*	
3ABA	II		A*	C*
	III		A*	C*
4ABA	I	C	C*	C
	IV	C	C*	C
INA	I	A	A	A
	II	A	A	A
	III	A	A	A

4.3.3.2. Co-crystals

Co-crystal refers to a multi-component crystal composed for at least two different compounds that are solids at room temperature.[48] A series of co-crystals were produced by dissolution and recrystallisation of a mixed suspension of INA and a second co-former (NA, 4HBA, or CBZ) in 1,4-dioxane. The formation of a co-crystal was assessed by diffraction analysis. The diffraction patterns of the three co-crystals systems produced in this work (INA:NA, INA:CBZ, and INA:4HBA) for electric field experiments are presented in Figure 4.5.

In all three solvents suspended particles of the co-crystals INA:NA and INA:CBZ collect on the cathode independently of the experimental solvent used (Table 4.5). The observed behaviour of both compounds were similar to NA and CBZ, respectively. In a sufficiently large electric field INA:4HBA crystals collect on the anode when they are suspended in toluene, while they collect at the cathode when they are dispersed in 1,4-dioxane or CPME (Table 4.5), which correspond to the same behaviour presented by 4HBA. The sign of the measured zeta-potential and electrophoretic mobility for INA:NA co-crystal suspensions in CPME agree with the observed motion in an inhomogeneous electric field. The findings of this study suggest that the compounds in a suspension mixture of each co-crystal with INA may be separated by the use of electric fields.

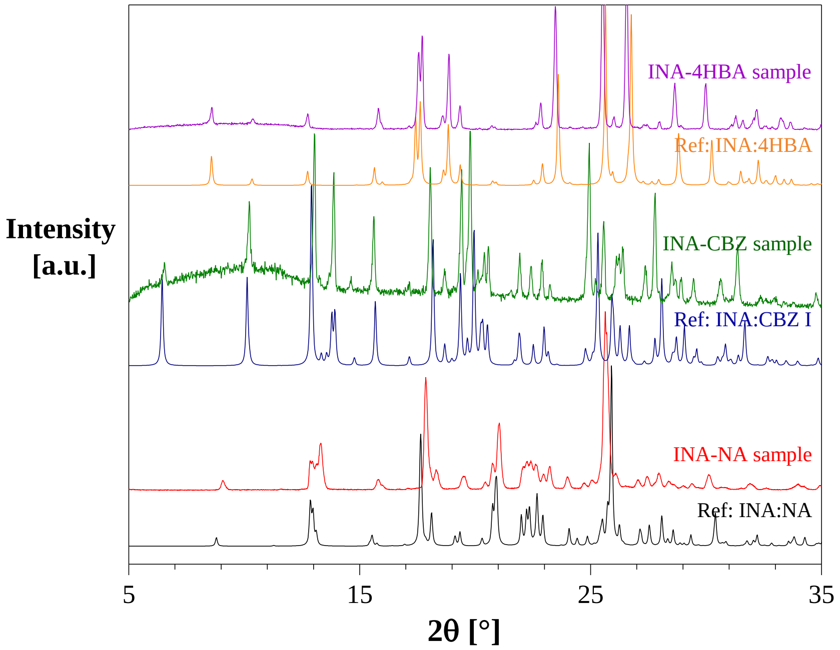

Figure 4.5. The XRPD patterns from co-crystallisation screening of INA with NA, CBZ, and 4HBA. The obtained diffraction patterns of the produced crystals were compared to the deposited structures in the Crystallographic Data Centre (CCDC) of INA:NA cocrystal (CCDC – UMUYOR),[49] INA:CBZ polymorphic form I (CCDC – LOFKIB),[50] and INA:4HBA (CCDC - VAKTOR).[51]

Table 4.5. Behaviour of the produced co-crystals in 1,4-dioxane, toluene, and CPME upon the application of a strong DC electric field. The co-crystals collected on the anode A or cathode C in the presence of a strong non-uniform electric field. Over the course of the experiments the motion of the dispersed crystals was monitored, and their collection at either the anode or cathode was monitored.

Compound	Polymorphic form	Solvent			ζ [mV]	μ_{EP} [(μm/s)/(V/cm)]
		1,4-dioxane	Toluene	CPME	CPME	CPME
INA:NA		C	C	C	2.0 ± 3.0	0.01 ± 0.02
INA:CBZ	I	C	C	C		
INA:4HBA		C	A	C		

4.3.3.3. Chiral compounds

Chirality can be loosely defined as a form of isomerism, associated to the different spatial arrangement of the constituent atoms of the molecules with respect an asymmetric centre. Therefore, the two different chiral form of the same molecule (called enantiomers) are non-superimposable mirror images of each other, and generally possess the same physical and chemical properties. These molecules however, differentiate in their optical activity, and based on the direction of the light rotation induced by the enantiomer, they are classified in dextrorotatory (D) or levorotatory (L). A racemic compound is a crystalline phase composed of both chiral forms of the same molecule that are present in a stoichiometric ratio in the same crystal lattice.[52] In this work, the behaviour of a number of chiral compounds were studied in the presence of a strong inhomogeneous field.

For naproxen and valine, particles in suspension of both the racemic and enantiopure compounds in a non-polar solvent accumulate on the same electrode (Table 4.6). However, valine crystals in toluene move towards a different electrode compared to the observed motion of the same suspensions in 1,4-dioxane or CPME.

Interestingly, the racemic compound of phenylalanine showed a different behaviour in an electric field compared to the enantiopure compound of both the D and L-enantiomers. In the presence of a potential difference above 2 kV, DL-Phe accumulates on the cathode while at approximately the same voltage D- and L-Phe collect on the anode. Our findings at least hint that the electrical properties of DL-Phe differs from D and L-Phe, and undergo dissimilar intermolecular interactions in the non-polar solvents. Zeta-potential measurements corroborated the experimental observation, i.e. the ζ and μ values of DL-Phe are positive while these factors are negative for D- and L-Phe. A significant difference between the enantiomer mobilities was measured, which may be related to measurement inaccuracy or crystal size differences.

Table 4.6. Behaviour of chiral compound in the experimental isolating solvents (1,4-dioxane, toluene, and CPME) upon imposing a potential difference between two rod shaped electrodes submerged in the suspension, which creates an inhomogeneous electric field within the suspension systems. Particles in suspension moved towards the anode A or cathode C when in the presence of a strong inhomogeneous electric field.

Compound	**Polymorphic form**	**Solvent**			**ζ (mV)**	**μ_{EP} [(μm/s)/(V/cm)]**
		1,4-dioxane	**Toluene**	**CPME**	**CPME**	**CPME**
RS-NPX		A	A	A		
S-NPX		A	A	A		
DL-Val		C	A	C		
L-Val		C	A	C		
D-Val		C	A	C		
DL-Phe		C	C	C	3.6 + 4.3	0.02 + 0.02
L-Phe	I	A	A	A	-26.1 + 2.6	-0.13 + 0.01
D-Phe	I	A	A	A	-11.8 + 2.3	-0.06 + 0.01

4.3.4. Behavioural study of suspended crystals in uniform electric fields

The electrophoretic motion of particles suspended in an apolar solvent was studied using a custom-made electrophoresis cell using CPME as solvent. The custom-made cell permits to eliminate or at least substantially downscale dielectrophoretic forces as they do not occur in a perfect homogeneous field. So we can study electrophoretic motion in the absence of dielectrophoretic effects.

Equilibrated suspensions of pure crystalline compounds in CPME were transferred to the cell in order to monitor the motion of the suspended crystals at different applied potentials using a high-speed camera attached to an optical microscope. After applying a DC voltage across two parallel plate electrodes in a levelled-walled rectangular channel, a uniform electric field arises. Therefore, a motion of the crystals towards one of the electrodes would reveal the presence of electrophoretic forces exerted on solid charged particles. This study was carried out using pure suspensions of CAF and NA in CPME of which the particles accumulate on respectively the anode and the cathode in a non-uniform electric field. The unexpected dissimilar behaviour of the racemic mixture of phenylalanine compared to that of the enantiomers of the chiral compound was also investigated in a uniform electric field.

4.3.4.1. Caffeine

In the absence of an electric field, the suspended CAF crystals in CPME settle at the bottom of the cell. Once the potential difference applied across the electrodes surpasses a certain threshold, the CAF crystals are first dragged towards the cathode for a fraction of time, and immediately after the crystals present an opposite mobility to the direction of the field and start collecting onto the positive electrode, revealing that they were negatively charged in the non-polar solvent CPME. Figure 4.6 shows the motion of the crystalline particles in a period time of 0.5 s. The velocities of the crystalline particles rapidly increase as the power supply reaches the set voltage, exhibiting a peak value within a few seconds. The rapid collection of the CAF particles on the anode under an applied potential of 5 kV (within 0.5 s), may reveal some loss of accuracy on the velocity measurements due to the limitations of the equipment to record the trajectory of the particles. However, the observed trends and estimated velocity values provided us with valuable information to interpret the electrokinetic phenomena acting on the crystalline phase.

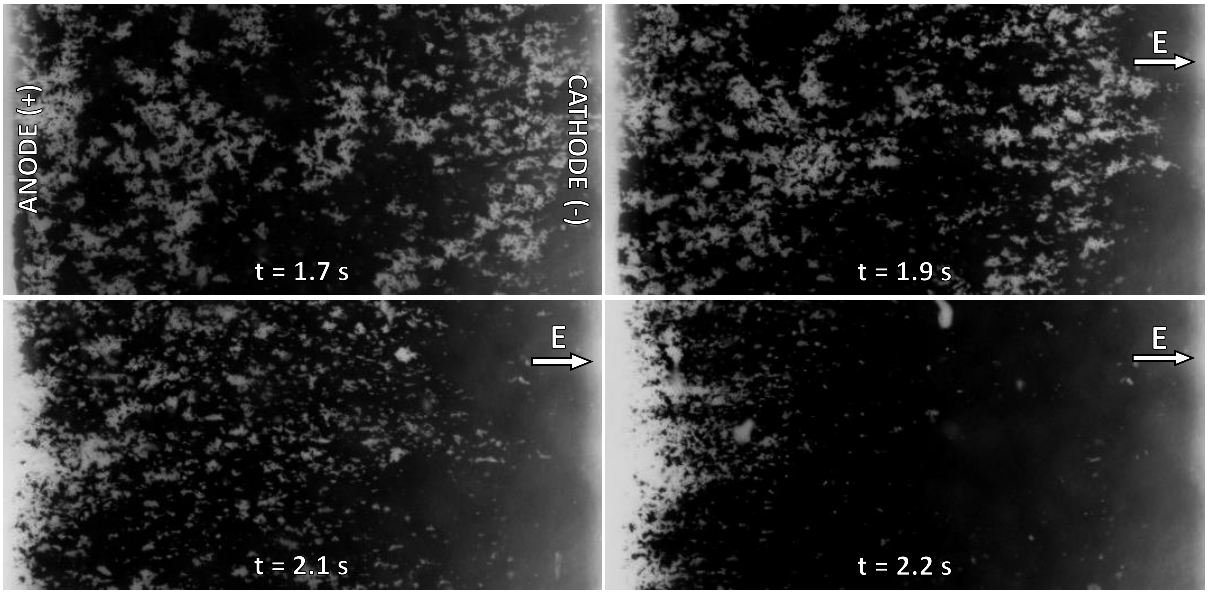

Figure 4.6. Images of CAF crystals suspended in CPME enclosed in a 5 mm squared channel in the presence of an electric field magnitude $E = 8.33 \times 10^5$ V/m. The frame shows the total width of the channel. A DC potential difference of 5 kV was set between the two plate electrodes, which was rapidly achieved by the used power supply. Upon imposing the electric field, the crystals slowly commence to move and rapidly accumulate on the positive electrode (anode). A number of crystalline particles are repelled and attracted back by the anode, which reveals a charge transfer phenomenon between the copper surface and the crystals.

After making physical contact with the anode, a number of particles moved to the centre of the cell and rapidly moved back to the anode. This phenomenon has been previously reported and related to surface charge interaction between particle and electrode in slightly polar solvents.[53,54] When a charged particle reaches the electrode of opposite sign, the letter injects charges onto the surface of the particle, which is repelled from the surface of the electrode when both share equal charges. In the bulk medium, the injected charges leak off though the liquid and the particle is attracted back by the same electrode.

The velocity of the crystals was quantitatively estimated with the use of PIVlab, that traces the particle mobility between consecutive images and calculates the average value of all the detected particles. Figure 4.7 shows the measured velocity trends measured for CAF crystals under electric fields of different magnitudes. Despite the large standard deviations, the results at least indicate that the magnitude of the velocity increases with increasing the applied potential difference and it is of opposite direction to the field. For instance, the mean-peak velocity in the presence of an electric field magnitude E = 833.3 V/mm was -1.84 ± 1.7 mm/s, which was 4.6 times greater compared to the peak velocity at E = 166.7 V/mm (-0.40 ± 0.6 mm/s). The initial movement of the CAF crystals in the direction of the field is capture by a small-positive velocity increase between 0 and 0.5 s. At the peak velocity, the mobility of the CAF crystals can be estimated from equation (4.3). The mobilities of the crystalline particles under strong electric fields ranged between -1.5 and -2.5 $m^2V^{-1}s^{-1}$, which according to the Hückel equation correspond to zeta-potential values between -30 to -50 mV. The estimated zeta-potential was significantly larger than that obtained PALS analysis. These findings are in accordance with Schreuer's,[55] who reported that the increase of the net charge of poly-hydroxystearic acid-coated poly(methyl methacrylate) particles in pure dodecane was proportional to the electric field amplitude. A large standard deviation was obtained for the velocity measurements using the PIVlab software. The circulation of particles between the electrode and the bulk medium and/or small particles undergoing Brownian motion detected by the software may contribute to error in the measurements.

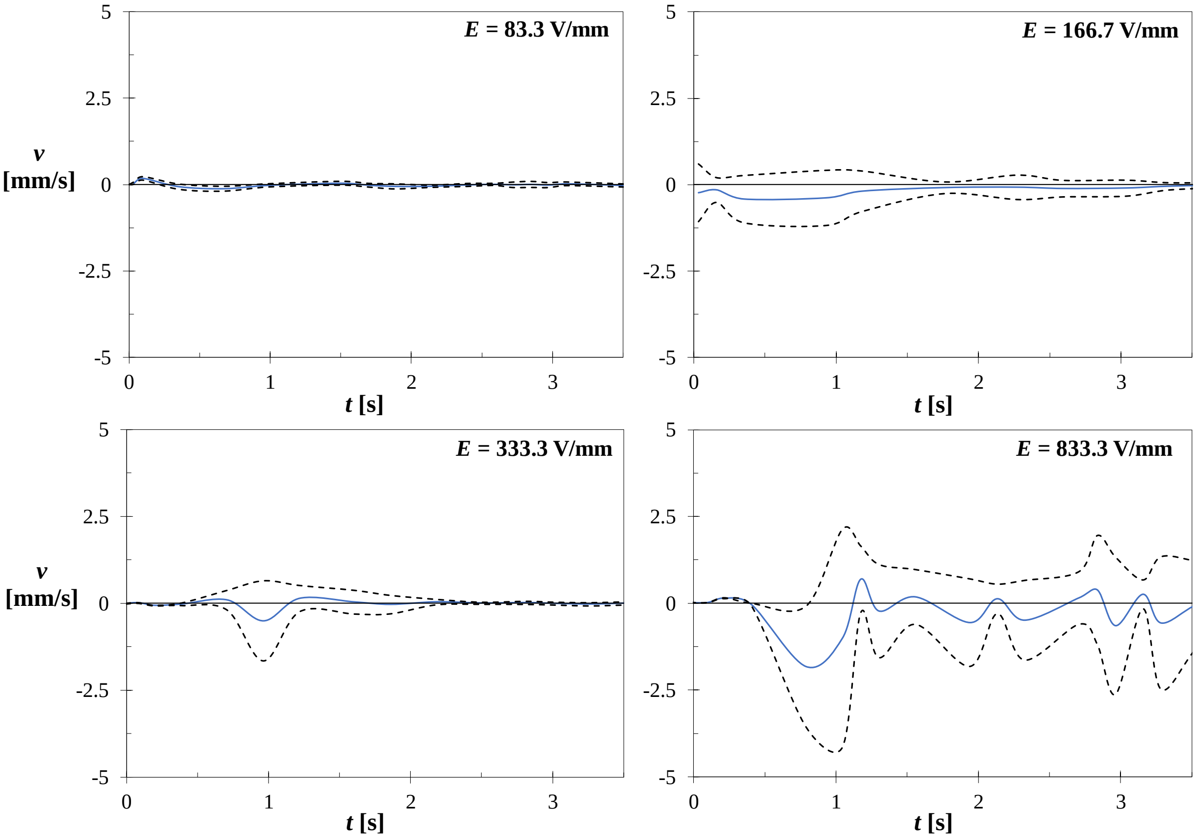

Figure 4.7. Measured velocity of CAF crystals in CPME under different electric field magnitudes. Using a custom-made electrophoresis cell and an optical microscope, the motion of the crystals in the presence of an applied electric field *E* = 83.3 V/mm, *E* = 166.7 V/mm, *E* = 333.3V/mm, and *E* = 833.3 V/mm was recorded. The blue lines represent the mean velocity over the course of electric field experiments. The dashed lines depict the standard deviation in the measurements obtained as calculated by PIVlab. The velocity is positive when moving to the cathode, and negative when moving to the anode.

4.3.4.2. Nicotinamide

The motion of the crystal occurs when the applied electric field is large enough that the electrokinetic forces dominate over friction and viscous forces. The randomly dispersed NA crystals in a suspension in CPME commence to migrate away from both electrodes when the applied potential difference reached 1 kV. While moving in the presence of the field, the solute particles interact with neighbouring crystals and form fibrillated structures parallel to the electric field direction (Figure 4.8). Under such strong electric field, the dielectric particles are polarized and form dipoles that align along the field direction. Once the particles are close enough, they are attracted head-to-tail by electrophoresis, forming large chains between the electrodes. Such behaviour has been described for different types of suspended particulate compounds.[29] The observed behaviour is a characteristic of electrorheological fluids,[56] that occurs in non-conductive suspensions. The one dimensional structures remained after reducing the potential to 0 V. Subsequently, the potential was increased to 2 kV, which was followed by the collapse of the chain arrangements and a subsequent inter-electrode circulation of the suspended crystals. This inter-electrode circulation suggests a similar charge exchange mechanism between the NA crystals with the electrodes and the liquid than that observed for CAF. However, in contrast to the CAF crystals, NA reached both electrodes. The circulation continues until the potential is ceased. After reducing the potential to 0 V, the solute particles re-arranges in the previously observed chain patterns which gradually disperse as the field fades. Some accumulation of NA crystals was detected on the surface of the cathode at the end of the experiment. Similar behaviour was observed under an applied potential of 5 kV.

The electric field experiments carried out in NA crystals dispersed in CPME showed that the manipulation of the particles into chains is feasible by controlling the strength of E. For the accumulation of NA crystals on the cathode a non-uniform electric field may be required. To investigate the behaviour of equilibrated suspensions of NA in CPME under a strong inhomogeneous electric field in the same setup, an electric field gradient can be induced in the rectangular channel by replacing the plate electrodes by rod copper wires. The application of a potential difference of 3 kV induces a very slow motion of the NA crystals towards the cathode, while particle-particle interaction into the fibrillated structures occurs at the same time. The collection of crystals on the cathode rapidly occurs under an applied potential of 5 kV, with no observable one dimensional structures forming. No motion of crystals was observed below 3 kV.

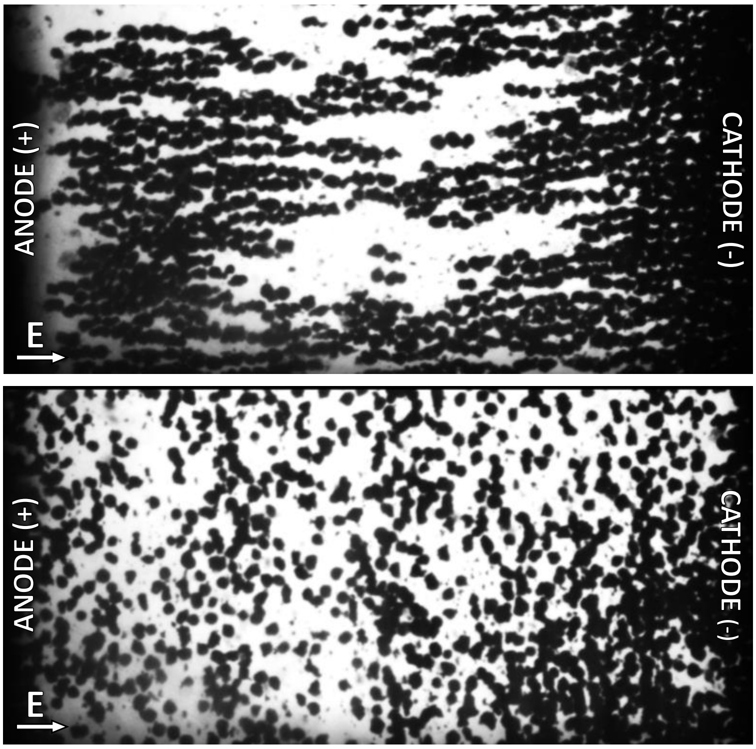

Figure 4.8. Images of NA crystals suspended in CPME confined in a custom-made electrophoresis cell. The width of the channel is 5 mm, that corresponds to the horizontal distance between the electrodes represented in the images. In the presence of an electric field magnitude of approximately $E = 1.67 \times 10^5$ V/m, the dispersed particles align and form chain structures in the direction of the electric field (top image). As the electric field increases, the structures disassemble and the crystals move between the two electrodes (bottom image).

Assuming that the gradient of the non-uniform electric between the electrodes is similar to the calculated field magnitude for the cylindrical setup, the field at a set potential of 3 kV changes from a minimum magnitude E = 422 V/m (in the centre of the channel) to a field maxima E = 1380 V/m (located on the surface of the electrodes). Figure 4.9 shows the evolution of the mean velocity over the course of the experiments carried out under potential differences of 3 and 5 kV. In the presence of a non-uniform electric field, the motion of the crystalline particles is dominated by the combined effect of electrophoresis and dielectrophoresis. In contrast to their behaviour in a uniform field, NA crystals accumulate on the cathode due to the considerably larger force exerted on the particles by both electrokinetic forces. The total force exerted on a spherical particle can be expressed as:[23]

$$\boldsymbol{F} = q\boldsymbol{E} + 2\pi\varepsilon_0\varepsilon_m r^3 f_{CM}\nabla\boldsymbol{E}^2 \tag{4.7}$$

where the first term of equation (4.7) is the electrophoretic force and the second term represents the dielectrophoretic force. The electrophoretic force is linear function of the charge (q) and electric field product, while the dielectrophoretic force is proportional to the square of the field gradient ($\nabla \boldsymbol{E}$), the radius of the solid particle (r), and the Classius-Mossotti factor (f_{CM}):

$$f_{CM} = \frac{\varepsilon_c - \varepsilon_m}{\varepsilon_c + 2\varepsilon_m} \qquad \textbf{(4.8)}$$

here ε_c refers to the dielectric constant of the solid. Under a DC electric field, the permittivity can be approximate to the electrical conductivity.[23]

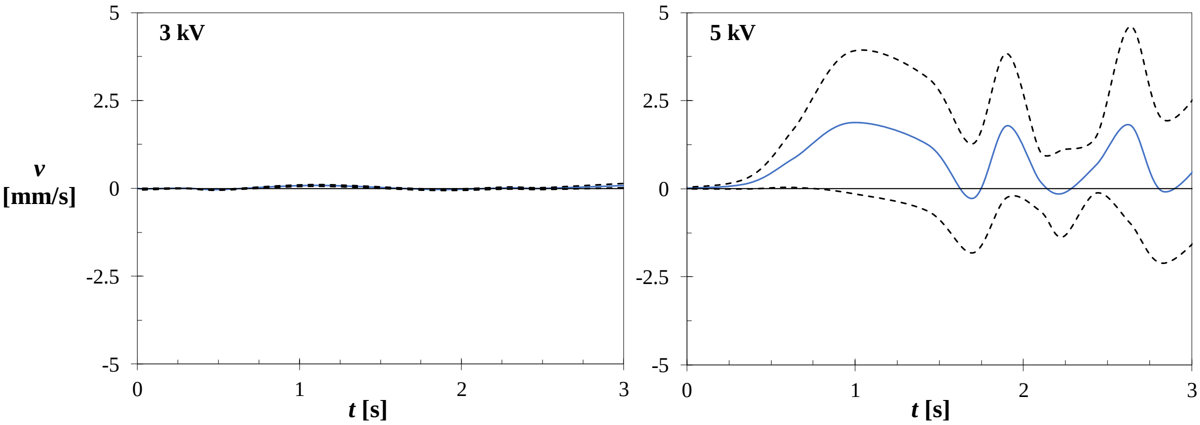

Figure 4.9. Mean velocity of NA crystals suspended in CPME under a non-uniform electric field. The motion of the crystalline particles upon the application of a DC potential difference of 3 kV, and 5 kV, was recorded using a high-speed camera connected to an optical microscope. An open licence software (PIVlab) was used to analysed the images and calculate the mean velocity of the crystals over the course of the experiments. The continuous blue lines are the mean velocity and the discontinued lines represent the standard deviations in the measurements.

4.3.4.3. DL- and D-Phenylalanine

The motion of DL-Phe and D-Phe crystals in CPME in the presence of a uniform electric field E = 166.7 V/mm is studied in the electrophoresis cell given the unexpected dissimilar behaviour of the chiral compounds. The obtained results are in line with the observed behaviour under a non-uniform electric field, which indicates that the racemic and enantiopure particles are respectively positively and negatively charged. As seen in Figure 4.10, the racemic DL-Phe have a positive velocity relative to the x-axis in the uniform electric field, which induces the accumulation of the racemic crystals on the cathode. On the other hand, D-Phe crystals present a velocity direction opposite to the electric field, which indicates the collection of the suspended crystals on the anode.

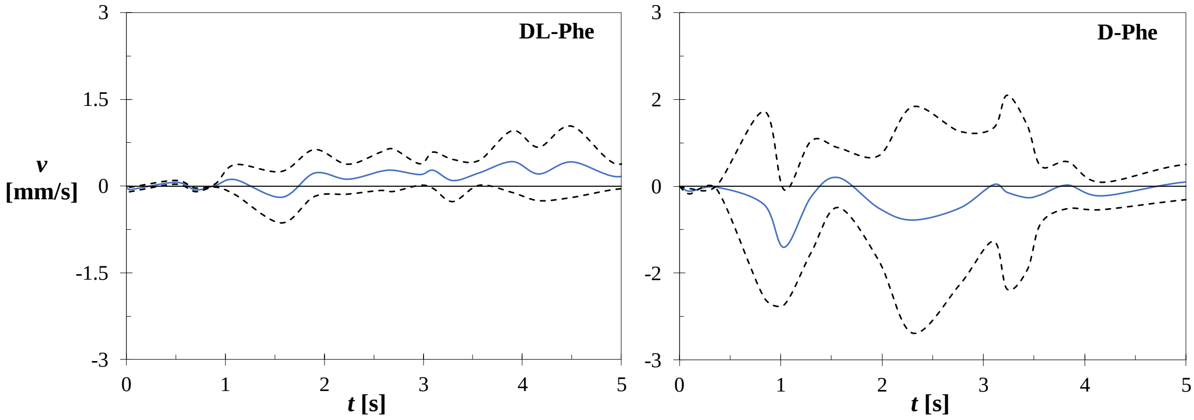

Figure 4.10. Measured velocity of DL-Phe and D-Phe crystals dispersed in CPME under a uniform electric field magnitude $E = 1.67 \times 10^5$ V/m. An optical microscope and an attached high-speed camera were used to record the crystals motion, and the images were analysed with an open licence software (PIVlab) to measure the crystal velocities. The mean velocity is represented by a blue line, and the standard deviation in the measurements are depicted by a discontinued black line.

4.4. Discussion

In this study, we have presented experiments that explore the behaviour of crystalline particles under uniform and non-uniform electric fields. These experiments were conducted using non-polar solvents that resist electrolysis. Undesired effects due to a strong applied electric field such as chemical reactions are minimized using non-polar solvents, that are characterized by strong electric resistance and small dielectric constants ($\varepsilon < 5$). Upon applying a potential difference of 9 kV to these solvents, no current above 0.002 mA was detected.

More polar solvents exhibited larger electric current values in the presence of a field, that may induce Faradaic reactions and Joule heating.[57] Through a further reduction of the distance between electrodes, lower voltages are required to produce a strong electric field and other weakly but more polar solvents could be used.[22]

Slight disturbances of the air-liquid interface were observed above a DC potential difference of 3 kV in solvents with a dielectric constant between $4.3 < \varepsilon < 5$. This fluid motion increased with the applied electric field, creating a perceivable whirl motion within the glass cylinder at elevated voltage values. This phenomenon, known as electro-osmosis has been previously reported in non-aqueous media under DC electric fields.[33] The applied potential triggers the motion of the counter ions shielding the electrical double layer of the electrodes and possibly on the cylinder's wall, inducing a drag force on the bulk fluid. The intensity of the electroosmotic phenomenon increases in fluids with larger dielectric constants.[33] Electro-osmosis is difficult to observe in non-polar solvents because ionic species may only be present as unknown traces of impurities in the solvent. Although electro-osmosis may contribute to the motion of the crystalline particles in non-polar suspensions around the electrodes we estimate this contribution to be minor.

The non-uniformity of the applied field was simulated with COMSOL Multiphysics, from which the electric field gradient is known. In the experiments in the inhomogeneous field, the suspended crystals always migrate towards the electric field maxima located on the electrode surface. This movement towards higher electric fields must be the action of dielectrophoretic forces: under the generated inhomogeneous electrostatic field, neutral particles get polarized and dragged by positive dielectrophoresis, assuming that the solid phase is more polarizable than the fluid medium. The collection of the particles at a specific electrode suggest that the studied particles are charged in the experimental solvents, and then attracted by the electrode of opposite charge by electrophoresis.

The charging mechanism of dispersed particles in weakly polar solvents is not well understood, but the general consensus relates the charging process to the preferential adsorption of ions on the particle surface.[55,58] The dissociation of surface groups of the solids and the presence of additives and/or impurities in the isolating liquid are the plausible source of the ionic species. Traces of water in the experimental solvents may influence the physical properties of the suspensions though the formation of micelle structures, the dissociation of ionic molecules by electrolysis, and affecting the acid-base character of the particle surface.[29,55,58] Karl-Fisher analysis carried out in 1,4-dioxane, toluene and CPME confirmed the presence of residual water in the non-polar solvents with absolute values of 0.012% (wt%), 0.029% (wt%), and 0.049% (wt%), respectively. Based on the presence of water and the donor and acceptor hydrogen concept introduced by Lykema in non-aqueous solvents,[32] the particular motion observed towards one of the electrodes is likely to be related to the acid strength of the compound relative to that of the solvent. In this context, the accumulation of a compound on opposite electrodes when suspended in different solvents may be explained by the amphoteric nature of that organic compound.[59] Our results tie well with previous studies wherein the surface charge of a given particle changes in dissimilar non-polar solvents.[60–62] The aminobenzoic isomers bare carboxyl and amino groups that are proton donor and acceptor. Thus, the surface properties of the crystals and the character of the solvent may influence the net charge of the compound, that bares positive and negative charged sites and therefore can be attracted toward opposite electrodes in the same solvent. The study of different crystalline structures of the same compound under an electrostatic field did not show a direct influence of the molecular arrangement or morphology on the particle behaviour. A deeper investigation is required to improve the control of suspended crystals by electric fields.

The zeta-potential analysis on a series of organic compounds corroborates the presence of charge on the particle surface. The measured polarity furthermore agrees with the monitored behaviour of the particles collecting on either the anode or the cathode. Thus, the migration towards a specific electrode may be predicted by the measured sign of the zeta-potential, although the obtained quantitative values of this property seemed rather inaccurate. In rare occasions, the PALS analysis reported a zeta-potential value of opposite sign for a given compound than that of the mean magnitude. This may be associated to the amphoteric character of the organic suspensions. According to equation (4.5), the zeta-potential magnitude is inversely proportional to the dielectric constant of the fluid media. This trend was observed on NA, INA, and 4HBA crystals suspended in the different solvents.

The presence of surface charge confirmed by zeta-potential analyses indicates that Columbic forces between the suspended particle and the electrode of opposite sign (electrophoresis) is the responsible phenomenon for the migration of the crystalline particles to a specific electrode. Therefore, a closer study on the particle behaviour under a homogeneous electric field was carried out under an optical microscope. Despite the large standard deviations, possible due to the erratic Brownian motion of fine particles detected by the camera and dissimilar friction and viscous forces experienced by the particles, the trajectory of CAF and Phenylanaline crystals matched with the motion observed under inhomogeneous fields. Once the applied potential is reached, the particles are dragged by electro-osmosis for a fraction of time and the motion is dominated by electrophoresis thereafter. It was also found that the velocity and mobility increased with the applied field. The mobility estimated for CAF at the peak velocity under potential different magnitudes of 0.5, 1, 2, and 5 kV were respectively -1.5, -2.5, -1.5, and -2.1 $m^2V^{-1}s^{-1}$. The estimate values show that the mobility is not proportional to the electric field strength. However, valid scientific conclusions regarding the relative influence of the field are difficult to form due to the large error in the measurements. The mobility is significantly larger compared to that measured in the zetaPALS equipment, which may be the result of counter ions being pulled from the electrical double layer surrounded the solid phase by a strong electric field. At elevated potentials the electric double layer may be completely stripped off from the solid, which then behaves as a charged particle. Thus, the velocity considerably increases in strong electric fields.[55,61] In this case, the zeta-potential cannot be calculated due to absence of an electrical double layer.

The formation of an electrical double layer explains the motion of the suspended particles towards a specific electrode. However, if the particles move only by electrophoresis, we would expect a direct migration towards the electrode, i.e. the shortest route available. Apparently, due to dielectrophoresis they get a significant tangential velocity component next to a radial velocity component due to electrophoresis, that might explain the observed phenomenon under an inhomogeneous electric field. Thus, we conclude that the overall motion may well be the result of the combined effects of dielectrophoresis and electrophoresis phenomena.

An interesting and distinctly different behaviour in a uniform electric field was observed for NA suspensions. Under strong electric fields, the suspension behaves as an electrorheological fluid. Particle chaining occurs when the induced dipole on the solid phase is significant to induce dipolar interaction between neighbouring particles. Thus, a larger polarizability of NA compared to CAF and Phenylalanine compounds may explain the dissimilar behaviour under uniform electric fields. At elevated potentials, electrode charge exchange is intensified and electrophoretic forces dictate the unpredictable inter-electrode motion of the particles. When the parallel plate electrodes of the electrophoresis cell were exchanged by rod shaped electrodes, the NA crystals migrated and accumulated on the negative electrode as seen during the non-uniform field experiments. The findings from this study reveal that electrophoresis and dielectrophoresis forces act on crystalline particles suspended in non-polar solvents. In a non-uniform electric field, a different number of compounds in dioxane, toluene, and CPME collect either on the anode or cathode. While some organic compounds, such as CAF and Phe presented the same behaviour under uniform and non-uniform electric fields, other compound (NA) may have dissimilar behaviours. Thus, the combined action of electrophoresis and dielectrophoresis rather than the single action of electrophoretic forces could be potentially exploited for the separation of particular systems following the strategy described by Li et al.[9]

4.5. Conclusions

Crystalline compounds suspended in non-polar solvents were studied in the presence of non-uniform and uniform DC electric fields. A number of single organic compound, including polymorphic forms of the same compounds, chiral compounds, and multi-component crystals such as co-crystals and racemic compounds were studied under strong inhomogeneous electric fields. Upon the generation of the electric field, the particles collect at a specific electrode. As different compounds collect at different electrodes, the separation of a complex mixture of crystalline phases in a non-polar solvent may be realized by the use of electric fields.

The use of non-polar solvent minimizes the generation of electric current in the system that may induce chemical reaction and the degradation of the solute. A strong electric field imposed in pure non-polar solvents creates a gentle swirl flow motion that may be associated to induced electro-osmotic flow. This flow is considered minor on the effects of suspended crystals in the presence of the field. The main forces acting on the particle surface were dielectrophoresis and electrophoresis. The suspended crystals showed tangential velocity to the electrodes, which may suggest the presence of dielectrophoretic forces. The electric field geometry causes a field gradient within the electric cell, inducing dielectrophoresis. The specific collection of the particles on one of the electrodes suggest the presence of a net charge on the solid phase, and therefore the attraction of the crystals towards the electrode of opposite charge by electrophoresis. The zeta-potential of the suspended particles was measured by a PALS analysis, and confirmed the observed behaviour. The charging mechanism seems to be associated with the acid character of the solid phase compared to that of the solvent. The presence of residual water in the non-polar solvents may enhance the proton donor and acceptor interactions in the non-aqueous systems.

4.6. References

1. Van Gerven, T. & Stankiewicz, A. Structure, energy, synergy, time-the fundamentals of process intensification. *Ind. Eng. Chem. Res.* **48**, 2465–2474 (2009).
2. Ter Horst, J. H., Schmidt, C. & Ulrich, J. *Fundamentals of Industrial Crystallization. Handbook of Crystal Growth: Bulk Crystal Growth: Second Edition* **2**, (Elsevier B.V., 2014).
3. Pohl, P., Bielawska-Pohl, A., Dzimitrowicz, A., Jamroz, P. & Welna, M. Impact and practicability of recently introduced requirements on elemental impurities. *TrAC - Trends Anal. Chem.* **101**, 43–55 (2018).
4. Gutmann, B., Cantillo, D. & Kappe, C. O. Continuous-flow technology - A tool for the safe manufacturing of active pharmaceutical ingredients. *Angew. Chemie - Int. Ed.* **54**, 6688–6728 (2015).
5. Urwin, S. J. *et al.* A Structured Approach To Cope with Impurities during Industrial Crystallization Development. *Org. Process Res. Dev.* **24**, 1443–1456 (2020).
6. (U.S.), N. R. C. *Separation & Purification: Critical Needs and Opportunities*. (1987).
7. Maggio, R. M., Calvo, N. L., Vignaduzzo, S. E. & Kaufman, T. S. Pharmaceutical impurities and degradation products: Uses and applications of NMR techniques. *J. Pharm. Biomed. Anal.* **101**, 102–122 (2014).

8. Moynihan, H. A. & Horgan, D. E. Impurity Occurrence and Removal in Crystalline Products from Process Reactions. *Org. Process Res. Dev.* **21**, 689–704 (2017).

9. Li, W. W., Radacsi, N., Kramer, H. J. M., van der Heijden, A. E. D. M. & ter Horst, J. H. Solid Separation from a Mixed Suspension through Electric-Field-Enhanced Crystallization. *Angew. Chemie Int. Ed.* 1–5 (2016).

10. Shaaban, S. & Abdel-Wahab, B. F. Groebke-Blackburn-Bienayme multicomponent reaction: emerging chemistry for drug discovery. *Mol. Divers.* **20**, 233–254 (2016).

11. Atkinson, M. B. J. *et al.* Using magnetic levitation to separate mixtures of crystal polymorphs. *Angew. Chemie - Int. Ed.* **52**, 10208–10211 (2013).

12. Wen, C. *et al.* Advances in ultrasound assisted extraction of bioactive compounds from cash crops – A review. *Ultrason. Sonochem.* **48**, 538–549 (2018).

13. Wang, J., Li, F. & Lakerveld, R. Process intensification for pharmaceutical crystallization. *Chem. Eng. Process. - Process Intensif.* **127**, 111–126 (2018).

14. Sekhon, B. An overview of capillary electrophoresis: pharmaceutical, biopharmaceutical and biotechnology applications. *J. Pharm. Educ. Res.* **2**, (2011).

15. Ptasinski, K. J. & Kerkhof, P. J. A. M. Electric Field Driven Separations: Phenomena and Applications. *Sep. Sci. Technol.* **27**, 995–1021 (1992).

16. Delgado, A. V., González-Caballero, F., Hunter, R. J., Koopal, L. K. & Lyklema, J. Measurement and interpretation of electrokinetic phenomena. *J. Colloid Interface Sci.* **309**, 194–224 (2007).

17. Seader, D. & Henley, E. J. *Separation process principles. John Wiley & Sons, Inc.* (2006).

18. Romero-Creel, M. F., Goodrich, E., Polniak, D. V. & Lapizco-Encinas, B. H. Assessment of sub-micron particles by exploiting charge differences with dielectrophoresis. *Micromachines* **8**, (2017).

19. Voeten, R. L. C., Ventouri, I. K., Haselberg, R. & Somsen, G. W. Capillary Electrophoresis: Trends and Recent Advances. *Anal. Chem.* **90**, 1464–1481 (2018).

20. El Deeb, S., Wätzig, H., Abd El-Hady, D., Sänger-van de Griend, C. & Scriba, G. K. E. Recent advances in capillary electrophoretic migration techniques for pharmaceutical analysis (2013–2015). *Electrophoresis* **37**, 1591–1608 (2016).

21. Hughes, M. P. *Nanoelectromechanics in Engineering and Biology.* (CRC Press, 2002).

22. Kim, D., Sonker, M. & Ros, A. Dielectrophoresis: From Molecular to Micrometer-Scale Analytes. *Anal. Chem.* **91**, 277–295 (2019).

23. Pysher, M. D. & Hayes, M. A. Electrophoretic and dielectrophoretic field gradient technique for separating bioparticles. *Anal. Chem.* **79**, 4552–4557 (2007).

24. Jiang, S., Jansens, P. J. & Ter Horst, J. H. Control over polymorph formation of o-aminobenzoic acid. *Cryst. Growth Des.* **10**, 2541–2547 (2010).

25. Svärd, M., Nordström, F. L., Jasnobulka, T. & Rasmuson, Å. C. Thermodynamics and nucleation kinetics of m-aminobenzoic acid polymorphs. *Cryst. Growth Des.* **10**, 195–204 (2010).

26. Gracin, S. & Fischer, A. Redetermination of the beta polymorph of p-amino-benzoic acid. *Acta Crystallogr. Sect. E* **E61**, 1242–1244 (2005).

27. Kulkarni, S. A., McGarrity, E. S., Meekes, H. & Ter Horst, J. H. Isonicotinamide self-association: The link between solvent and polymorph nucleation. *Chem. Commun.* **48**, 4983–4985 (2012).

28. Ter Horst, J. H., Deij, M. A. & Cains, P. W. Discovering New Co-Crystals. *Cryst. Growth Des.* **9**, 1531–1537 (2009).

29. Hao, T. *Electrorheological Fluids: The Non-aqueous Suspensions.* (Elsevier B.V., 2005).

30. Kamali, N., Gniado, K., McArdle, P. & Erxleben, A. Application of Ball Milling for Highly Selective Mechanochemical Polymorph Transformations. *Org. Process Res. Dev.* **22**, 796–802 (2018).

31. Thielicke, W. & Stamhuis, E. J. PIVlab – Towards User-friendly, Affordable and Accurate Digital Particle Image Velocimetry in MATLAB. *J. Open Res. Softw.* **2**, (2014).

32. Lyklema, J. Principles of the stability of lyophobic colloidal dispersions in non-aqueous media. *Adv. Colloid Interface Sci.* **2**, 67–114 (1968).

33. Chang, F.-M., Chang, T.-W., Sheng, Y.-J. & Tsao, H.-K. Size-dependent electro-osmosis in a microchannel with low-permittivity , salt- free media. *Appl. Phys. Lett.* **97**, (2010).

34. Dukhin, A. S. & Goetz, P. J. How non-ionic "' electrically neutral "' surfactants enhance electrical conductivity and ion stability in non-polar liquids. **588**, 44–50 (2006).

35. Smallwood, I. M. Handbook of Organic Solvent Properties. *Butterworth-Heinemann* 332 (1996).

36. Watanabe, K., Yamagiwa, N. & Torisawa, Y. Cyclopentyl Methyl Ether as a New and Alternative Process Solvent. *Org. Process Res. Dev.* **11**, 251–258 (2007).

37. Rana, V. A., Chaube, H. & Gadani, D. H. Dielectric permittivity , density , viscosity and refractive index of binary mixtures of anisole with methanol and 1-propanol at different temperatures. *J. Mol. Liq.* **164**, 191–196 (2011).

38. Kingsbury, C., Christopher J. Commons, C. J., Sanchez-Arlt, R. W., Abrahams, B. F. & Robson, R. CCDC 1557139: Experimental Crystal Structure Determination. *CSD Commun.* (2017).

39. Brown, C. J. The Crystal Structure of Anthranilic Acid. *Proc. R. Soc. A* 185–199 (1968).

40. Boone, C. D. G., Derissen, J. L. & Schoone, J. C. Anthranilic acid II (o-aminobenzoic acid). *Acta Crystallogr. Sect. B* **33**, (1977).

41. Hardy, G. E., Kaska, W. C., Chandra, B. P. & Zink, J. I. Triboluminescence-Structure Relationships in Polymorphs of Hexaphenylcarbodiphosphorane and Anthranilic Acid, Molecular Crystals, and Salts. *J. Am. Chem. Soc.* **103**, 1074–1079 (1981).

42. Voogd, J., Verzijl, B. H. M. & Duisenberg, A. J. M. m-Aminobenzoic acid. *Acta Crystallogr. Sect. B* **36**, (1980).

43. Williams, P. A., Hughes, C. E., Lim, G. K., Kariuki, B. M. & Harris, K. D. M. Discovery of a new system exhibiting abundant polymorphism: M -aminobenzoic acid. *Cryst. Growth Des.* **12**, 3104–3113 (2012).

44. Lai, T. F. & Marsh, R. E. The crystal structure of p-aminobenzoic acid. *Acta Crystallogr.* **22**, (1967).

45. Alleaume, M. & Salas-Cimingo, G. p-Aminobenzoic acid. *Comptes Rendus Seances l'Academie des Sci. Ser. C* **262**, (1966).

46. Aakeröy, C. B., Beatty, A. M., Helfrich, B. A. & Nieuwenhuyzen, M. Do polymorphic compounds make good cocrystallizing agents? A structural case study that demonstrates the importance of synthon flexibility. *Cryst. Growth Des.* **3**, 159–165 (2003).

47. Li, J., Bournea, S. A. & Caira, M. R. New polymorphs of isonicotinamide and nicotinamide. *Chem. Commun.* **47**, 1530–1532 (2011).

48. Grothe, E., Meekes, H., Vlieg, E., Ter Horst, J. H. & De Gelder, R. Solvates, Salts, and Cocrystals: A Proposal for a Feasible Classification System. *Cryst. Growth Des.* **16**, 3237–3243 (2016).

49. Báthori, N. B., Lemmerer, A., Venter, G. A., Bourne, S. A. & Caira, M. R. Pharmaceutical Co-crystals with isonicotinamide-vitamin B3, clofibric acid, and diclofenac-and two isonicotinamide hydrates. *Cryst. Growth Des.* **11**, 75–87 (2011).

50. Ter Horst, J. H. & Cains, P. W. Co-crystal polymorphs from a solvent-mediated transformation. *Cryst. Growth Des.* **8**, 2537–2542 (2008).

51. Vishweshwar, P., Nangia, A. & Lynch, V. M. Supramolecular synthons in phenol–isonicotinamide adducts. *Cryst. Eng. Comm.* **5**, 164–168 (2003).

52. Srisanga, S. & Ter Horst, J. H. Racemic compound, conglomerate, or solid solution: Phase diagram screening of chiral compounds. *Cryst. Growth Des.* **10**, 1808–1812 (2010).

53. Vissers, T., Imhof, A., Carrique, F., Delgado, Á. V. & van Blaaderen, A. Electrophoresis of concentrated colloidal dispersions in low-polar solvents. *J. Colloid Interface Sci.* **361**, 443–455 (2011).

54. Espin, M. J., Delgado, A. V & Rejon, L. Electrorheologial properties of hematite/silicone oil suspensions under DC fields. *J. Non-Newtonian Fluid Mech.* **125**, 1–10 (2005).

55. Schreuer, C., Vandewiele, S., Strubbe, F., Neyts, K. & Beunis, F. Electric field induced charging of colloidal particles in a nonpolar liquid. *J. Colloid Interface Sci.* **515**, 248–254 (2018).

56. Halsey, T. C. Electrorheological Fluids. *Science (80-.).* **258**, 761–766 (1992).

57. Xuan, X. Recent advances in direct current electrokinetic manipulation of particles for microfluidic applications. *Electrophoresis* **40**, 2484–2513 (2019).

58. Ohshima, H. & Furusawa, K. *Electrical Phenomena at Interfaces: Fundamentals: Measurements, and Applications.* (Marcel Dekker, Inc., 1998).

59. Roberts, G. S., Wood, T. A., Frith, W. J. & Bartlett, P. Direct measurement of the effective charge in nonpolar suspensions by optical tracking of single particles. *J. Chem. Phys.* **126**, (2007).

60. Gacek, M. M. & Berg, J. C. The role of acid – base effects on particle charging in apolar media. *Adv. Colloid Interface Sci.* **220**, 108–123 (2015).

61. Hsu, C. Electrophoretic mobility measurement in low dielectric constant medium. (1987).

62. Kitahara, A. Zeta potential in nonaqueous media and its effect on dispersion stability. *Prog. Org. Coatings* **2**, 81–98 (1973).

Chapter 5. Enhanced Nucleation of Isonicotinamide under Strong non-Uniform DC Electric Fields

Abstract

The effects of a strong non-uniform electric field have been studied in the crystallisation of isonicotinamide in 1,4-dioxane. Cooling crystallisation of isonicotinamide solutions in the presence of an electric field with a strength of 4.15 x 10^6 V/m, induces nucleation at lower supersaturations compared to untreated solutions for the same solution composition, with increasing recovery obtained in when a field is applied to the metastable solutions. Isonicotinamide preferentially nucleates on the surface of the anode in the presence of the field, crystals are generally formed on the opposite electrode with a delay with respect to the crystal formation on the anode. In addition, isonicotinamide solutions saturated at 35 °C and lower temperatures, only presented crystals during cooling in the presence of the electric field. Induction time measurements of metastable solutions in the presence and absence of the electric field reveal an enhanced effect of the external field. Nucleation probability increases with the strength of the applied potential. This effect is more relevant in solutions with superaturation ratios below 1.2, as then the nucleation in solutions in absence of electric field is close to zero. The enhancement effect might be explained by the increase of the effective supersaturation generated in the near the surface of the electrodes caused by electrokinetic forces that arise in the presence of an electric field. This phenomenon may enhanced the nucleation parameters as a consequence of the local higher supersaturation. The preferential nucleation of isonicotinamide at the anode corroborates the presence of local regions of higher supersaturation near the electrode, and suggests that the use of electric fields enables spatial and temporal control over the crystallisation process.

5.1. Introduction

Crystallisation is a unit operation widely used in the pharmaceutical industry for the separation and purification of active pharmaceutical ingredients (APIs) and intermediate products. The quality of the crystalline product can be tailored during the crystallisation process, enabling formulations that must meet tight specifications before the product is launched to the market. Thus, control over crystallisation processes is perceived as an opportunity to optimise production of drugs with desire properties.[1–3] In the case of crystallisation from solution, there are three main crystallisation control technologies: process control,[4] the use of auxiliary phases,[5,6] and the implementation of external fields. External fields enable crystallisation control by acting on local conditions. This characteristic of the external fields has been exploited to better understand the thermodynamics and kinetics of the crystallisation process, as they provide a reliable method to locate and observe nuclei formation.[7] Different classes of external forces have been investigated for the control of the nucleation phenomenon, being the use of laser,[8,9] ultrasound,[10,11] magnetic fields, [12,13] microwaves,[14] and electric fields[15–17] the main energy sources.

An electric field is a carrier of energy which contribution to the Gibbs free energy of cluster formation may affect the nucleation thermodynamics and kinetics of a system in a metastable state.[18] Crystallisation under electric fields is a broadly researched topic, with practical use in diverse areas.[19–21] This type of external force has been amply studied in the biopharmaceutical field, where several publications reported significant acceleration of the nucleation process with lower number of crystals but of larger size formed,[22–25] improved crystal quality,[26,27] and spatial and temporal control[28,29] of protein crystallisation under direct and alternating current (DC and AC, respectively) electric fields. However, despite the wide research conducted on the application of this external force to crystallisation processes, the stochastic nature of nucleation and the delay in the detection of the first nucleus make its mechanistic effect on phase transformation unclear.[30]

Unlike the vast research on macromolecule solutions under electric fields, the study of the effects of this external force in crystallisation of small organic molecules is, to the best of our knowledge, scarce. Hu et al. [31] studied the effects of pulse electric fields of high magnitude to sucrose solutions. The electric field showed a reduction of induction times and improved crystal quality similar to the results reported in proteins, but the total nuclei number increased in sucrose systems. They relate this result to an acceleration effect on nucleation driven by the external force, and argued that this effect was proportional to the field magnitude. An additional investigation on sucrose conducted by Parniakov[16] corroborated the acceleration of crystallisation under strong electric fields, added that increasing the number of electric pulses applied to solution have a positive effect on nucleation rates. In both studies, the temperature increase and the apparition of bubbles after applying a strong potential into the sugar solution suggests the generation of Faradaic reactions that complicates the identification of the effects of the electrostatic field. However, despite an electric field nucleation enhancement was reported in sucrose, the mechanism under the positive effect of the field was overlooked. In a different study, Abel *et al.*[32] preferentially nucleated glycine γ under strong DC electric fields. They ascribed this preferential polymorphic nucleation to the orientation of the polar molecules with the electric field. Recently, Li et al.[33] published the in-situ separation of complex mixtures the combined action of the electric fields and cooling crystallisation. Although they reported that crystallisation occurs on the surface of the electrodes during the purification process, the manuscript is focussed on the separation of crystals rather than the effect of the field on the crystallisation.

We aim at establishing whether an inhomogeneous electric field influences the nucleation behaviour of a small non-polar organic molecule and to elucidate the mechanism through which the electric field may affect the crystallisation process. Internal DC electric fields of various magnitudes have been applied to induce crystallisation of isonicotinamide solutions in the metastable zone. The use of a dielectric solvent, 1,4-dioxane, permits the use of potentials up to 9 kV avoiding unwanted Faradaic reactions. From cloud point temperatures, induction times, and probability measurements in the presence and absence of an electric field, a quantitative analysis of nucleation kinetics was carried out.

5.2. Experimental Methods

Isonicotinamide (INA) ReagentPlus® (99%) and 1,4-dioxane anhydrous (99.8%) were purchased from Sigma-Aldrich (United Kindgom) and used as received. For all the experiments conducted under the same conditions, 50 mL stock solutions of the model compound saturated in the dielectric solvent at different temperatures were prepared in order to minimize concentration variations amongst samples. The solutions were stirred at a temperature (T^*) 10 °C above the saturation temperature for 5 h to ensure dissolution of the crystalline solute. Subsequently, samples of 6 mL were obtained by transferring the mixed solution to 8 mL glass vials. These samples were placed in a paraffin oil (Nujol light oil; Alfa Aesar, United Kingdom) bath set at T^* and left under stirring for a minimum of 8 h. Temperature and stirring control was achieved by a heat/stirring plate (ADS-HP-ST Asynt) connected to a thermocouple immersed in the oil bath.

5.2.1. Setup

The setup described in Chapter 4 was used in this study with some modification to allow simultaneous crystallisation experiments in the presence and absence of an electric field. All the experiments were conducted using direct current (DC) with a maximum potential applied of 9 kV, corresponding to an electric field magnitude ranging between 0 and $4.15\text{x}10^6$ V/m. The crystallisation process was continuously monitored using a Logitech B525 webcam. A schematic of the setup is presented in Figure 5.1.

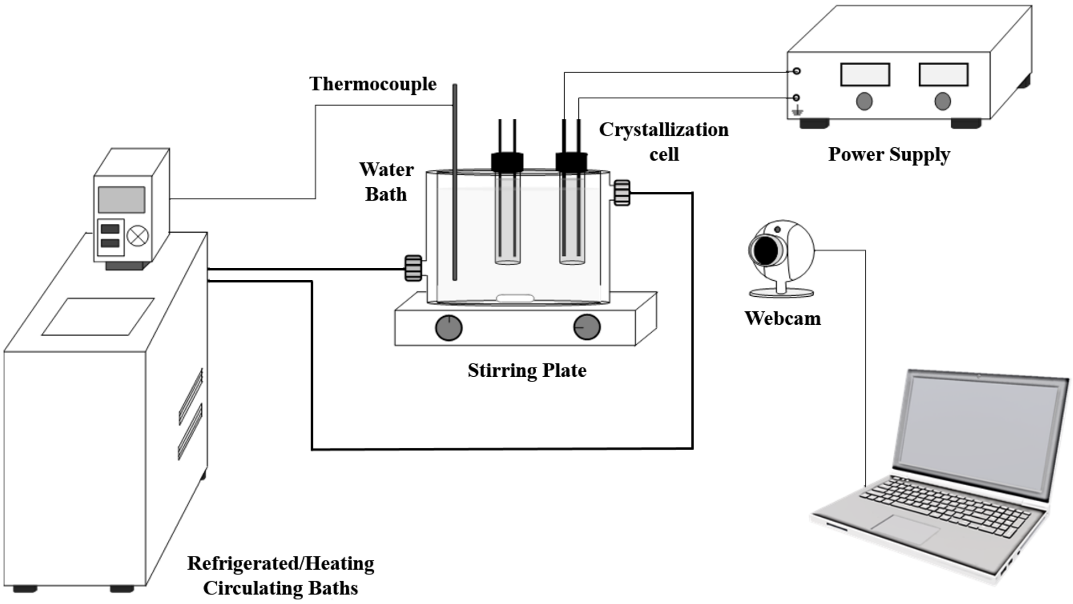

Figure 5.1. Schematic diagram of the experimental set-up used for the assessment of the effects of strong electric fields on crystallisation of isonicotinamide in 1,4-dioxane. The setup comprises a high voltage (HV) power supply, custom-made crystallisation cells, and a temperature control and monitor stations.

5.2.2. Field Distribution Simulations

Electric field and potential distributions inside the crystalliser were simulated using the AC/DC module of COMSOL Multiphysics version 5.4 by creating a 2D model representing a cross section of the crystalliser. The simplified model consisted in a circular outer wall of 16 mm diameter containing two copper electrodes of 1 mm diameter separated by 6 mm from the centre of each other. The maximum potential applied in the course of crystallisation experiments in the presence of an electric field was 9 kV. This value was defined as the boundary condition at the surface of one of the electrodes. The second electrode and the outer wall of the crystalliser were grounded (U = 0 V). The dielectric constant of the medium was set as 2.2, corresponding to that of 1,4-dioxane.[34]

Under static conditions,[35] the electric field vector ($\boldsymbol{E}$) is related to the electric potential scalar (U) by a gradient relationship:

$$\boldsymbol{E} = -\nabla U \tag{5.1}$$

Considering an isotropic dielectric medium, in which the permittivity (ε) is constant, the governing equation of the electric potential in COMSOL takes the form of the Laplace's equation[35,36]

$$-\nabla \cdot (\varepsilon_0 \varepsilon_m \nabla U) = 0 \tag{5.2}$$

where ε_m and ε_0 are the relative permittivity of the medium and the permittivity of the free space, respectively. After defining the cell geometry and the boundary conditions, COMSOL Multiphysics generated a mesh over 10^5 elements. By solving equations (5.1) and (5.2) and combining the results obtained for each mesh, the magnitude of the electric field can be obtained from the norm of the field distribution.

5.2.3. Electric Field Enhanced Cloud Point Temperatures

To study the effects of strong electric fields on crystallisation of INA in 1,4-dioxane, saturated solutions at a temperature ranging from 30 to 45 °C were prepared by dissolving known amounts of the model compound in the dielectric solvent. Cloud points were measured in the presence and absence of a DC electric field using 6 mL sample composition at various saturation temperatures T_s = 30, 32.5, 35, 40 and 45 °C. Two equilibrated samples were taken from the oil bath at T^* = T_s+10 °C, the stirrers were removed and the standard caps replaced by the solvent addition caps with the copper wires. The undersaturated samples were placed in a water bath set at the same temperature than the oil bath, and left for 30 min to establish the initial temperature T^* in solution. Immediately after the potential difference between the electrodes of one of the crystallisers was gradually increased to 9 kV and the solution temperature was reduced to 14 °C at a rate of 0.25 °C/min. The crystallisation process was monitored by a webcam. Times and temperatures of the detection of the first crystals on the electrodes and in the bulk were recorded for each isolated experiment. To avoid misinterpretation of the effects of the electric fields on crystallisation that may be caused by surface differences of the electrodes, the two sets of crystalline caps were interchanged in consecutive experiments. Figure 5.2.a shows the temperature and electric field profiles over the experimental period.

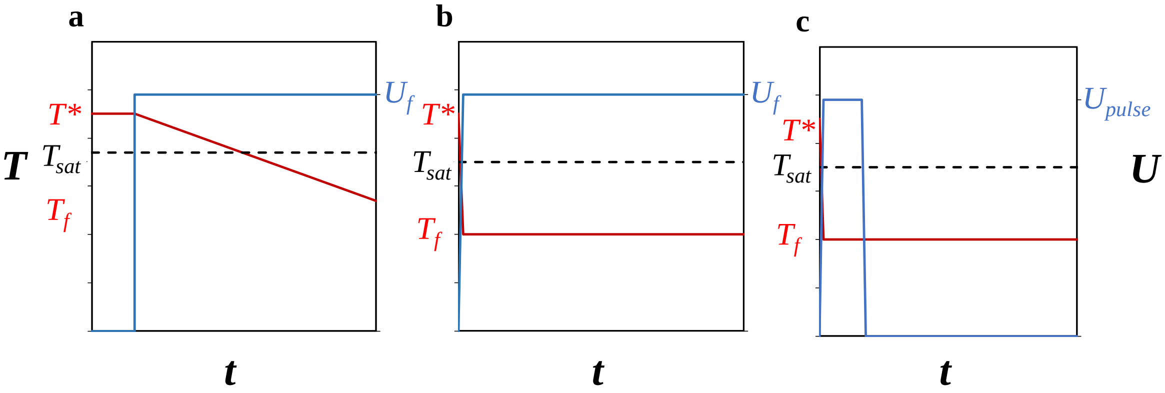

Figure 5.2. Schematic of the temperature (T) and DC potential (U) profiles as a function of time (t) applied during the investigation of effects of strong electric field on: **a.** cloud points, **b.** induction times, and **c.** nucleation probability. The initial temperature T^*, the final temperature T_f , and the potential applied and energy pulse potential (U_f and U_{pulse}, respectively) are represented in the figure. The blue line represents the potential profile, and the red line is the temperature. The dashed line depicts the saturation temperature T_{sat}.

Upon completion of the cooling crystallisation experiments, INA crystals collected on the surface of the electrodes were manually recovered with the help of a spatula. The suspension was filtrated to retrieved the material remaining in the bulk solution. All residues were placed in a desiccator under vacuum for drying. Following weight measurement of the dry product, the yield was calculated by:

$$y\,(\%) = \frac{m}{V(c - c^*)} \cdot 100 \tag{5.3}$$

where m (mg) is the mass of the recovered product, c and c^* are the overall concentration and the concentration at the final temperature in mg·mL^{-1} units, and V (mL) is the total volume.

5.2.4. Electric Field Enhanced Induction Times

The investigation of the effects of an electric field on induction times was conducted in 65 samples of supersaturation ratios raging from S = 1.2 to 1.35. INA solution samples saturated at 35 °C and equilibrated at T^* = 45 °C were subjected to temperature quenching to different final temperatures T_f = 27, 28, 29, and 30 °C. The combination of concentration and temperature resulted in supersaturation ratios S = 1.20, 1.25, 1.30, and 1.35 for these samples. Nucleation in absence and presence of an electric field with a magnitude of 4.15 MV/m were studied simultaneously for the entire range of supersaturation ratios. Following temperature quenching, each crystallisation experiment ran for 3 h at T_f, monitored with a Logitech B525 webcam. A schematic of the temperature and potential profiles used in induction time experiments is shown in Figure 5.2.b. Induction time and location of the first crystals appearing either on anode, cathode or bulk were recorded. The temperature was monitored using thermocouples connected to a TC-08 thermocouple data logger.

In a small number of experiments crystal formation occurred inside the PTFE sleeves. As this crystallisation in the presence of an electric field never preceded the formation of crystals on the electrodes, it was assumed that the effect of the electric field on crystallisation on the electrodes was unaffected by this.

5.2.5. Electric Pulse Energy Enhanced Nucleation Kinetics

INA solutions saturated at 35 °C were equilibrated at T= 45 °C to ensure clear solutions. These samples were quenched to different temperatures ranging from 29.5 to 31 °C in order to create supersaturation degrees S = 1.16, 1.2, or 1.23. Crystallisation studies at the same supersaturation ratio were carried out in samples subjected to an electrostatic pulse and an untreated sample simultaneously. A minimum number of 10 experiments were conducted for each supersaturation condition and applied potential. The pulse treatment was conducted using a single electric pulse energy of 5 or 9 kV imposed for 5 or 15 minutes. The experiments finalised after 3 h, after which experiments were checked to determine whether crystallisation occurred. Additional experiments were carried out by imposing electric pulse of 1.5 and 3 kV for 5 min. Temperature and potential profiles as a function of time are shown in Figure 5.2.c.

5.2.6. X-ray Powder Diffraction (XRPD)

Crystalline recovered samples were placed on a multi-well plate supported on a polyimide film, and placed in a Bruker D8 Discover diffractometer (GX002103 - Priscilla). The analysis was conducting using a monochromatic source radiation (Cu Kα1 λ = 1.54056 Å), and the data was collected at ambient temperature over a 2θ range of 3° to 40° at a scan rate of 0.015°/s.

5.3. Results

The temperature dependent solubility of INA in 1,4-dioxane shown in Figure 5.3 was measured in Chapter 3. The obtained data displays a typical solubility profile, in which the solubility of INA exponentially increases with increasing temperature. At 30 °C the solubility is 23.2 mg/mL. An increase of 20 °C roughly doubles the solubility of INA in the organic solvent, in agreement with Black's rule.[37] The variation of the clear point temperature for a sample is presented as the standard variation of the clear points obtained during the consecutive heating and cooling cycles. The deviation in the produced data is below ±1 °C for all the samples analysed, except for the clear points of sample composition 41.3 mg/mL with a deviation of ±1.1 °C. The fit to the experimental data permits the prediction of the saturation temperature for a given composition.

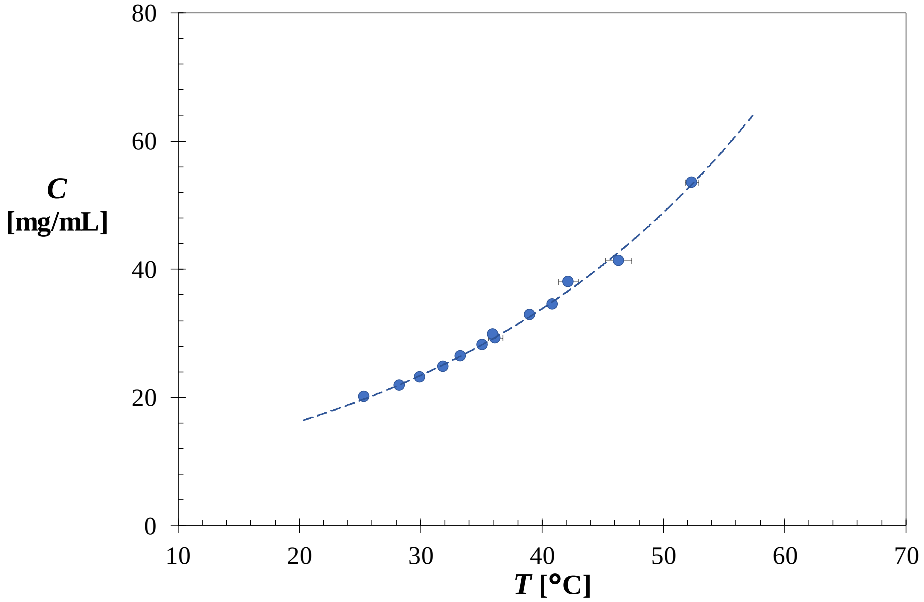

Figure 5.3. Temperature dependent solubility of INA in 1,4-dioxane. Each point represents the average of four clear point temperatures measured for the same sample concentration *C* (mg/mL) in a Crystal16 workstation. The blue line is the predicted solubility obtained from the fit of the experimental data.

5.3.1. Electric field simulation

Figure 5.4 shows a two-dimensional model of the crystalliser containing the two electrodes. The two rod-shaped copper electrodes are depicted as plane white discs of 1 mm diameter separated by 6 mm from each other. The outer circumference represents the inner wall of the crystalliser, which has a diameter of 16 mm. The electric field is simulated by imposing a potential DC difference of 9 kV between the electrodes.

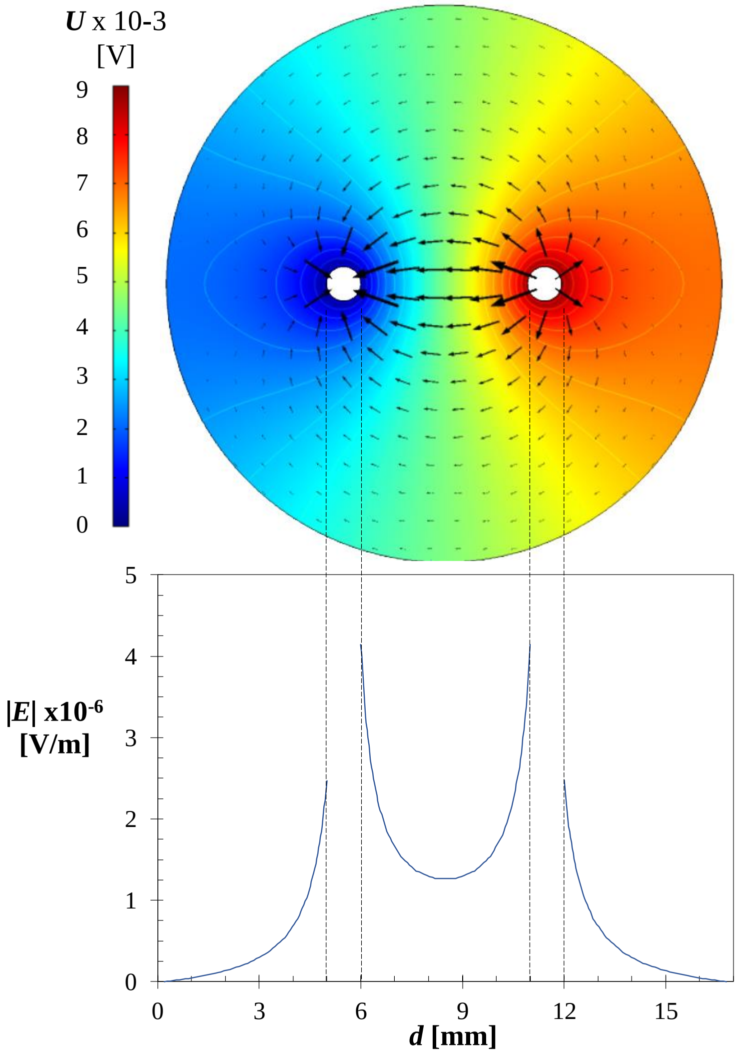

Figure 5.4. Two-dimensional model of a cross section of the crystalliser perpendicular to the electrodes that are contained in the cell. The surface contour represents the electric potential distribution when a potential difference of 9 kV is applied between the electrodes (anode and cathode are depicted as white discs situated at the right hand side and left hand within the cell model, respectively). The electric field vector is represented by black arrows which sizes are proportional to the field strength at that position. The magnitude of the electric field along a straight line crossing the crystalliser and intersecting both electrodes is shown in the bottom graph. The broken lines align with the electrodes (white discs) of the upper and bottom schemes.

The simulation exhibits regions of strong electric field in the vicinity of the electrodes, with a maximum electric field magnitude of 4.15 MV/m at the electrodes surface. The field strongly decreases with the distance from the electrodes, for instance obtaining a value of 1.26 MV/m in the centre of the crystalliser between the 2 electrodes. Regions of field strength minima are located near the inner wall of the vial, set as a boundary condition $U = 0$ V. The geometry of the crystallisation cell gives rise to field gradients that indicate the electric field is non-uniform.

5.3.2. Electric Field Enhanced Cloud Point Temperatures

Cloud point temperature measurements in the presence and absence of the electric field obtained from solutions saturated between 30 and 45 °C are presented in Figure 5.5. In absence of the electric field, crystals appear in the course of the spontaneous crystallisation experiments in samples saturated at 40 and 45 °C, which correspond to initial compositions of 33.8 and 40.6 mg/mL. Below sample composition of 33.8 mg/mL no crystals were detected, possibly due to an insufficient supersaturation degree to trigger nucleation. Heterogeneous nucleation seems to be promoted by the surface of the copper electrodes since the detection of crystals at the electrode precedes to that in the bulk. For instance, nucleation at the electrode occurred in one of the samples saturated at 40 °C, with a measured cloud point of 19 °C while crystals in the bulk were not observed even until the end of the cooling at 14 °C. INA solutions saturated at 45 °C produce crystals on the surface of the electrodes and in the bulk solution.

In the presence of an inhomogeneous electric field, INA crystals are generally detected at higher temperatures on the anode, followed by crystallisation on the cathode, and the detection of crystals in the bulk at the lowest temperature. In samples with concentrations of 28.2 mg/mL, crystals are generally first formed on the anode, with a maximum nucleation temperature measured at 26.8 °C. Crystals are then detected on the surface of the cathode, with nucleation temperatures ranging from 26 to 17 °C. Finally, nucleation occurs in the bulk with nucleation temperatures below 21.5 °C. Under an electric field created by a potential difference of 9kV, crystals were detected in experiments carried out in sample concentrations greater or equal to 25.7 mg/mL. At this sample concentration, crystals formed only at the anode upon reaching a temperature of 19.1 °C. No visible crystalline material was observed in INA solutions saturated at 30 °C, even with an electric field present.

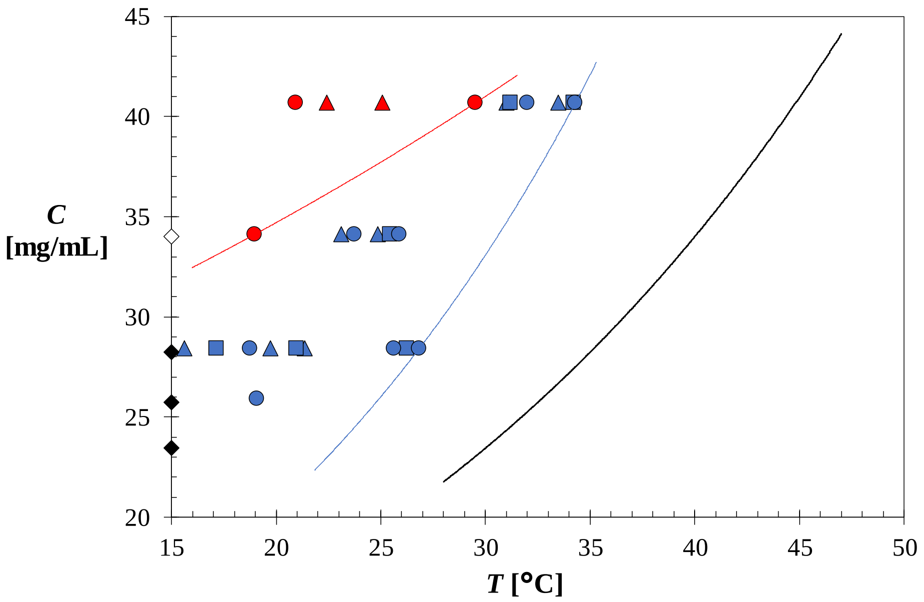

Figure 5.5. Cloud point temperatures of solutions of INA in 1,4-dioxane upon cooling in the presence and absence of an electrostatic field with a cooling rate of 0.25 °C/min. Cloud points were taken as the temperature at which the first crystal was detected by the eye. INA crystals formed at the electrodes (●) and in the bulk (▲) in the absence of an electric field. Under a potential of 9 kV crystals, crystals were detected at the anode (●), cathode (■), and in the bulk (▲). The blue and red lines are a guide to the eye for the highest cloud point temperatures measured in the absence (red) and presence (blue) of a strong electrostatic field. The black line represents the INA solubility. The symbol on the concentration-axis represents the absence of crystal detection when cooling until 14 °C during a cloud point temperature measurement experiment carried out in absence (◇) and presence (◆) of an electric field.

The cloud point temperatures are shifted towards higher values in the presence of the electric field. For instance, the first crystal observed in samples saturated at 45 °C under an electric field is 4.8 °C higher than that without electric field. This temperature difference increases to 6.9 °C with reference to nucleation in the absence of a field in samples saturated at 40 °C (34 mg/mL). These results indicate a strong impact of the electric field on crystal nucleation, which effect is more significant at low supersaturation. Figure 5.6 shows the effect of the electric field on cooling crystallisation of INA in dioxane for a sample composition of 28.1 mg/mL. In the presence of the field crystallisation occurred on both electrodes, while no visible crystals were detected during cooling in the absence of the electric field.

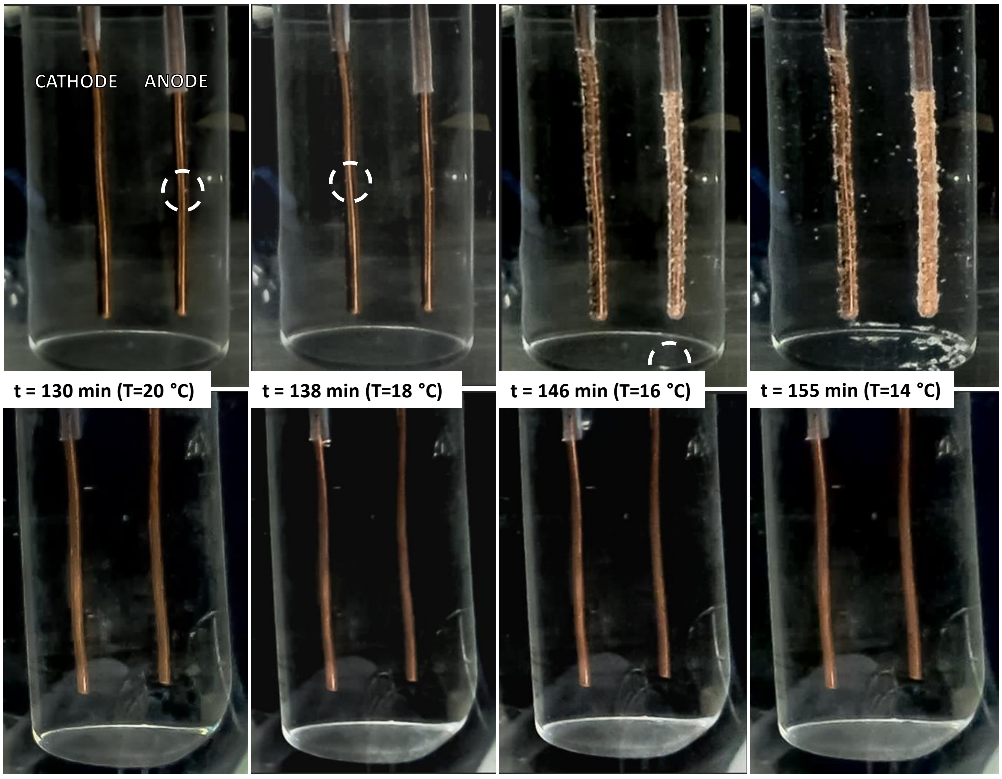

Figure 5.6. Evolution of the crystallisation process in an INA solution saturated at 35 °C in 1,4-dioxane during cooling crystallisation from 45 to 14 °C at a cooling rate of 0.25 °C/min in the presence (top images) and in absence (bottom images) of an electric field. INA crystals were first visible after 105 min on the surface of the anode, followed by crystals forming at the cathode and in the bulk at 112 and 118 minutes, respectively. No visible crystals were produced during cooling in the absence of the electric field.

Table 5.1 summaries the average value of the recovery yield. In the absence of an electric field, only samples saturated at 45 °C (41 mg/mL) produced enough crystals to determine the recovery yield. A comparison with electric field assisted crystallisation shows that the average recovery in the presence of the field is substantially higher. As the crystals form earlier on in the process and perhaps in larger numbers, the crystallisation process elapses for a longer time allowing for the solution to be depleted from a larger part of its supersaturation.

The XRPD patterns from the recovered crystals produced by cooling crystallisation of sample composition of 41 mg/mL are presented in Figure 5.7.a. The collected materials from the electrodes and bulk in untreated samples and from the anode and cathode in samples subjected to a strong non-uniform electric field show similar diffractograms. The XRPD data of the crystals from the anode was compared to the reference INA diffraction patterns compiled on the Cambridge Crystallographic Data Centre (CCDC), indicating the dominant presence of form III (Figure 5.7.b).

Table 5.1. Average values of the recovery yield of INA after cooling crystallisation in the presence and absence of a non-uniform electrostatic field generated upon applying a potential difference of 9 kV. In the presence of the field, enough material for recovery calculations was obtained from samples saturated at 35 °C and experiments conducted at higher saturation temperatures. Crystals were recovered from the anode and cathode, but no enough crystals were produced in the bulk for yield calculation. In the absence of the field, only crystallisation carried out on samples saturated at 45 °C produced enough crystals to estimate the recovery. The crystals in the absence of the field were recovered from the electrodes surface (no difference between anode or cathode as no electric field was applied) and from the bulk solution.

U **[kV]**	***c*** **[mg/mL]**	**Average recovery yield [%]**			
		Electrode		Bulk	Total
		Anode	Cathode		
0	28.2	0		0	0
	34.0	0		0	0
	41.0	7.07		28.2	35.3
9	28.2	40.1	4.03	1.40	45.5
	34.0	38.6	29.0	-	67.6
	41.0	45.3	27.8	-	73.1

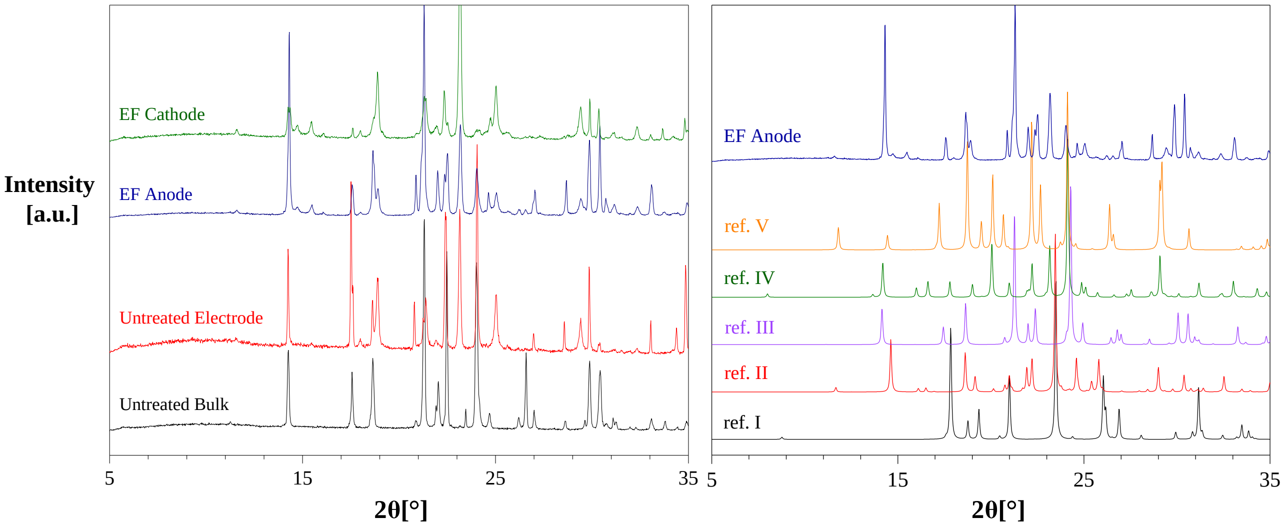

Figure 5.7. a: XRPD patterns of crystals recovered from the anode (9kV, Anode) and cathode (9kV, Cathode) upon completion of experiments assisted by an electric field, and patterns of bulk INA crystals produced in absence of an electric field (0kV, Bulk) and the surface of the copper electrodes (0kV, Electrode). All experiments were carried out on INA solutions saturated at 45 °C. **b:** Comparison of the diffraction spectra measured for the crystals produced on the anode in the presence of an electric field (EF Anode) to the referenced patterns of INA in the CCDC: INA (EHOWIH01),[38] INA II (EHOWIH02),[38] INA III (EHOWIH03),[39] INA IV (EHOWIH04),[40] and INA V (EHOWIH05) showing the dominant presence of form III.[40]

5.3.3. Electric Field Enhanced Induction Times

Induction times and localisation of the INA crystals measured in the presence and absence of a DC electric field are presented in Figure 5.8. In the absence of the electric field, induction time measurements show large variations in experiments with the same supersaturation ratio. For instance, crystallisation experiments performed at $S = 1.25$ show a variation in induction time from 1263 s to 9067 s in 12 experiments. The induction time variations between samples is typical for such measurements in small volumes.[41] In successful crystallisation experiments, nucleation preferentially occurs in the bulk solution and rarely took place on copper surface.

The effect of an electric field on induction time was studied under a potential difference of 9 kV. In 33 experiments carried out using supersaturated solutions of a supersaturation ratio ranging between 1.20 and 1.35, the induction time varies from 244 to 5894 s. The variation on the measurements demonstrates the stochastic nature of the nucleation process. The experimental data reflects a strong dependency of the induction time on supersaturation and the presence of the electric force. The observed localisation of crystallisation is analogous to the results obtained in the cloud points study. In the presence of an electric field, crystals were consistently first detected on the surface of the anode, followed by crystallisation at the cathode and in the bulk. The time difference between nucleation at the anode and in other regions of the crystalliser increases at lower supersaturations, which suggests that control over localisation of nucleation may be attained by the use of electric fields under suitable conditions.

A significant induction time difference was measured in the presence of electric field compared to untreated experiments, which was inversely proportional to the supersaturation ratio. The detection of the first crystals in solutions saturated at $S = 1.35$ is delayed by 407 s in spontaneous nucleation experiments with respect to crystallisation assisted by electric forces. When the experiments were carried out in solutions saturated at $S = 1.2$, the induction time difference was greater than 3000 s. Additionally, all supersaturated solution with S = 1.30 crystallise in the presence of the electric field, while 5 out of 9 experiments showed crystals under the same saturation conditions in untreated experiments. O. Parniakov *et al.*[16] reported a negligible reduction of the induction time of sucrose crystallisation after imposing an electric field. They related the absence of significant electric field effects to a reduction of the local supersaturation as a result of the elevation of temperature caused by the flow of an electric current through a conductive media. In this study, the Joule heating was neglected since the current was limited below 2 μA by the use of a highly insulating solvent.[42]

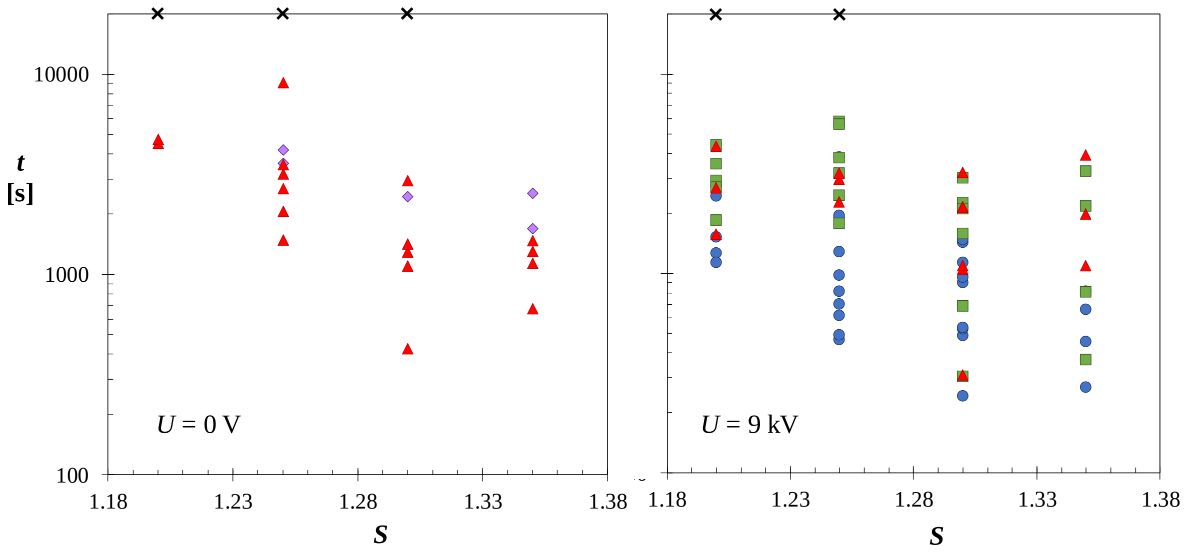

Figure 5.8. Induction time measurements of INA in 1,4-dioxane at supersaturation ratios S = 1.2, 1.25, 1.3, and 1.35 (generated by quenching a solution composition of 28.2 mg/mL initially at 45 °C to temperatures T_f = 27, 28, 29 and 30 °C) in the absence (U = 0 V) and in the presence of a strong non-uniform electric field created by a potential difference U = 9 kV. In untreated experiments, crystals were detected in the bulk solution and on the electrode surface, ▲ and ◆ respectively. During the course of electric field experiments, crystals were detected in the bulk ▲, in the surface of the anode ● and on the surface of the cathode ■. The **X** symbol denotes experiments in which no crystals were produced within 3 h.

A comparison of the experimentally obtained induction times at the electrodes (in the absence of an electric field) and at the anode (under a potential of 9 kV) indicates that the difference observed on nucleation is consequence of the externally applied field rather than the effect of a heterogeneous element (copper surface). Even after accounting for the large variation on the induction times, it can be concluded that the presence of the field accelerates the nucleation process. The results of nucleation rate study conducted for the nucleation on the surface of electrodes are presented in Figure 5.9.

Nucleation can be considered a random process in which the probability of nucleus formation in an isolated experiment is independent of other experiments performed under equal conditions. Thus, the probability $P(t)$ to measure an induction time less than or equal to t is given by

$$P(t) = \frac{M^{+}(t)}{M} \tag{5.4}$$

where $M^{+}(t)$ is the number of successful crystallisation experiments at time t and M is the total number of experiments conducted at equal supersaturation, volume and temperature conditions. To determine the effect of the electric field on nucleation, the probability distribution of crystallisation on the anode, where nucleation is generally first detected under an inhomogeneous electric field, is compared with the first crystallisation events in the absence of an electric field. The probability distributions data is shown in Figure 5.10. Under the same volume and temperature conditions, the probability distribution $P(t)$ approaches to one in a shorter time at higher supersaturation ratios. This trend is more pronounced in the presence of an electric field, indicating an acceleration of the nucleation rates with respect to spontaneous nucleation. For instance, the probability of an induction time $t \leq 5000$ s is 42% for samples saturated at $S = 1.25$, while in the presence of the field under equal conditions the nucleation probability is 83%.

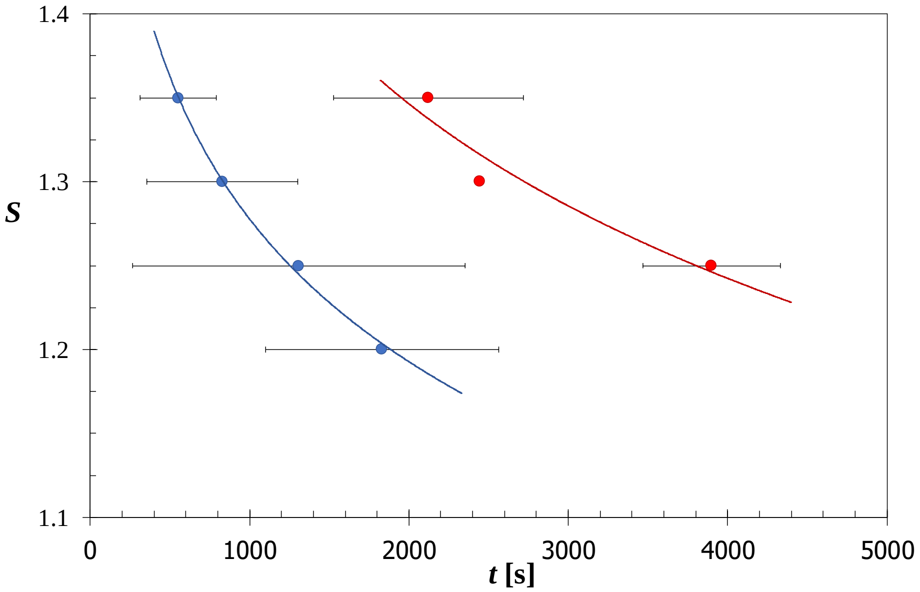

Figure 5.9. Induction time on the surface of the copper electrodes dependent supersaturation. The nucleation time was significantly reduced under a potential difference of 9kV (blue) compared to spontaneous nucleation (red). As expected, induction times exhibit a large variation in the presence and absence of the electric field due to the stochastic nature of nucleation, but still the effect of the electric field is apparent.

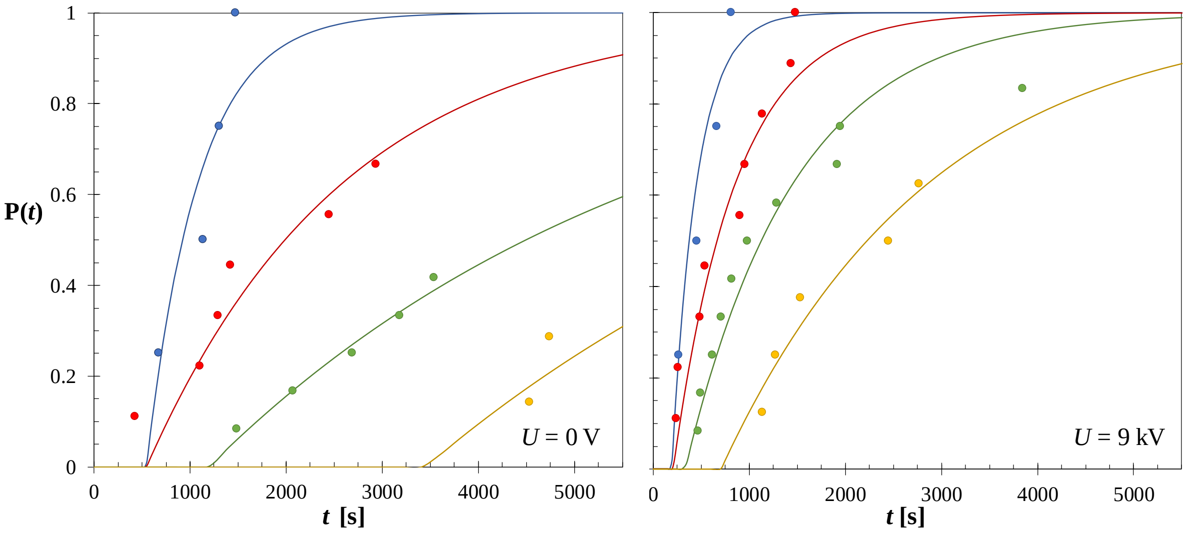

Figure 5.10. Probability distribution of the induction time data obtained from solutions of INA in 1,4-dioxane for spontaneous nucleation and under a potential difference of 9 kV at various supersaturation ratios. Supersaturation was generated by decreasing the temperature from 45 °C to 27 °C (S = 1.35), 28 °C (S = 1.30), 29 °C (S = 1.25), and 30 °C (S = 1.20). The solid lines represent the fit curves estimated by fitting the parameters t_g and J to the experimental data.

The experimental probability distribution can be fitted to the cumulative distribution function proposed by S. Jiang and J. H. ter Horst[41] to derive kinetic information of the nucleation process:

$$P(t) = 1 - \exp\left(-JV\left(t - t_g\right)\right) \tag{5.5}$$

According to equation (5.5), the cumulative probability of detecting a crystal in an interval between 0 and t, is a function of the sample volume V, nucleation rate J, and growth time t_g, which accounts for the delay in the detection of the nucleus. Thus, nucleation rates J and growth times t_g can be estimated from the fitting to the experimentally determined probability distribution. The estimated parameters are listed in Table 5.2.

S. Jiang et al.[41] suggested that a total number of 80 induction times per experimental condition is sufficient to determine the nucleation rate with 80% accuracy. Unfortunately, it was not possible to carry out the proposed number of isolated experiments due to the lengthy and non-automated procedure followed in this study. Despite the smaller number of experiments, the estimated nucleation rates J and growth times t_g suggest that apart from the clear effect of supersaturation, a positive effect on the kinetics of the phase transition occurs in the presence of the electric field.

Table 5.2. Nucleation rate J and growth time t_g determined from the fit of the probability distribution of induction times measured in the absence (U = 0 V) and presence of an electric field (U = 9 kV) by the cumulative distribution function described by equation (5.5). The parameters were estimated using Matlab R2018a.

U [kV]	S	J [m^{-3}s^{-1}]	ΔJ [m^{-3}s^{-1}]	t_g [s]	Δt_g [s]
0	1.35	306	279	542	341
	1.30	80	23	542	231
	1.25	35	19	1189	891
	1.20	30	-	3444	-
9	1.35	633	374	194	92
	1.30	254	44	210	65
	1.25	146	24	335	78
	1.20	76	21	708	261

We obtained higher nucleation rates and lower growth times in crystallisation experiments assisted by a potential difference of 9 kV. The Classical Nucleation Theory (CNT) gives an expression for the stationary nucleation rate $J(S)$ as a function of the supersaturation ratio S:

$$J(S) = AS\exp\left(\frac{-B}{\ln^2 S}\right) \tag{5.6}$$

where, the thermodynamic parameter B contains information of the magnitude of the nucleation work, i.e. the energy barrier for nucleation, while the pre-exponential factor A accounts for the kinetics of the process. The linearization of equation (5.6) shown in Figure 5.11, allows for the characterisation of its main parameters.

$$ln\left(\frac{J}{S}\right) = ln(A) - \frac{B}{ln^2 S} \tag{5.7}$$

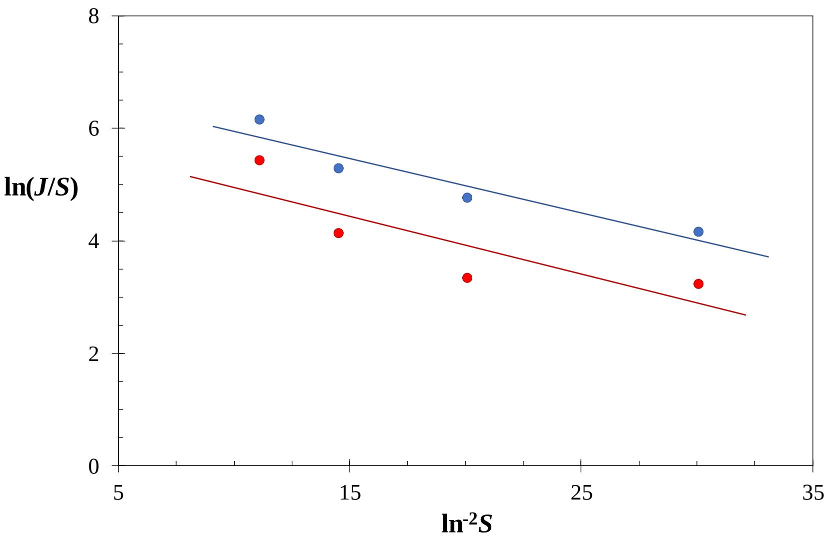

Figure 5.11. Experimental nucleation rate in absence and presence of an electric field generated by 9kV between the electrodes, plotted using equation (5.7). The solid lines represent the best fit in the presence (blue) and absence (red) of an electric field. The kinetic A and thermodynamic B parameters of the stationary nucleation rate can be obtained from the intercept and slope of the fit line.

Table 5.3 displays the estimated parameters from the best-fit straight line, which has slope B = 0.1 and an intercept ln$A$ = 6.0 for untreated experiments, and B and ln$A$ are respectively 0.1 and 6.9 in the presence of an electrostatic field. Although the calculated kinetic parameter shows a significant difference between untreated and electric field experiments, a large error was obtained for the calculation of A, that may indicate that the deviations between the two experiments is within the experimental error. In the same context, the exponential parameter B shows a larger energy barrier in the absence of the field compared to the value in the presence of an electric field. The relative error for this parameter suggest that the difference between the calculated values are not significant.

Table 5.3. Kinetic A and thermodynamic B parameters values determined from the linearization of the stationary nucleation rate. ΔA and ΔB refer to errors on estimated values.

U [kV]	A [m^{-3}s^{-1}]	ΔA [m^{-3}s^{-1}]	B [-]	ΔB [-]
0	391	375	0.10	0.05
9	1011	469	0.10	0.02

5.3.4. Effects of an electric pulse energy on nucleation kinetics

A second protocol was carried out to study the effect of electric fields of different magnitudes on nucleation rate. For this, INA solutions at various supersaturation levels were subjected to a single electric pulse energy ranging from 0 to 9 kV over either 5 or 15 min. The probability of nucleation due to a particular field pulse $P'(U)$ at a constant overall supersaturation (Figure 5.2c) was calculated from the fraction of successful crystallisation experiments assisted by the electric field corrected for the fraction of successful experiments in absence of the field:

$$P'(U) = \frac{P(U) - P(0)}{1 - P(0)} \tag{5.8}$$

where $P(U)$ and $P(0)$ are the probability of nucleation within 3 h after the application of an energy pulse U for the treated and untreated experiments, respectively. A minimum number of 10 spontaneous crystallisation experiments and 10 electric pulse crystallisations were carried out simultaneously using different supersaturation ratios, generated by quenching INA solutions saturated at 35 °C to temperatures ranging from 29.5 to 32 °C. For instance, a supersaturation degree S = 1.2 was obtained by decreasing the temperature of the INA solution to 30 °C. After applying an electric pulse of 5 kV to a supersaturated solution S = 1.2, 7 out of 12 experiments showed crystals, which gave a probability P (5 kV) = 0.58. In 10 experiments at the same supersaturation, P (9 kV) = 0.75. The overall nucleation probability at S = 1.2 for a total number of 20 experiments was P (0) = 0.25, which gives P'(5 kV) = 0.44 and P'(9 kV) = 0.67.

Figure 5.12 presents the enhanced effect on the nucleation probability upon applying an electrostatic pulse. The probability of detecting a crystal during the course of the experiments seems to increase with increasing the supersaturation ratio and the applied potential. The probability of nucleation at a supersaturation ratio S = 1.16 is $P'(U)$ = 0.31 and 0.54 upon applying a pulse of 5 and 9 kV, respectively. If we consider that a significant difference between experiments occurs when the P'(9 kV) > P'(5kV) + 1/N, where N is the number of experiments, nucleation is affected by increasing the electric field from 5 kV to 9 kV for S = 1.2 and 1.16. However, the probability of nucleation at S = 1.23 after applying an energy pulse of 5 and 9 kV were equal $P'(U)$ = 0.86, which indicates a potential threshold above which nucleation is not perceivable affected by increasing the energy input for the number of experiments conducted. In order to analyse this hypothesis, we carried out additional experiments decreasing the pulse time and applying pulses of potential values U = 1.5, 3, 5, and 9 kV. The proposed experiments presented the same *P'(U)* for electric pulses of 3 to 9 kV, however the probability dropped when the applied potential was 1.5 kV. These results reveal a steady increase of probability as a function of the applied voltage, reaching a *plateau* at 3 kV.

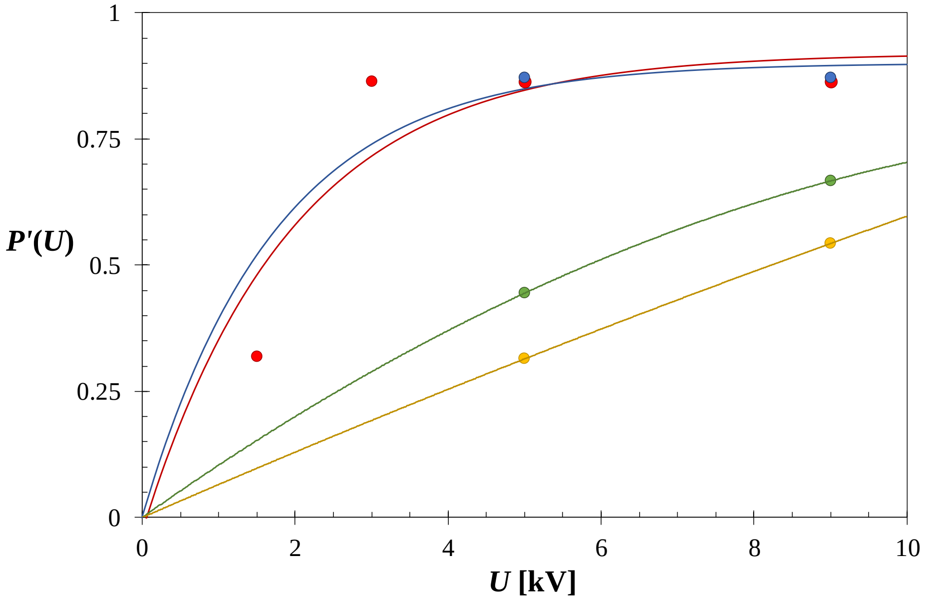

Figure 5.12. Enhancement of nucleation probability by the action of a strong DC electric field. The probability distributions of INA solutions at supersaturation ratios $S = 1.23$ (blue), 1.2 (green), and 1.16 (yellow) are presented for electric pulse magnitudes of 0, 5, and 9 kV applied over 15 min. Probability data from the analysis of a shorter pulse time (5 min) at 0, 1.5, 3, 5, and 9 kV applied to supersaturated solutions S = 1.23, is included (red) in the figure. The solid lines are a guide to the eye for the trend of the experimental data.

Assuming that nucleation occurs within the pulse time, the probabilities obtained at different supersaturation values and pulse energy inputs can be used to determine the nucleation rate using the following expression:

$$J = -\frac{ln\left(1 - P(U)\right)}{V\,\Delta t} \qquad \textbf{(5.9)}$$

Equation (5.9) was obtained by solving equation (5.5) for the nucleation rate *J*. Here Δt is the pulse time, *P(U)* is the probability of detecting a crystal within the course of the experiment at a given potential, and *V* is the sample volume. The growth time *tg* was removed as the pulse experiment takes a waiting time of 3 hours to let the nuclei formed in the pulse grow out to a detectable size. The estimated nucleation rates at different applied potentials are presented in Table 5.4. The large error calculated for the nucleation rate is probably related to an insufficient number of experiments carried out for each supersaturation under given experimental conditions.

Table 5.4. Determined stationary nucleation rate from equation (5.10) at various potentials and pulse times. The calculated rates are displayed alongside their associated error. The experiments with an asterisk were performed with an electric pulse of 5 instead of 15 minutes.

U [kV]	S	J [$m^{-3}s^{-1}$]	ΔJ [$m^{-3}s^{-1}$]
0	1.23*	172*	49*
	1.23	65	17
	1.20	53	24
	1.16	25	17
1.5	1.23*	385*	176*
3	1.23*	1279*	527*
5	1.23*	1279*	527*
	1.23	444	177
	1.20	162	63
	1.16	128	56
9	1.23*	1279*	527*
	1.23	444	177
	1.20	257	93
	1.16	170	72

Figure 5.13 shows the nucleation rates as a function of the applied electric pulse magnitude for different supersaturation ratios. An electric pulse energy of 5 and 9 kV applied for 15 minutes shows an enhanced effect on nucleation kinetics compared to untreated crystallisation experiments. The effect of increasing the potential magnitude is also noticeable at supersaturation ratios S = 1.16 and 1.20. However, this effect is not perceived at higher supersaturation values, indicating that stronger potential difference will not induce significant changes in the nucleation rate. Additional experiments were carried out using a shorter pulse time (5 minutes) to investigate a larger range of potential magnitudes and determine the potential at which the effect of increasing electric field on nucleation kinetics reaches the described *plateau*. According to equation (5.9), nucleation rate is inversely proportional to the pulse time, therefore INA solutions subjected to 5 min pulse time present higher nucleation rate J values at the same supersaturation. The nucleation rates indicate a clear effect of the electric pulse of 5 minutes on nucleation kinetics, with a maximum rate measured for electric pulses of 3, 5, and 9 kV.

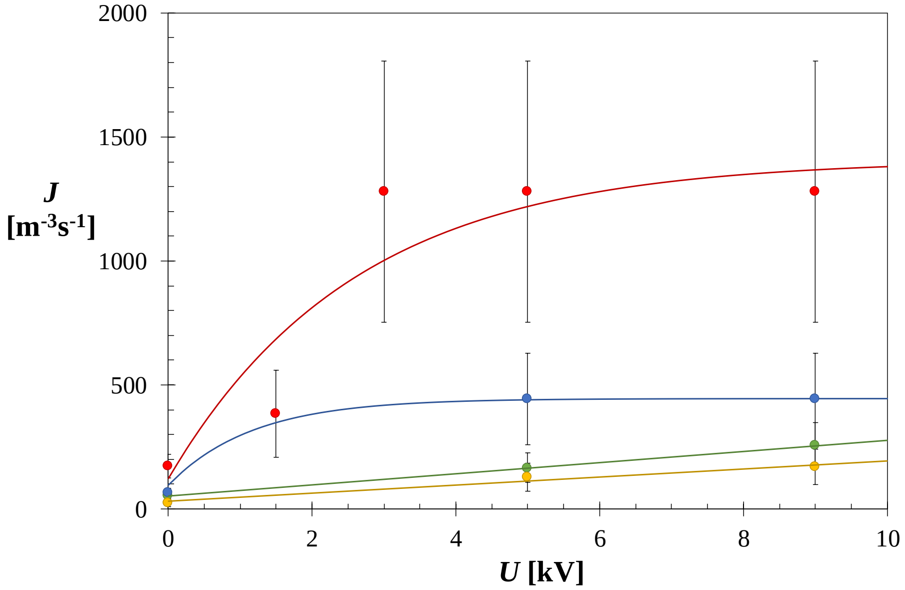

Figure 5.13. Nucleation rate at various potential pulses and pulse times determined from equation (5.9). Crystallisation trials were carried out in a series of INA solutions of different supersaturation ratios: *S* = 1.16 (yellow), *S* = 1.2 (green), and *S* = 1.23 (blue) in the absence of an electric field and after the application of an electric pulse of 5 and 9 kV for 15 min. Additionally, INA suspensions of *S* = 1.23 (red) were subjected to electric pulses of 1.5, 3, 5, and 9 kV sustained for 5 min. Solid lines are included in the figure as a guide to the eye for the trend of the estimated *J*.

Following nucleation rates determination, the thermodynamic *B* and kinetic *A* parameters of the stationary nucleation rate at different applied voltages were determined. Figure 5.14 shows that ln*(A)* (the intercept) is roughly 1.5 times greater in the presence of an electric field, but *B* (the slope) only shows minor variations up to 10%. It is difficult to assess the significance of these changes with just three data points, but the data suggests that nucleation is affected by the presence of the field.

The quantitative estimation of the thermodynamic and kinetic parameters are shown in Table 5.5. It seems that there is a significant dependence of *A* on *U* but maybe not of *B*, since the electric pulse energy significantly increases the A parameter while B is practically the same for untreated and electric field experiments.

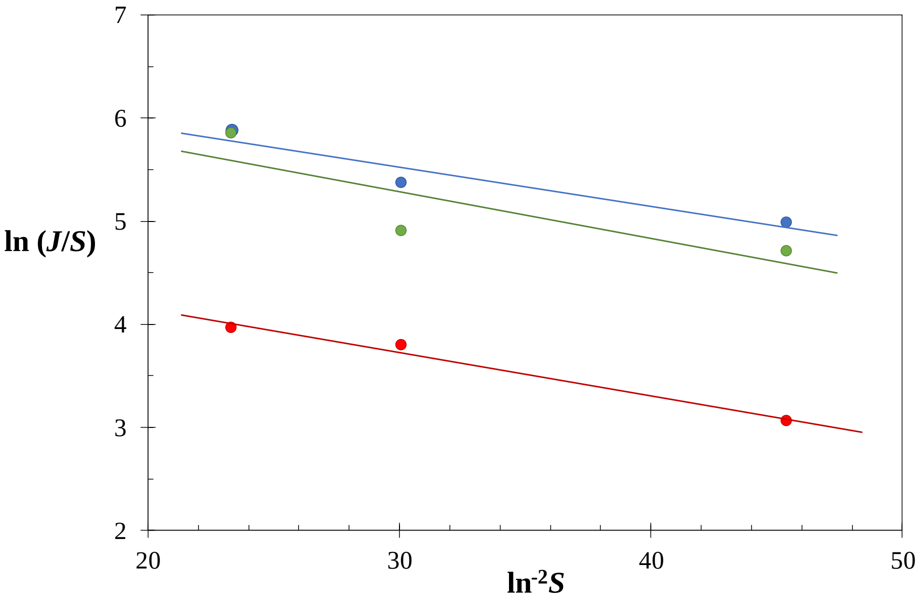

Figure 5.14. Linearization of the nucleation rates determined from the experimentally measured induction times of INA solutions at different supersaturation ratios and applied pulse energy. The linearization was conducted from the experiments subjected to electric pulses of 15 min duration and 0 V (red), 5 kV (green), and 9 kV (blue). The solid lines represent the best straight line fittings to data.

Table 5.5. The determined kinetic A and thermodynamic B parameters were obtained from the linearization of the nucleation rate from the CNT. The slope and the intercept of the best straight lines fittings of Figure 5.14 were used to calculate B and A, respectively. ΔA and ΔB refers to the error on the calculated parameters.

U [kV]	A [$m^{-3}s^{-1}$]	ΔA [$m^{-3}s^{-1}$]	B	ΔB
0	146	27	0.042	0.005
5	815	863	0.047	0.031
9	789	332	0.038	0.012

5.4. Discussion

Over the course of all the experiments aimed at assess the effects of electric fields on crystallisation, no current flow above the detection limits of the power supply (±2 μA) was observed. Thus, the occurrence of chemical reactions during the experimental period was discarded.

5.4.1. Nucleation enhancement and control of INA by a strong electrostatic field

The experimental determination of the effects of a strong DC electric field on the crystallisation of INA was conducted using an optical technique, thus a crystal has to grow to a considerable size in order to be detected, with the consequent delay and error in the measurements. Assuming that the same delay is applicable to all the experiments, a positive effect of the electric field on nucleation was elucidated from the performed experiments.

The application of an electric field to metastable solutions showed a shift in cloud points towards higher temperatures compared to spontaneous crystallisation experiments, with successful crystallisation of INA in dioxane occurring exclusively under an electric field in samples saturated at 32.5 and 35 °C during cooling from 45 to 14 °C. As more crystals are nucleating at low supersaturation ratios, the deposition rate is higher and recovery increases. In addition, a preferential nucleation of INA on the surface of the anode was observed in all crystallisation experiments under a strong non-uniform electric field. A maximum temperature difference between crystals detected at the anode and cathode of 1 °C occurred in samples saturated at 45 °C. The temperature difference increased for samples saturated at lower temperatures, with successful crystallisation experiments occurring exclusively at the anode surface in INA solutions saturated at 35 °C. Induction time measurements under an electrostatic field also presented a delay in the detection of crystals formed at the cathode with respect to the anode. This delay was inversely proportional to the supersaturation ratio. The preferential localisation and acceleration of INA nucleation on the surface of the anode under a strong non-uniform electric field may enable spatial and temporal control of the nucleation process, similar to the crystallisation control of proteins driven by electric fields reported by Hammadi and Veesler.[28]

Nucleation rates determined from probability distributions measured at different supersaturation levels, reflected an acceleration of the nucleation process due to the electric field. This phenomenon was directly proportional to the supersaturation ratio and field intensity. The nucleation probability measured using a pulse energy, increased with increasing applied potential until reaching a *plateau* at 3 kV at supersaturation $S = 1.23$. At lower supersaturation values, the probability of nucleation is higher at 9 kV compared to 5 kV pulse.

In a theoretical study of the thermodynamic effects of the electric field on nucleation, Kaschiev[18] showed that the electrostatic energy can be added to the chemical potential difference between the two phases, generating an effective driving force $\Delta\mu'$ given by the following equation:

$$\Delta\mu' = \Delta\mu + \frac{3\varepsilon_0\varepsilon_m(\varepsilon_c - \varepsilon_m)v_0}{2(\varepsilon_c + 2\varepsilon_m)}E^2 \tag{5.10}$$

here, v_0 refers to the molecular volume of the new phase, ε_c is the dielectric constant of the solid phase, and $\Delta\mu = k_BT\ln S$ is the driving force for nucleation. In agreement with Isard[43] and Warshavsky[44] studies, equation (5.10) predicts that a sufficiently strong electric field is able to increase ($\varepsilon_c > \varepsilon_m$), decrease ($\varepsilon_c < \varepsilon_m$), or have no effect ($\varepsilon_c = \varepsilon_m$) on the effective driving force in the nucleation process. The effective supersaturation parameter ($k_BT\ln S + c_\varepsilon E^2$) is translatable to the stationary rate equation and therefore, affects the nucleation rate:

$$J(S) = AS\exp\left(\frac{-B}{(k_BT\ln S + c_\varepsilon E^2)^2}\right) \tag{5.11}$$

The pre-exponential and/or the exponential factors may also be affected by the presence of the electric field, having an impact on the nucleation rate. For instance, from experimental data, the pre-exponential factor A seems to be affected by the presence of a strong electric field, accelerating nucleation kinetics

5.4.2. Nucleation mechanisms under electric fields

Induction time measurements enable the determination of crystallisation kinetics and thermodynamics data of the model compound. From the gained information, feasible mechanisms underlying the observed phenomena are discussed. On the basis of equation (5.6), the electric field may affect the supersaturation term S, the thermodynamic factor B, and/or the kinetic factor A. The evaluation of the different parameters was carried out by using the data obtained from the electric pulse treatment, as the estimated nucleation rates, exponential and pre-exponential factors have the lowest errors for untreated experiments (0V) and crystallisations under a potential difference of 9 kV.

Interpretation of the supersaturation term S. In his theoretical analysis of nucleation under electrostatic fields, Kashchiev[18] affirmed that a strong electric field may affect nucleation kinetics by increasing the magnitude of the effective supersaturation term. Hence, an evaluation of the supersaturation requirement for spontaneous nucleation to reach the same nucleation rate measured under a strong potential (9 kV) can be conducted by the help of equation (5.6).

Accordingly, the supersaturation must increase *ca.* 1.75 times in the absence of the field to equalize the nucleation rate estimated under the electrostatic field of 4.15 MV/m at $S = 1.16$. This value corresponds to an increase of $k_BT\ln S$ by 22.5 times. Under experimental conditions ($\varepsilon_m = 2.2$, $v_0 = 0.17$ nm^3, $E = 4.15$ MV/m) and assuming that $\varepsilon_c > \varepsilon_m$ (as discussed in Chapter 4), the magnitude of the dielectric parameter is relatively small compared to the chemical potential. The estimated value of the dielectric parameter is approximately $c_\varepsilon E^2 \approx 10^{-6}\, k_BT$. To produce the required increment of the dielectric term, an electric field magnitude of approximately 8 x 10^9 V/m must be imposed within the solution. Thus, we can conclude that under experimental conditions the electric field is insufficient to provide the estimated supersaturation difference, and therefore other phenomena must contribute to the larger nucleation rate under an electric field.

Interpretation of the exponential factor *B*. The low values of the thermodynamic parameter (ranging from 0.035 to 0.15) obtained from all the experiments suggests that heterogeneous nucleation occurred.[45] The exponential factor *B* provides information of the nucleation work associated to the creation of a new phase. This parameter relates the interfacial energy between the nucleus, the solution, and in the case of heterogeneous nucleation, heterogeneous particles. For heterogeneous nucleation, an effective interfacial energy γ_{ef} can be estimated from the following equation:[41]

$$B = \frac{4}{27}\frac{c^3 v_0^2 \gamma_{ef}^3}{k_B^3 T^3} \quad \textbf{(5.12)}$$

where $c = (36\pi)^{1/3}$ is the sphere shape factor. For the determination of γ_{ef}, an exponential factor $B = 0.04$ was used, corresponding to the determined value from the pulse energy study. The estimated effective interfacial energy at 30 °C was approximately 2 mJ/m^2. Comparing the effective interfacial energy to the homogeneous parameter γ, the activity factor $\psi = \gamma_{ef}/\gamma$ can be calculated, which accounts for the nucleation work reduction in heterogeneous processes. According to Jiang *et. al*,[41] the interfacial energy γ of spherical nuclei can be written as

$$\gamma = 0.514 k_B T \frac{1}{v_0^{2/3}} \ln\left(\frac{1}{N_A v_0 C^*}\right) \quad \textbf{(5.13)}$$

where N_A is the Avogadro's number and C^* is the molar solubility of the model compound in mol/L. The estimated activity factor at 30 °C was $\psi \approx 0.1$, which reflects a substantially decrease in the nucleation work, indicating that heterogeneous nucleation was the plausible mechanism on untreated and systems subjected to an electric field.

No significant difference of B in the presence and absence of an electric field indicates that the nucleation work to form a nucleus is unaffected by the electric field. The nucleation work estimated from the exponential factor $B = 0.04$ at $S = 1.20$ was approximately $1.2k_BT$.

$$\frac{W^*}{k_BT} = \frac{B}{ln^2S} \tag{5.14}$$

<u>Interpretation of the pre-exponential factor A.</u> The obtained kinetic parameter A showed a significant difference between experiments conducted in the presence and absence of electric field. This parameter is proportional to the Zeldovich factor z, the attachment frequency f^*, and the concentration of nucleation sites C_0.[46]

$$A = zf^*C_0 \tag{5.15}$$

In this study, an electrically-driven flow was observed following the application of an elevated potential in initial solutions. While no observable motion of the liquid-air interface occurred upon applying a voltage to the pure solvent, a swirl motion between the two electrodes is created when the electric field is applied to solution samples. This phenomenon may generate concentration gradients within the system, leading to a larger f^* as a result of increasing molecular diffusion. The orientation of the solute molecules with the electric field may lead to a higher frequency of successful attachments, and consequently to the increase of the kinetic factor.

After a new phase emerges, an electrical double layer is formed in the solid/liquid interface. Assuming the permittivity of INA is greater than that of the solvent, a greater number of charges are located in the molecule side of the EDL, which induces a motion of the subcritical clusters to the electric field maxima by dielectrophoresis. Motion of nanomolecules induced by DEP has been previously reported.[47,48] A concentration of nucleation sites near both electrodes may occur due to the rise of electrokinetic forces. The larger amount of INA crystals found at the anode could be explained by the presence of negative charges in the solid surface of the particle induced in the solvent or by the electric field. Schreuer[49] described the origin of charges in submicron electrically neutral polymers in non-polar solvents as a result of ions being pulled from the particles by strong electric fields. Traces of water in the solvent or on hygroscopic particles contributing to the ionization of these particles or the dissociation of surface groups provides a plausible explanation of the origin of the charge.[50,51] Electrophoretic forces may act on negatively charged INA particles, inducing a preferential motion towards the anode. Recently, W. W. Li *et al.*[33] described the collection of INA crystals at the anode by the action of an inhomogeneous electric field, and ascribed the observed phenomenon to dielectrophoretic and electrophoretic forces acting on the crystalline material.

5.5. Conclusions

The presence of an electric field affects the crystallisation of INA in 1,4-dioxane. In the presence of a strong inhomogeneous DC electric field nucleation is triggered at higher temperatures while shorter induction times and higher nucleation probabilities are measured. The electric field assisted crystallisation results in higher recovery with no measured effect on the crystal form. Additionally, the preferential crystallisation of INA at the anode exhibited in all the experiments subjected to an electrostatic field suggests that the field enables spatial and temporal control over the nucleation process. Once an INA monomer is formed, they may migrate towards the electrode due to positive dielectrophoresis acting on the monomer and driven its motion towards the strong electric field region. A preferential particle motion towards the anode due to negatively charged particles being attracted to the electrode by electrophoresis may explain this particular behaviour.

Nucleation rates were calculated from the number of successful cooling crystallisations experiments in the absence and presence of an electric field. This data was used to analyse the mechanistic effect of electric fields in the crystallisation of INA. The crystallisation of INA occurred via heterogeneous nucleation in the presence and absence of the field. In the presence of an electric field, the field seems to significantly affect the nucleation kinetics. A possible explanation is the generation of an electrically-driven flow within the crystalliser, which increases the number of monomers near the electrode surface, i.e increase of local supersaturation close to the copper surface, with the consequent increase of nucleation sites and frequency of successful attachments of building units.

5.6. References

1. Harrington, T. S., Phillips, M. A. & Srai, J. S. Reconfiguring global pharmaceutical value networks through targeted technology interventions. *Int. J. Prod. Res.* **7543**, 1–17 (2017).
2. Wang, J., Li, F. & Lakerveld, R. Process intensification for pharmaceutical crystallization. *Chem. Eng. Process. - Process Intensif.* **127**, 111–126 (2018).
3. Brown, C. J. *et al.* Enabling precision manufacturing of active pharmaceutical ingredients: workflow for seeded cooling continuous crystallisations. *Mol. Syst. Des. Eng.* **3**, 518–549 (2018).
4. Fujiwara, M., Nagy, Z. K., Chew, J. W. & Braatz, R. D. First-principles and direct design approaches for the control of pharmaceutical crystallization. *J. Process Control* **15**, 493–504 (2005).
5. Parambil, J. V., Poornachary, S. K., Hinder, S. J., Tan, R. B. H. & Heng, J. Y. Y. Establishing template-induced polymorphic domains for API crystallisation: the case of carbamazepine. *CrystEngComm* **17**, 6384–6392 (2015).
6. Song, R. Q. & Cölfen, H. Additive controlled crystallization. *CrystEngComm* **13**, 1249–1276 (2011).
7. Revalor, E. *et al.* Usual and unusual crystallization from solution. *J. Cryst. Growth* **312**, 939–946 (2010).
8. Javid, N., Kendall, T., Burns, I. S. & Sefcik, J. Filtration suppresses laser-induced nucleation of glycine in aqueous solutions. *Cryst. Growth Des.* **16**, 4196–4202 (2016).
9. Iefuji, N. *et al.* Laser-induced nucleation in protein crystallization: Local increase in protein concentration induced by femtosecond laser irradiation. *J. Cryst. Growth* **318**, 741–744 (2011).
10. Forbes, C., Nguyen, T. T. H., O’Leary, R. L. & Price, C. J. Elucidating the mechanism of paracetamol sonocrystallization for product purity enhancement. **045017**, 045017 (2018).
11. Crespo, R., Martins, P. M., Gales, L., Rocha, F. & Damas, A. M. Potential use of ultrasound to promote protein crystallization. *J. Appl. Crystallogr.* **43**, 1419–1425 (2010).
12. Sudha, C., Sivanarendiran, R. & Srinivasan, K. Influence of magnetic field on the nucleation rate control of mono paracetamol. *Cryst. Res. Technol.* **50**, 230–235 (2015).
13. Nakamura, A. *et al.* Improvement in quality of protein crystals grown in a high magnetic field gradient. *Cryst. Growth Des.* **12**, 1141–1150 (2012).
14. Radacsi, N., Ter Horst, J. H. & Stefanidis, G. D. Microwave-assisted evaporative crystallization of niflumic acid for particle size reduction. *Cryst. Growth Des.* **13**, 4186–4189 (2013).
15. Hou, D. & Chang, H. ac field enhanced protein crystallization. *Appl. Phys. Lett.* **223902**, 22–25 (2008).
16. Parniakov, O., Adda, P., Bals, O., Lebovka, N. & Vorobiev, E. Effects of pulsed electric energy on sucrose nucleation in supersaturated solutions. *J. Food Eng.* **199**, 19–26 (2017).
17. Li, F. & Lakerveld, R. Influence of Alternating Electric Fields on Protein Crystallization in Microfluidic Devices with Patterned Electrodes in a Parallel-Plate Configuration. *Cryst. Growth Des.* **17**, 3062–3070 (2017).
18. Kashchiev, D. Nucleation: Basic Theory with Applications. in *Butterworth-Heinemann* 315–329 (2000).
19. Budevski, E., Staikov, G. & Lorenz, W. J. Electrocrystallization Nucleation and growth phenomena. *Electrochim. Acta* **45**, 2559–2574 (2000).
20. Trzaska, M. & Trzaska, Z. Nanomaterials Produced by Electrocrystallization Method. in *Nanomaterials Produced by Electrocrystallization Method. Handbook of Nanoelectrochemistry: Electrochemical Synthesis Methods, Properties and Characterization Techniques* 1–27 (2016). 21. Jha, P. K. *et al.* A review on e ff ect of DC voltage on crystallization process in food systems. *Innov. Food Sci. Emerg. Technol.* **42**, 204–219 (2017).
22. Penkova, A. *et al.* Enhancement and suppression of protein crystal nucleation due to electrically driven convection. *J. Cryst. Growth* **275**, 1527–1532 (2005).
23. Wakamatsu, T. & Ohnishily, Y. Transparent cell for protein crystallization under low applied voltage. *Jpn. J. Appl. Phys.* **50**, 5–7 (2011).

24. Taleb, M. *et al*. Crystallization of proteins under an external electric field. *J. Cryst. Growth* **200**, 575–582 (1999).

25. Taleb, M., Didierjean, C., Jelsch, C., Mangeot, J. P. & Aubry, A. Equilibrium kinetics of lysozyme crystallization under an external electric field. *J. Cryst. Growth* **232**, 250–255 (2001).

26. Pareja-rivera, C. *et al*. Recent Advances in the Understanding of the Influence of Electric and Magnetic Fields on Protein Crystal Growth. *Cryst. Growth Des.* **17**, 135–145 (2017).

27. Mirkin, N., Frontana-Uribe, B. A., Rodriguez-Romero, A., Hernandez-Santoyo, A. & Moreno, A. The influence of an internal electric field upon protein crystallization using the gel-acupuncture method. *Acta Crystallogr. Sect. D* 1533–1538 (2003).

28. Hammadi, Z., Astier, J. P., Morin, R. & Veesler, S. Spatial and temporal control of nucleation by localized DC electric field. *Cryst. Growth Des.* **9**, 3346–3347 (2009).

29. Hammadi, Z., Astier, J. P., Morin, R. & Veesler, S. Protein crystallization induced by a localized voltage. *Cryst. Growth Des.* **7**, 1472–1475 (2007).

30. Paul, E. L., Tung, H. H. & Midler, M. Organic crystallization processes. *Powder Technol.* **150**, 133–143 (2005).

31. Hu, B., Huang, K., Zhang, P. & Zhong, X. Z. Pulsed Electric Field Effects on Sucrose Nucleation at Low Supersaturation. *Sugar Tech* **17**, 77–84 (2015).

32. Aber, J. E., Arnold, S., Garetz, B. A. & Myerson, A. S. Strong dc Electric Field Applied to Supersaturated Aqueous Glycine Solution Induces Nucleation of the Polymorph. *Phys. Rev. Lett.* **145503**, 1–4 (2005).

33. Li, W. W., Radacsi, N., Kramer, H. J. M., van der Heijden, A. E. D. M. & ter Horst, J. H. Solid Separation from a Mixed Suspension through Electric-Field-Enhanced Crystallization. *Angew. Chemie Int. Ed.* 1–5 (2016).

34. Nath, J. & Pandey, J. G. Excess molar volumes, relative permittivities, and refractive indexes of 1,1,2,2-tetrachloroethane + pyridine, +anisole, +methyl ethyl ketone, and +1,4-dioxane at 303.15 K. *J. Chem. Eng. Data* **41**, 844–847 (1996).

35. Kara, A., Kalenderli, Ö. and Mardikyan, K. Effect of dielectric barriers to the electric field of rod-plane air gap. in *Proceedings of the COMSOL Users Conference* (2006).

36. COMSOL Multiphysics. *AC/DC Module User ' s Guide. Manual* (2017).

37. Black, S., Dang, L., Liu, C. & Wei, H. On the measurement of solubility. *Org. Process Res. Dev.* **17**, 486–492 (2013).

38. Aakeröy, C. B., Beatty, A. M., Helfrich, B. A. & Nieuwenhuyzen, M. Do polymorphic compounds make good cocrystallizing agents? A structural case study that demonstrates the importance of synthon flexibility. *Cryst. Growth Des.* **3**, 159–165 (2003).

39. Li, J., Bourne, S. A. & Caira, M. R. New polymorphs of isonicotinamide and nicotinamide. *Chem. Commun.* **47**, 1530–1532 (2011).

40. Eccles, K. S. *et al*. Expanding the crystal landscape of isonicotinamide: concomitant polymorphism and co-crystallisation. *Cryst. Eng. Comm.* 6923–6925 (2011).

41. Jiang, S. & Horst, J. H. Crystal Nucleation Rates from Probability Distributions of Induction Times. *Cryst. Growth Des.* **11**, 256–261 (2011).

42. Castellanos, A. & Perez. Electrohydrodynamic Systems. in *Springer Handbook of Experimental Fluid Mechanics* 1317–1333 (2007).

43. Isard, J. O. Calculation of the influence of an electric field on the free energy of formation of a nucleus. *Philos. Mag.* (1977).

44. Warshavsky, V. B. & Shchekin, A. K. The effects of external electric field in thermodynamics of formation of dielectric droplet. *Colloids Surfaces A Physicochem. Eng. Asp.* **148**, 283–290 (1999).

45. Kulkarni, S. A., Kadam, S. S., Meekes, H., Stankiewicz, A. I. & Horst, J. H. Crystal Nucleation Kinetics from Induction Times and Metastable Zone Widths. *Cryst. Growth Des.* **13**, 2435–2440 (2013).

46. Ter Horst, J. H., Schmidt, C. & Ulrich, J. *Fundamentals of Industrial Crystallization. Handbook of Crystal Growth: Bulk Crystal Growth: Second Edition* **2**, (Elsevier B.V., 2014).

47. Hölzel, R., Calander, N., Chiragwandi, Z., Willander, M. & Bier, F. F. Trapping single molecules by dielectrophoresis. *Phys. Rev. Lett.* **95**, 18–21 (2005).

48. Zheng, L., Li, S., Burke, P. J. & Brody, J. P. Towards single molecule manipulation with dielectrophoresis using nanoelectrodes. *Proc. IEEE Conf. Nanotechnol.* **1**, 437–440 (2003).

49. Schreuer, C., Vandewiele, S., Strubbe, F., Neyts, K. & Beunis, F. Electric field induced charging of colloidal particles in a nonpolar liquid. *J. Colloid Interface Sci.* **515**, 248–254 (2018).

50. Lyklema, J. Principles of the stability of lyophobic colloidal dispersions in non-aqueous media. *Adv. Colloid Interface Sci.* **2**, 67–114 (1968).

51. Gacek, M. M. & Berg, J. C. The role of acid-base effects on particle charging in apolar media. *Adv. Colloid Interface Sci.* **220**, 108–123 (2015).

Chapter 6. Concomitant Separation through Electric Field Enhanced Crystallisation in Mixed Suspensions

This chapter is the result of a strong cooperation between the University of Strathclyde and Delft University of Technology. The work presented in this Chapter was carried out by the author, with the exception of section 6.3.4 which was jointly written by Dr. Weiwei Li (Delft University of Technology) and the author of this thesis following Li's experimental work.

Abstract

Electric Field Enhanced Crystallisation (EFEC) enables simultaneous crystallisation and separation of crystalline particles from their mixtures in non-polar solvents. To show this, the isolation of the crystalline phases suspended in a number of multi-component systems was successfully carried out by EFEC in dioxane and toluene at a potential difference of 5 - 7.5 kV. The successfully separated systems include 1) caffeine and nicotinamide in 1,4-dioxane, 2) an active pharmaceutical ingredient (aspirin) and one of its impurities (salicylsalicylic acid) in toluene, and 3) a co-crystal (carbamazepine:isonicotinamide) and one of its co-former in 1,4-dioxane. Upon application of an electric field, the compounds in the suspension accumulate on different electrodes, from which they can be collected. Except for the co-crystal, all the recovered solids at the end of the process presented purities greater than 93 %wt. The separation method has been further developed for its application on mixtures of compounds such as caffeine and isonicotinamide that collect at the same electrode in an electric field. By a two-step seeded crystallisation process in the presence of the field, both compounds were isolated with purity values greater than 95%. Thus, EFEC offers an alternative separation method for the isolation of suspensions of crystalline phases in a complex mixture.

6.1. Introduction

Crystallisation has been extensively implemented in the pharmaceutical industry for the separation and purification of active pharmaceutical ingredients (APIs) and intermediate compounds since a desirable particulate product of high purity can be obtained.[1,2] However, product purity is compromised if impurities are present in the final product.[3,4] The toxicology, stability and bioavailability of a drug substance can be significantly affected by the presence of even a small amount of impurities alongside the drug product, influencing the performance of the medicine and its suitability to be released into the market. One way impurities such as unreacted reagents, by-products, and degradation products end up in a crystalline product is by concomitant crystallisation with the API.[5] Examples of such process-related impurities are the crystallisation of a less soluble compound such as fumaric acid during the crystallisation of malenic acid in water,[6] the formation of a mix of crystalline phases including L-leucine and L-valine during the crystallisation of L-isoleucine,[7] and the co-crystallisation of melamine with one of its impurity products (cyanuric acid) from hydrolysis.[3] Re-crystallisation and washing operations are frequently used for the removal or reduction of impurities to acceptable levels. However, these operations are not always effective, and multiple purification processes are required to isolate the final product, with the consequent impact in production costs and process time.[8,9]

For this reason, a process technology that couples the direct isolation and crystallisation of an API from a mixed suspension entails a new challenge for chemical processes and crystallisation technology. In this context, process intensification though alternating (AC) and direct current (DC) electric fields has been studied for the manipulation of colloids and crystallisation enhancement.[10–14] Although the use of electric fields has proved effective for the control of particles, these studies were conducted in pure suspensions or solutions of a single compound and the effects of the field on multi-component mixtures was overlooked. Li et al.[15] demonstrated that pure crystalline organic particles undergo rotational motion in suspension, and selectively collect on one of the electrodes under a strong non-uniform electric field. This behaviour was observed upon generating a potential difference above 1 kV between two electrodes submerged in a suspension of a given crystalline phase. The rotational motion and selective accumulation on one electrode were ascribed to dielectrophoresis and electrophoresis. This phenomenon, combined with cooling crystallisation, was exploited to successfully isolate and immobilize on the surface of opposite electrodes caffeine (CAF) and phenazine crystals from their mixed suspension in 1,4-dioxane.

Our aim is to show that this novel electric field driven separation technique, named Electric Field Enhanced crystallisation (EFEC), offers an alternative separation and purification process, in which the crystallisation and in-situ separation of multi-component mixtures can be realized simultaneously. A series of systems were selected based on the dissimilar behaviour of the compounds under an electric field observed in Chapter 4 (Table 6.1). In order to study the suitability of the technique for the separation of impurities that may be presence within an API product, EFEC has been applied to a multicomponent system of an API (aspirin) and one of its process-related impurities (salicylsalicylic acid), and to a mixture of a co-crystal (isonicotinamide:carbamazepine) and one of its co-formers (isonicotinamide). First, caffeine and nicotinamide crystals were separated in-situ from their mixture by EFEC in order to become familiarized with the separation technique. Finally, due to the applicability limitation of the EFEC separation to multi-component systems that are attracted to opposite electrodes, the separation technique was further developed to effectively separate crystalline particles with similar behaviour in a non-uniform electric field (Table 6.1).

Table 6.6. Behaviour of the studied crystalline compounds under a non-uniform electric field. Upon the application of a strong inhomogeneous electric field, the suspended crystals in dioxane or toluene collect at a specific electrode as a result of electrokinetic forces exerted on the crystalline particles.

Compound	Acronym	Behaviour of crystals under non-uniform electric field
Aspirine	**ASP**	Anode
Caffeine	**CAF**	Anode
Isonicotinamide	**INA**	Anode
Nicotinamide	**NA**	Cathode
Salicylsalicylic acid	**SSA**	Cathode
Isonicotinamide:Carbamazepine	**INA:CBZ**	Cathode

6.2. Experimental

Isonicotinamide (INA) ReagentPlus (99%), Carbamazepine (CBZ), Nicotinamide (NA) HPLC (≥99.5%), Caffeine (CAF) ReagentPlus, Aspirin impurity E (SSA), and 1,4-dioxane anhydrous (99.8%) were purchased from Sigma-Aldrich (Merck KGaA, Darmstadt, Germany). O-Acetylsalicylic acid (ASP, ≥99%), Toluene (≥99%) GRP RectaPur, Methanol HiPerSolv Chromanorm R. Pe for HPLC Gradient Grade (≥99.8%), and Acetic acid ACS reagent (≥99.7%) were supplied by VWR (VWR International Limited, United Kingdom). All the solutes and reagents were used as received, without further purification. Distilled water was produced in-house using a Direct-Q UV water purification system (Merck Millipore, United Kingdom).

The solubility of the pure compounds, ASP, CAF, CBZ, INA, NA, and SSA in the solvent systems used in this studied were measured as a function of the temperature in Chapter 3.

6.2.1. Co-crystal Screening

A co-crystal screening was carried on mixtures of CAF and NA, CAF and INA, and INA and CBZ in dioxane, and on a mixture of ASP and SSA in toluene following the method developed by Ter Horst *et. al.*[16] The molar fraction solubilities x_A* and x_B* of the pure components A and B in a given solvent at a reference temperature T* were used to determine the composition of the sample mixtures (x_A,x_B) containing A, B, and solvent by using the expression:

$$\frac{x_B}{x_B^*} = 1 - \frac{x_A}{x_A^*} \tag{6.1}$$

The temperature dependent solubility of the mixtures with composition (x_A,x_B) in either 1,4-dioxane or toluene were studied in a Crystal16 workstation (Technobis Crystallisation Systems, The Netherlands). The mixtures were prepared by adding a known volume of the appropriate solvent to HPLC vials containing pre-weighed amounts of the crystalline materials. The vials were placed in the setup and subjected to consecutive heating and cooling cycles over a temperature range between a minimum of 0 and a maximum temperature of 70 °C. The samples were magnetically stirred at 700 rpm during the entire experimental period. The clear point temperature for a given sample composition was determined as the point at which the light transmission through the sample was 100%, i.e. the suspension turns into a clear solution. The heating rate was set at 0.3 °C/min, which is considered sufficiently slow for an accurate estimation of the saturation temperature T_S through the clear point temperature.[17]

Upon clear point determination, a pseudo-binary phase diagram is created by plotting the solvent-excluded mole fraction of one of the compounds y_A against the saturation temperature, with y_A given by:

$$y_A = \frac{x_A}{x_A + x_B} \tag{6.2}$$

According to equation (6.2), a pure binary system of A with a concentration x_A* is given by y_A = 1. On the other hand, y_A = 0 indicates that the solution only contains the compound B with a concentration x_B*. Therefore, the saturation temperature at y_A = 1 and y_A = 0 correspond to the reference T*. The saturation temperature of intermediates values of y_A are compared to the solubility behaviour of the pure compounds in the solvent system, which allows for the identification of a tri-phasic domain of solution A and B, in which the formation of a co-crystal may occur.

6.2.2. Electric Field Enhanced Crystallisation (EFEC)

In a previous chapter (Chapter 4), the particular behaviour of a number of crystalline particles suspended in apolar solvents was investigated in the presence of a strong non-uniform electric field. According to the observed behaviour, a number of multi-component systems were selected to attempt the separation of the compounds in the system by EFEC.

6.2.2.1. Separation of Compounds that Collect on Counter Electrodes.

The setup used to carry out the separation of multi-component mixtures was described in Chapter 4. A mixed suspension of the solutes A and B in an approximately 6 mL of an apolar solvent was prepared at T^*_{high} = 22 °C. For the separation of ASP and SSA, ASP was slightly grinded with the use of a mortar and a pestle due to the large crystal size of the received material. A coated PTFE magnetic bar was added to the vial before being placed in a water bath at T^*_{high}. After a minimum of 30 min under stirring, the magnetic bar was removed and the lid of the vial was replaced by a cap with adapted electrodes. Subsequently, the temperature was linearly reduced to a final temperature T^*_{low} (15 °C for EFEC separation in dioxane and 10 °C in toluene) at a set rate of 0.25 °C/min in the presence of an electric field, generated by potential difference of a maximum magnitude of 7.5 kV. The experiments were kept at the final temperature in the presence of the electric field for a minimum of 6 h before the potential difference was gradually reduced to 0 V. Once the power supply was switched off, the crystals on both electrodes were separately recovered and isolated by filtration under reduced pressure over a Buchner funnel.

For the separation of the co-crystal from one of its co-formers, a mixed suspension of INA and CBZ was prepared by adding 7 mL of dioxane to a glass vial containing approximately 125 mg of INA and 250 mg of CBZ. A coated PTFE stirring bar was added to the vial, and the mixture was left overnight under stirring in an oil bath (Nujol light oil; Alfa Aesar, United Kingdom) set at 22 °C. A thermocouple immersed in the oil bath and connected to a heating/stirring plate (ADS-HP-ST Asynt) allowed for temperature control. Approximately 6 mL of the equilibrated suspension was filtered through a 0.45 μm PTFE membrane syringe filter (VWR North America) into an 8 mL glass vial containing a magnetic stirrer. Thus, a saturated solution of INA and CBZ was obtained at T^*_{high} = 22 °C. Subsequently, approximately 130 mg of the crystalline solids of INA and 40 mg of the co-crystal of INA and CBZ were seeded to the solution and a magnetic bar was added to the vial prior placing the sample in a water bath at T^*_{high}. After a minimum of 30 min under stirring, the stirrer was removed and the lid of the vial was replaced by the custom-made cap with adapted copper electrodes. The vial containing the multi-component mixture was placed in a water bath, and a non-uniform electric field was generated by gradually imposing a DC potential difference between of 7.5 kV across the electrodes. Thereafter, the temperature was linearly reduced to a final temperature T^*_{low} = 15 °C at a set rate of 0.25 °C/min. The sample was held at the final temperature in the presence of the field for 6 h before linearly reducing the potential. The crystals on both electrodes were then separately recovered and filtered under vacuum.

6.2.2.2. Separation of Compounds that Collect at the Same Electrode.

A 6 mL solution of A and B saturated in one of the compounds (e.g., crystal phase A) was prepared at the saturation temperature of this solute (T^*_A) in an 8 mL crystal vial. Subsequently, seed crystals of compound A were added to produce a saturated suspension of A in a undersaturated solution of the crystalline phase B. Upon equilibration for a minimum of 30 minutes under stirring, the vial cap was replaced by the in-house lid with adapted electrodes. The crystalliser containing the suspended solids in the mixed solution was placed in a water bath at T^*_A and a DC potential difference of 7.5 kV was gradually applied to the system. Temperature and applied potential control were realized by using the setup described in Chapter 4. Thereafter, the temperature was linearly reduced at 0.17 °C/min to the saturation temperature T^*_B of compound B. Once the system was at temperature T^*_B, the potential difference was gradually reduced to zero and seed crystals of compound B were added to the system. Then, the polarity of the power supply was reversed, and a potential difference of -7.5 kV was applied within the suspension. The system underwent a second cooling step to T_{low} at a set rate of 0.17 °C/min and held at temperature in the presence of the field overnight before gradually reducing the potential difference to 0 V. The crystals attached to each electrode were separately recovered and isolated by filtration under vacuum.

6.2.3. High Performance Liquid Chromatography (HPLC)

Purity assessment was conducted in an Agilent 1100 Series HPLC instrument (Agilent Technologies Inc., USA) equipped with a G1314 variable wavelength UV detector (with a detection limit over a range of 190 to 600 nm), a G1311A quaternary pump, a G1322A degasser, and a 100 positions sample plate adapted to a G1313A autosampler. An Agilent Zorbax Eclipse Plus C_{18} reverse-packing column (4.6 x 250 mm, 5 µm) was used throughout HPLC analyses.

To determine the purity of the solid product recovered from the EFEC separation of CAF and NA, and CBZ and INA mixtures, approximately 5 mg of the solid material was dissolved in 5 mL of a buffer solution of distilled water and methanol in a 30/70 %v/v ratio.[18,19] The solution was stirred at ambient for approximately 18 h before filtered through a syringe filter with a 0.45 µm PTFE membrane and degassed in an ultrasonic bath. The clear solution was transferred to 1.5 mL glass vials for HPLC analysis. The analysis was carried out using an injection volume of 5 µL and an isocratic elution with an eluent flow rate of 1 mL/min. The column temperature was set at 30 °C, and the detection wavelength was programme at 260 nm. The experimental time for each sample was 7 minutes with a washing step of the injection needle in pure methanol after each injection. The recovered solids from the electric field separation of ASP and SSA were dissolved in a mobile phase prepared by mixing 12 mL of acetic acid and 450 mL of water in a volumetric flask, and bringing the volume up to 1 L by addition of methanol.[20] The analysis was conducted at 25 °C, with an eluent flow rate of 1.6 mL/min, and the UV detector was set at 254 nm wavelength. The experimental time was 10 minutes per sample. Data acquisition, processing, and HPLC control was carried out with an Agilent OpenLab CDS ChemStation Edition software (Agilent Technologies Inc., USA). The resulting chromatograms displayed in Figures 6.2.a to 6.2.c show that the retention of the different compounds in the same multi-component system provides an acceptable resolution for the identification of the different solutes in the sample, validating both HPLC methods.

The concentration of each analyte in a sample was obtained by extrapolation of the experimental chromatographic peaks versus the calibration curve. To determine the calibration curves, stock solutions of approximately 1 mg/mL of pure ASP, CAF, CBZ, INA, NA, and

SSA were prepared in the appropriate buffer. Subsequently, standard solutions over a concentration range of 0.01 to 1 mg/mL were obtained by making successive dilutions of the stock solution using the appropriate mobile phase. Each standard solution was prepared in triplicate and analysed following the procedures described above. The peak area of each compound from the resolved chromatogram was plotted against the concentration, obtaining a linear response over the used concentration range, with a correlation coefficient higher than $r^2 = 0.993$ (Figure 6.2.d). Assuming that the recovered solids contains solely the two crystalline components of the prepared mixed suspensions, the purity of a compound A was calculated as the percentage of the weight of A in the sample. The reported purity of each sample collected from EFEC experiments is the average of at least two separate HPLC analyses. The co-crystal purity was determined on the basis of the moles of INA in the co-crystal, assuming a 1:1 ratio of INA and CBZ in the crystalline structure.

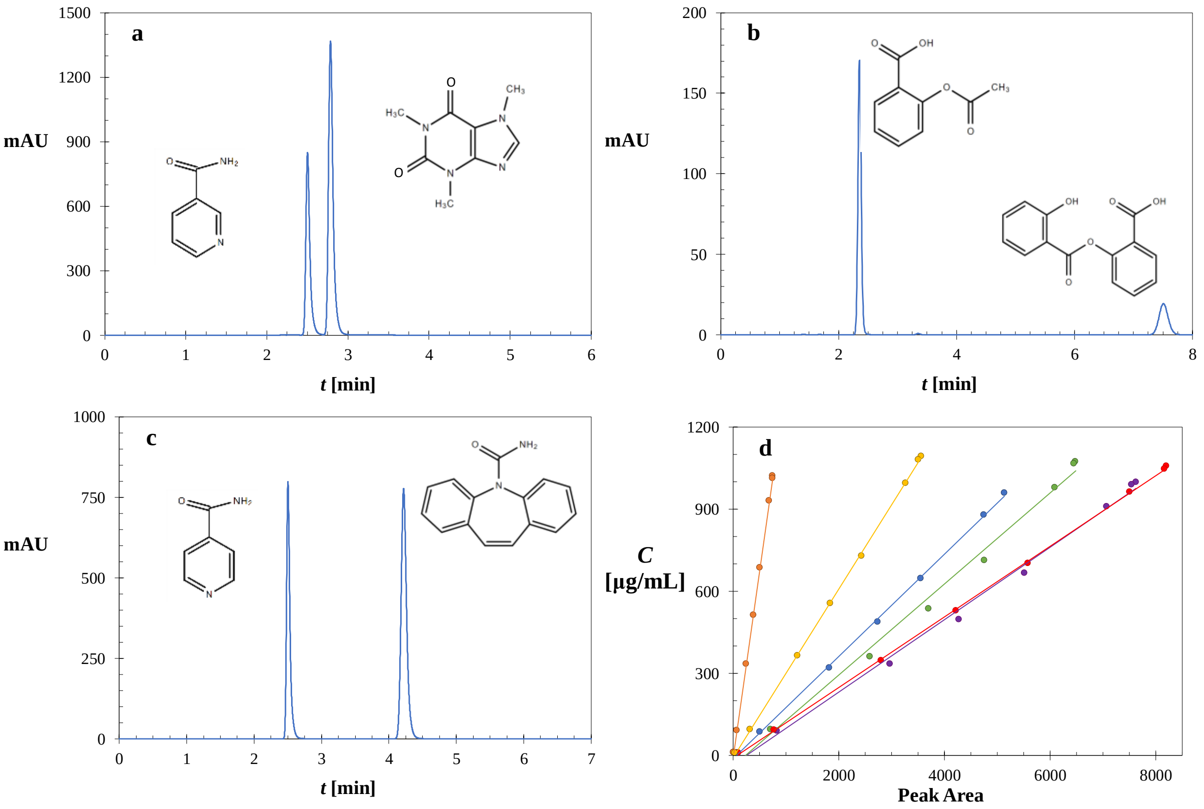

Figure 6.1. Chromatograms exhibiting the separation of NA and CAF (a), INA and CBZ (b) in water/methanol (30/70 v/v), and the separation of ASP and SSA in an acetic acid/water buffer diluted with methanol (c). Figure 3.d shows the HPLC calibration curves for INA (●), CBZ (●), NA (●) and CAF (●) in water/methanol (30/70 %v/v) as a mobile phase, and ASP (●) and SSA (●) in mobile phase composed of 12 mL of acetic acid and 450 mL of water diluted to 1 L with methanol

6.2.4. Proton Nuclear Magnetic Resonance (^{1}H-NMR)

The purity of the solid product recovered from the two-steps EFEC carried out on CAF and INA mixtures was assessed in an Agilent 400 MHz NMR spectrometer (Agilent Technologies Inc., USA). Approximately 25 mg of the crystalline material was dissolved in 1 mL of chloroform (0.03% TMS, >99.96%, euriso-top)/Methanol-d4 (>99.8%, euriso-top) buffer with a 50/50 %v/v ratio. Based on the NMR spectra, the INA/CAF mass ratio $w_{INA/CBZ}$ is expressed as follows:

$$w_{INA}/_{CBZ} = \frac{I_{INA}}{I_{CAF}} \cdot \frac{N_{CAF}}{N_{INA}} \cdot \frac{M_{INA}}{M_{CAF}} \tag{6.3}$$

where I_i refers to the area of the INA (at 8.7 ppm) or CAF (at 4.0 ppm) peaks, N_i is the number of protons contributing to each peak ($N_{INA} = 2$, $N_{CAF} = 1$), and M_i is the molecular weight of the compound. The subscript i stands for INA or CAF.

6.2.5. Yield

Upon completion of the cooling crystallisation experiments, crystals collected on the surface of the electrodes were placed in a desiccator under vacuum for drying. Following weight measurement of the dry product, the recovery yield was calculated using the following expression:

$$y = \frac{m}{V(c - c^*)} \cdot 100 \tag{6.4}$$

where m is the mass of the recovered solids, V is the volume, and c and c^* are the overall concentration and the concentration of the solution at the final temperature, respectively.

6.2.6. X-Ray Powder Diffraction (XRPD)

The identification of the crystalline phase of the recovered material was conducted on a Bruker D8 Discover diffractometer (GX002103 - Priscilla) equipped with a Cu anode (Cu Kα1 λ = 1.54056 Å), monochromator, a Vantec PSD detector, and a multipostion x-y sample stage. Transmission XRPD data was collected at ambient temperature over a 2θ range of 4 to 35° with a 0.015° step size and 1 s per step counting time. The samples were mounted on a sample plate supported on a polyimide film, which oscillated at 0.3 mm/s in the x-y plane during the analysis to minimise preferential orientation. XRPD analysis on the material recovered from CAF-INA systems was carried out in a Bruker D2 Phaser (Bruker AXS GmbH, Germany) using monochromatic radiation and a Cu anode (Cu Kα1 λ = 1.54056 Å). Data collection over a 2θ range of 8 to 50° was conducted with a 0.022° step size.

6.3. Results

The manipulation of suspended solids in a fluid medium by electric fields requires an elevated potential difference applied to the system. This may lead to unwanted Faradaic reactions.[21,22] However, apolar solvents with limited electrical conductivity can be used to minimize the generation of electric currents, and therefore minimizing electrolysis. In a previous chapter (Chapter 4), we demonstrated that potentials up to 9 kV applied to crystalline solids suspended in apolar solvents did not produce electrical currents above ±2 mA. Therefore, apolar solvents, defined by those with a relative permittivity $\varepsilon_S \leq 5$,[23] were selected for the isolation of the compounds in a multi-component mixture through EFEC. In addition to the dielectric characteristics of the solvent, the solubility of the model compounds in a solvent system determined the selection of the solvent. High solubility values may impede the correct monitoring of the process during cooling, and the accumulation of a large amount of crystals on one of the electrode could complicate their immobilization on the surface of the electrode due to the excess of weight.

The separation study was carried out in multi-component systems in 1,4-dioxane, which has a relative permittivity of 2.2 and the solubility values for the studied compounds ranged from approximately 10 to 40 mg/mL over the experimental temperature. ASP and SSA showed larger solubilities in dioxane, with values up to 700 mg/mL. Therefore, an alternative solvent was used for their separation by EFEC. Toluene was selected for the separation study of the latter solutes by EFEC due to its low relative permittivity (ε_l = 2.38) and the lower solubilities of both compounds in the apolar solvent (< 10 mg/mL).

6.3.1. Separation of Caffeine and Nicotinamide from a mixed suspension.

In a previous chapter (Chapter 4) we observed that CAF and NA crystals on pure suspensions of the compounds in dioxane collect on counter electrodes. Crystals of CAF were attracted by the anode while crystals of NA accumulated on the cathode upon the application of a non-uniform electric field. This behaviour in the electric field seems to be the result of the combination of electrokinetic forces acting on the solid particles, generating a motion in the direction of the high electric field regions by dielectrophoresis and towards the electrode of opposite charge to that of the particle by electrophoresis.

Prior attempting the separation of both compounds from their mixture, a co-crystallisation screening was carried out on suspensions of CAF and NA in dioxane. The pseudo-binary phase diagram resulting from the co-crystallisation screening (Appendix C.1) exhibits a single eutectic point, which indicates that pure crystals of both compounds are present in their mixture in dioxane and no co-crystal forms under these conditions. This screening further allows for the identification of the tri-phasic domain of solid CAF and NA in solution. Within the tri-phasic domain the separation of these compounds may be realized by the use of electric fields.

A mixed suspension with an initial concentration of 29 mg/mL of CAF and 36 mg/mL of NA was prepared in dioxane at 22 °C and subjected to the EFEC separation method detailed in Figure 6.2. Crystalline particles in the suspension start to move and collect on both electrodes upon imposing a strong DC potential difference of 7.5 kV. The slow temperature decrease induces the crystallisation and growth of the compounds on the electrodes, with the consequent immobilization of the material on the copper surface.

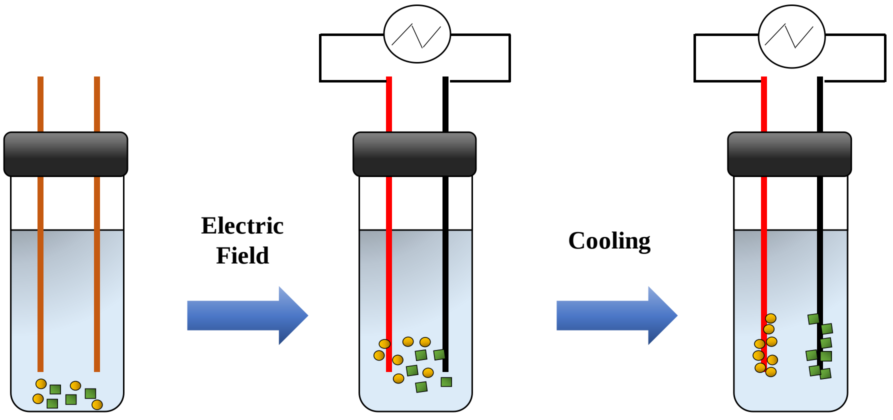

Suspension of crystals A (●) and B (🟩)

Crystals A and B move around the electrodes and eventually accumulate on them

Upon cooling down, crystals A and B immobilized on the electrode surfaces

Figure 6.2. Schematic diagram of the EFEC separation procedure for suspensions of compounds in apolar solvent that collect on opposite electrodes in the presence of a strong non-uniform direct-current electric field.

At the end of the EFEC separation study, the solids from the anode and cathode (Figure 6.3.a) were individually recovered and characterised for purity and yield. The phase diagram of CAF and NA in dioxane showing the initial and final compositions are presented in Figure 6.4. The solid material recovered from the anode showed a purity of 95.5 ± 3 %wt, with an approximate yield of 51%. The solids collected from the cathode exhibited a purity of 94 ± 3 %wt of NA, with a yield of *ca*. 42%. The crystalline products retrieved from both electrodes were analysed by XRPD (Appendix C.2). The diffractogram of the crystalline products retrieved from the anode is consistent with the form beta of CAF.[24] A small peak at approximately 15° may correspond to the presence of a small amount of NA crystals in the sample. The XRPD pattern of the crystals from the cathode is similar to the reported polymorphic form I of NA,[25] and displays an additional peak at 12.1°, which may relate to a small amount of CAF crystals in the crystalline material.

The obtained results indicated that the separation of CAF and NA from a mixed suspension of both compounds in dioxane is feasible by EFEC with purities larger than 94%. However, a relative low yield was obtained for both solid phases. An incomplete immobilization of the crystalline particles on the electrodes, crystals remaining in the bulk, and part of the immobilized crystals being scrubbed off when the electrodes were removed contributed to the low recovery.

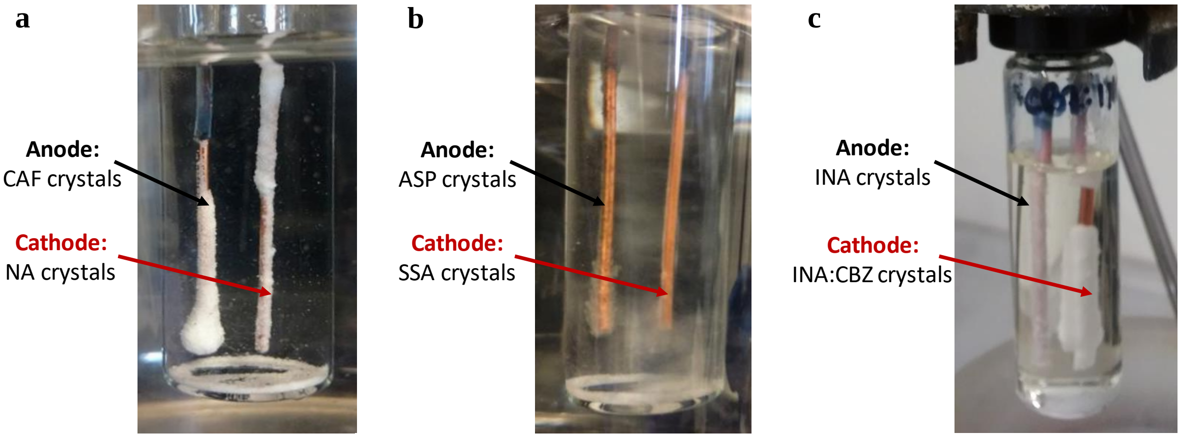

Figure 6.3. Crystals immobilized on the anode and cathode at the end of an EFEC separation process. **(a)** CAF and NA in dioxane. The separately recovered material showed purity values of 95.5% on CAF and 94% of NA. **(b)** ASP and SSA in toluene. The material collected from the anode and cathode exhibited a purity greater than 93% and 98% for ASP and SSA, respectively. Both layers appear partly transparent which makes them difficult to visualize. **(c)** INA and CBZ:INA in dioxane. The crystalline product collected from the anode was composed of mainly INA with a purity of 95.5%. From the cathode, the main product was the CBZ:INA co-crystal with a purity of 69.3%. In all experiments some crystals remain at the bottom of the crystalliser. A higher field or an optimized cell geometry may be necessary to improve the yield.

6.3.2. Separation of Aspin and Salicylsalicylic acid from a mixed suspension.

Salycicylsalicylic acid (SSA), also called salsalate, is one of the reported impurities that forms during the synthesis of aspirin (ASP) or due to the degradation of the API.[26] When a non-uniform electric field is imposed to pure suspensions of these compounds, they collect on opposite electrodes (Chapter 4). Additionally, the pseudo-binary diagram obtained from mixtures of these compounds in toluene (Appendix C.1) indicates that mixtures of both compounds in the apolar solvent consist of pure crystals of the solid materials. Therefore, the separation of the pure compounds from a multi-component mixture in toluene may be realized by the use of EFEC.

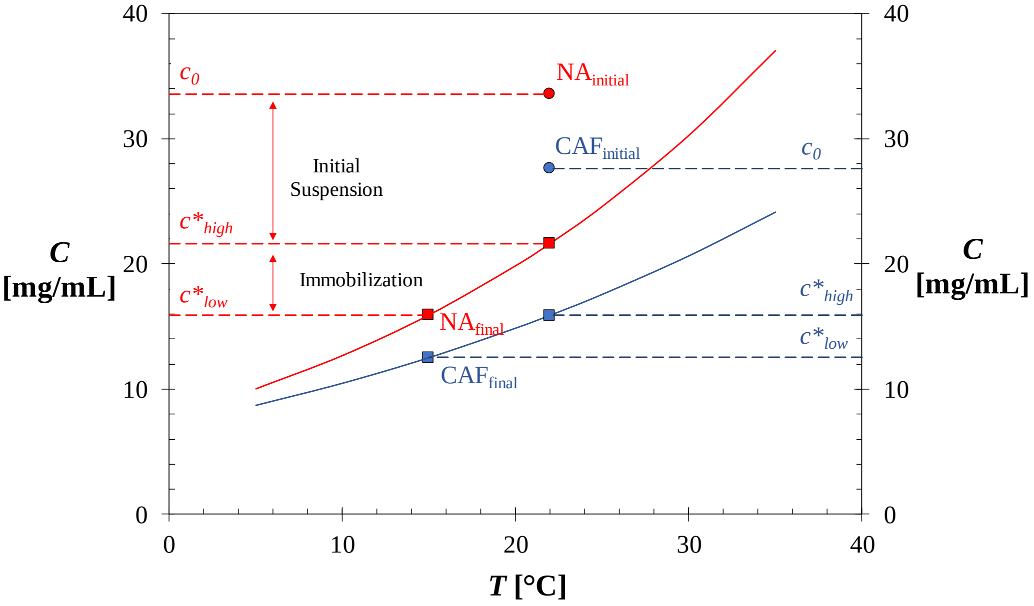

Figure 6.4. Temperature dependent solubility in mg/mL of pure CAF (blue line) and NA (red line) in 1,4-dioxane. The initial overall concentration c_0 (○) and the solubilities at the initial c^*_{high} and final temperatures c^*_{low} (□) of CAF (blue) and NA (red) used for the separation study are depicted in the figure. The difference between the overall concentration and c^*_{high} is the initial suspension density, and the difference between c^*_{high} and c^*_{low} represents how much the crystals can grow, e.g. the initial suspension density of NA in the figure is approximately 12 mg/mL, and the available supersaturation to induced growth on the electrodes during EFEC is 5.7 mg/mL. Process yield can be estimated from the fraction of the recovered crystals against c_0-c^*_{low}.

A DC potential difference of 7.5 kV was applied to a 6 mL suspension of 7 mg/mL of ASP and 12 mg/mL of SSA in toluene at 22 °C. The application of the strong potential induces a vigorous fluid motion. This behaviour seems different from the CAF and NA systems, and may be the result of a larger charge density of ASP and SSA or differences in particle size that result in a rapid motion of the crystalline particles in the electric field dragging the surrounding fluid medium with more intensity. Thus, the potential difference has to be optimized for each system in order to balance collection at electrode and suspension movement, so that a sufficiently strong electric field to trigger the motion of the particles towards the electrode can be developed, but not too fast to disrupt the form layer at electrode. In this context, a simple optimization by the eye revealed that an applied potential of 5.5 kV to a suspension of ASP and SSA mixture in toluene, with a suspension density of approximately 20 mg/mL, induces the motion of crystals and prevent strong fluid flow within the crystalliser.

Since ASP and SSA crystals have distinctive sizes and shapes, the collection of different types of crystals on opposite electrodes upon the application of an inhomogeneous electric field suggest that the separation of the two solid phases occurred in the suspension. In order to promote the immobilization of the crystal layers on the electrodes, crystal growth was stimulated by cooling from 22 °C to 10 °C. Figure 6.5 shows the initial and final conditions of the EFEC separation of ASP and SSA.

An initial suspension density of approximately 5 mg/mL of ASP and 3 mg/mL of SSA in toluene underwent EFEC separation. At the end of the purification process, the solid product immobilized on both electrodes (Figure 6.3.b) were separately recovered for characterisation. The solid material collected from the anode was 93.8 ± 0.1 %wt of ASP, while the crystals recovered from the cathode showed a purity of 98.4 ± 0.9 %wt of SSA. The XRPD data of the solids (Appendix C.2) showed that the main crystalline phases on the anode and cathode were consistent with ASP form I[27] and the reference pattern of SSA,[28] respectively. Although the separation of both compounds was achieved with higher purity values, the yield of ASP and SSA were very low, with respective values of 25.9% and 32.4%. The large amount of crystals remaining unattached to the electrode at the end of the process indicates that the low yield may be associated to an insufficient supersaturation to enable the grow and immobilization of the particles on the surface of the electrodes. The available supersaturation for mass growth between 22 and 10 °C is 1.3 mg/mL for ASP and 4.1 mg/mL for SSA. A larger supersaturation for mass growth might result from the use of a different solvent system and/or a higher initial and/or lower final temperature.

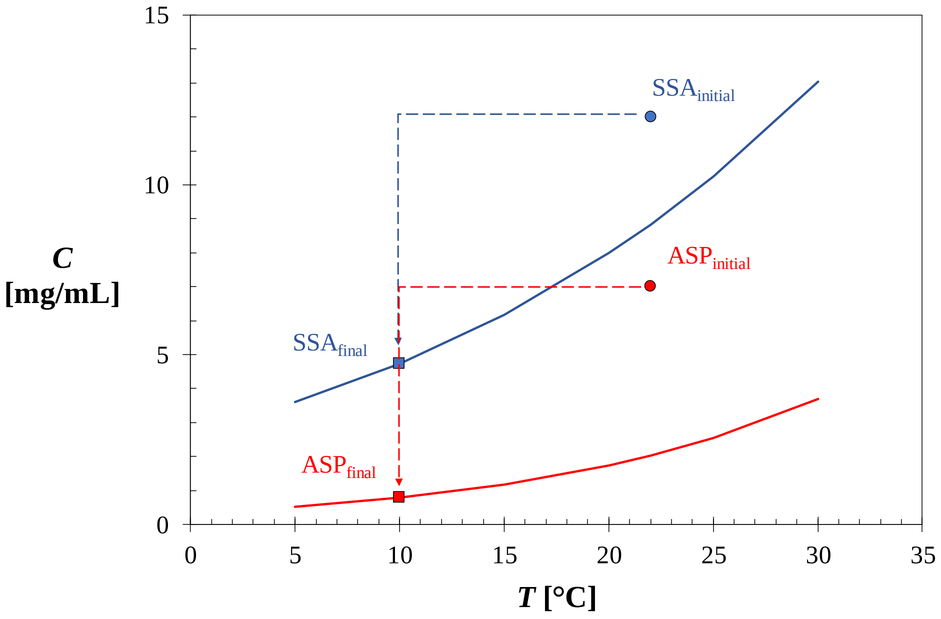

Figure 6.5. Schematic diagram of the initial and final conditions of the EFEC separation of ASP and SSA in toluene. The blue and red lines represent the solubility of SSA and ASP estimated by using the semi-empirical van 't Hoff model. The arrows indicate the evolution of the system through the experimental period: crystallisation from 22 to 10 °C, and equilibration at the final temperature.

6.3.3. Separation of Isonicotinamide and Carbamazepine:Isonicotinamide co-crystal from a mixed suspension.

In Chapter 4, the behaviour of CBZ:INA co-crystal was studied under a strong inhomogeneous electric field. Upon the application of the electric field, co-crystal particles suspended in dioxane collect on the cathode. Since one of the co-formers that forms the co-crystal accumulates on the anode under the same conditions, the separation of both compounds from their mixture in dioxane was attempted by EFEC.

The co-crystal screening of CBZ and INA reveals that a more stable form is produced at particular concentration regions of both materials in dioxane (Appendix C.1). To prepare the CBZ:INA co-crystal, the crystallisation conditions were defined from the isothermal ternary phase diagram of the pure compounds and solvent at the initial and final temperatures. The phase diagrams were constructed from the fit of the pure component and co-crystal solubilities to the van 't Hoff parameters of CBZ and INA in dioxane (Chapter 3). Figure 6.6 shows the isothermal phase diagram at 22 and 15 °C. The isothermal phase diagrams were plotted assuming that the solubility of the pure compounds are not affected by the presence of the second compound unless that they co-crystallise, and that the co-crystal solubility can be described by a constant solubility product.[16] Consequently, the diagrams exhibit straight lines for the solubility of the pure compounds and a curved co-crystal solubility line. The delimited regions in the phase diagrams represents the conditions at which a pure compound (INA, CBZ, or CBZ:INA) or a mixture of co-crystal and co-former are in thermodynamic equilibrium with the solvent at constant temperature. Pure CBZ:INA co-crystal was produced by dissolution and re-crystallisation of a mixed suspension composition ($x_{\mathrm{INA}} = 0.02$,, $x_{\mathrm{CBZ}} = 0.02$). The produced crystalline material was consistent with INA:CBZ form I[17] (Appendix C.2) The analysis of the solids by HPLC indicates a 1:1 co-formers ratio in the crystalline structure.

Following the production of the co-crystal, its separation from one of the co-formers (INA) was carried out using a strong electric field. To conduct EFEC experiments on CBZ-INA systems, the mixture concentration was determined by using the isothermal phase diagram at the initial and final temperatures (Figure 6.6).

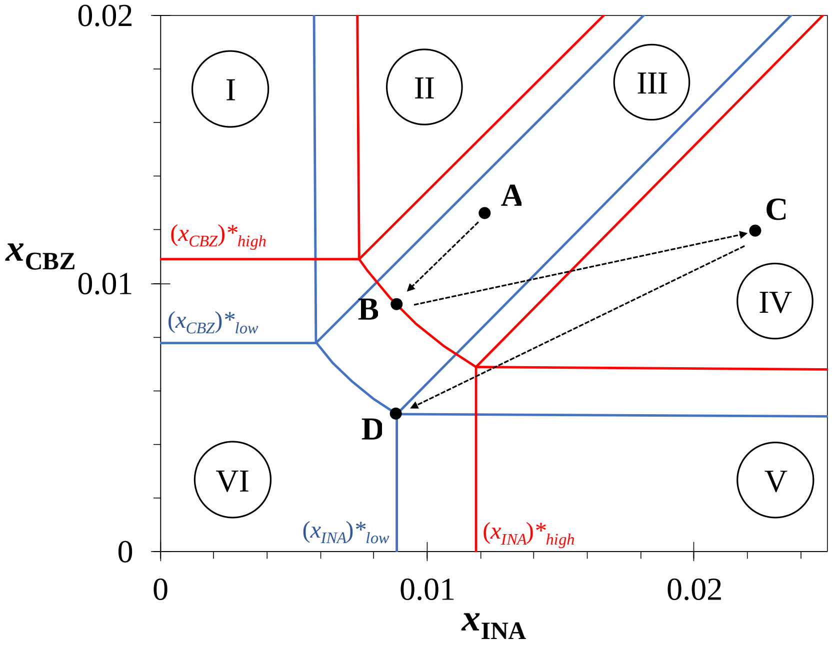

Figure 6.6. Schematic of the CBZ-INA system evolution over the EFEC separation process represented in a phase diagram of the 1:1 ratio CBZ:INA co-crystal at 22 °C (red lines) and 15°C (blue lines). The straight and curvature lines delimit the regions in which: I. CBZ and solution, II. CBZ, CBZ:INA, and solution, III. CBZ:INA and solution, IV. INA, CBZ:INA, and solution, V. INA and solution, and VI. solution are in thermodynamic equilibrium. The solubility of pure CBZ at the initial temperature $T^*_{high} = 22$ °C and final temperature $T^*_{low} = 15$ °C are respectively represented by $(x_{CBZ})^*_{high}$ and $(x_{CBZ})^*_{low}$. The solubilities of pure INA at T^*_{high} and T^*_{low} are $(x_{INA})^*_{high}$ and $(x_{INA})^*_{low}$. The equilibrium concentration of the co-crystal at the initial and final temperatures are depicted by the curvature red and blue lines, respectively. The arrows and points A, B, C, and D represent the composition evolution of the CBZ and INA mixtures over an EFEC separation process. Points A and C are overall compositions. The overall composition of C is made by adding INA and the co-crystal to point B. Points B and D refer to the equilibrium concentrations at 22 and 15 °C, respectively.

The overall composition of the resulting suspension is described by point C ($x_{\mathrm{CBZ}} = 0.011$, $x_{\mathrm{INA}} = 0.021$) in the phase diagram, which correspond to a suspension density of 30.8 mg/mL composed of 15.9 mg/mL of CBZ:INA and 14.8 mg/mL of INA. The suspension was cooled from 22 to 15 °C in the presence of an electric field, inducing the accumulation of crystals on both electrodes. At the end of the experiment, the solution was equilibrated at the eutectic point D, with a composition ($x_{\mathrm{CBZ}} = 0.005$, $x_{\mathrm{INA}} = 0.009$). This gives an overall suspension density of 16.4 mg/mL of INA and 24 mg/mL of CBZ:INA. During this process and the subsequent 6 h at 15 °C in the presence of the field, layers of the solid materials developed on both electrodes (Figure 6.3.c). The total amount of the product recovered from the anode was 42 mg with a purity of 95.5 ± 0.9 %wt in INA, which results in a yield of 40.7 %. The material retrieved from the cathode was 103 mg with a purity in the co-crystal of 69.3 ± 4.9% estimated from a 1:1 molar ratio between the CBZ and INA in the crystalline phase. The recovery of the co-crystal from the cathode yielded 49.5%. The solid material from each electrode were analysed by XRPD (Appendix C.2), which confirmed that the main phase on the cathode was the form I of the co-crystal,[17] and the main crystalline phase on the anode corresponded to the reference INA form I.[29] Although INA was recovered with a high purity from the anode, the purity of the co-crystal was below 70%, which suggests that the stoichiometry was off due to an excess of INA. Dipole-dipole interaction between INA molecules in the two different crystal phases may explain the unexpected higher concentration of INA impurities on the cathode. A deeper study into the co-crystal and co-former separation may be needed to optimize the separation of both compounds. On the other hand, it seems that mainly the co-crystal grows during the immobilization phase, possibly because a rapid formation of the co-crystal with a lower solubility. A large amount of crystals remained in the bulk at the end of the EFEC process, which reveals a poor immobilization of the crystals on the electrodes. The optimization of the cell geometry, a higher initial temperature, and/or a longer period at the final temperature in the presence of the electric field might contribute to rise the yield.

6.3.4. Separation of Compounds that Collect at the same electrode.

The separation of compounds that collect on the same electrode under a strong electric field was attempted in INA and CAF mixtures in 1,4-dioxane. This model system was selected after preliminary tests showed the same behaviour of both compounds in the presence of the field (Chapter 4). Additionally, further solubility analysis confirmed that INA and CAF do not show co-crystal formation in dioxane (Appendix C.1).

The two-step cooling EFEC procedure described in Figure 6.7 for the separation of compounds with the same behaviour in a non-uniform electric field, is only effective if the crystalline phase that is first immobilized remains and continues growing on the electrode during the second cooling step once the direction of the electric field is reversed. To verify this, a suspension of pure INA in dioxane underwent the two-steps cooling procedure. Upon applying the first cooling step in the presence of the field, the suspended crystals accumulated on the anode and formed a layer onto the electrode. Before commencing the second cooling step, the polarity of the power supply was reversed. The immobilized layer remained on the electrode, showing that the immobilization in the first cooling step is sufficiently strong to withstand the electrophoretic forces acting on the crystals. At the end of the two-steps procedure, the weight of the recovered material indicates that INA grew on the surface of the original anode during the second cooling step. No visible crystals immobilized on the new anode. The obtained results indicate that the developed two-step EFEC procedure is suitable for the separation of compounds that present the same behaviour under an electric field.

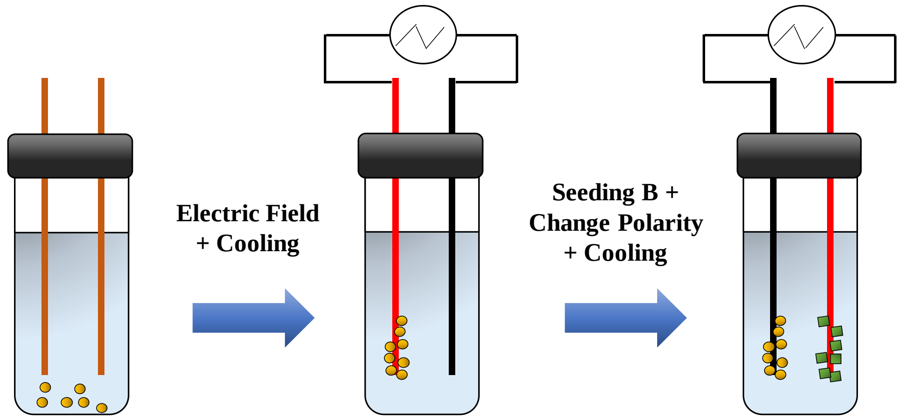

Suspension of crystals A (●) in a solution of A and B (🟩)

Crystals accumulate and grow on one electrode (e. g. anode), which induces its immobilization

Crystal A and B grow and immobilized at the new cathode and anode, respectively

Figure 6.7. Schematic diagram of the EFEC separation procedure for mixtures of crystalline compounds that collect on the same electrode under the application of a strong non-uniform electric field.

Following the verification of the immobilization of the crystals on one electrode during the two-step cooling EFEC, the separation of a mixed solution of INA (23.4 mg/mL) and CAF (33.9 mg/mL) in 1,4-dioxane was carried out in an 8 mL glass vial. At 40 °C in equilibrium, the suspension consisted of only CAF crystals (5.9 mg/ml) while INA was undersaturated in solution (c_{INA} = 23.4 mg/mL < c^*_{INA}= 33.8 mg/ml). After equilibration, a DC potential difference of 7.5 kV was applied to the suspension, inducing the motion and accumulation of suspended crystals on the anode. The immobilisation of the crystals on the surface of the electrode was realised by cooling to 30 °C at a set rate of 0.17 °C/min and holding the temperature overnight in the presence of the electric field. Subsequently, 49.8 mg of INA crystals were added to the system, and an applied potential difference of -7.5 kV was maintained during the second cooling crystallisation step from 30 to 15 °C. An approximately suspension density of 8.3 mg/mL of INA is then produced as CAF crystals were immobilized onto the original anode. After approximately 15 h, a layer of crystals formed on the new anode, while the formed layers during the first cooling remained on the counter electrode. Figure 6.8 presents the evolution of CAF and INA through the separation process. At the end of the experiment, 76.8 mg of crystalline product with a purity in CAF of 95% weight was recovered from the original anode, which results in a yield of 59.8%. The residue from the new anode (55.2 mg) was 98.3%wt of INA, with a yield of 49.5%. The NMR spectra are shown in Appendix C.3. XRPD analysis reveal that the form β of CAF[24] and INA form I[29] were the main phases recovered from the original and the new anode, respectively (Appendix C.2).

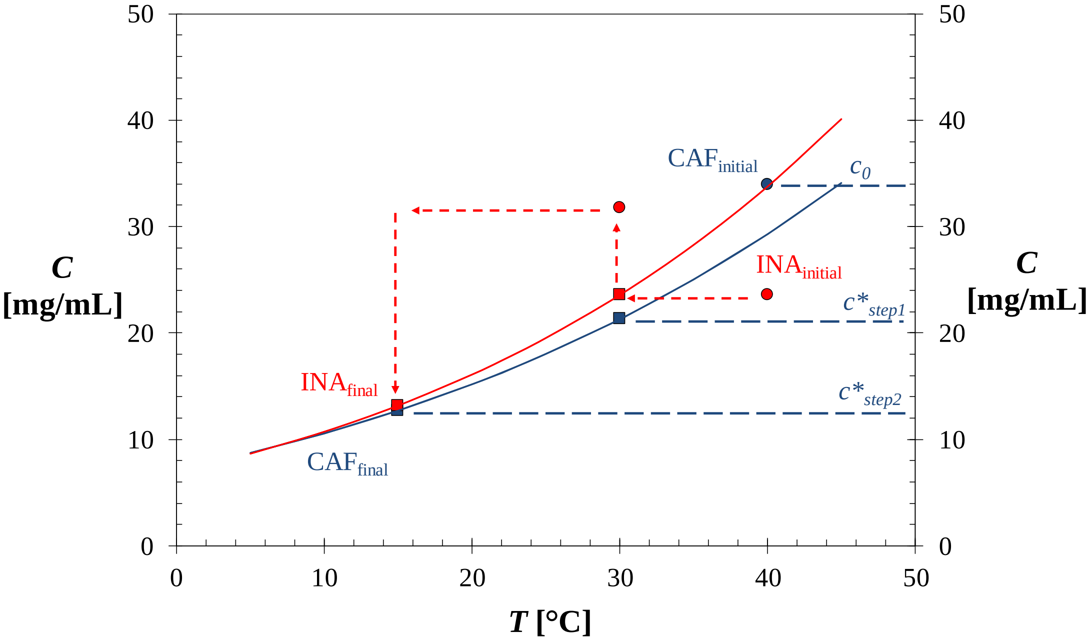

Figure 6.8. Schematic diagram of the process evolution for the two steps cooling EFEC. The initial and final conditions for each step are represented by ● and ■, respectively. The blue and red lines represent the solubility of CAF and INA estimated from the van 't Hoff equation. For CAF, c_0 is the initial concentration and c^*_{step1} and c^*_{step2} are the concentration at equilibrium at the end of each cooling step. The red arrows indicate the evolution of INA through the experimental period: crystallisation from 45 to 30 °C, seeding, and equilibration at the final temperature T = 15 °C.

A second suspension supersaturated initially with INA and undersaturated with CAF underwent the two-steps cooling EFEC, with INA crystals that remained in the suspension at the end of the first cooling step moving towards the new anode after reversing the polarity. Unattached INA particles may lower the purity of the second compound by their accumulation at the new anode upon reversing the electric field direction. Thus, a filtration step after the first cooling to remove unattached crystals may minimize the presence of impurities on the second electrode. A two-steps cooling EFEC was then attempted in a 6 mL mixture composed of approximately 21 mg/mL of CAF and 39 mg/mL of INA in 1,4-dioxane prepared at 40 °C, which corresponds to a suspension density of 5.2 mg/mL of INA in an undersaturated solution of CAF. During the application of the electric field and cooling crystallisation from 40 to 30 °C, INA crystals attach to the anode while CAF remains dissolved in solution at the final temperature. The electrodes are then withdrawn from the solution and placed into a solution saturated with both CAF and INA at 30 °C. Afterwards, 49.8 mg of CAF crystals were seeded and, at a reversed polarity, a DC potential difference of -7.5 kV was established between the electrodes before the temperature was reduced to 15 °C.

The final conditions were held overnight and the crystalline product collected on both electrodes (Figure 6.8) were separately recovered and characterised by ^{1}H-NMR and XRPD. A total amount of 54.6 mg of INA with a purity of 98.9% was recovered from the original anode, which corresponded to a yield of 37.5%. The yield of CAF from the new anode was 61.8%, resulting from 63 mg of collected product with a purity of 94.9%. The XRPD patterns from the material collected from the new and the original anode exhibit only crystalline CAF form beta[24] and INA form I,[29] respectively. Therefore, this second approached to separate compounds that collect on the same electrode prevents contamination of the product on the new anode by the unattached crystals at the end of the first cooling step.

6.4. Discussion

A strong inhomogeneous electric field applied to a suspension of crystals in non-polar solvents triggers a selective motion of the suspended particles towards one of the electrodes. In a previous study (Chapter 4) we demonstrated that organic crystals of small molecules suspended in non-polar solvents gained a surface charge.

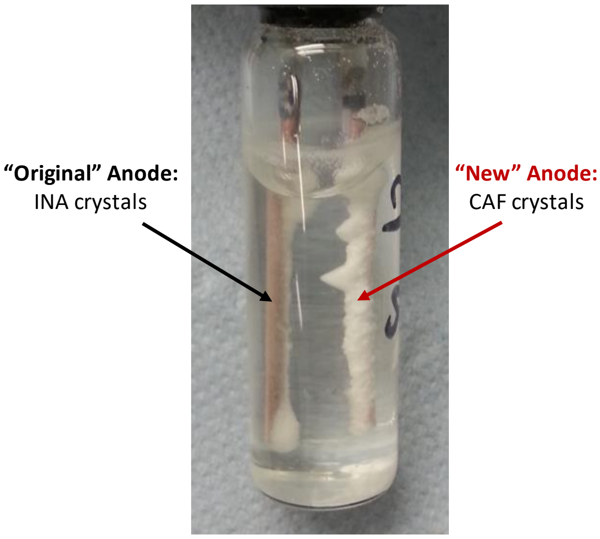

Figure 6.9. The two-step cooling EFEC separation was successfully applied for the separation of particles that collect on the same electrode in the presence of an electric field. The recovered crystals from the original anode showed a purity of 98.9% on CAF, while on the new anode INA crystals were recovered with a purity of ca. 95%.

In the presence of a sufficiently strong electric field (> 0.4 MV/m), the crystalline particles are attracted to the electrode of opposite polarity by electrophoresis. Assuming a larger polarizability of the solid phase than the fluid medium, the crystals are subjected to the combined force of electrophoresis and positive dielectrophoresis towards the strong electric field region located at the electrode surface. The net charge gained by particles in non-polar solvents has been discussed by Schreuer et al.[30] who described a charging mechanism in which the surface charge originates from dissociation of bounded ions to the particle due to the application of an electric field. In this work, we have exploited the electrokinetic phenomena for the separation of complex mixtures of crystals of small organic molecules. To carry out the separation of the crystalline phases in a complex mixture by a single cooling step EFEC, a number of prerequisites have to be fulfilled. First, the compounds to be separated have to collect on opposite electrodes, from which pure crystals of each phase can be separately recovered. Additionally, the target compounds should not form mixed solid phases such as co-crystals, as the process occurs in the compositional region in the phase diagram where mixed solid phases are likely to form. Additionally, the electrical conductivity of the solvent should be low to prevent electrical current and faradaic reactions. The solubility of the organic compounds in the mixture should be high enough to achieve considerable yields, while the suspension density in the process should be low enough to prevent an excessive collection of crystals on the electrode, that may impede their immobilization on the electrode surface.

First, to become familiarized with the EFEC technique, we attempted the separation of CAF and NA from their mixture in dioxane. Upon application of an electric field, a collection of crystalline phases on both electrodes occurs. The immobilization of the crystals on the surface of the electrode can be induced by reducing the temperature, which prompts the formation of layers of crystals on the electrode due to crystal growth at the expense of supersaturation. Purity values larger than 94% were obtained by EFEC separation, which indicates the effectiveness of the purification method driven by electric fields. Following the separation of CAF and NA, the suitability of the technique to isolate an API from one of its synthesis-related impurities was assessed in a mixture of ASP and SSA in toluene. The application of the purification technique to this mixture showed purities of approximately 94 %wt of ASP and 98 %wt of SSA from the solids separately recovered from the anode and cathode.

The separation of compounds that collect on opposite electrodes was also carried out in a co-crystal (INA:CBZ) and co-former (INA) mixture. Although the solids on the anode showed a purity of 96 %wt of INA, the purity of the co-crystals based on the moles of INA in the CBZ:INA phase was approximately 70%. In a previous study on pure suspension of INA in dioxane, Li et al.[15] observed that the suspended particles form a bridge structure upon the application of an elevated potential difference between the electrodes (7.5 kV). This behaviour may relate to the dipole-dipole interaction between NA particles and formation of a electrorheological fluid discussed in Chapter 4. Therefore, upon the application of the potential difference and provided a greater dielectric constant of INA compared to the fluid medium, the form dipole interacts with similar particles by dielectrophoresis, inducing the formation of head-to-tail chains structures. In the co-crystal mixture, this interaction may occur between INA and the similar crystal in the co-crystal system, which could induce the presence of INA impurities in the INA:CBZ phase immobilize on the electrode. A further investigation into the crystallisation condition, e.g. reducing the seed amount of INA crystal, may provide the optimum conditions to enhance the purity of the isolated co-crystals by EFEC.

The applicability of the separation method can be extended to systems of compounds that collect at the same electrode in the presence of an electric field. The two-step cooling EFEC process proposed for this is validated by the separation of a CAF and INA mixture in 1,4-dioxane resulting in purities larger than 94 %wt. In the two-step cooling EFEC process the first step, in which immobilization of crystals of one compound takes place in a solution undersatured with the other compound, is followed by the second step in which the seeded second compound crystals to the saturated solution are collected and immobilized on the counter electrode by reversing the applied polarity and cooling crystallisation. The immobilized crystals of the first compound remain on the original electrode, withstanding the electrokinetic forces towards the other electrode and even growing on the electrode during the second cooling step. This suggests that supersaturation is consumed by crystal growth instead of bulk crystal nucleation that would form particles that are attracted by the opposite electrode. For the two steps cooling EFEC separation, non-immobilized crystals from the first cooling step may be a considerable source of impurities in the second compound product layer. This can be minimized by adjusting the composition of the system or by introducing a recycling step in which the suspended crystals are removed from solution before starting the second step.

Although separation was achieved with high purity values, the yield was lower than 62% for all the EFEC separation processes. The low yield may be associated to an incomplete immobilization of the crystals on the electrodes. This might explain the significantly lower yield obtained in the separation of ASP and SSA from their mixture in toluene. The low solubility change of both compounds in the solvent system provides a small mass of growth of the crystals on the electrodes, which might compromise the immobilization of the layers. Additionally, crystalline material being scrubbed off when retrieving the electrodes and seed crystals remaining on the bottom of the crystalliser over the course of the experiments may also contribute to the low yield. The yield limitation of the method could then be also minimized through an improved geometry of the electric cell based on hydrodynamic simulations combining the effect of both electrokinetic forces and the resulting fluid dynamics.

6.5. Conclusions

The Electric Field Enhanced Crystallisation (EFEC) method described by Li et. al.[15] has been successfully applied for the separation of the crystalline phases of mixtures of CAF and NA, ASP and SSA, and CBZ:INA and INA suspended in non-polar solvents. A combination of electrophoresis and dielectrophoresis exerted on the compounds in the mixture induces a translation motion of the crystalline particles that collect on a specific electrode. This behaviour of the particles under an electric field enables their separation on opposite electrode by exploiting their different electrical properties. Once the different crystals are on different electrodes they can be immobilized in the surface of the electrodes by reducing the temperature. In addition, a two-steps EFEC method has been developed for the separation of compounds that collect on the same electrode with high purity solid phases collected from each electrode.

Therefore, the in-situ separation and concomitant crystallisation of mixtures of crystalline solutes in non-polar solvents can be realised through EFEC. An apparent limitation of the technique is the low recovery. Inefficient immobilization of the compounds on the surface of the electrode and the loss of crystalline material during the removal of the electrodes seem to be the main contribution to the low yield. An optimization of the crystallisation conditions may help to enhance the yield of the process. In addition, the loss of the material, and seed crystals remaining at the bottom of the crystalliser may be minimized by using a different crystallisation cell geometry that permits a better distribution of the electrokinetic forces.

6.6. References

1. Garside, J. Industrial crystallization from solution. *Chem. Eng. Sci.* 40, 3–26 (1985).
2. Ter Horst, J. H., Schmidt, C. & Ulrich, J. *Fundamentals of Industrial Crystallization. Handbook of Crystal Growth: Bulk Crystal Growth: Second Edition* 2, (Elsevier B.V., 2014).
3. Urwin, S. J. *et al.* A Structured Approach To Cope with Impurities during Industrial Crystallization Development. *Org. Process Res. Dev.* 24, 1443–1456 (2020).
4. Qiu, F. & Norwood, D. L. Identification of pharmaceutical impurities. *J. Liq. Chromatogr. Relat. Technol.* 30, 877–935 (2007).
5. Moynihan, H. A. & Horgan, D. E. Impurity Occurrence and Removal in Crystalline Products from Process Reactions. *Org. Process Res. Dev.* 21, 689–704 (2017).
6. Black, S., Dang, L., Liu, C. & Wei, H. On the Measurement of Solubility. *Org. Process Res. Dev.* 17, 486–492 (2013).
7. Koolman, H. C. & Rousseau, R. W. Effects of Isomorphic Compounds on the Purity and Morphology of L-Isoleucine Crystals. *AIChE J.* 42, 147–153 (1996).
8. Deng, Y. *et al.* Process Development and Synthesis of Birinapant: Large Scale Preparation and Acid-Mediated Dimerization of the Key Indole Intermediate. *Org. Process Res. Dev.* 20, 242–252 (2016).
9. Duan, S. *et al.* Palbociclib Commercial Manufacturing Process Development . Part I : Control of Regioselectivity in a Grignard-Mediated S N Ar Coupling. *Org. Process Res. Dev.* 20, 1191–1202 (2016).
10. Revalor, E. *et al.* Usual and unusual crystallization from solution. *J. Cryst. Growth* 312, 939–946 (2010).
11. Li, F. & Lakerveld, R. Influence of Alternating Electric Fields on Protein Crystallization in Microfluidic Devices with Patterned Electrodes in a Parallel-Plate Configuration. *Cryst. Growth Des.* 17, 3062–3070 (2017).
12. Koizumi, H., Tomita, Y., Uda, S., Fujiwara, K. & Nozawa, J. Nucleation rate enhancement of porcine insulin by application of an external AC electric field. *J. Cryst. Growth* 352, 155–157 (2012).
13. Salafi, T., Zeming, K. K. & Zhang, Y. Advancements in microfluidics for nanoparticle separation. *Lab Chip* 17, 11–33 (2017).
14. Tao, Y., Ren, Y., Yan, H. & Jiang, H. Continuous separation of multiple size microparticles using alternating current dielectrophoresis in microfluidic device with acupuncture needle electrodes. *Chinese J. Mech. Eng.* 29, 325–331 (2016).

15. Li, W. W., Radacsi, N., Kramer, H. J. M., van der Heijden, A. E. D. M. & ter Horst, J. H. Solid Separation from a Mixed Suspension through Electric-Field-Enhanced Crystallization. *Angew. Chemie Int. Ed.* 1–5 (2016).

16. Ter Horst, J. H., Deij, M. A. & Cains, P. W. Discovering New Co-Crystals. *Cryst. Growth Des.* 9, 1531–1537 (2009).

17. Ter Horst, J. H. & Cains, P. W. Co-crystal polymorphs from a solvent-mediated transformation. *Cryst. Growth Des.* 8, 2537–2542 (2008).

18. Li, M., Qiao, N. & Wang, K. Influence of sodium lauryl sulfate and Tween 80 on carbamazepine-nicotinamide cocrystal solubility and dissolution behaviour. *Pharmaceutics* 5, 508–524 (2013).

19. Maeta, A., Sano, M., Fukuwatari, T. & Shibata, K. Simultaneous measurement of nicotinamide and its catabolites, nicotinamide N-oxide, N1-methyl-2-pyridone-5-carboxamide, and N1-methyl-4-pyridone-3-carboxamide, in mice urine. *Biosci. Biotechnol. Biochem.* 78, 1306–1309 (2014).

20. Reepmeyer, J. C. & Kirchhoefer, R. D. Isolation of salicylsalicylic acid, acetylsalicylsalicylic acid, and acetylsalicylic anhydride from aspirin tablets by extraction and high-pressure liquid chromatography. *J. Pharm. Sci.* 68, 1167–1169 (1979).

21. Nanev, C. Recent Insights into the Crystallization Process; Protein Crystal Nucleation and Growth Peculiarities; Processes in the Presence of Electric Fields. *Crystals* 7, 310 (2017).

22. Hammadi, Z. & Veesler, S. S. New approaches on crystallization under electric fields. *Prog. Biophys. Mol. Biol.* 101, 38–44 (2009).

23. Van Der Hoeven, P. C. & Lyklema, J. Electrostatic stabilization in non-aqueous media. *Adv. Colloid Interface Sci.* 42, 205–277 (1992).

24. Lehmann, C. W. & Stowasser, F. The crystal structure of anhydrous β-caffeine as determined from X-ray powder-diffraction data. *Chem. - A Eur. J.* 13, 2908–2911 (2007).

25. Wright, W. B. & King, G. S. D. The crystal structure of nicotinamide. *Acta Crystallogr.* 7, 283–288 (1954).

26. Acharya, S., Daniel, A., Gyadangi, B. & Ramsamy, S. Isolation, characterization of a potential degradation product of aspirin and an HPLC method for quantitative estimation of its impurities. *J. Chromatogr. Sci.* 53, 1491–1497 (2015).

27. Wheatley, P. J. The Crystal and Molecular Structure of Aspirin. *J. Chem. Soc.* 6036–6048 (1964).

28. Greener, B., Archibald, S. J. & Hodkinson, M. Hydrogen bonding in amorphous salsalate. *Agnew. Chem. Int. Ed.* 39, 3601–3604 (2000).

29. Aakeröy, C. B., Beatty, A. M., Helfrich, B. A. & Nieuwenhuyzen, M. Do polymorphic compounds make good cocrystallizing agents? A structural case study that demonstrates the importance of synthon flexibility. *Cryst. Growth Des.* 3, 159–165 (2003).

30. Schreuer, C., Vandewiele, S., Strubbe, F., Neyts, K. & Beunis, F. Electric field induced charging of colloidal particles in a nonpolar liquid. *J. Colloid Interface Sci.* 515, 248–254 (2018).

31. Habgood, M., Deij, M. A., Mazurek, J., Price, S. L. & Ter Horst, J. H. Carbamazepine co-crystallization with pyridine carboxamides: rationalization by complementary phase diagrams and crystal energy landscapes. *Cryst. Growth Des.* 10, 903–912 (2010).

Chapter 7. Conclusions

The isolation of a valuable product from process impurities is a demanding and challenging task in highly regulated industries such as pharmaceuticals. Crystallisation is commonly applied for impurity removal. However, the purification technique may be inefficient when the physicochemical properties of the product and impurity are similar, such as in chiral systems, or when the impurity concomitant crystallise alongside the product. These crystallisation issues can be overcome by the integration of electric fields as a process intensification method. In this thesis, the interactions between an externally applied electric field of an elevate amplitude and suspensions of crystalline particles, and between the field and solutions of organic compounds were investigated.

To study the effects of electric fields on suspensions of crystalline particles and crystallising solutions, we need well-defined systems to enable the design of crystallisation processes. In Chapter 3, a thermodynamic study of 18 APIs in three non-polar systems was carried out. Non-polar solvents minimize chemical reactions upon the application of an electric field, and therefore this type of solvents has been used for crystallization and separation processes in the presence of electric fields. The temperature dependent solubility shows greater solubility values of the studied compounds in 1,4-dioxane compared to that in toluene and cyclopentyl methyl ether, which may be related to the greater hydrogen bonding propensity of dioxane. The solubility data can be correlated by empirical models, such as the van' t, Apelblat, or the λh equations. From these models, the van' t Hoff equation provides a simple tool to extrapolate and interpolate the solubility data of the studied compounds at any given temperature with small deviations from the measured solubilities.

The activity coefficient is accessible from solubility data and the thermodynamic properties of the solid phase, and provides information of the solubility behaviour of a given system. All the studied compounds in toluene positively deviate from ideality, while the activity coefficient of the same compound in the other two solvents exhibit positive and negative deviations. The energy interaction between the solute and solvent molecules was estimated from the Wilson equation, which describes the deviation from ideality using activity coefficient values.

Subsequently, in Chapter 4 we identified the mechanisms behind the effect of electric fields on well-defined equilibrated suspensions. Uniform and non-uniform direct-current (DC) electric fields applied across equilibrated systems contained in custom-made electric cells trigger a motion of particles in suspension, that migrate towards a specific electrode. A crystalline compound suspended in a given solvent always collect at the same electrode. This particular motion was corroborated by changing the polarity of the power supply, inducing the detachment of the particles from an electrode and their motion towards the counter electrode. Different compounds show dissimilar behaviour in the electric field, which at least hints that the separation of complex mixtures can be achieved by the use of electric fields. To manipulate suspended particles, a large potential difference needs to be applied. Under these conditions, non-polar solvents resist electrical current and therefore, chemical reactions are minimized. The application of a non-uniform electric field to neat solvents induces a swirl motion, referred to as electro-osmotic flow. This phenomenon is however considered to have a minor effect on the behaviour of particles under an electric field. Particle motion in an electric field occurs due to the combination of different electrokinetic phenomena. In the presence of an inhomogeneous electric field, the suspended crystals show a tangential velocity to the electrodes, which indicates the presence of positive dielectrophoresis. The specific collection on one of the electrodes is likely the result of electrophoretic forces acting on the particle surface, which implicates that the organic crystals gain a net charge in the used fluid media. Thus, the application of an electric field initiates a motion towards the electrode of opposite charge due to Coulomb forces. The sign of the zeta-potential, which was obtained by light scattering measurements, was consistent with the observed behaviours.

Following the study of the interactions of an electric field with suspension of particles, the crystallisation enhancement effect of a strong field on a small organic molecule (isonicotinamide) in 1,4-dioxane is described in Chapter 5. Undersaturated solutions of the organic compound in the apolar solvent underwent cooling crystallisation in the presence and absence of the electric field. In the presence of a strong DC electric field, nucleation occurs at higher temperatures and thus lower supersaturations. This phenomenon contributes to the increase of the process yield in the presence of the field. Under an electric field, the probability of nucleation increases and the induction time decreases. The effect of the field strength was roughly inversely proportional to the supersaturation ratio. Nucleation rates were determined from successful crystallisation experiments. A comparison of the nucleation rate between untreated systems and systems under an electric field suggests that the presence of the field enhances nucleation kinetics. A plausible explanation is an increased localized supersaturation of isonicotinamide in the vicinity of the electrodes due to electrokinetic forces attracting the monomer of the organic compound towards the electrode, which results in the increase of the frequency of successful attachments of building units.

Since the application of an electric field allows for the manipulation of particles in a suspension (Chapter 4) and enhances the phase separation process (Chapter 5), this phenomenon can be combined with crystallisation to in-situ isolate a target product at the same time that promotes crystallisation. In Chapter 6, complex mixtures of compounds that collect on opposite electrodes under an electric field underwent cooling crystallisation in the presence of a strong non-uniform electric field. Three different systems were studied, comprising: 1) caffeine and nicotinamide, 2) aspirin from one of its synthesis impurities (salsalate), and 3) isonicotinamide:carbamazepine co-crystal and isonicotinamide. Upon the application of the field, electrokinetic forces trigger the collection of the crystalline particles on both electrodes. The immobilization of the crystals on the electrode surface is induced by crystals growth at the expend of supersaturation once the suspended particles collect at the electrodes. The crystalline phases separately collected from both electrodes showed purities greater than 93%, with the exception of the co-crystal.

Additionally, a two-step method was developed for the separation of compounds with similar behaviour in the electric field. Isonicotinamide and caffeine crystals were separated with purities greater than 95% using this novel method. Therefore, the in-situ separation and concomitant crystallisation of binary solute mixtures of crystalline compounds can be realized in non-polar solvents.

The work conducted in this thesis provides a deeper understanding of the interactions between an electric field and suspensions of crystalline particles and between the electric field and crystallisation processes. The application of the field triggers a particular motion of particles in suspension and enhances the crystallisation process of small organic molecules. By relating particle and solution properties to the observed phenomena we can anticipate the effects of the electric field. Thus, the electric field phenomena can be exploited to purify and separate two crystalline products in one single step, offering an intensification tool for crystallisation processes.

7.1. Recommendations

The electric field separation technique proved to be effective in isolating and purifying the crystalline phases in a mixture, and therefore can be implemented in manufacturing operations to aid purification and separation processes. However, the low recovery yield obtained or the use of apolar solvents may be seen as a limitation of the technique. The findings in this thesis provide noteworthy contribution for further research into the optimization of the separation technique driven by electric fields.

As discussed in Chapter 4, the behaviour of crystalline particles in an electric field depends on the surface charge. The origin of the net charge is system dependent, and therefore the use of surface modifiers such as surfactants have been used to control the surface charge of colloidal particles. On the basis of surfactant and colloid properties, the interaction between them will induce positive or negative charges on the particle surface. The investigation of this phenomenon on suspensions of crystalline particles could bring forth a method to manipulate the surface charge and therefore, influence the behaviour of the particles in an electric field to isolate a target compound.

The strength of the electric field, and therefore the electrokinetic phenomena acting on the suspended particles, and the effect of the field on crystallising solutions varies with the shape of the cell and/or electrode configuration. Thus, the optimization of the field geometry allows for a better control over suspended particles and nucleation. This optimization can be realized based on the studied mechanistic effects of the electric fields on suspensions of particles (Chapter 4) and crystallising solutions (Chapter 5). In addition, this investigation can be aided by hydrodynamic simulation analyses of the suspended particles in the electric field, which may allow to predict the behaviour of the particles and design the conditions to effectively purify and separate complex mixtures. The investigation into different cell geometries could result in an increase of both the recovery yield and the throughput of the method. For instance, an automated device with multiple outlets could operate in continuous to separate the compounds in a flowing media in different streams. Alternatively, by reducing the scale of the crystallisation cell, weaker electric fields can be used for the manipulation of particles, which may allow for the use of a more extensive variety of solvent systems.

Appendix A.

A.1. DSC analysis of 18 API and intermediates.

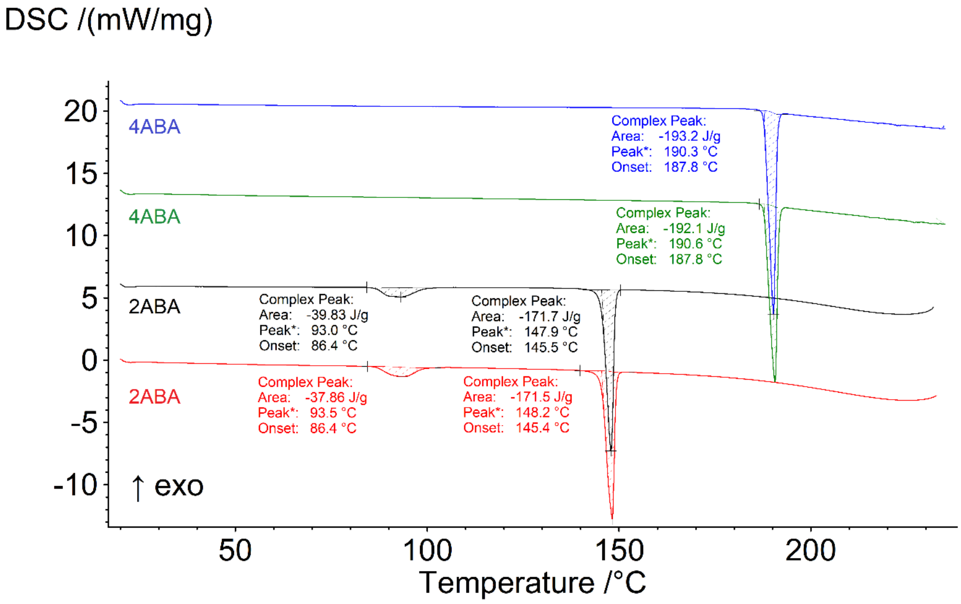

Figure A.1. DSC spectra of 4ABA (blue), repeated 4ABA (green), 2ABA (black), and repeated for 2ABA (red). A single endothermic event with an onset temperature at approximately 188 °C and a peak temperature of 190 °C was measured for 4ABA. Two endothermic events was observed for 2ABA. The first event occurred at an onset temperature of *ca*. 86 °C, while the second event was observed at an onset temperature of 145 °C.

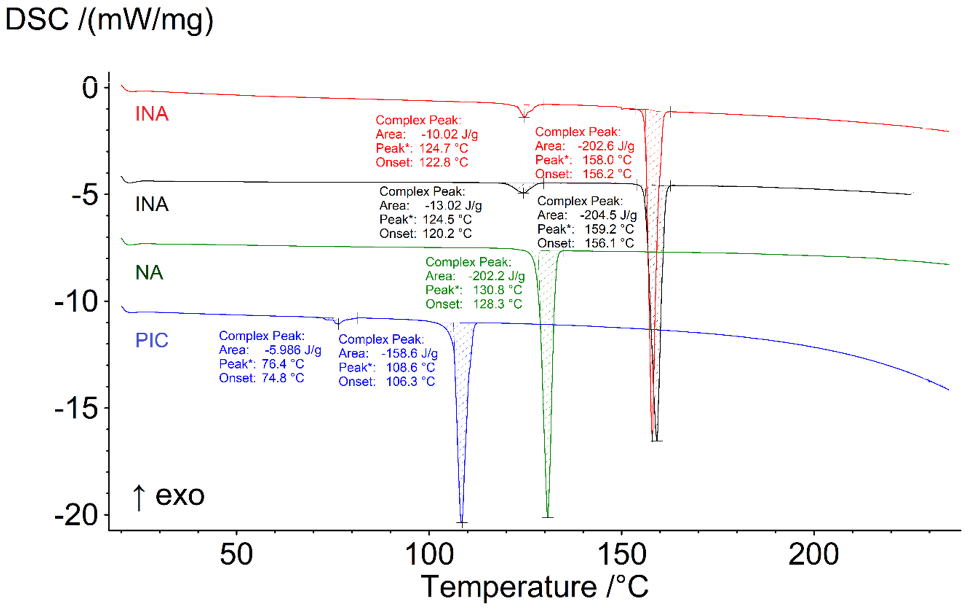

Figure A.2. DSC spectra of PIC (blue), NA (green), INA (black), and repeated for INA (red). A single endothermic event was observed for NA, with an onset temperature at approximately 128 °C. Two endothermic events were observed for PIC and INA. For PIC, the first event occurred at an onset temperature of *ca*. 75 °C, the second event was observed at an onset temperature of 106 °C. For INA, the peak temperatures of the first and second endothermic events were respectively 125 °C and 159 °C.

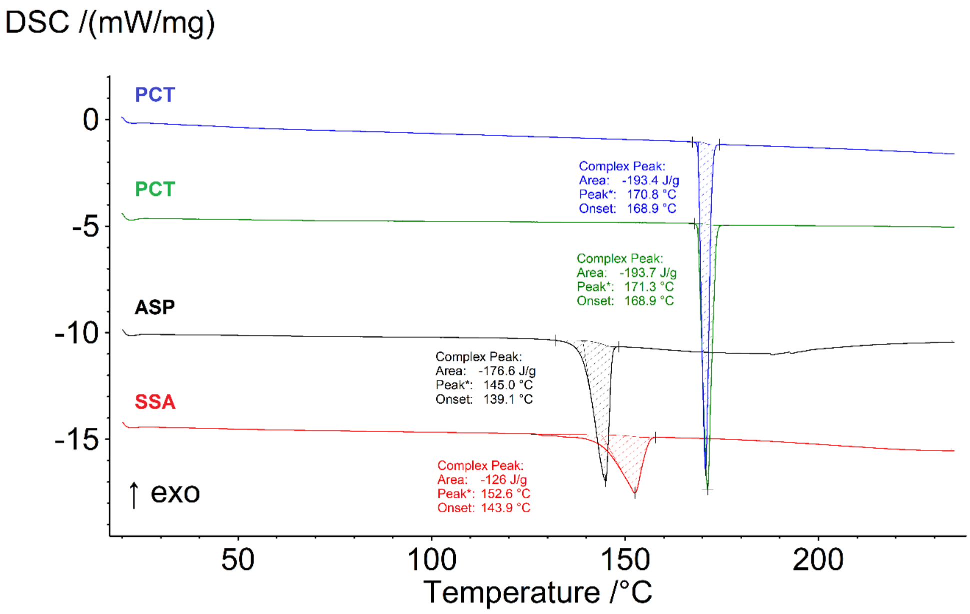

Figure A.3. DSC analysis data for PCT (blue), repeated PCT (green), ASP (black), and SSA (red). The thermal analyses showed a single endothermic event for all the compounds, with peak temperatures for PCT, ASP and SSA of approximately 171 °C, 145 °C, and 153 °C, respectively.

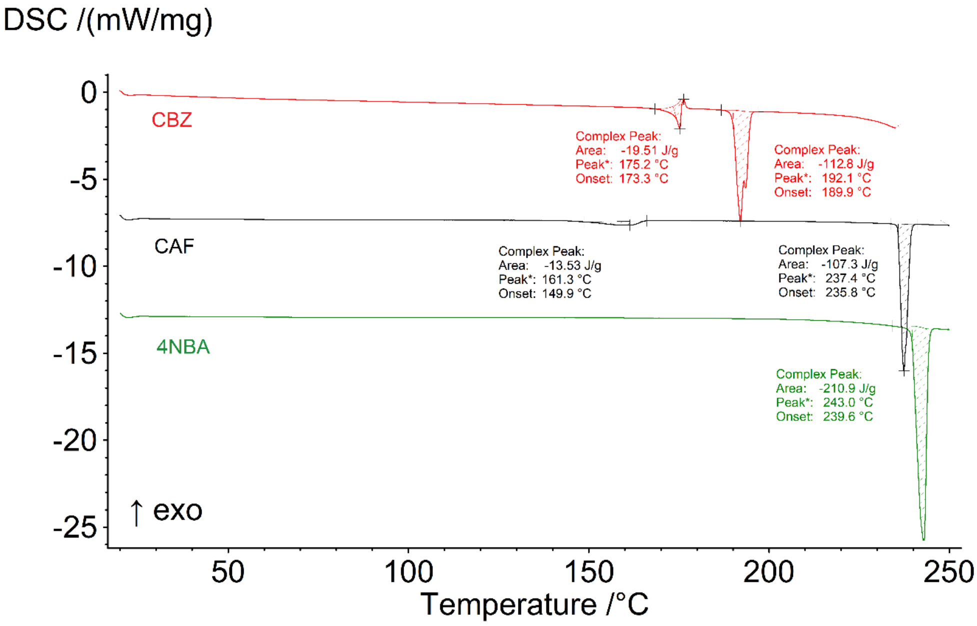

Figure A.4. DSC spectra of 4NBA (green), CAF (black), and CBZ (red). A single thermal event was observed for 4NBA with an onset temperature of approximately 240 °C. For CAF, a small thermal event was observed with an onset temperature of *ca.* 150 °C, and a main endothermic event with an onset temperature at 236 °C. CBZ showed two endothermic events with an onset temperature of approximately 173 °C and 190 °C.

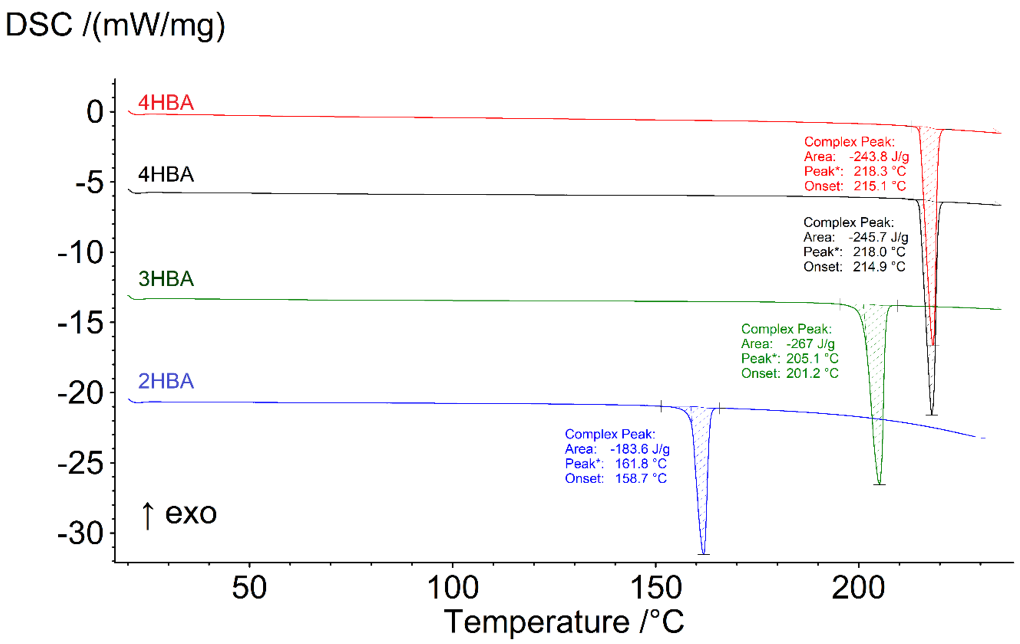

Figure A.5. DSC spectra from the thermal analysis conducted for 4HBA (red), repeated 4HBA (black), 3HBA (green), and 2HBA (blue). A single endothermic event was observed for all the compounds, with peak temperatures at *ca*. 162 °C, 205 °C, and 218 °C for 2HBA, 3HBA, and 4HBA, respectively.

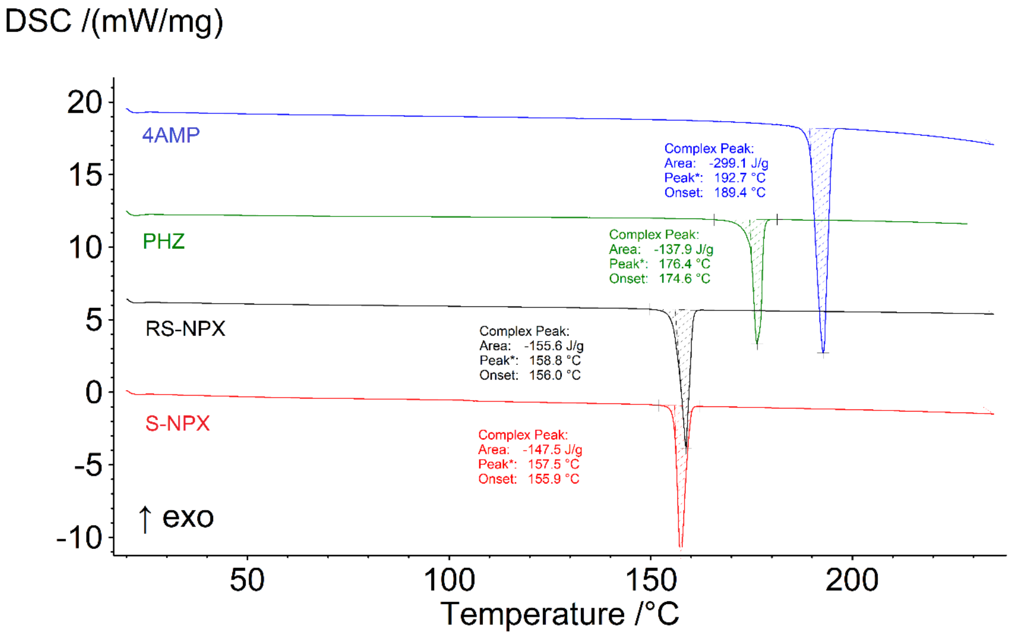

Figure A.6. DSC data for 4AMP (blue), PHZ (green), RS-NPX (black), and S-NPX (red). A single thermal event was observed for all the studied compounds at onset temperatures of approximately 189 °C, 175 °C, 156 °C, and 156 °C for 4AMP, PHZ, RS-NPX, and S-NPX, respectively.

A.2. XRPD Analysis of 18 APIs and intermediates.

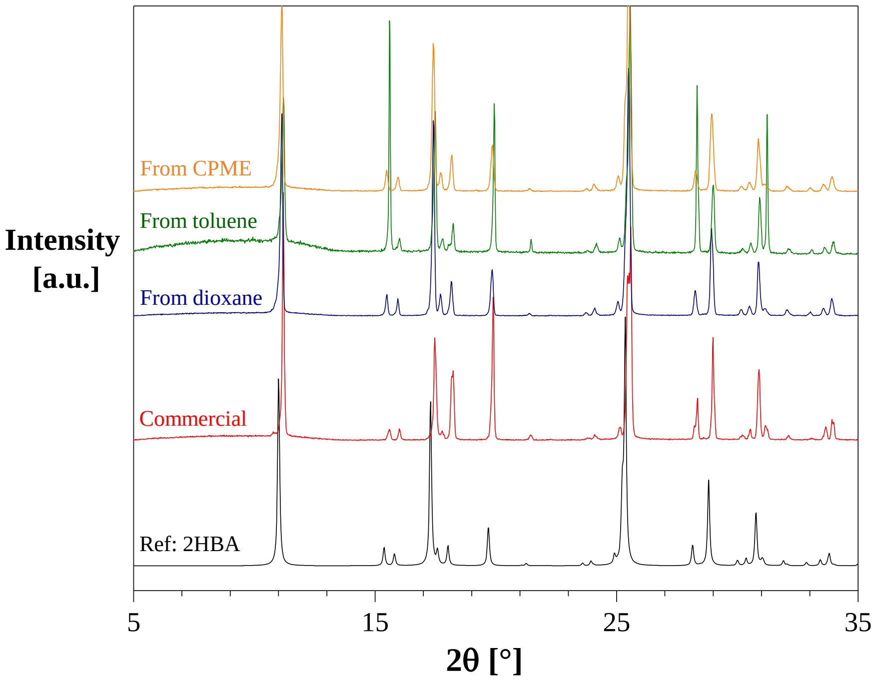

Figure A.7. XRPD spectra of the supplied 2HBA material (red) and the recovered solids from their suspensions in dioxane (blue), toluene (green) and CPME (orange) after 5 days under stirring at approximately 500 rpm at ambient temperature. All the spectra were consistent with the reference SALIAC01 of 2HBA deposited in the CCDC database.

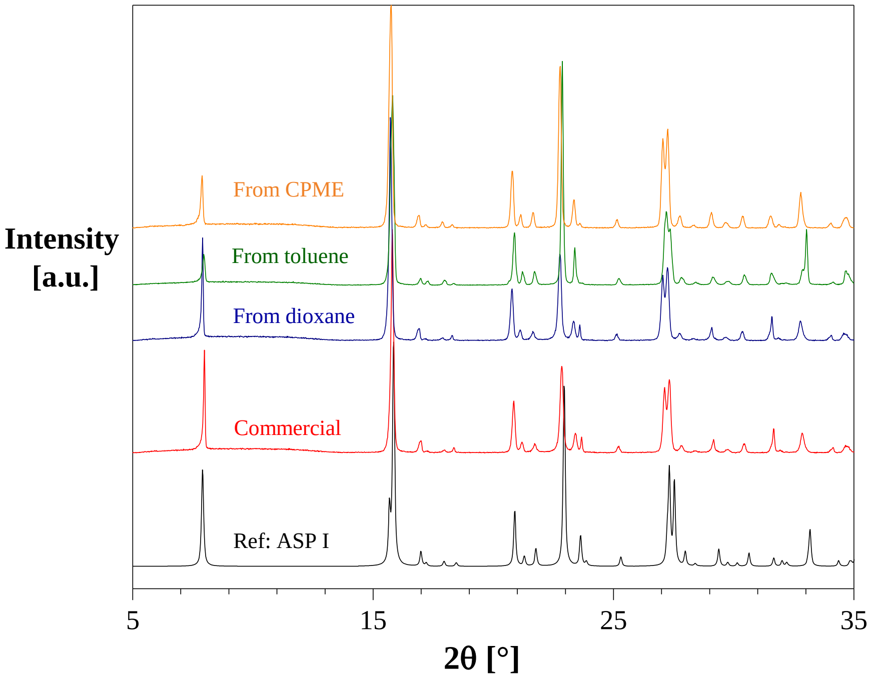

Figure A.8. XRPD spectra of the supplied ASP material (red) and the recovered solids from their suspensions in dioxane (blue), toluene (green) and CPME (orange) after 5 days under stirring at approximately 500 rpm at ambient temperature. All the spectra were consistent with the reference form I (ACSALA) of ASP deposited in the CCDC database.

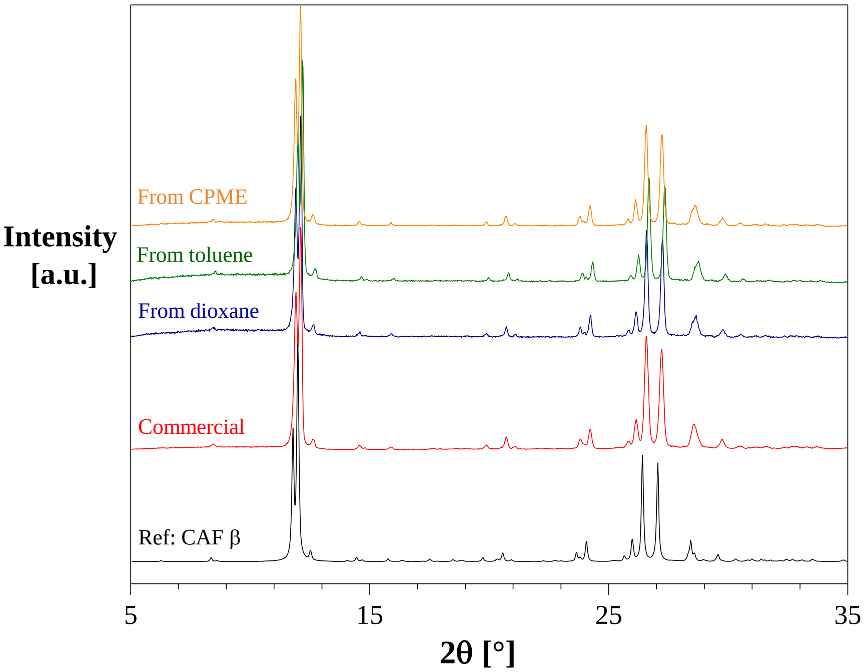

Figure A.9. XRPD spectra of the supplied CAF material (red) and the recovered solids from their suspensions in dioxane (blue), toluene (green) and CPME (orange) after 5 days under stirring at approximately 500 rpm at ambient temperature. All the spectra were consistent with the reference β form (NIWFEE03) of CAF deposited in the CCDC database.

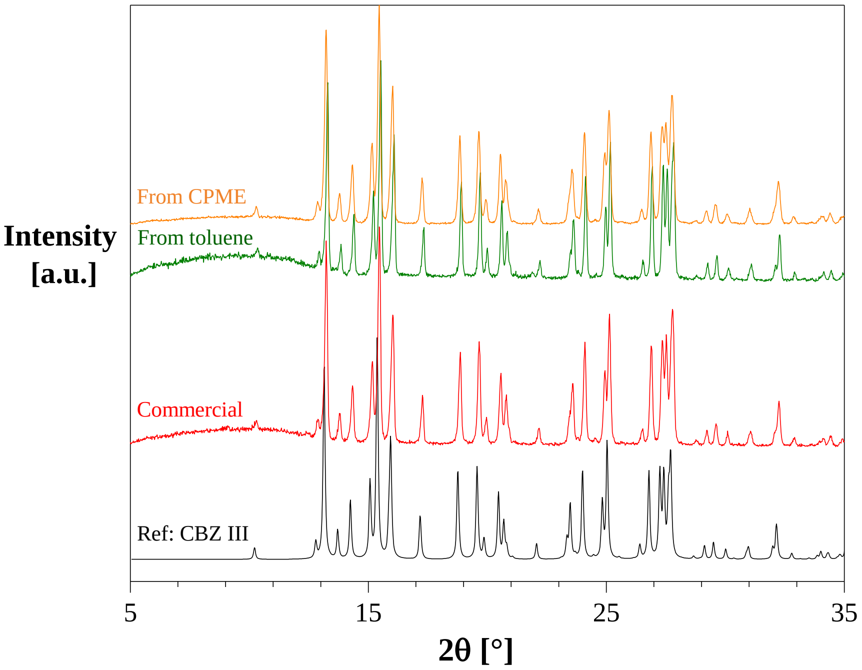

Figure A.10. XRPD spectra of the supplied CBZ material (red) and the recovered solids from their suspensions in toluene (green) and CPME (orange) after 5 days under stirring at approximately 500 rpm at ambient temperature. All the spectra were consistent with the reference form III (CBMZPN01) of CBZ deposited in the CCDC database.

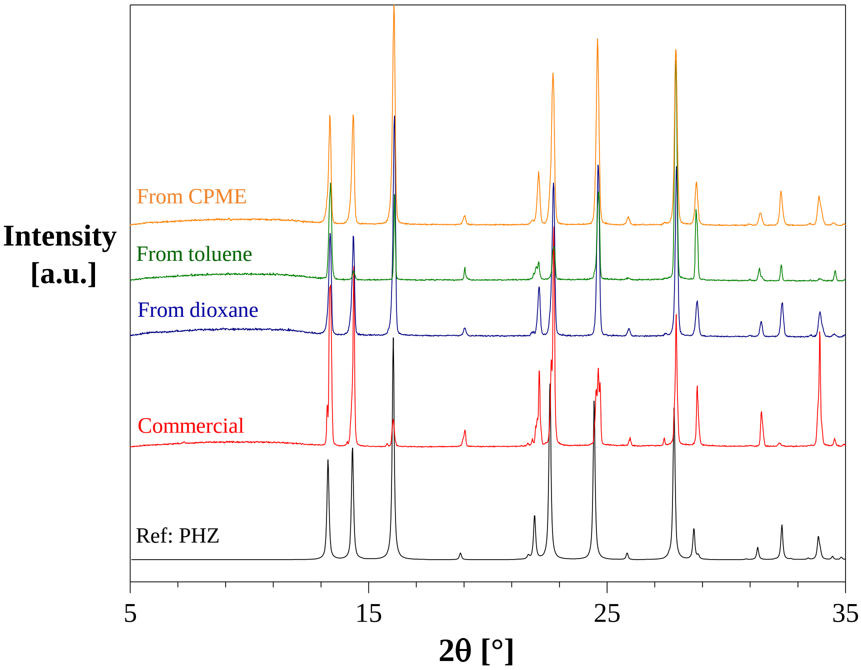

Figure A.11. XRPD spectra of the supplied PHZ material (red) and the recovered solids from their suspensions in dioxane (blue), toluene (green) and CPME (orange) after 5 days under stirring at approximately 500 rpm at ambient temperature. All the spectra were consistent with the reference GEPNOG of PHZ deposited in the CCDC database.

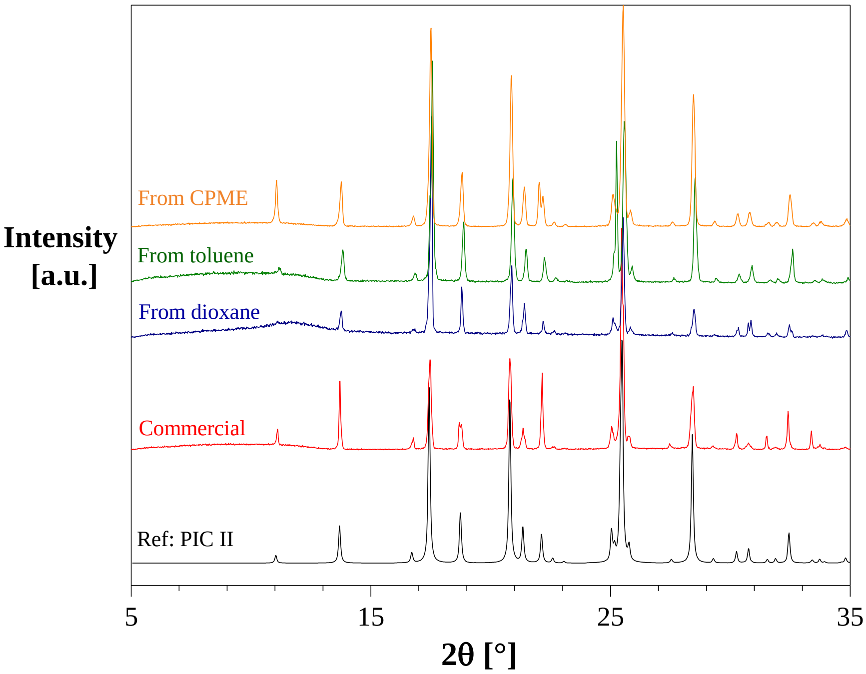

Figure A.12. XRPD spectra of the supplied PIC material (red) and the recovered solids from their suspensions in dioxane (blue), toluene (green) and CPME (orange) after 5 days under stirring at approximately 500 rpm at ambient temperature. All the spectra were consistent with the reference form II (PICAMD) of PIC deposited in the CCDC database.

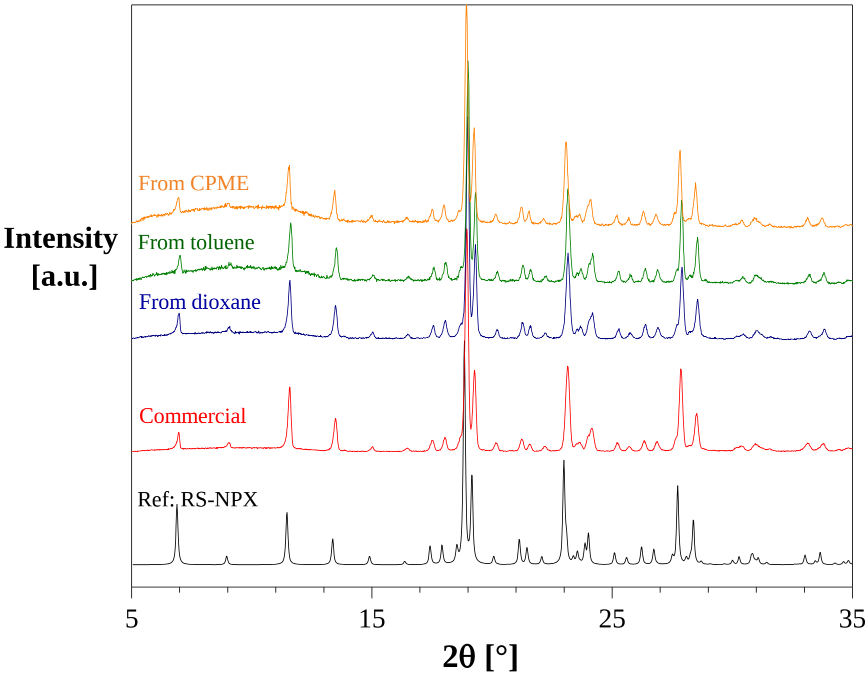

Figure A.13. XRPD spectra of the supplied RS-NPX material (red) and the recovered solids from their suspensions in dioxane (blue), toluene (green) and CPME (orange) after 5 days under stirring at approximately 500 rpm at ambient temperature. All the spectra were consistent with the reference PAPTUX of RS-NPX deposited in the CCDC database.

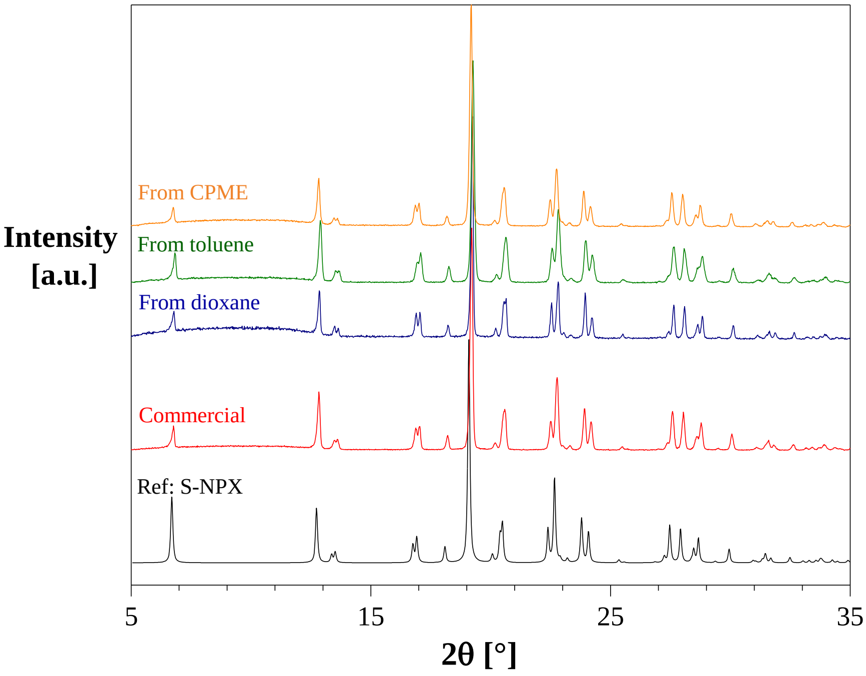

Figure A.14. XRPD spectra of the supplied S-NPX material (red) and the recovered solids from their suspensions in dioxane (blue), toluene (green) and CPME (orange) after 5 days under stirring at approximately 500 rpm at ambient temperature. All the spectra were consistent with the reference COYRUD13 of S-NPX deposited in the CCDC database.

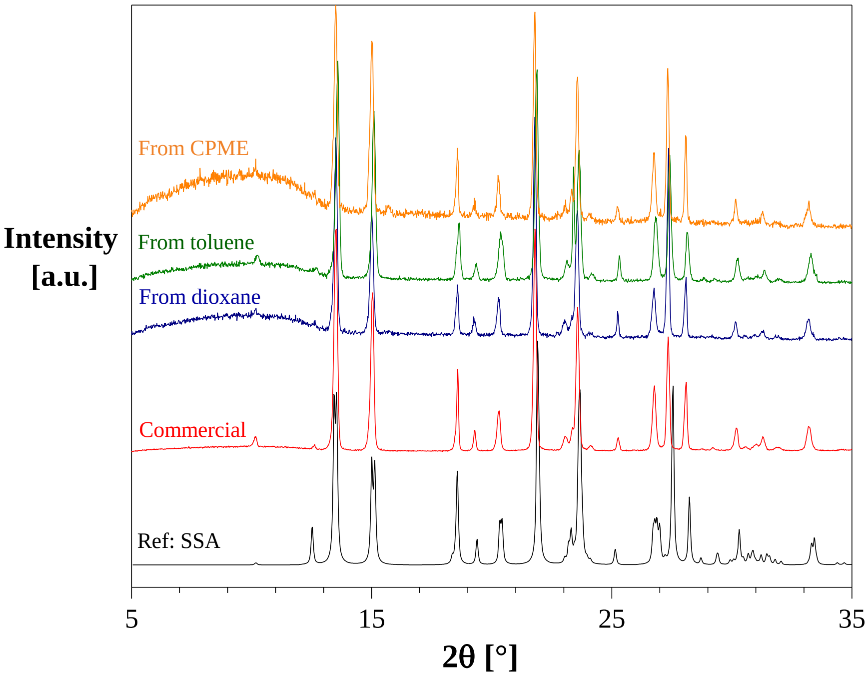

Figure A.15. XRPD spectra of the supplied SSA material (red) and the recovered solids from their suspensions in dioxane (blue), toluene (green) and CPME (orange) after 5 days under stirring at approximately 500 rpm at ambient temperature. All the spectra were consistent with the reference WOQDAH of SSA deposited in the CCDC database.

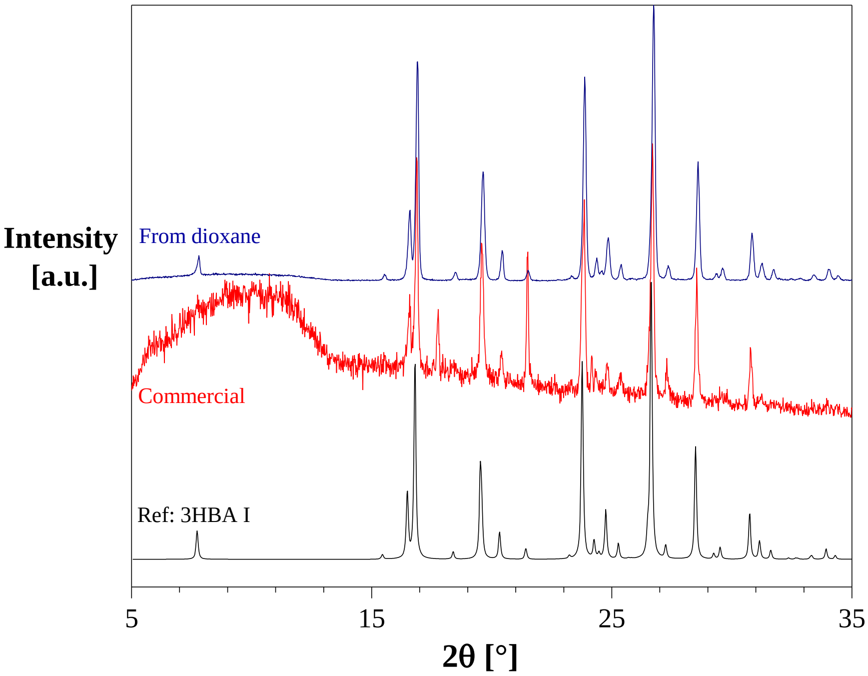

Figure A.16. XRPD spectra of the supplied 3HBA material (red) and the recovered solids from their suspensions in dioxane (blue) after 5 days under stirring at approximately 500 rpm at ambient temperature. All the spectra were consistent with the reference form I (BIDLOP) of 3HBA deposited in the CCDC database.

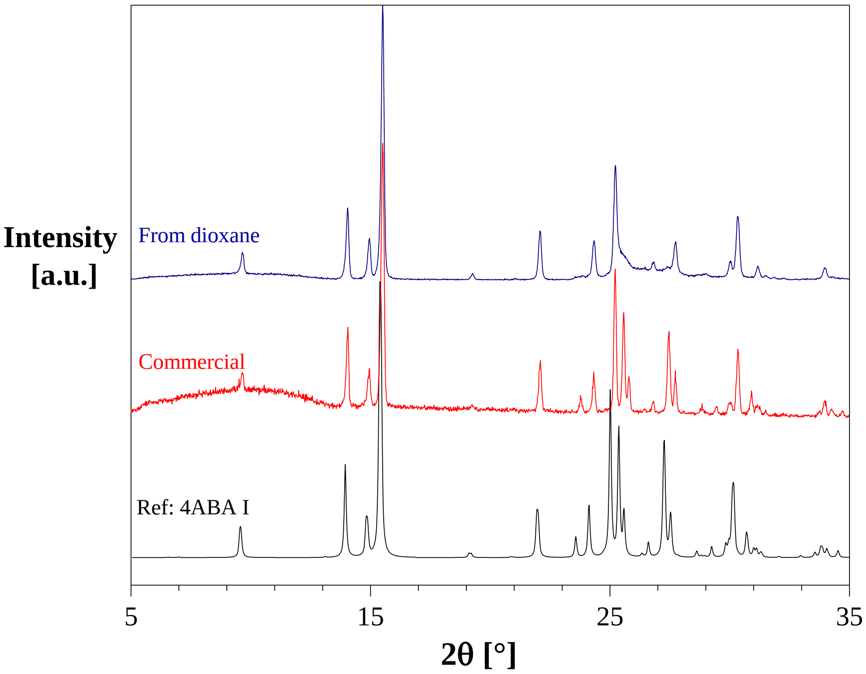

Figure A.17. XRPD spectra of the supplied 4ABA material (red) and the recovered solids from their suspensions in dioxane (blue) after 5 days under stirring at approximately 500 rpm at ambient temperature. All the spectra were consistent with the reference form I (AMBNAC01) of 4ABA deposited in the CCDC database.

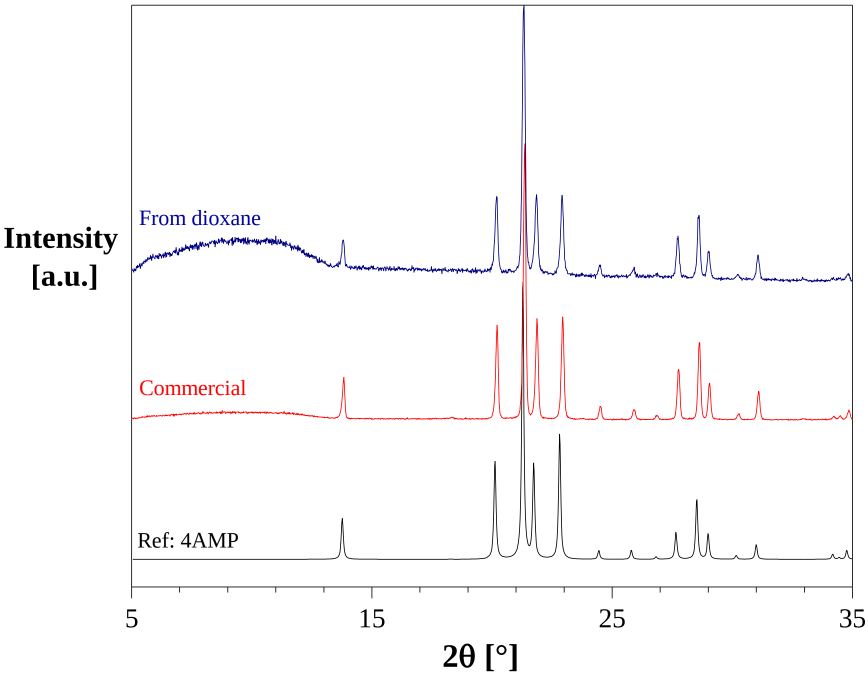

Figure A.18. XRPD spectra of the supplied 4AMP material (red) and the recovered solids from their suspensions in dioxane (blue) after 5 days under stirring at approximately 500 rpm at ambient temperature. All the spectra were consistent with the reference AMPHOL of 4AMP deposited in the CCDC database.

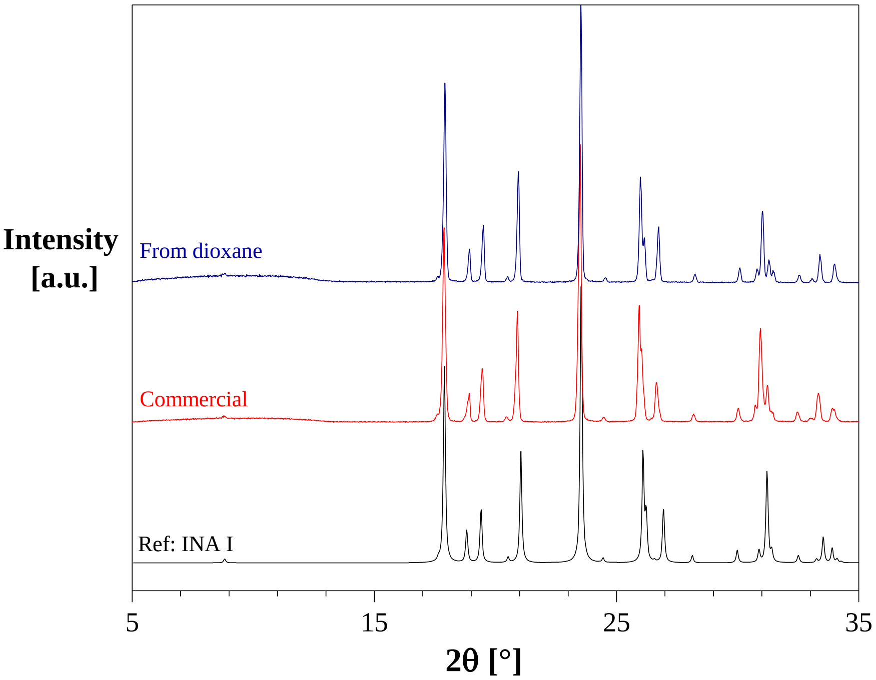

Figure A.19. XRPD spectra of the supplied INA material (red) and the recovered solids from their suspensions in dioxane (blue) after 5 days under stirring at approximately 500 rpm at ambient temperature. All the spectra were consistent with the reference form I (EHOWIH01) of INA deposited in the CCDC database.

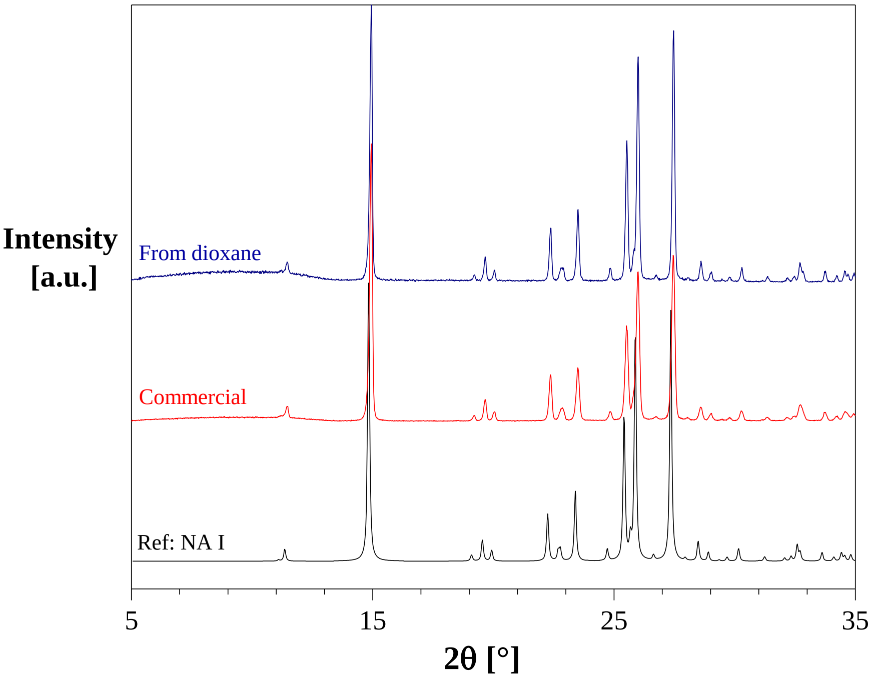

Figure A.20. XRPD spectra of the supplied NA material (red) and the recovered solids from their suspensions in dioxane (blue) after 5 days under stirring at approximately 500 rpm at ambient temperature. All the spectra were consistent with the reference form I (NICOAM) of NA deposited in the CCDC database.

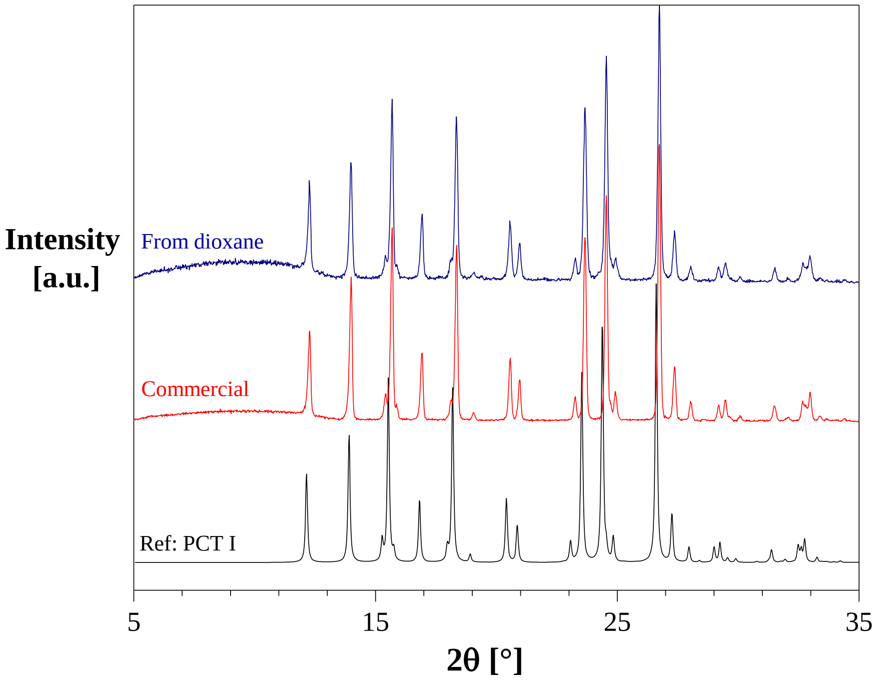

Figure A.21. XRPD spectra of the supplied PCT material (red) and the recovered solids from their suspensions in dioxane (blue) after 5 days under stirring at approximately 500 rpm at ambient temperature. All the spectra were consistent with the reference form I (HXACAN01) of PCT deposited in the CCDC database.

A.3. Experimental solubility data and data correlation using different thermodynamic models of the studied compounds across three apolar solvents.

Table A.1. Mole fraction of the experimental solubility data (x_{exp}) compared to the correlated solubility data (x_{corr}) obtained for 18 APIs and intermediates in dioxane using three semi-empirical equations: van 't Hoff, Apelblat, and the λh equations, and four activity coefficient models: Margules, van Laar, Wilson, and NRTL.

Solute	T [°C]	x_{exp}	x_{corr}							
			van 't Hoff	Apelblat	λh model	Margules	van Laar	Wilson	NRLT α = 0.3	NRLT unrestricted α
2ABA	22.5	0.251	0.250	0.251	0.252	0.228	0.251	0.250	0.244	0.253
	31.4	0.275	0.276	0.276	0.275	0.267	0.274	0.273	0.273	0.275
	35.2	0.287	0.287	0.287	0.286	0.285	0.286	0.284	0.287	0.286
	51.7	0.338	0.337	0.338	0.338	0.368	0.339	0.339	0.350	0.340
2HBA	47.7	0.334	0.335	0.335	0.334	0.331	0.334	0.335	0.339	0.336
	43.7	0.323	0.323	0.323	0.323	0.312	0.319	0.321	0.325	0.323
	48.4	0.337	0.337	0.337	0.336	0.333	0.335	0.336	0.340	0.337
	52.4	0.350	0.349	0.349	0.349	0.350	0.345	0.346	0.350	0.347
	57.7	0.365	0.366	0.365	0.366	0.376	0.365	0.366	0.370	0.367
ASP	36.2	0.164	0.162	0.165	0.162	0.150	0.160	0.160	0.160	0.163
	44.5	0.191	0.191	0.188	0.191	0.186	0.191	0.191	0.191	0.189
	52.6	0.218	0.222	0.219	0.222	0.227	0.225	0.225	0.225	0.223
	58.3	0.246	0.246	0.247	0.247	0.257	0.247	0.248	0.248	0.248
	59.4	0.258	0.251	0.253	0.251	0.258	0.246	0.246	0.246	0.249
	38.9	0.171	0.172	0.172	0.171	0.162	0.170	0.171	0.171	0.171

	42.4	0.183	0.184	0.182	0.183	0.177	0.183	0.183	0.183	0.182
	56.9	0.236	0.240	0.240	0.240	0.251	0.244	0.244	0.244	0.244
CAF	37.2	0.011	0.011	0.011	0.011	0.011	0.011	0.011	0.011	0.011
	43.7	0.014	0.014	0.013	0.014	0.013	0.013	0.013	0.013	0.013
	46.0	0.014	0.015	0.014	0.014	0.014	0.014	0.014	0.014	0.014
	53.8	0.018	0.018	0.018	0.018	0.018	0.018	0.018	0.018	0.018
	48.4	0.016	0.016	0.015	0.015	0.015	0.015	0.015	0.016	0.016
	58.4	0.021	0.020	0.021	0.020	0.021	0.021	0.021	0.022	0.022
	36.6	0.010	0.011	0.011	0.011	0.011	0.011	0.011	0.010	0.010
	30.0	0.008	0.009	0.009	0.009	0.009	0.009	0.009	0.009	0.009
	24.4	0.008	0.008	0.007	0.008	0.007	0.007	0.007	0.007	0.008
	40.7	0.012	0.012	0.012	0.012	0.012	0.012	0.012	0.012	0.012
CBZ	37.2	0.022	0.022	0.022	0.019	0.024	0.022	0.022	0.022	0.022
	46.8	0.032	0.032	0.032	0.030	0.033	0.032	0.032	0.032	0.032
	50.4	0.036	0.037	0.036	0.036	0.037	0.037	0.037	0.036	0.036
	54.8	0.043	0.044	0.044	0.044	0.043	0.044	0.044	0.043	0.043
	56.6	0.047	0.047	0.047	0.048	0.045	0.047	0.047	0.047	0.047
	59.3	0.052	0.052	0.052	0.053	0.049	0.052	0.052	0.052	0.052
	59.8	0.054	0.053	0.054	0.055	0.050	0.053	0.053	0.054	0.054
RSNPX	39.5	0.105	0.106	0.106	0.105	0.101	0.106	0.106	0.106	0.106
	43.3	0.116	0.115	0.115	0.115	0.114	0.115	0.115	0.115	0.115
	45.6	0.122	0.122	0.122	0.122	0.122	0.121	0.122	0.121	0.122
	47.9	0.128	0.128	0.128	0.128	0.130	0.127	0.128	0.128	0.128
	49.8	0.132	0.133	0.133	0.134	0.138	0.134	0.134	0.134	0.134
SNPX	37.9	0.130	0.131	0.130	0.130	0.126	0.132	0.132	0.130	0.131
	43.7	0.145	0.145	0.145	0.145	0.148	0.146	0.146	0.147	0.146
	46.8	0.155	0.154	0.154	0.154	0.160	0.153	0.153	0.155	0.153
	49.7	0.161	0.162	0.162	0.162	0.173	0.162	0.163	0.166	0.163
	31.5	0.116	0.116	0.115	0.116	0.104	0.115	0.116	0.112	0.116
	39.0	0.134	0.133	0.133	0.133	0.129	0.133	0.133	0.132	0.133
PHZ	45.6	0.049	0.049	0.049	0.049	0.051	0.050	0.049	0.049	0.049
	39.3	0.040	0.041	0.041	0.041	0.041	0.041	0.041	0.041	0.041
	32.4	0.033	0.034	0.034	0.034	0.033	0.033	0.033	0.033	0.033
	29.4	0.031	0.031	0.031	0.031	0.030	0.030	0.031	0.030	0.031
	32.9	0.034	0.034	0.034	0.034	0.034	0.034	0.034	0.034	0.034
	35.7	0.038	0.037	0.037	0.037	0.037	0.037	0.037	0.037	0.037
	40.4	0.043	0.042	0.042	0.043	0.043	0.043	0.043	0.043	0.043
PIC	31.2	0.175	0.175	0.176	0.174	0.182	0.174	0.174	0.182	0.174
	39.5	0.226	0.227	0.227	0.228	0.229	0.227	0.227	0.229	0.227
	44.0	0.259	0.260	0.260	0.262	0.260	0.261	0.261	0.260	0.261
	47.0	0.286	0.284	0.284	0.285	0.281	0.286	0.286	0.281	0.286
	50.3	0.317	0.313	0.312	0.313	0.306	0.314	0.314	0.306	0.314
	53.1	0.342	0.339	0.338	0.339	0.329	0.338	0.338	0.329	0.339
	55.7	0.357	0.364	0.364	0.363	0.350	0.360	0.360	0.350	0.361
SSA	53.4	0.268	0.268	0.268	0.267	0.250	0.251	0.259	0.257	0.266
	59.4	0.284	0.284	0.284	0.284	0.289	0.284	0.283	0.288	0.284
	51.3	0.263	0.263	0.263	0.261	0.238	0.240	0.252	0.248	0.261
	61.8	0.291	0.291	0.291	0.292	0.306	0.299	0.294	0.301	0.292
	57.2	0.278	0.278	0.278	0.278	0.275	0.273	0.276	0.278	0.279
	64.2	0.298	0.297	0.298	0.299	0.322	0.313	0.305	0.314	0.300
4ABA	25.1	0.068	0.068	0.068	0.068	0.066	0.067	0.068	0.068	0.068
	38.4	0.094	0.094	0.094	0.094	0.094	0.094	0.094	0.094	0.094
	44.6	0.108	0.108	0.108	0.108	0.110	0.109	0.109	0.109	0.109
	51.7	0.127	0.127	0.127	0.127	0.129	0.127	0.127	0.127	0.127
	28.1	0.073	0.073	0.073	0.073	0.072	0.073	0.073	0.073	0.073
	31.5	0.080	0.080	0.080	0.080	0.079	0.080	0.080	0.080	0.080
	47.5	0.116	0.116	0.116	0.116	0.117	0.115	0.116	0.116	0.116
	53.2	0.131	0.131	0.131	0.131	0.133	0.131	0.131	0.131	0.131
4AMP	30.7	0.025	0.025	0.025	0.025	0.025	0.025	0.025	0.025	0.025
	31.4	0.026	0.026	0.026	0.026	0.026	0.026	0.026	0.026	0.026
	37.7	0.031	0.031	0.031	0.032	0.032	0.031	0.031	0.032	0.031
	24.7	0.021	0.021	0.021	0.021	0.020	0.021	0.021	0.021	0.021
	39.0	0.032	0.032	0.032	0.033	0.034	0.033	0.033	0.033	0.032
3HBA	35.7	0.194	0.195	0.195	0.195	0.169	0.177	0.189	0.185	0.197

	39.8	0.204	0.203	0.203	0.202	0.181	0.182	0.192	0.191	0.200
	43.6	0.211	0.210	0.210	0.210	0.196	0.191	0.201	0.201	0.208
	32.2	0.188	0.188	0.188	0.188	0.156	0.169	0.181	0.175	0.189
	39.9	0.203	0.203	0.203	0.203	0.183	0.184	0.194	0.192	0.202
	45.6	0.214	0.214	0.214	0.214	0.204	0.197	0.206	0.207	0.213
	48.3	0.219	0.219	0.219	0.219	0.216	0.204	0.213	0.215	0.220
	37.7	0.197	0.198	0.198	0.198	0.176	0.182	0.193	0.190	0.201
	52.2	0.227	0.227	0.227	0.228	0.233	0.214	0.224	0.227	0.229
4HBA	26.5	0.080	0.080	0.080	0.080	0.073	0.078	0.077	0.080	0.081
	31.0	0.088	0.088	0.088	0.088	0.082	0.086	0.085	0.088	0.088
	38.0	0.102	0.101	0.101	0.102	0.098	0.100	0.098	0.102	0.101
	42.6	0.111	0.111	0.111	0.111	0.109	0.110	0.108	0.112	0.111
	46.8	0.119	0.120	0.120	0.120	0.119	0.119	0.118	0.121	0.121
	51.4	0.131	0.131	0.131	0.131	0.131	0.128	0.128	0.130	0.131
INA	35.1	0.019	0.020	0.019	0.019	0.019	0.020	0.019	0.020	0.019
	28.3	0.015	0.015	0.015	0.015	0.015	0.015	0.015	0.015	0.015
	39.0	0.023	0.022	0.022	0.023	0.023	0.022	0.022	0.022	0.022
	36.2	0.020	0.020	0.020	0.020	0.020	0.020	0.020	0.020	0.020
	33.3	0.018	0.018	0.018	0.018	0.018	0.018	0.018	0.018	0.018
	25.4	0.014	0.013	0.014	0.013	0.013	0.014	0.014	0.014	0.014
	40.9	0.024	0.024	0.024	0.024	0.024	0.024	0.024	0.024	0.024
	31.9	0.017	0.017	0.017	0.017	0.017	0.017	0.017	0.017	0.017
	46.3	0.028	0.029	0.029	0.030	0.029	0.029	0.029	0.029	0.029
	36.0	0.020	0.020	0.020	0.020	0.020	0.020	0.020	0.020	0.020
	30.0	0.016	0.016	0.016	0.016	0.016	0.016	0.016	0.016	0.016
	52.4	0.036	0.035	0.036	0.037	0.036	0.036	0.036	0.036	0.036
	42.2	0.026	0.025	0.025	0.025	0.025	0.025	0.025	0.025	0.025
NA	34.1	0.025	0.024	0.025	0.024	0.024	0.024	0.024	0.024	0.024
	36.8	0.027	0.027	0.027	0.027	0.027	0.027	0.027	0.027	0.027
	38.4	0.029	0.029	0.029	0.029	0.029	0.029	0.029	0.029	0.029
	40.2	0.031	0.031	0.031	0.031	0.031	0.031	0.031	0.031	0.031
	42.3	0.033	0.033	0.033	0.034	0.033	0.033	0.033	0.033	0.033
4NBA	23.8	0.036	0.037	0.037	0.039	0.040	0.037	0.040	0.040	0.038
	30.1	0.048	0.047	0.047	0.048	0.048	0.046	0.049	0.050	0.047
	33.1	0.053	0.052	0.053	0.053	0.052	0.051	0.054	0.055	0.053
	37.7	0.062	0.061	0.062	0.062	0.059	0.060	0.062	0.064	0.062
	41.5	0.070	0.070	0.070	0.069	0.064	0.067	0.070	0.071	0.070
	46.2	0.080	0.082	0.080	0.080	0.072	0.078	0.080	0.082	0.081
PCT	64.7	0.045	0.045	0.044	0.044	0.043	0.045	0.045	0.045	0.045
	62.2	0.039	0.039	0.039	0.039	0.039	0.039	0.039	0.039	0.039
	63.5	0.042	0.042	0.042	0.042	0.041	0.042	0.042	0.042	0.042
	63.8	0.042	0.042	0.042	0.042	0.042	0.042	0.042	0.042	0.042
	61.4	0.037	0.037	0.037	0.037	0.038	0.037	0.037	0.037	0.037
	64.1	0.043	0.043	0.043	0.043	0.042	0.043	0.043	0.043	0.043

Table A.2. Mole fraction of the experimental solubility data (x_{exp}) compared to the correlation solubility data (x_{corr}) obtained for 10 APIs and intermediates in CPME using three semi-empirical equations: van 't Hoff, Apelblat, and the λh equations, and four activity coefficient models: Margules, van Laar, Wilson, and NRTL.

Solute	T [°C]	x_{exp}	x_{corr}							
			van 't Hoff	Apelblat	λh model	Margules	van Laar	Wilson	NRLT α = 0.3	NRLT unrestricted α
2ABA	35.3	0.155	0.157	0.155	0.156	0.144	0.153	0.149	0.147	0.151
	24.7	0.137	0.135	0.137	0.135	0.108	0.127	0.120	0.115	0.121
	42.4	0.171	0.173	0.170	0.172	0.172	0.171	0.171	0.172	0.173
	52.1	0.194	0.196	0.195	0.196	0.217	0.202	0.207	0.212	0.208
	61.1	0.223	0.219	0.223	0.221	0.263	0.233	0.244	0.253	0.244
2HBA	64.1	0.299	0.297	0.299	0.301	0.325	0.280	0.311	0.318	0.303
	43.6	0.252	0.251	0.252	0.249	0.217	0.284	0.237	0.229	0.243
	57.4	0.280	0.282	0.281	0.282	0.289	0.281	0.289	0.289	0.287
	49.7	0.264	0.265	0.264	0.263	0.248	0.279	0.259	0.255	0.262
	59.9	0.289	0.288	0.288	0.289	0.301	0.275	0.294	0.297	0.288

ASP	43.2	0.059	0.060	0.060	0.060	0.059	0.059	0.059	0.059	0.061
	47.4	0.068	0.068	0.068	0.068	0.069	0.069	0.069	0.069	0.069
	49.7	0.074	0.073	0.073	0.073	0.076	0.076	0.076	0.076	0.073
	52.6	0.079	0.079	0.080	0.079	0.084	0.084	0.084	0.084	0.080
	39.9	0.055	0.055	0.055	0.054	0.052	0.052	0.052	0.052	0.055
	41.1	0.057	0.057	0.057	0.056	0.055	0.055	0.055	0.055	0.057
	45.9	0.064	0.065	0.065	0.065	0.065	0.065	0.065	0.065	0.065
CAF	34.6	0.001	0.001	0.001	0.001	0.001	0.001	0.001	0.001	0.001
	47.2	0.002	0.002	0.002	0.002	0.002	0.002	0.002	0.002	0.002
	58.8	0.004	0.004	0.004	0.004	0.003	0.004	0.004	0.003	0.004
	39.9	0.002	0.002	0.002	0.001	0.002	0.002	0.002	0.002	0.002
	52.4	0.003	0.003	0.003	0.003	0.003	0.003	0.003	0.003	0.003
	54.2	0.003	0.003	0.003	0.003	0.003	0.003	0.003	0.003	0.003
	58.1	0.003	0.004	0.004	0.004	0.003	0.003	0.003	0.003	0.003
CBZ	35.0	0.002	0.002	0.002	0.002	0.002	0.002	0.002	0.002	0.002
	42.0	0.002	0.002	0.002	0.002	0.002	0.002	0.002	0.002	0.002
	50.6	0.003	0.003	0.003	0.003	0.003	0.003	0.003	0.003	0.003
	58.3	0.004	0.004	0.004	0.004	0.004	0.004	0.004	0.004	0.004
	59.3	0.004	0.004	0.004	0.004	0.004	0.004	0.004	0.004	0.004
RSNPX	48.5	0.036	0.037	0.036	0.037	0.038	0.038	0.038	0.038	0.036
	34.2	0.025	0.025	0.025	0.023	0.021	0.022	0.020	0.021	0.025
	42.9	0.031	0.032	0.031	0.031	0.030	0.031	0.030	0.030	0.031
	51.4	0.040	0.040	0.040	0.040	0.043	0.043	0.043	0.043	0.040
	56.6	0.047	0.046	0.047	0.048	0.053	0.051	0.053	0.053	0.047
SNPX	41.7	0.042	0.042	0.042	0.042	0.040	0.040	0.040	0.040	0.042
	45.2	0.047	0.047	0.047	0.047	0.046	0.046	0.047	0.046	0.047
	54.2	0.061	0.062	0.061	0.062	0.065	0.065	0.065	0.065	0.061
	60.4	0.075	0.074	0.075	0.075	0.081	0.083	0.081	0.081	0.075
	37.5	0.037	0.037	0.037	0.037	0.034	0.034	0.034	0.034	0.037
PHZ	28.0	0.022	0.022	0.022	0.022	0.021	0.022	0.022	0.022	0.022
	36.9	0.029	0.029	0.030	0.030	0.029	0.029	0.029	0.029	0.029
	32.6	0.026	0.026	0.026	0.026	0.025	0.025	0.026	0.026	0.026
	40.9	0.033	0.033	0.033	0.033	0.033	0.033	0.033	0.033	0.033
	45.1	0.039	0.038	0.038	0.038	0.038	0.038	0.038	0.038	0.038
	53.7	0.047	0.048	0.048	0.048	0.050	0.050	0.048	0.048	0.048
PIC	42.1	0.040	0.041	0.040	0.041	0.039	0.040	0.040	0.040	0.040
	51.0	0.060	0.058	0.059	0.059	0.055	0.059	0.059	0.059	0.059
	27.0	0.022	0.021	0.022	0.021	0.023	0.022	0.021	0.021	0.022
	36.0	0.031	0.031	0.031	0.031	0.031	0.031	0.031	0.031	0.031
	49.2	0.053	0.054	0.054	0.055	0.051	0.054	0.054	0.054	0.053
SSA	60.8	0.176	0.177	0.176	0.178	0.203	0.197	0.196	0.200	0.192
	46.6	0.148	0.149	0.148	0.150	0.132	0.135	0.137	0.134	0.142
	50.1	0.156	0.156	0.156	0.156	0.147	0.148	0.149	0.148	0.151
	52.5	0.160	0.161	0.161	0.161	0.158	0.158	0.159	0.159	0.160
	50.8	0.158	0.157	0.158	0.157	0.150	0.150	0.152	0.151	0.153
	54.6	0.166	0.165	0.165	0.165	0.168	0.166	0.166	0.167	0.165
	56.8	0.170	0.169	0.170	0.169	0.180	0.177	0.176	0.179	0.174

Table A.3. Mole fraction of the experimental solubility data (x_{exp}) compared to the correlation solubility data (x_{corr}) obtained for 10 APIs and intermediates in toluene using three semi-empirical equations: van ‘t Hoff, Apelblat, and the λh equations, and four activity coefficient models: Margules, van Laar, Wilson, and NRTL.

Solute	**T [°C]**	x_{exp}	x_{corr}							
			van 't Hoff	**Apelblat**	**λh model**	**Margules**	**van Laar**	**Wilson**	**NRLT α = 0.3**	**NRLT unrestricted α**
2ABA	35.7	0.013	0.013	0.013	0.012	0.013	0.013	0.013	0.013	0.013
	43.6	0.018	0.018	0.018	0.018	0.017	0.018	0.018	0.018	0.018

	52.8	0.026	0.027	0.026	0.027	0.024	0.028	0.027	0.028	0.027
	22.4	0.007	0.007	0.007	0.006	0.008	0.007	0.007	0.007	0.007
	33.8	0.012	0.012	0.012	0.011	0.012	0.012	0.012	0.012	0.012
	39.5	0.015	0.015	0.015	0.015	0.015	0.015	0.015	0.015	0.015
	49.1	0.024	0.023	0.023	0.023	0.021	0.024	0.024	0.024	0.024
	52.9	0.026	0.027	0.026	0.028	0.025	0.028	0.028	0.028	0.028
2HBA	32.5	0.007	0.007	0.007	0.007	0.008	0.007	0.007	0.007	0.007
	41.0	0.011	0.011	0.011	0.011	0.011	0.011	0.011	0.011	0.011
	50.3	0.017	0.017	0.016	0.017	0.016	0.016	0.017	0.016	0.017
	53.7	0.019	0.019	0.019	0.020	0.018	0.019	0.019	0.019	0.019
	55.9	0.021	0.021	0.022	0.022	0.020	0.021	0.021	0.021	0.021
	59.1	0.025	0.025	0.025	0.025	0.022	0.025	0.025	0.025	0.025
	60.2	0.027	0.026	0.027	0.026	0.023	0.027	0.027	0.027	0.027
ASP	48.1	0.008	0.008	0.007	0.007	0.008	0.008	0.008	0.008	0.008
	53.5	0.010	0.011	0.011	0.011	0.011	0.010	0.010	0.010	0.010
	54.7	0.011	0.011	0.012	0.012	0.011	0.011	0.011	0.011	0.011
	57.0	0.014	0.013	0.013	0.013	0.012	0.013	0.013	0.013	0.014
	54.0	0.011	0.011	0.011	0.011	0.011	0.011	0.011	0.011	0.011
CAF	19.0	0.003	0.003	0.003	0.002	0.002	0.003	0.003	0.003	0.003
	33.3	0.004	0.004	0.004	0.004	0.004	0.004	0.004	0.004	0.004
	41.2	0.005	0.005	0.005	0.006	0.005	0.005	0.005	0.005	0.005
	28.1	0.003	0.003	0.003	0.004	0.003	0.003	0.003	0.003	0.003
	35.4	0.005	0.005	0.004	0.005	0.005	0.005	0.004	0.004	0.004
	47.6	0.007	0.007	0.007	0.007	0.007	0.007	0.007	0.007	0.007
CBZ	40.8	0.002	0.002	0.002	0.002	0.002	0.002	0.002	0.002	0.002
	52.2	0.004	0.004	0.004	0.004	0.004	0.004	0.004	0.004	0.004
	62.2	0.006	0.006	0.006	0.006	0.006	0.006	0.006	0.006	0.006
	28.7	0.001	0.001	0.001	0.001	0.001	0.001	0.001	0.001	0.001
	46.5	0.003	0.003	0.003	0.003	0.003	0.003	0.003	0.003	0.003
	55.4	0.004	0.004	0.004	0.004	0.004	0.004	0.004	0.004	0.004
	59.0	0.005	0.005	0.005	0.005	0.005	0.005	0.005	0.005	0.005
RSNPX	46.8	0.006	0.006	0.006	0.006	0.006	0.006	0.006	0.006	0.006
	52.7	0.008	0.008	0.008	0.008	0.008	0.008	0.008	0.008	0.008
	59.3	0.012	0.012	0.012	0.012	0.011	0.012	0.012	0.012	0.012
	61.4	0.013	0.013	0.013	0.014	0.012	0.014	0.014	0.014	0.014
	39.0	0.004	0.004	0.004	0.004	0.004	0.004	0.004	0.004	0.004
	48.3	0.006	0.006	0.007	0.006	0.007	0.006	0.006	0.006	0.006
	53.0	0.009	0.008	0.009	0.008	0.008	0.008	0.008	0.008	0.008
	54.8	0.010	0.009	0.009	0.009	0.009	0.009	0.009	0.009	0.009
SNPX	34.7	0.006	0.006	0.006	0.005	0.006	0.006	0.006	0.006	0.006
	50.0	0.012	0.012	0.012	0.012	0.012	0.012	0.012	0.012	0.012
	59.5	0.019	0.019	0.019	0.020	0.018	0.019	0.019	0.019	0.019
	42.7	0.008	0.008	0.008	0.008	0.008	0.008	0.008	0.008	0.008
	46.7	0.010	0.010	0.010	0.010	0.010	0.010	0.010	0.010	0.010
PHZ	9.8	0.015	0.015	0.015	0.015	0.014	0.014	0.015	0.015	0.015

	16.7	0.020	0.019	0.019	0.019	0.018	0.019	0.019	0.019	0.019
	21.1	0.022	0.022	0.022	0.022	0.022	0.022	0.022	0.022	0.022
	24.8	0.025	0.025	0.025	0.025	0.025	0.025	0.025	0.025	0.025
	28.2	0.027	0.028	0.028	0.028	0.028	0.028	0.028	0.028	0.028
	39.4	0.039	0.039	0.039	0.039	0.040	0.040	0.039	0.039	0.039
	45.1	0.046	0.046	0.046	0.046	0.049	0.048	0.046	0.046	0.046
	49.2	0.053	0.052	0.052	0.052	0.055	0.054	0.052	0.052	0.052
	55.6	0.062	0.061	0.062	0.062	0.067	0.065	0.062	0.062	0.062
PIC	37.2	0.020	0.020	0.020	0.020	0.020	0.019	0.019	0.019	0.019
	49.6	0.038	0.038	0.038	0.039	0.033	0.038	0.038	0.038	0.038
	27.9	0.012	0.012	0.012	0.012	0.014	0.012	0.012	0.012	0.012
	36.6	0.019	0.019	0.019	0.019	0.020	0.019	0.019	0.019	0.019
	46.8	0.033	0.033	0.033	0.033	0.030	0.032	0.032	0.032	0.032
	57.3	0.055	0.057	0.057	0.057	0.045	0.058	0.057	0.058	0.057
	58.3	0.062	0.059	0.060	0.060	0.047	0.065	0.063	0.065	0.064
SSA	56.1	0.017	0.017	0.017	0.016	0.016	0.017	0.017	0.017	0.017
	60.3	0.019	0.020	0.019	0.020	0.020	0.020	0.019	0.019	0.019
	62.8	0.022	0.022	0.022	0.023	0.022	0.022	0.022	0.022	0.022
	54.6	0.016	0.016	0.016	0.015	0.015	0.016	0.016	0.016	0.016
	62.1	0.021	0.021	0.021	0.022	0.021	0.021	0.021	0.021	0.021

Appendix B.

B.1. XRPD Analysis: Identification of crystalline structure of the input material.

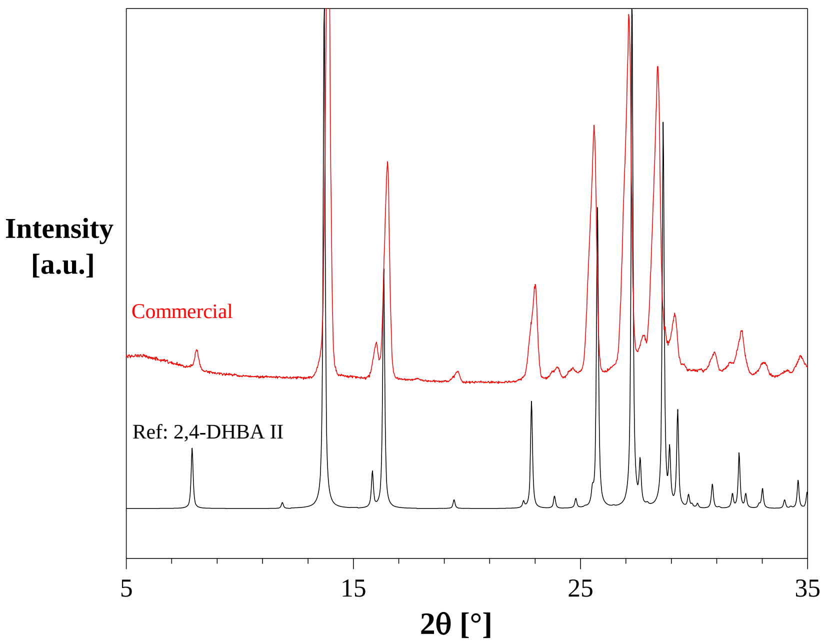

Figure B.1. XRPD data of the 2,4-DHBA compound supplied by Sigma-Aldrich. The obtained diffractogram of the material was consistent with the reference form II (ZZZEEU04) pattern of 2,4-DHBA deposited in the CCDC database.

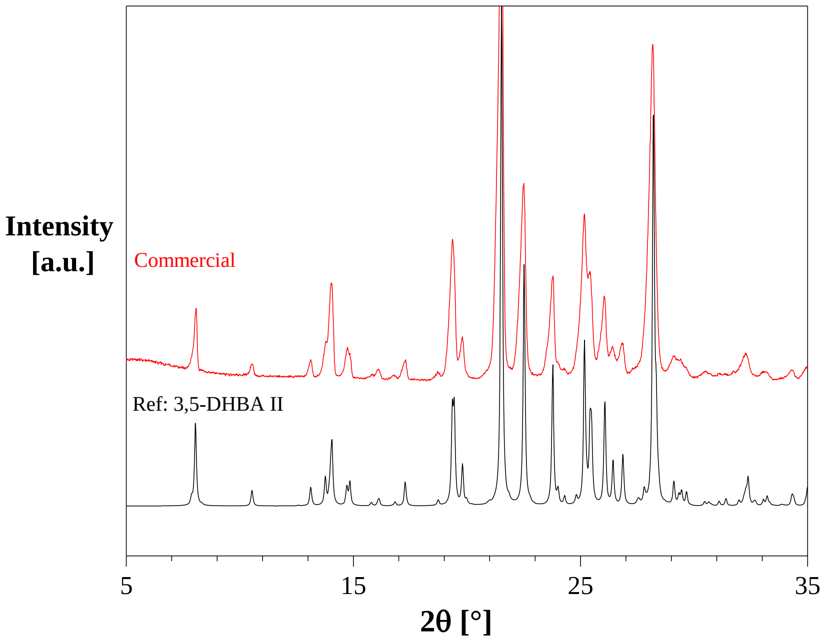

Figure B.2. XRPD data of the 3,5-DHBA compound supplied by Sigma-Aldrich. The obtained diffractogram of the material was consistent with the reference form II (WUYPOW01) pattern of 3,5-DHBA deposited in the CCDC database.

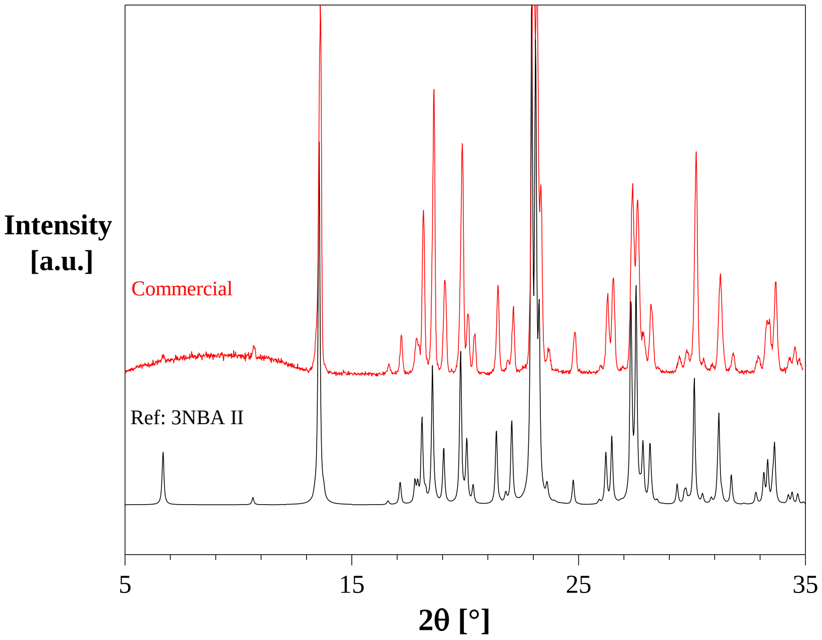

Figure B.3. XRPD data of the 3NBA compound supplied by Sigma-Aldrich. The obtained diffractogram of the material was consistent with the reference form II (MNBZAC04) pattern of 3NBA deposited in the CCDC database.

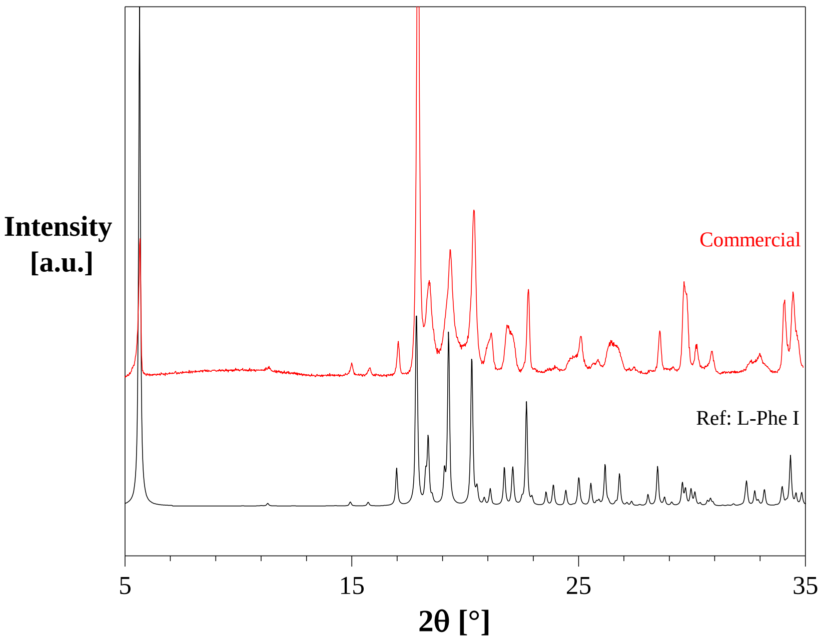

Figure B.4. XRPD data of L-Phe compound supplied by Sigma-Aldrich. The obtained diffractogram of the material was consistent with the reference form I (QQQAUJ06) pattern of the enantiopure compound deposited in the CCDC database.

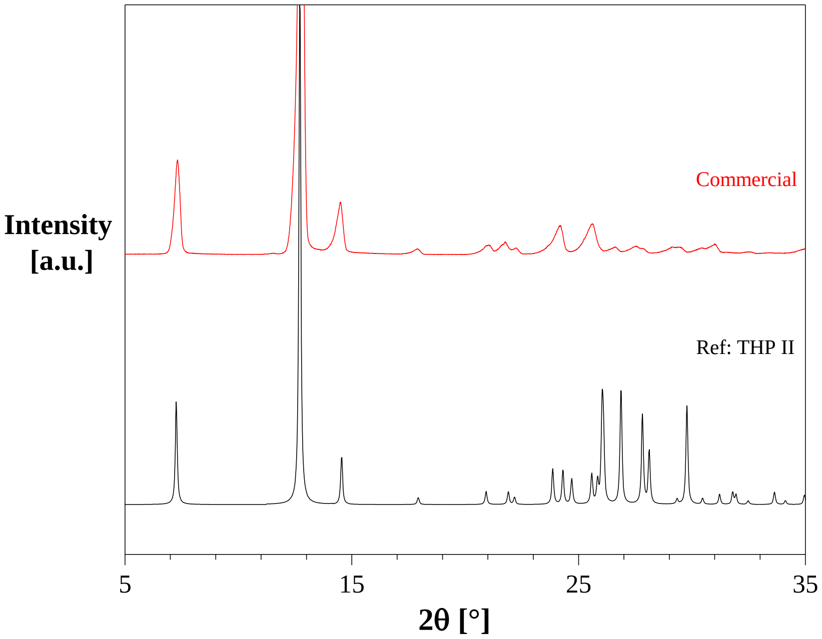

Figure B.5. XRPD data of the THP compound supplied by Sigma-Aldrich. The obtained diffractogram of the material was consistent with the reference form II (BAPLOT06) pattern of THP deposited in the CCDC database.

B.2. XRPD Analysis: Investigation of the crystalline structure of a given compound in different solvents.

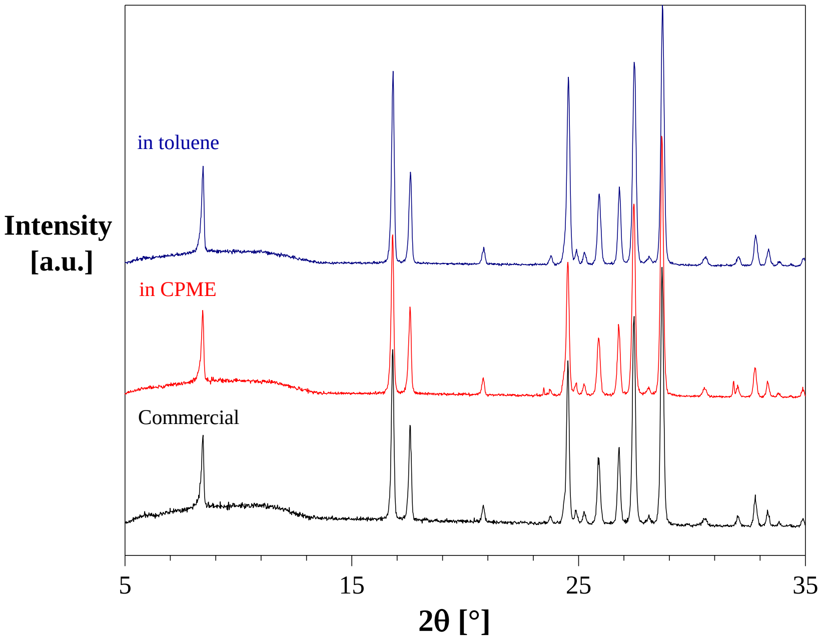

Figure B.6. XRPD spectra of the 3ABA crystals recovered from equilibrated suspensions in toluene and CPME. The recovered solids produced a similar pattern to the 3ABA compound supplied by Alfa Aesar.

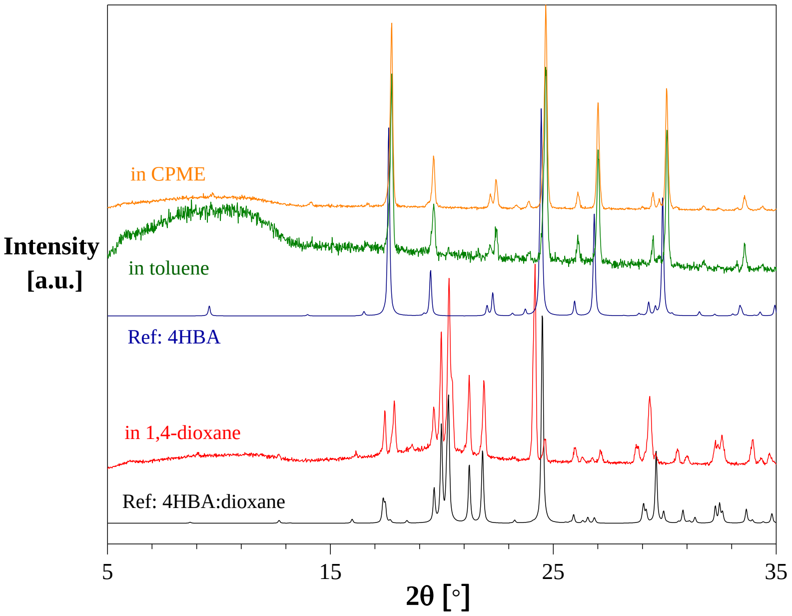

Figure B.7. XRPD spectra of the recovered 4HBA crystals dispersed in 1,4-dioxane (red), toluene (green), and CPME (orange). The patterns were compared to the Cambridge Crystallographic Data Centre (CCDC) references of the 4HBA solvate with 1,4-dioxane – CCDC: PATGEZ (black), and the pure compound – CCDC: JOZZIH (blue). The recovered crystals from the equilibrated suspension of 4HBA in 1,4-dioxane produced a similar diffraction pattern to the referenced solvate. This pattern shows additional peaks at 19° and 25° that suggests the presence of 4HBA crystals. The XRPD analysis indicates that the peaks of the recovered crystals from toluene and CPME suspensions were consistent with the pure 4HBA.

B.3. XRPD Analysis: Comparison between untreated and electrified suspensions.

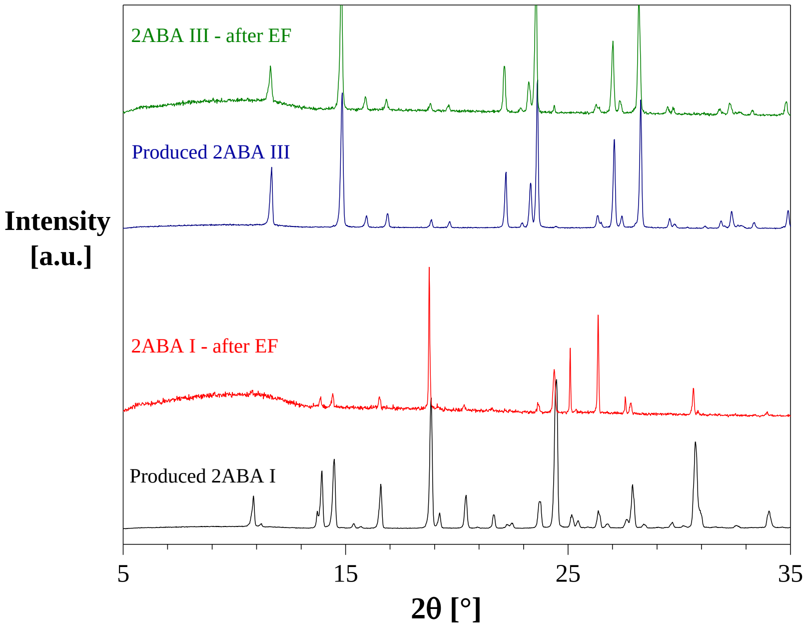

Figure B.8. XRPD patterns of the recovered solids from pure suspensions of 2ABA form I and II after the application of a strong electric field. The spectra of the crystalline material subjected to an electric field were compared to the diffractograms of the produced form I and form II of the crystalline compound. The XRPD data indicates that the crystalline structure is not influenced by the electric field.

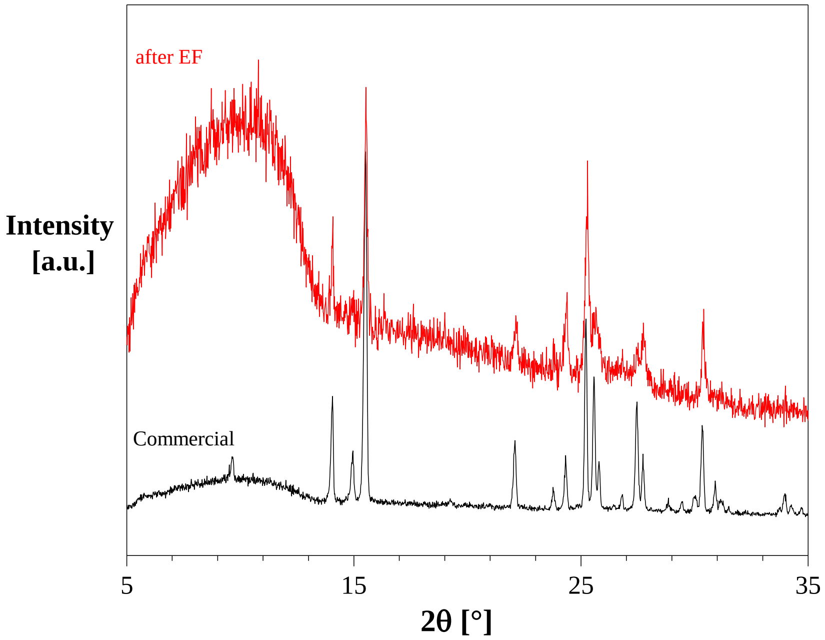

Figure B.9. XRPD patterns of the solids recovered from a suspension of 4ABA in CPME after the application of an electric field. The pattern was similar to the produced pattern of the supplied 4ABA compound by VWR Chemicals. The XRPD data indicates that the crystalline structure is not influenced by the electric field.

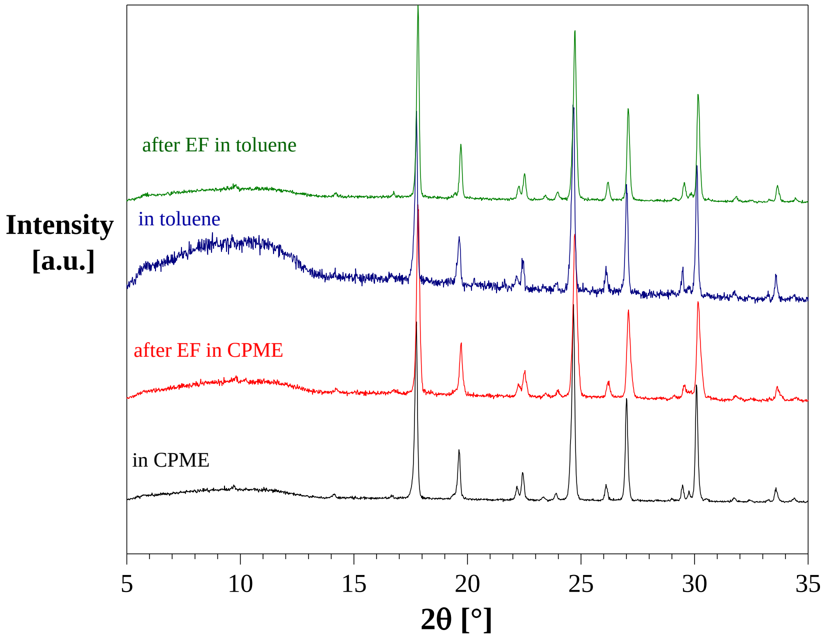

Figure B.10. XRPD patterns of the recovered solids from pure suspensions of 4HBA in toluene and CPME after the application of an electric field. The obtained patterns were compared to the diffractograms of the solids recovered from unelectrified suspensions of the crystalline compound in the same solvent systems. The XRPD data indicates that the crystalline structure is not influenced by the electric field.

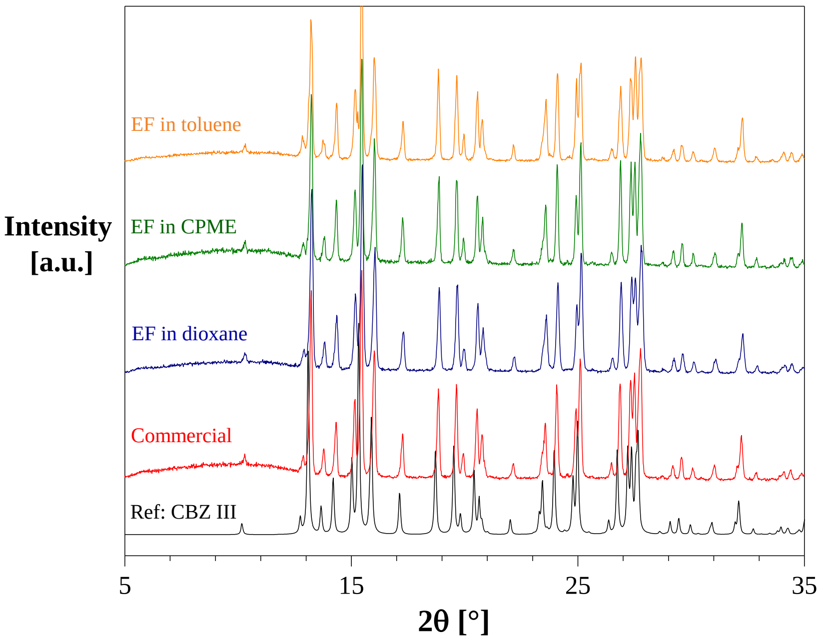

Figure B.11. XRPD spectra of the recovered CBZ crystals in dioxane (blue), CPME (green), and toluene (orange) after the behavioural study of the crystalline compound under an inhomogeneous electric field. The diffractograms were compared to the input material. The XRPD data indicates that the crystalline structure is not influenced by the electric field. The XRPD data were consistent with CBZ form III (CCDC: CBMZPN01).

B.4. Co-crystal Screening

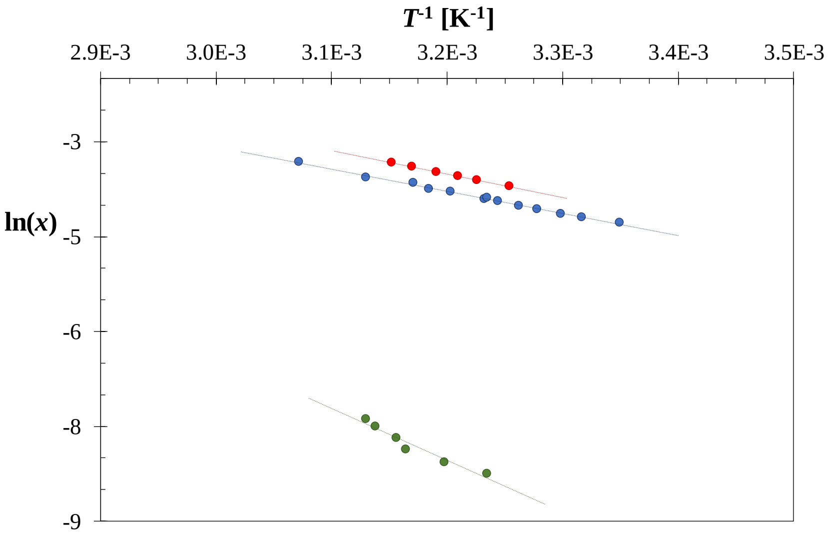

Figure B.12. The van 't Hoff plots of INA (●), NA (●), and mixtures of both compounds were prepared using their individual solubilities at a given temperature T^* to screen the formation of INA:NA co-crystals (●). For instance, the measured solubility of INA and NA at 25 °C (x_{INA} = 13 mmol/mol and x_{NA} = 17 mmol/mol) were used to prepare a mixed suspension of both compounds, expressed as the product of both components as ($x_{\mathrm{INA}} \cdot x_{\mathrm{NA}}$) = 0.2 mmol/mol. The lower solubility of the mixture suggests the formation of a more stable (co-crystal) phase.

B.5. Optical Microscopy: Images of produced polymorphic forms of 4ABA and INA

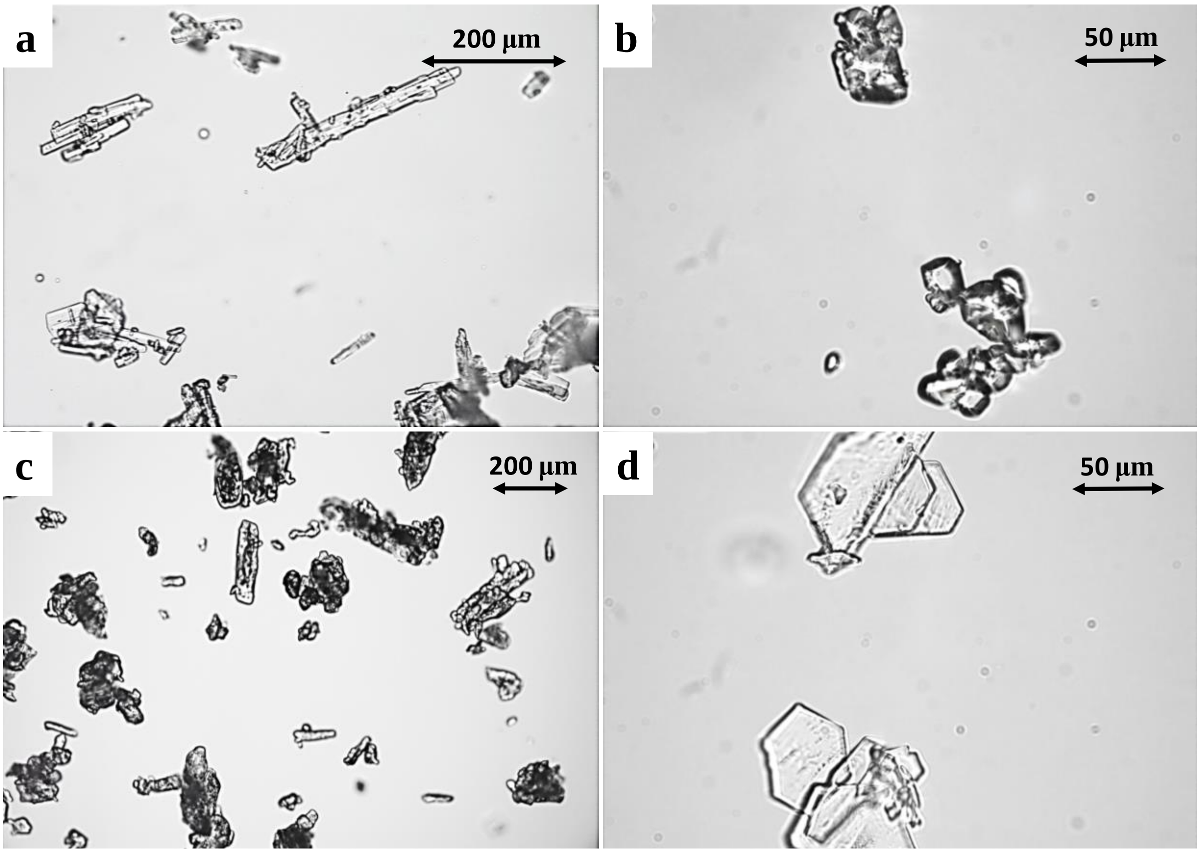

Figure B.13. Crystalline particle images captured by an optical microscope Leica DM6000M. Different polymorphic forms of the same organic compound were obtained by solvent-mediated transformation. The commercial product of 4ABA (a) and INA (c) correspond to the polymorphic form I of the compound. The form IV of 4ABA (b) and III of INA (d), were obtained from recrystallization of the procured crystalline material in water and 1,4-dioxane, respectively.

Appendix C.

C.1. Pseudo-Binary Phase Diagrams.

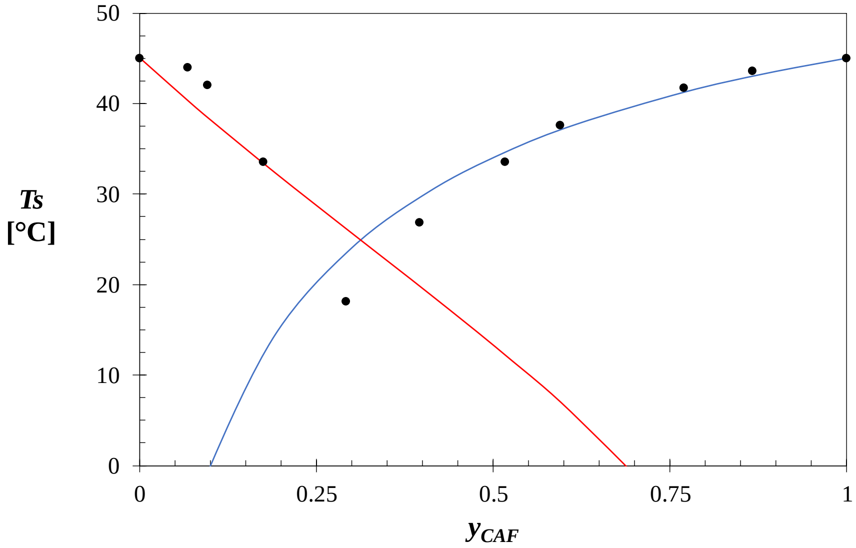

Figure C.1. Pseudo-binary phase diagram of CAF-NA combination in 1,4-dioxane. The saturation temperature T_S at different compositions of the single compounds, represented by a red line for NA and a blue line for CAF, were predicted using the van't Hoff equation. At the chosen reference temperature T^* = 45 °C, the solubilities of the pure compounds CAF and NA in dioxane are x_{CAF}^* = 13.9 and x_{NA}^* = 37.0 mmol/mol, which correspond to solvent excluded mole fractions $y_{CAF} = 1$ and $y_{CAF} = 0$. From $y_{CAF} = 0$, the saturation temperature decreases towards a minimum of 18.1 °C at y_{CAF} = 0.29, and increases to the saturation temperature of pure CAF solution at y_{CAF} = 1. No indication of a more stable was observed, which would be described by the presence of two eutectic points.

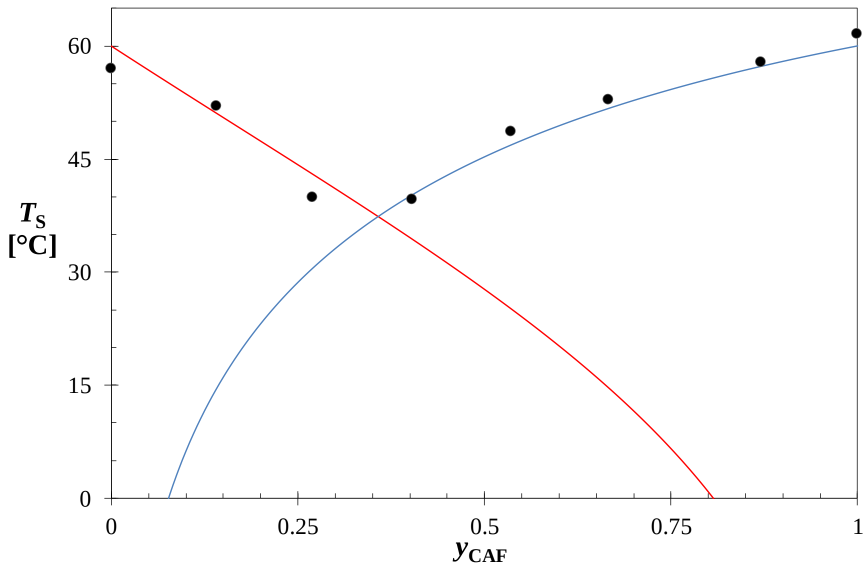

Figure C.2. Pseudo-phase diagram of CAF-INA combination in 1,4-dioxane. The saturation temperature of CAF and INA mixtures was represented against the solvent-excluded mole fraction of CAF. The red and blue lines depict the predicted saturation temperature of pure INA and CAF, respectively using the determined Van't Hoff parameters. A single eutectic point at y_{CAF} = 0.35 indicates the absence of a more stable phase, and therefore a mixure of INA and CAF in 1,4-dioxane consists of a mixed of pure crystals.

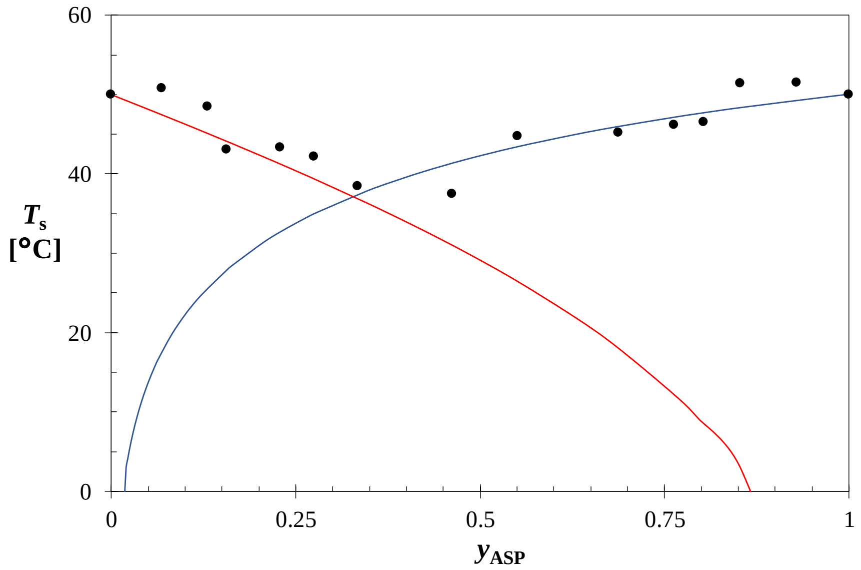

Figure C.3. Pseudo-binary phase diagram of the ASP-SSA combination in toluene. The solid lines represent the saturation temperature T_S of pure ASP (blue) and SSA (red) in toluene predicted using the van't Hoff parameters. The ASP solvent-excluded mole fraction plot shows that at $y_{ASP} = 0$ (corresponding to a saturated solution of SSA) the saturation temperature is 50 °C. The saturation temperature decreases to a minimum at approximately $y_{ASP} = 0.4$. At this point, T_S begin to rises as the amount as ASP is more abundant in solution. The absence of a region of higher T_S at intermediated values of y_{ASP} indicates ASP and SSA are not co-crystal formers.

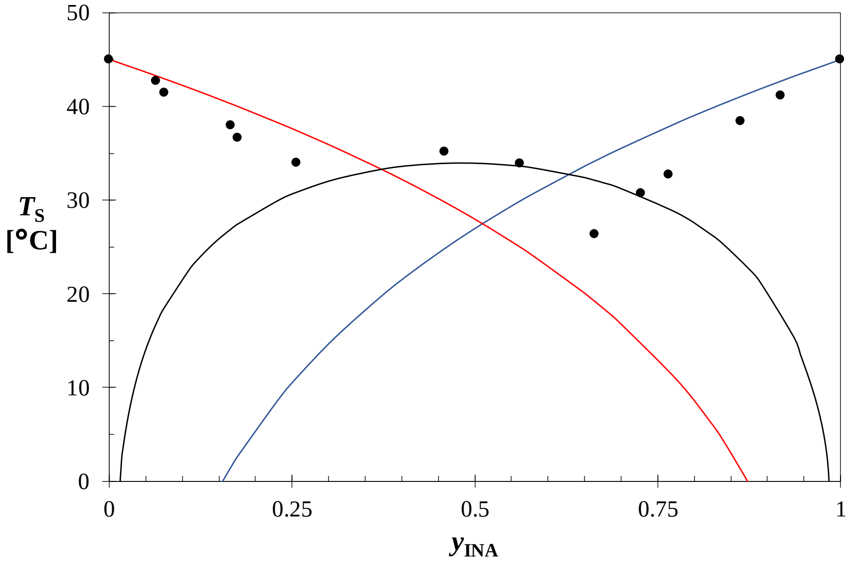

Figure C.4. Pseudo-binary diagram of the solvent-excluded mole fraction of INA against the saturation temperature T_S. The solid lines represent the predicted T_S of CBZ (red) and INA (blue) using the determined van't Hoff parameters (Chapter 4). The greater T_S of the composition mixtures between $y_{INA} = 0.3$ to 0.6 compared to that of the pure compounds, indicates that a more stable phase was formed. The black curve depicts the solubility of the co-crystal as the product of both solutes.

C.2. XRPD Analysis.

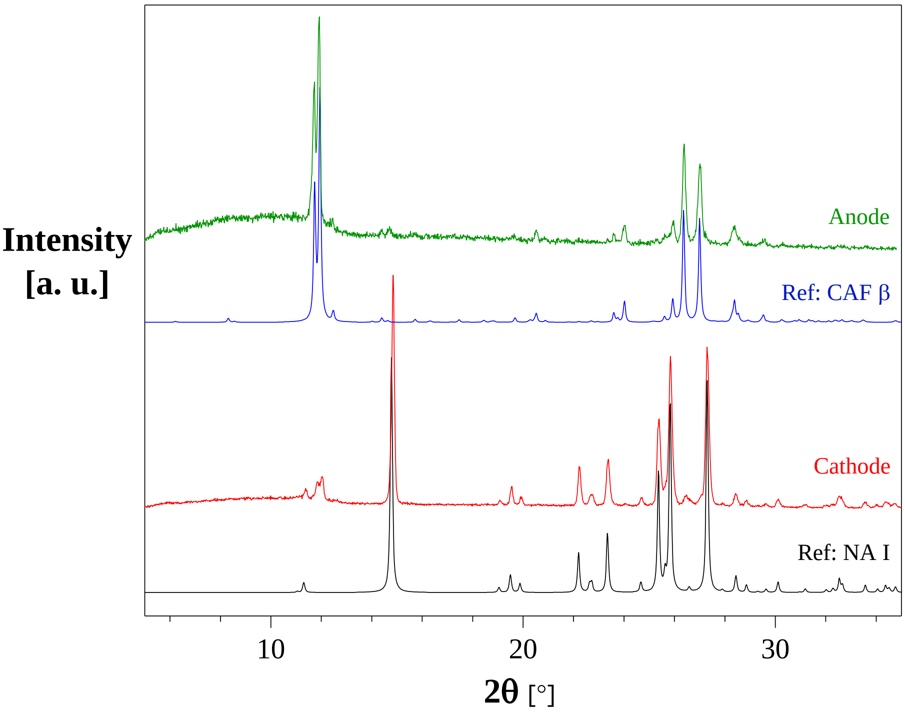

Figure C.5. The X-Ray diffraction patterns obtained from the crystalline material recovered from the anode (green) and cathode (red) at the end of the EFEC carried out on a mixture of CAF and NA in dioxane were compared to the reported crystalline structure NA form I – CCDC: NICOAM (black) and CAF polymorph β – CCDC: NIWFEE03 (blue).

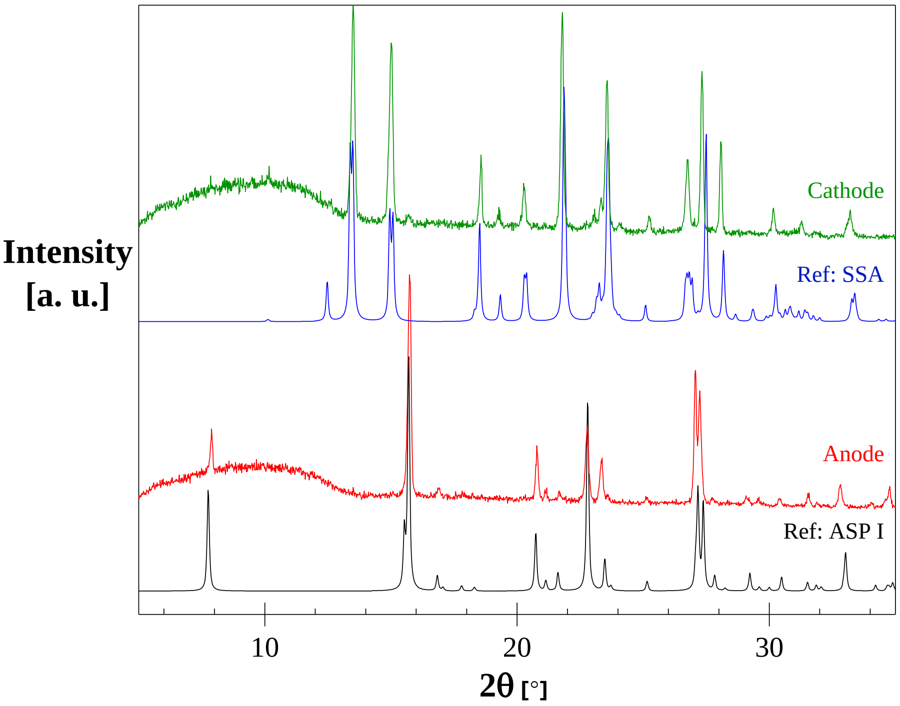

Figure C.6. The XRPD patterns of the crystalline product recovered from the anode (red) and cathode (green) at the end of the EFEC carried out on a mixture of ASP and SSA crystals in toluene compared to reference patterns of aspirin – CCDC: ACSALA (black) and salicylsalicylic acid – CCDC: WOQDAH (blue).

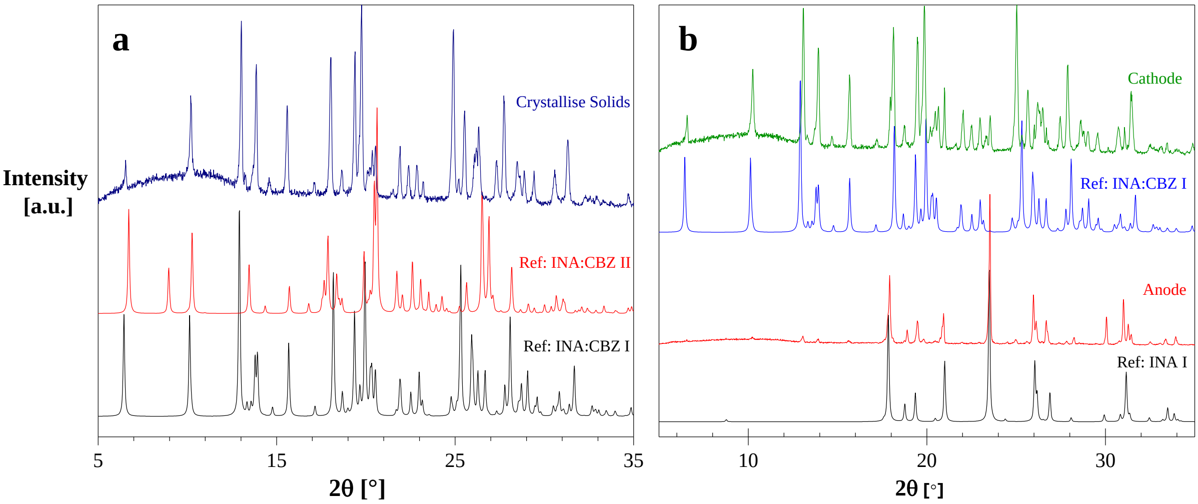

Figure C.7. a: The XRPD diffractogram resulting from co-crystallization product was compared to the reported forms of CBZ:INA (The Cambridge Crystallographic Data Centre (CCDC): LOFKIB and LOFKIB01. The patterns indicate that the product is consistent with the form I of the co-crystal. **b:** The X-ray diffraction patterns generated from the crystalline product recovered from the anode and cathode at the end of an EFEC experiment carried out on a mixture of the INA:CBZ co-crystal and INA in dioxane. The patterns from the cathode (green) was similar to INA:CBZ form I – CCDC: LOFKIB (blue). The XRPD data from the crystals attached to the anode (red) was compared to the reference INA from I – CCDC: EHOWIH01 (black). The crystalline product from the cathode was mainly the form I of the co-crystal.

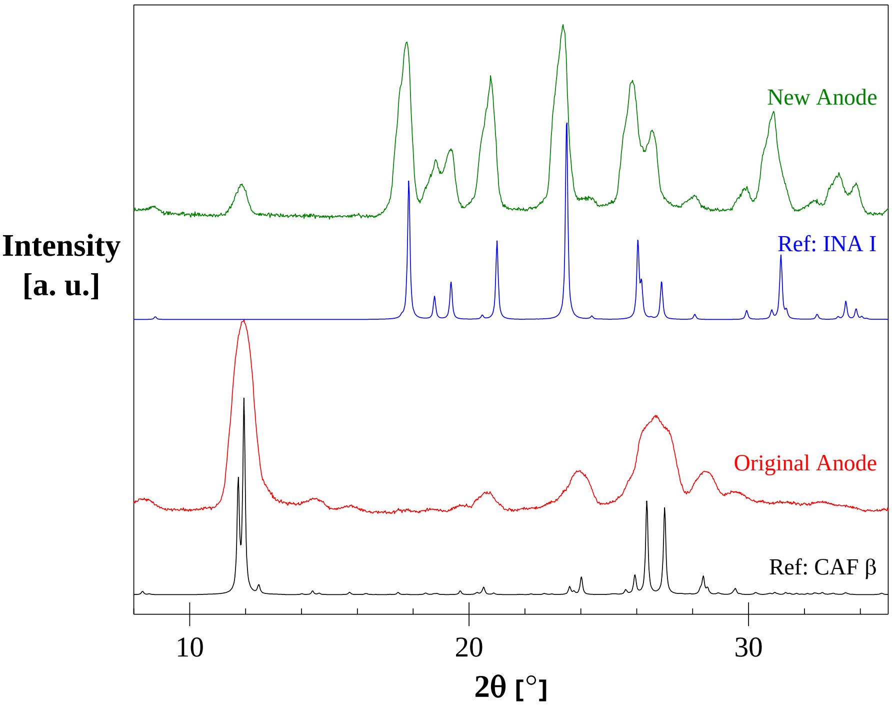

Figure C.8. XRPD data from the crystalline products recovered at the end of the EFEC separation conducted on a mixture of INA and CAF in dioxane was compared to the reference CAF β (CCDC: NIWFEE03) and INA I (CCDC: EHOWIH01). The diffraction pattern from the crystals on the "new" anode was similar to INA I with CAF impurities detected at 12°. The pattern from the crystals retrieved from the "original" anode correspond to the crystal structure of CAF form β.

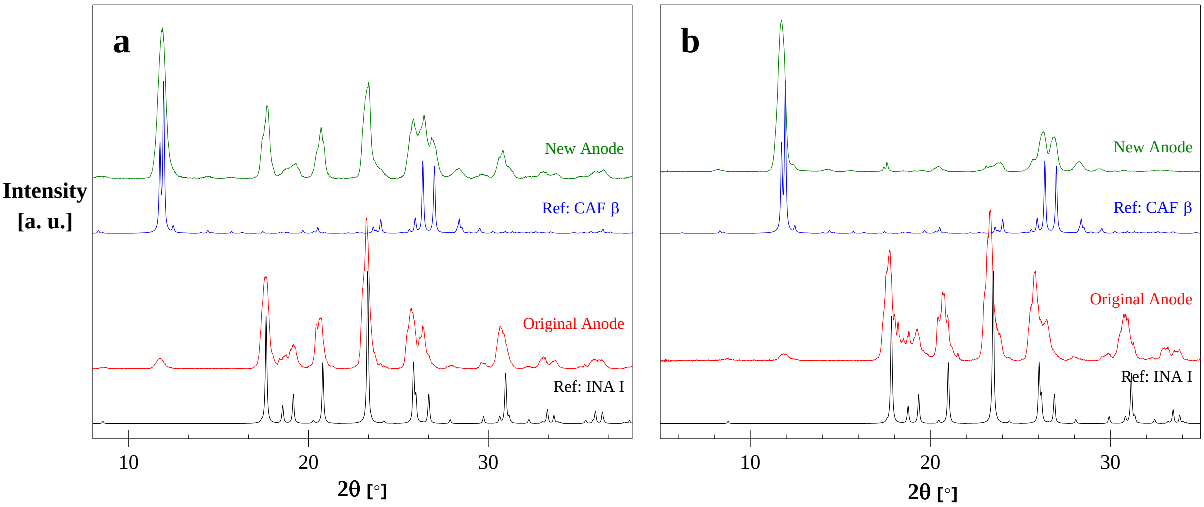

Figure C.9. XRPD difractograms obtained at the end of the end of EFEC carried out on mixtures of INA and CAF in dioxane. **a**: XPRD pattern from the material retrieved after the two-steps EFEC showed the contamination of CAF by INA crystals after reversing the electric field direction. **b**: The addition of a recycling stage after immobilization of INA on the original anode resulted on INA form I (CCDC: EHOWIH01) on the original anode and CAF from β (CCDC: NIWFEE03) on the new anode.

C.3. ^{1}H-NMR: Crystal purity assessment

Table C.1. NMR data for the purity assessment of the crystals collected from the original and new anode. The purity of the crystalline phases in the analysed samples (w_{INA} and w_{CAF}) are calculated from the peak areas corresponding to INA and CAF in the NMR spectrum.

	I_{INA} (a.u.)	$w_{\mathrm{CAF/INA}}$	w_{CAF} (wt%)	W_{INA} (wt%)
Original Anode	5.8	0.05	95.0	5.0
New Anode	6226.7	58.67	1.68	98.3

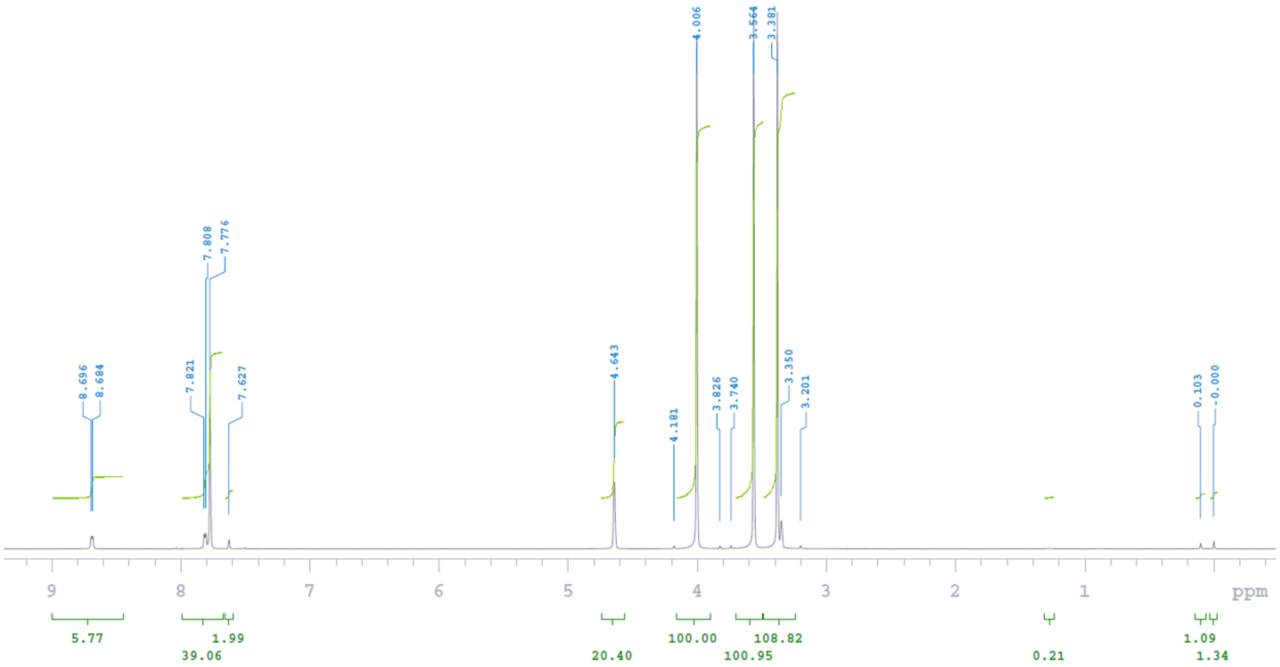

Figure C.10. NMR spectrum of the solids recovered from the original anode. The INA peak and the CAF peaks were identified at 8.7 and 4 ppm, respectively.

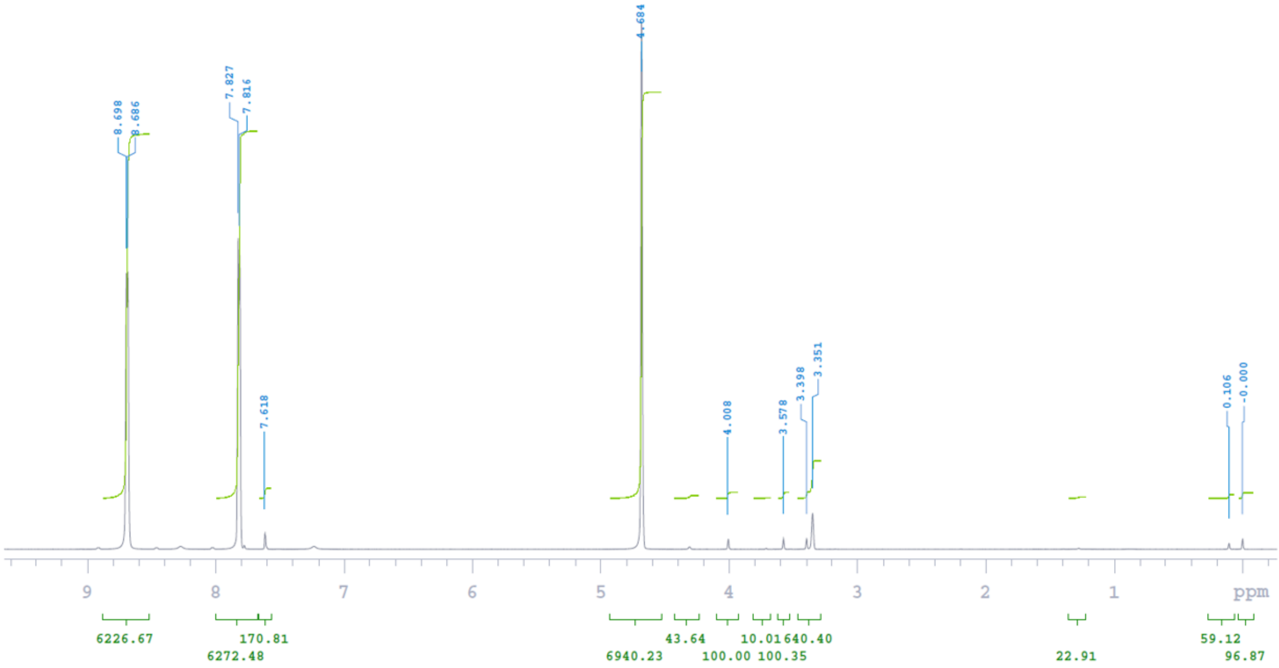

Figure C.11. NMR spectrum of the solids recovered from the new anode. The INA peak and the CAF peaks were identified at 8.7 and 4 ppm, respectively.